Summer 8-4-2020

Constraining H0 with ROTSE Low z Supernovae and Baryon Acoustic Oscillations with DESI High z Galaxies and Quasars

Ryan Staten
Southern Methodist University, rstaten@smu.edu

CONSTRAINING H_0 WITH ROTSE LOW Z SUPERNOVAE
AND BARYON ACOUSTIC OSCILLATIONS WITH DESI
HIGH Z GALAXIES AND QUASARS

Approved by:

Dr. Robert Kehoe
Professor of Physics

Dr. Fred Olness
Professor of Physics

Dr. Jodi Cooley
Associate Professor of Physics

Dr. J. Craig Wheeler
Professor of Astronomy

CONSTRAINING H_0 WITH ROTSE LOW Z SUPERNOVAE AND BARYON ACOUSTIC OSCILLATIONS WITH DESI HIGH Z GALAXIES AND QUASARS

A Dissertation Presented to the Graduate Faculty of the

Dedman College

Southern Methodist University

in

Partial Fulfillment of the Requirements

for the degree of

Doctor of Philosophy

with a

Major in Physics

by

Ryan Staten

B.S., Physics, Southwestern University

August 4, 2020

Acknowledgments

Graduate school has been a challenging experience, with many ups and downs along the way. There are a number of people that have helped me through this long, yet gratifying experience that deserve my many thanks.

I would first like to thank my mother Donna Staten for everything she has done for me throughout my life. Without her, I would never have been able to become the person I am today. I would also like to thank my father Thomas Staten for helping me move to a new city, preparing for my new life in Dallas, and supporting me throughout this process. My younger brother Alex has been a constant inspiration for me through our mutual love of both music and physics.

I am incredibly grateful for the love and support of my partner Lyndahl Himes. As a fellow graduate student, she understands the trials and tribulations that I have endured, and deserves an enormous amount of credit for helping through these times. I would also like to thank my graduate school comrades and beloved friends Matthew Feickert, Eric Godat, and Daniel Jardin for everything they have done for me over the past few years. Without having them alongside, I would not have been able to make it to this point.

My advisor Robert Kehoe has provided ceaseless help and support throughout my time as his advisee, graciously providing me the opportunity to join his research group. I have thoroughly enjoyed my time working with him as a part of the ROTSE and DESI experiments. I would like to thank Govinda Dhungana for helping me become involved in this group, providing much needed help for research endeavors with respect to both experiments.

I very much appreciate Sarah Eftekharzadeh for continuously giving me kind and uplifting support and motivation.

I am incredibly grateful for the help of Coyne Gibson and the McDonald Observatory staff for helping me restore and maintain the ROTSE-IIIb telescope. This effort would never have been possible without their help. I am also grateful for the help of Stephen Bailey and the DESI data system and clustering groups for their consistent guidance on my software and analysis developments over the past several years.

I will forever appreciate the SMU physics department for providing the opportunity to pursue a Ph.D. as a member of their department. Both Lacey Breaux and Michele Hill have continuously helped everyone involved, consistently ensuring the functionality and cohesion of the department. I would like to thank Steve Sekula for his uplifting support of all graduate students as students, researchers, and teaching assistants each and every year. The late Kent Hornbostel provided expert guidance as my professor in a number of courses, with many kind words along the way.

I would very much like to thank my committee members including Fred Olness for his positive help not only as the leader of my dissertation committee, but also for his help throughout my teaching assistantships under his guidance. I would also like to thank Jodi Cooley for her support as a committee member, from before qualification all the way up to my thesis defense. J. Craig Wheeler also deserves my gratitude, for his help as a committee member and as a wonderful collaborator with respect to our ROTSE analyses.

In summation, I am immensely grateful for everyone that has supported me throughout my time as a graduate student. This would never have been possible without the love and support of my dearest friends and family and the incredible environment provided by the SMU community.

Staten, Ryan B.S., Physics, Southwestern University

Constraining H_0 with ROTSE Low z Supernovae
and Baryon Acoustic Oscillations with DESI
High z Galaxies and Quasars

Advisor: Dr. Robert Kehoe
Doctor of Philosophy degree conferred August 4, 2020
Dissertation completed July 23, 2020

Observations of supernovae (SNe) and galaxies provide the ability for astrophysicists and cosmologists to understand the expansion history of the universe. Through photometric observations of SNe by the ROTSE-III experiment, I examine the ability to use core collapse supernovae as distance probes to their host galaxies and subsequently determine the expansion of the local universe. In particular, I test the viability of stripped envelope SNe as candidates for the expanding photosphere method and use distance measurements to Type IIP SNe the calculate the Hubble constant of the local universe. Through spectroscopically observing galaxies and quasars, the DESI experiment looks to determine the expansion history of the universe to distances farther than 10 billion light years away. For this experiment, I work to develop spectroscopic simulations and a spectroscopic reduction pipeline to be used for data quality assessment. Additionally, I examine the effects of observing conditions on the ability to extract cosmological parameters by measuring the effects of baryon acoustic oscillations seen in the clustering measurements of galaxies and quasars.

TABLE OF CONTENTS

LIST OF FIGURES

LIST OF TABLES

This dissertation is dedicated to all of my wonderful friends and family that have helped me through this process, and my adorable dogs Baxter and Bailey that continuously provide unconditional love and support.

Chapter 1

Introduction

The universe is in a state of continuous expansion and the rate at which it expands at different times can offer insight into many fundamental aspects of physics and cosmology. Cosmological distance measurements are required to study this expansion, where many techniques are used to determine distances to various astrophysical sources ranging from variable stars to galaxies. The objective of this thesis is to perform cosmological distance measurements to the host galaxies of supernovae and determine the expansion rate of the local universe, and to examine the effects of observational systematics on distance scales revealed in the clustering measurements of galaxies and quasars. This chapter describes the road leading to modern cosmology, its current interpretation, and the mathematical and conceptual framework behind the topics of this thesis.

1.1. From Newton to Cosmology

Before the early 20th century, gravitational physics was described by Newtonian mechanics. This was a very good approximation for simple stellar orbits and most of what we see in the solar system. However, there was one particular anomaly that called this formalism into question. Early observations of Mercury show that its orbit displays unusual behavior, leading to the postulation of another planet influencing Mercury's orbit in order to describe this motion using Newtonian mechanics. However, we now know that this planet does not exist, as Albert Einstein was able to solve the issue by providing a mathematical framework that describes spacetime as a four-dimensional curved space using Riemannian geometry [1]. It turns out that this anomalous behavior can actually be described by the precession of the perihelion of Mercury, or the point at which it is closest to the sun [2].

Einstein's equations have been solved in many ways, including solutions describing the universe and its expansion properties. The expansion of the universe was theoretically predicted by Alexander Friedmann [3] and Georges Lemaître using general relativity in 1927 [4]. These predictions were experimentally verified by Edwin Hubble [5] in 1929, by examining the redshift of galactic spectra. Hubble's efforts did indeed provide the first evidence of an expanding universe and paved the way for modern cosmology. By comparing recessional velocity to distance, Hubble was able to form a relationship that describes the expansion rate. This relationship,

$$v = H_0 d, \tag{1.1}$$

postulates a constant, H_0, that was initially thought to be the same throughout the entire expansion history of the universe. Although Hubble's initial estimate for the expansion rate of the universe was highly overestimated at a value of 500 km/s/Mpc using the distances and velocities to stars and nebulae [5], it certainly paved the way for modern cosmology.

As the number of observations of spectral redshift continued to increase, the notion of an expanding universe became solidified. However, in the late 1990s, measurements of Type Ia supernovae (SNe Ia) over the redshift range $0 < z < 1$ by two independent groups radically changed our understanding of the nature of this expansion [6] [7]. Deviations from previous measurements imply that as one looks further back in time, an accelerated expansion of the universe is observed. This accelerated expansion can be described as the vacuum energy density, where a cosmological constant was initially inserted into Einstein's equations to counter the notion that his equations allow for an expanding universe.

The standard model of Big Bang cosmology is described by the Lambda cold dark matter model (ΛCDM). This model describes the accelerated expansion of the universe using the cosmological constant (Λ), with the large scale structure of galaxy clusters and superclusters described by cold dark matter (CDM). Cold dark matter is often hypothesized as weakly interacting massive particles (WIMPs) traveling at speeds much less than the speed of light.

ΛCDM still requires observational verification and relies on the general theory of relativity as its mathematical framework.

1.2. General Relativistic Description of the Universe

While Newtonian mechanics depicts the interactions of gravitational bodies using Euclidean geometry where time and space are separate entities, the general theory of relativity combines space and time into a 4-D spacetime. This theory uses Riemannian geometry to describe the curvature of spacetime, where straight world lines described by Newtonian mechanics now become geodesics in curved spacetime.

1.2.1. The spacetime interval and metric tensor

The spacetime interval is the most general expression for distances in this 4-D differentiable manifold, given by

$$ds^2 = g_{\mu\nu} dx^\mu dx^\nu \tag{1.2}$$

where $g_{\mu\nu}$ is the metric tensor

$$g_{\mu\nu} = \begin{pmatrix} g_{00} & g_{01} & g_{02} & g_{03} \\ g_{10} & g_{11} & g_{12} & g_{13} \\ g_{20} & g_{21} & g_{22} & g_{23} \\ g_{30} & g_{31} & g_{32} & g_{33} \end{pmatrix}, \tag{1.3}$$

and μ and ν represent spatial and temporal coordinates ranging from 0 to 3, summed over using the Einstein convention. In Euclidean space, the metric tensor is simply the Kronecker delta, $\delta_{\mu\nu}$, which is $g_{\mu\nu} = 0$ for $\mu \neq \nu$ and $g_{\mu\nu} = 1$ for $\mu = \nu$. In spherical coordinates using

$g_{\mu\mu}$=(-1,1,1,1), this can be more explicitly written as

$$ds^2 = -dt^2 + dr^2 + d\theta^2 + d\phi^2. \tag{1.4}$$

In Riemannian space, however, any deviations from the Kronecker delta, or Minkowski space, represent the curving of spacetime due to the gravitational influence of a massive body.

1.2.2. Einstein's field equation

Using the metric tensor and spacetime interval, one can derive the energy and momentum dynamics of a given system via the Einstein field equation

$$G_{\mu\nu} = R_{\mu\nu} - \frac{1}{2}Rg_{\mu\nu} + \Lambda g_{\mu\nu}, \tag{1.5}$$

where $G_{\mu\nu}$ is the 4×4 Einstein tensor given by

$$G_{\mu\nu} = 8\pi T_{\mu\nu} \tag{1.6}$$

using geometrized units of $G = c = 1$. $T_{\mu\nu}$ is the 4×4 stress energy tensor, which describes the energy and momentum density and flux, as well as the pressure and shear stress shown in Figure 1.1. Equation 1.5 also includes the Ricci scalar

$$R = g^{\mu\nu}R_{\mu\nu} \tag{1.7}$$

and the 4×4 Ricci curvature tensor

$$R_{\mu\nu} = R^{\alpha}_{\mu\alpha\nu} = \partial_\alpha \Gamma^{\alpha}_{\nu\mu} - \partial_\nu \Gamma^{\alpha}_{\alpha\mu} + \Gamma^{\alpha}_{\alpha\beta}\Gamma^{\beta}_{\nu\mu} - \Gamma^{\alpha}_{\nu\beta}\Gamma^{\beta}_{\alpha\mu}, \tag{1.8}$$

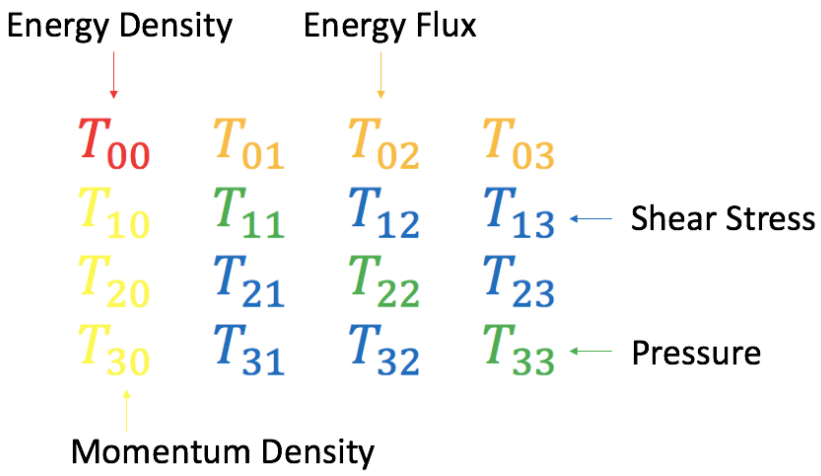

Figure 1.1: A physical representation of the components of the stress energy tensor, $T_{\mu\nu}$.

where

$$\Gamma^{\alpha}_{\mu\nu} = g^{\alpha\beta}\Gamma_{\beta\mu\nu} = \frac{1}{2}g^{\alpha\beta}(\partial_\nu g_{\beta\mu} + \partial_\mu g_{\beta\nu} - \partial_\beta g_{\mu\nu}) \tag{1.9}$$

are the Christoffel symbols that allow one to use the spacetime interval to calculate solutions to the Einstein field equation. The Ricci tensor essentially represents the amount of curvature or deformation in a given space defined by the spacetime metric and the Christoffel symbols provide the connection to this metric. These symbols are members of the SO(3,1) Lorentz group for general relativity. The final element of the field equation is Λ, or the cosmological constant.

1.2.3. The Friedmann-Lemaître-Robertson-Walker metric

Under the assumption of an isotropic and homogeneous universe, one can derive the Friedmann-Lemaître-Robertson-Walker (FLRW) metric

$$ds^2 = -dt^2 + a(t)^2\Big(\frac{dr^2}{1-kr^2} + r^2(d\theta^2 + sin^2\theta d\phi^2)\Big), \tag{1.10}$$

where $a(t)$ is the scale factor of the universe and k is the curvature parameter belonging to the set $\{-1, 0, 1\}$, representing negative, zero, and positive curvature of the universe, respectively.

Determining the time evolution of the scale factor $a(t)$ requires solutions to the field equation. This metric implies that $R_{\mu\nu}$ and R become

$$R_{\mu\nu} = \begin{pmatrix} -3\frac{\ddot{a}}{a} & 0 & 0 & 0 \\ 0 & \frac{a(t)\ddot{a}(t)+2\dot{a}(t)^2+2k}{1-kr^2} & 0 & 0 \\ 0 & 0 & r^2(a(t)\ddot{a}(t)+2\dot{a}(t)^2+2k) & 0 \\ 0 & 0 & 0 & r^2(a(t)\ddot{a}(t)+2\dot{a}(t)^2+2k)sin^2\theta \end{pmatrix} \tag{1.11}$$

and

$$R = 6\left(\frac{\ddot{a}(t)}{a(t)} + \frac{\dot{a}(t)^2}{a(t)^2} + \frac{k}{a(t)^2}\right), \tag{1.12}$$

respectively. The solutions are the Friedmann equations that describe the evolution of an expanding isotropic and homogeneous universe, given by

$$\frac{\dot{a}^2 + k}{a^2} = \frac{8\pi\rho + \Lambda}{3} \tag{1.13}$$

and

$$\frac{\ddot{a}}{a} = -\frac{4\pi}{3}(\rho + 3p) + \frac{\Lambda}{3}, \tag{1.14}$$

where ρ and p are density and pressure, respectively.

1.3. Cosmological Parameters

In order to use the FLRW metric for cosmology, the cosmological principle stating that the universe is isotropic and homogeneous on large scales must be satisfied. Observations

of temperature fluctuations of the cosmic microwave background (CMB), most recently via the Planck satelitte [8], show that the universe is statistically isotropic down to 1 part in 10^5. Additionally, astronomical surveys such as the Baryon Oscillation Spectroscopic Survey (BOSS) [9] show that homogeneity is observable in the clustering of galaxies on cosmological scales. Therefore, based on current observational evidence, the FLRW metric can be employed for cosmological modeling.

1.3.1. Hubble Parameter and Cosmological Redshift

While Equation 1.1 includes the Hubble constant which represents the current value of the Hubble parameter, it can be related to the Friedmann solutions using

$$H \equiv \frac{\dot{a}}{a}, \tag{1.15}$$

where $a(t)$ describes the relative expansion of the universe with a=1 at present, and H is the Hubble parameter that characterizes the expansion history of the universe. Observations of SNe Ia [6] [7] indicate that H is increasing.

If a photon is emitted by a source that is traveling away from the observer, its wavelength will be stretched as specified by the Doppler effect, defined as redshift. This implies that due to the expansion of the universe, the wavelength of a photon emitted by an astrophysical source will be stretched. If this is the case, however, there is a distinction between this and the Doppler effect as the lengthened wavelength is due to the expansion of space itself rather than the receding source. If this effect is purely due to cosmological expansion, it is deemed cosmological redshift. The most general expression for nonrelativistic redshift is given by

$$v = cz \tag{1.16}$$

where v is the velocity of the source, c is the speed of light, and z is redshift.

Cosmological redshift can be related to the scale factor and thus the Hubble parameter through

$$a(t) = \frac{1}{1+z}. \tag{1.17}$$

This quantity is very important in observational cosmology as it provides a means of connecting an observable property of cosmological objects with a mathematical cosmological framework.

1.3.2. Cosmological Equation of State and Density Paramter

As can be seen by the Friedmann Equations 1.13 and 1.14, the physical properties that govern the evolution of the expansion of the universe are pressure and density. This shows that the universe can be characterized as a perfect fluid, where only the diagonal elements of the stress energy tensor are nonzero (see Figure 1.1). The cosmological equation of state, w, is therefore represented by

$$w = \frac{p}{\rho} \tag{1.18}$$

or the ratio of the pressure and density. Solving for pressure and inserting w into the second Friedmann solution 1.14, the Friedmann acceleration equation becomes

$$\frac{\ddot{a}}{a} = -\frac{4\pi}{3}(1+3w)\rho + \frac{\Lambda}{3}. \tag{1.19}$$

Solving this yields a universe that is dominated by either matter, radiation, or the cosmological constant when w is equal to 0, $\frac{1}{3}$, or -1, respectively. Additionally, this means that one can now parameterize the expansion history and potential fate of the universe using only its density.

The total density of the universe can be expressed as the combination of density contributions from matter, radiation, and the cosmological constant, given by

$$\rho = \rho_m + \rho_r + \rho_\Lambda. \tag{1.20}$$

If both the curvature of the universe k and Λ are set to zero, one can solve for the critical density. The result is

$$\rho_{crit} = \frac{3H^2}{8\pi}, \tag{1.21}$$

showing that the critical density relies entirely upon the Hubble parameter. Using ρ and ρ_{crit}, the density parameter is defined as

$$\Omega = \frac{\rho}{\rho_{crit}} \tag{1.22}$$

where Ω can be broken into constituent contributions from matter (Ω_m), radiation (Ω_r), and the cosmological constant (Ω_Λ). If $\Omega<1$, then the universe is open and will expand forever. If $\Omega=1$, then the universe is flat. If $\Omega>1$, then the universe is closed and will eventually collapse.

1.4. Cosmological Distance Measurements

A large portion of cosmological analysis that is not purely theoretical requires distance measurements. Unfortunately, based on the vastness of the cosmos and the scale of these distances, this is not straightforward. While distance measurements to stars in the Milky Way can rely on simple concepts such as parallax, extragalactic measurements become much more complicated. Cosmological distance measurements rely on concepts that are not intuitive or obvious based on initial observations, but instead on detailed studies that allow inferences and standardizations to be made. Observations of Cepheid variable stars, RR Lyrae stars, normal novae, globular clusters, etc. in galaxies in the local group initiated the

idea of a cosmic distance ladder, where certain objects can be used to probe farther and farther regions of the universe [10].

1.4.1. Luminosity Distance

One such way of calculating the distance to an object millions of light years away is by determining its luminosity distance. For nearby objects, such as stars in the Milky Way, this quantity can be calculated using the relation

$$M = m - 5(\log_{10} D_L - 1), \tag{1.23}$$

where D_L is the luminosity distance measured in parsecs. To find this distance, one simply needs to know the apparent magnitude of an object, m, which represents its brightness as measured by a ground or space based telescope, and the absolute magnitude, M, which represents its brightness at a distance of 10 parsecs away. However, the apparent magnitude of an object does not account for deviations from Euclidean space, so for farther objects one must use the relationship

$$D_L = \sqrt{\frac{L}{4\pi F}}, \tag{1.24}$$

where F is the observed flux and L is the bolometric luminosity. Here, factors such as redshift and the curvature of spacetime must be taken into account in order to accurately calculate the relation between observed and actual luminosity. If one has a way of knowing the actual luminosity of an object, then this ratio can be used to determine distance. Thus, this relation becomes less clear for distant objects such as quasars, where cosmological parameters are not as well defined. For this work, luminosity distance is of particular interest as it is used to calculate the distances to host galaxies of supernovae.

1.4.2. Angular Diameter Distance

Another means of calculating large scale distances is by finding the angular diameter distance. It is defined as the ratio between the actual size of an astrophysical object and its apparent angular size as viewed from an Earth or ground based telescope,

$$D_A = \frac{x}{\theta}. \tag{1.25}$$

Calculating the angular diameter distance requires an assumption based on cosmology and can be related to the transverse comoving distance by

$$D_A = \frac{D_M}{1+z}, \tag{1.26}$$

where the comoving distance, D_M, represents a distance that accounts for cosmological expansion. This is important for calculating distances billions of light years away using baryon acoustic oscillations (BAO) where current probes are pushing to the frontiers of cosmology.

1.5. Supernovae

Massive stars greater than 8 solar masses end their lives in cataclysmic events called supernovae (SNe). A supernova is a stellar explosion, ejecting much, if not all, of the interstellar material at speeds up to 30,000 km/s. All stars begin their life by fusing hydrogen into helium. As the hydrogen is exhausted, the fusion rate can no longer generate sufficient pressure to support its weight. Gravity then collapses the star, raising the temperature. This leads to the fusion of hydrogen into helium. The cycle then repeats, resulting in the fusion of helium into carbon where low mass stars contain an electron degenerate core, thus halting the fusion process. For lower mass stars, this is where the cycle ends and no carbon fusion occurs.

1.5.1. Type Ia Supernovae

If one of these degenerate stars such as a white dwarf is in a binary system, the binary companion may spill out of its Roche lobe when it moves into the red giant phase, where the Roche lobe is the region around a star in a binary system in which orbiting material is gravitationally bound. This results in the gravitational accretion of mass from the companion star. Once the accretion of mass is sufficient to raise the mass of the degenerate white dwarf close to the Chandrasekhar mass [11] ($\sim$1.44 solar masses), the temperature of the interior rises, causing a runaway nuclear fusion reaction. The fusion of carbon inside the white dwarf under immense pressure causes an explosion that releases enough energy to cause a supernova, although the exact details of this critical time are still a subject of strong debate and study. While this "single degenerate" scenario involves what is thought to be a more massive companion, an additional "double degenerate" scenario has been suggested in which two white dwarfs coalesce and similarly result in a cataclysmic explosion [12]. In this scenario, the total degenerate mass is potentially greater than the Chandrasekhar mass. These scenarios describe Type Ia SNe.

1.5.2. Core Collapse Supernovae

For higher mass stars (greater than 8 solar masses), carbon continues to burn into neon, oxygen, and silicon. Once the fusion process reaches iron it can no longer continue, as the binding energy of iron would require energy put into the system rather than released and could not provide pressure to support the star. At this point, pressure caused by nuclear fusion and electron degeneracy can no longer support compression of gravity. As the core approaches the Chandrasekhar mass through core convergence [13], the atoms travel at relativistic speeds and the core begins to collapse. The nuclear shells surrounding the iron core decrease in density. Outside of the carbon shell resides the helium shell. If hydrogen remains after stellar mass loss, a hydrogen shell resides outside of the helium shell. In a

fraction of a second, this compression of stellar material at speeds up to 70,000 km/s causes the outer layers of the star to be ejected. The collapse causes the temperature in the core to rapidly increase, releasing large amounts of high energy gamma rays. These high energy photons break up the iron nuclei into constituent nuclei through photodisintegration. As the core continues to collapse, reverse beta decay occurs, releasing large amounts of high energy neutrinos. Once the innermost parts of the core collapse past the point of the nuclear density at which protons and neutrons are bound in atomic nuclei, the contraction slows and the matter rebounds in a shock wave of ejected material.

The result of these explosions of energy is a core collapse supernova (CCSN). Core collapse SNe describe all types of SNe other than SNe Ia. Typically, several solar masses of material are ejected with a neutron star left as the supernova remnant. Upon explosion, ejecta velocities are typically of the order 10,000 km/s with temperatures of approximately 10,000 K.

1.5.2.1. Subclasses of Core Collapse SNe

These mechanisms describe the progenitors of SNe, however there are subclasses largely based on elements contained in the circumstellar ejecta. Before a supernova event occurs, stars with radiative hydrogen envelopes are blue supergiants, stars with convective hydrogen envelopes are red supergiants, and stars with no hydrogen at all are helium or carbon stars [14]. The features due to chemical elements found in the spectra of SNe allow us to classify them as different types as seen in Figure 1.2. Because the observable spectral elements can change over time, red and blue supergiants can produce Types II and Ib SNe, helium stars can produce Types Ib, Ic, and Ib/c SNe, and carbon stars can produce type Ic SNe [14].

The main difference between Type I and Type II is the presence of hydrogen, where Type II SNe possess a hydrogen envelope. For a Type IIb, helium is seen to be the dominant

element, while Types IIP, IIL, and IIn show helium, but are still hydrogen dominant. Type IIP SNe display a plateau phase in their photometric light curves due to a hydrogen envelope surrounding them. During this phase, a recombination wave propagates through the envelope leaving chemical features outside of the wave that are optically thin. Once recombination is complete after approximately 100 days, the light curve drops drastically and the plateau phase ends. This is contrary to what is seen for other CCSNe, where most or all of the hydrogen in the outer layer is ejected. Type IIL SNe are defined by their linear decline in brightness over time and Type IIn SNe are defined by narrow hydrogen features seen in their spectra. Type II SNe also possess strong magnesium, silicon, and sulfur features, with iron lines appearing at early and late times in the spectra. For Type Ia SNe, silicon and oxygen are present, while helium is not. For Types Ib and Ic, silicon is either very weak or nonexistent in the spectra, while helium is present in SNe Ib and nonexistent in SNe Ic.

1.5.3. Supernova Distance Measurements

In order to understand properties of the early universe, one must observe higher and higher cosmological distances. This requires either more sophisticated technology or simply brighter objects that can be seen at larger distances (or both). The luminosity of SNe allows one to observe the more distant universe as they can emit enough energy to outshine entire galaxies.

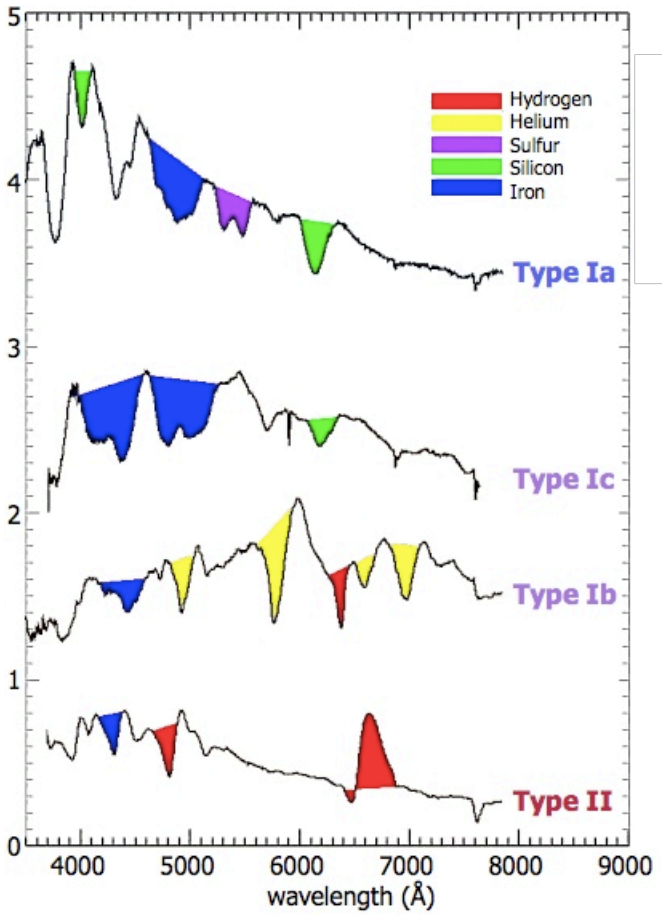

Figure 1.2: Example spectra for different types of SNe [15]. The colored regions indicate absorption or emission features due to chemical elements in the spectra that help determine the classification of each event.

1.5.3.1. Δm_{15} Method for SNe Ia

In general, it is beneficial to have various types of distance measurements at your disposal in order to cross check and validate such measurements. For instance, SNe Ia have been used by many to determine cosmological distance measurements using the fact that they can be standardized using a simple relationship, the Δm_{15} relation [6] [7]. In the 1970s and 1980s, several astronomers observed that the lower the peak magnitude of SNe Ia, the quicker it faded from this maximum [16] [17]. This was improved in the 1990s and became known as the Phillip's relation [18]. As it was further improved [19] [20], it is now known as the Δm_{15}

method,

$$M_{max}(B) = -21.726 + 2.698\Delta m_{15}, \tag{1.27}$$

which examines the relationship between peak luminosity and the rate at which luminosity declines in the first 15 days after maximum brightness for SNe Ia.

In particular, B band magnitude, which represents the optical magnitude as measured by the blue or "B" passband, is used to allow the standardization of objects seen in Figure 1.3. Thus, SNe Ia have been deemed "standardizable candles" that can therefore be used to probe various properties of the universe.

When observing SNe Ia in the 1990s, The High-z Supernova Search Team [6] and the Supernova Cosmology Project [7] used the Δm_{15} relation to calculate the distance to SNe Ia out to $z \sim 1$. In particular, they have been used to measure the mass density, dark energy density, curvature of the universe, and expansion history. The results suggest that the universe adheres to a flat cosmology and a non-zero cosmological constant.

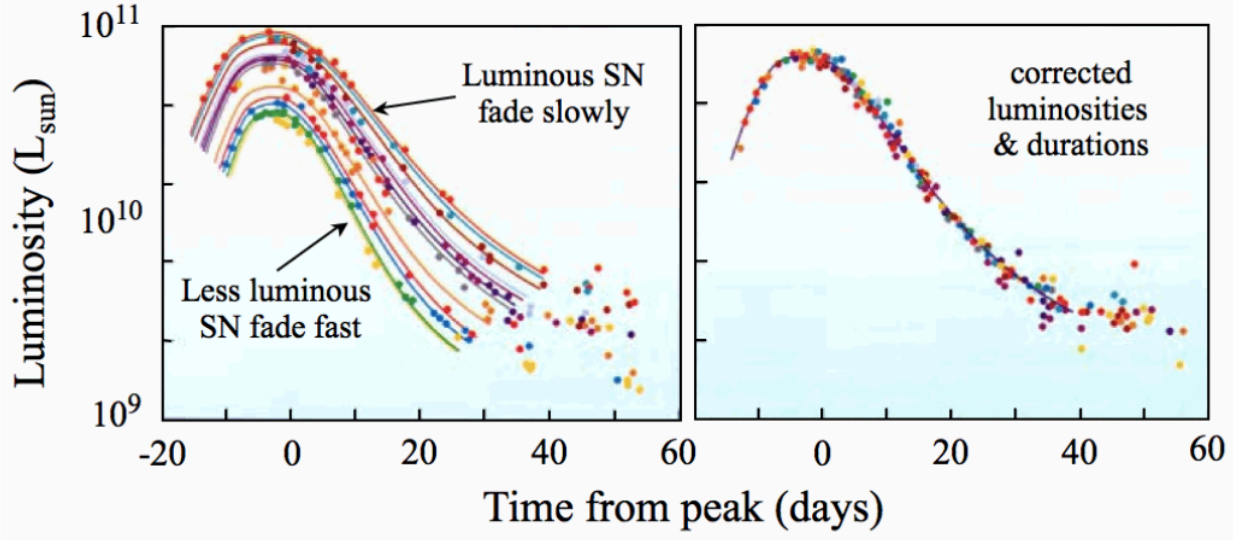

Figure 1.3: A simple representation of the Δm_{15} method [21]. The difference in B magnitude over a 15 day period from peak brightness can be used to standardize a SN Ia event.

It should be noted, however, that this approach is purely empirical and based on a physical conception of SNe Ia progenitors. There could be underlying effects such as the progenitor method and whether they are caused by a single or double degenerate star scenario [12] that affect cosmological measurements. Additionally, a variety of Type Ia SNe have been observed [22], which call into question how standardizable they may actually be. This, combined with the problems of absolute magnitude calibration, could lead to additional systematic effects that alter their distance measurements.

1.5.3.2. Expanding Photosphere Method for CCSNe

In addition to SNe Ia, other types of SNe have been used to probe cosmological expansion. A method that can be employed to calculate the distances to the host galaxies of core collapse SNe is the expanding photosphere method (EPM), which uses the opacity of the photosphere of Type II SNe (SNe II) to probe the distance to the underlying host galaxy [23] [24]. In particular, Type IIP SNe are used, as the distinct plateau feature seen in their light curves indicates an opaque photosphere that is mostly comprised of hydrogen and helium [23] [25]. In Chapter 5, I apply the EPM to SN 2007gr, a Type Ic SN, showing the potential for this method to be used for other types of SNe.

As certain types of core collapse SNe eject circumstellar material, their photospheres radiate as opaque blackbodies. This physical property is the basis for this method, but there are several underlying assumptions regarding these objects that allow them to be used for the EPM. These assumptions are [24]: the expansion of ejected material is spherically symmetric, the ejecta expand homologously, and the ejecta is optically thick. An additional assumption is that the photosphere radiates as a blackbody, so that a Planckian spectrum is observed, providing an accurate effective temperature. Using the initial work of Kirshner et. al [23], a number of type IIP SNe have now been used to accurately measure distances [26] [27] [25].

In order to calculate the distance to these objects, one must know the radius of the photosphere at multiple epochs (the radius of the progenitor can be neglected). This can be obtained using the photospheric velocity over time via

$$R_{phot} = v_{phot}(t - t_e). \tag{1.28}$$

Meanwhile, the observed flux density at a given wavelength λ is

$$f_\lambda = \theta^2 \zeta^2 \pi B_\lambda(T), \tag{1.29}$$

where ζ is a dilution factor based on the surrounding atmosphere of the supernova, B_λ is the Planck function at a given wavelength, and the angular radius, θ, is defined as

$$\theta = \frac{R_{phot}}{D} = \frac{1}{\zeta}\sqrt{\frac{f_\lambda(1+z)}{\pi B_\lambda(T)}}. \tag{1.30}$$

The dilution factor, ζ, is due to several factors including the electron-scattering in the photosphere and the emission from overlying layers [26]. Combining this information with the bolometric flux, temperature, and dilution factor due to atmospheric effects, the angular diameter distance can be inferred by fitting the linear relationship

$$t = t_e + D\left(\frac{\theta}{v_{phot}}\right). \tag{1.31}$$

This method has been applied mostly to SNe IIP, as the plateau phase of the light curves of these objects imply that they satisfy all of these conditions. While it has been applied to other Type II SNe [28], this method has not been applied extensively to other types of core collapse objects such SNe Ib, Ib/c, and Ic.

1.6. Large Scale Structure and Baryon Acoustic Oscillations

In order to probe cosmology at distances farther than the farthest observed SNe, other methods must be employed. After the Big Bang, the universe was comprised of a plasma including ordinary matter, dark matter, and dark energy, all of which were coupled together. After about 380,000 years, the universe cooled enough for matter and radiation to decouple, allowing the formation of atoms. Before this recombination, the dense plasma experienced contractions due to gravity and expansions from heat due to photon and matter interactions. These actions countered each other, creating oscillations that we call baryon acoustic oscillations (BAO). These acoustic waves were comprised of baryons and photons. However, when radiation was able to propagate freely, interactions between baryons and photons no longer occurred, relieving the pressure causing the oscillations. This left a shell of baryonic matter at the scale of oscillation, where baryons and dark matter formed overdense regions at this characteristic scale. This pattern has been seen in the temperature anisotropies of the cosmic microwave background (CMB) through satellite experiments such as COBE [29], WMAP [30], and Planck [31].

As the universe evolved and galaxies formed, they began to congregate in groups and clusters. The initial energy density fluctuations of the early universe led to the coherent structure observed in galaxy clustering. Measurements of the clustering of galaxies describe the Large Scale Structure (LSS) of the universe. LSS surveys such as the BOSS experiment [32] observe the effects of BAO at a characteristic scale in clustering measurements, allowing BAO to be used as a standard cosmological ruler. Results of the BOSS experiment show in Figure 1.4 that this feature can be seen as a peak in the distribution of matter at approximately 100 Mpc/h.

1.6.1. Two Point Correlation Function

In order to measure the clustering of galaxies, the two point correlation function (2PCF) is used. To calculate this function, it is necessary to have data points corresponding to 3-D coordinates on the sky. For large scale structure surveys, this catalog is often comprised of galaxies or quasars. A random catalog is also necessary, where coordinates on the sky are randomly distributed according to the geometry of the observing footprint of the given survey. The most common estimator of the 2PCF is the Landay and Szalay [33] estimator, defined by

$$\xi(r) = \frac{DD(r) - 2DR(r) + RR(r)}{RR(r)}. \tag{1.32}$$

In this equation, $DD(r)$ represents the number of pair counts of individual data points separated by a distance r. Similarly, $DR(r)$ represents the number of pair counts of data and random points separated by a distance r, and $RR(r)$ represents the number of random points separated by a distance r. An example of these distributions is shown in Figure 1.5.

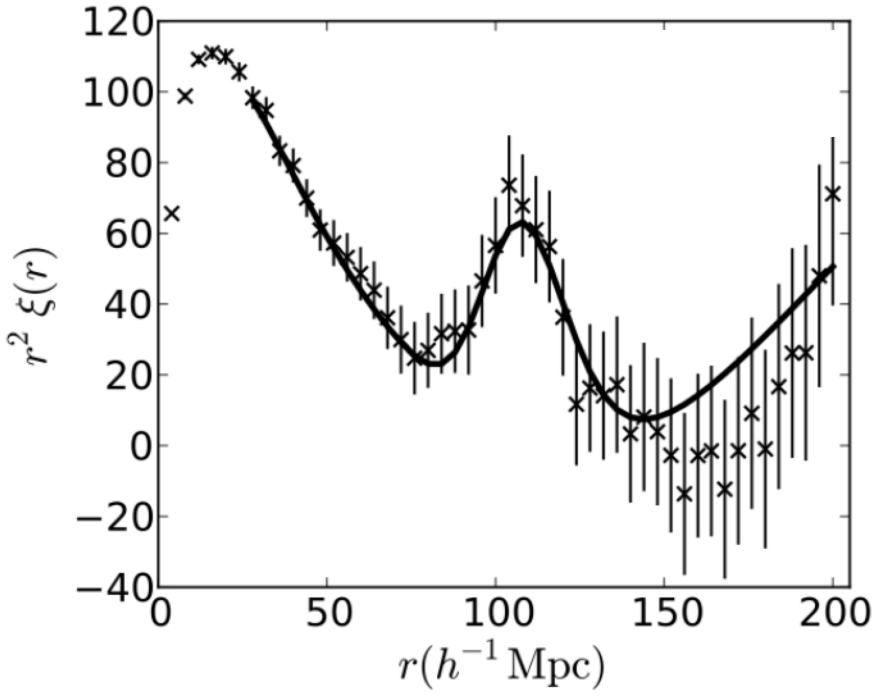

Figure 1.4: BOSS results showing the BAO feature as an excess in the distribution of matter at a scale of ∼100 Mpc/h [34].

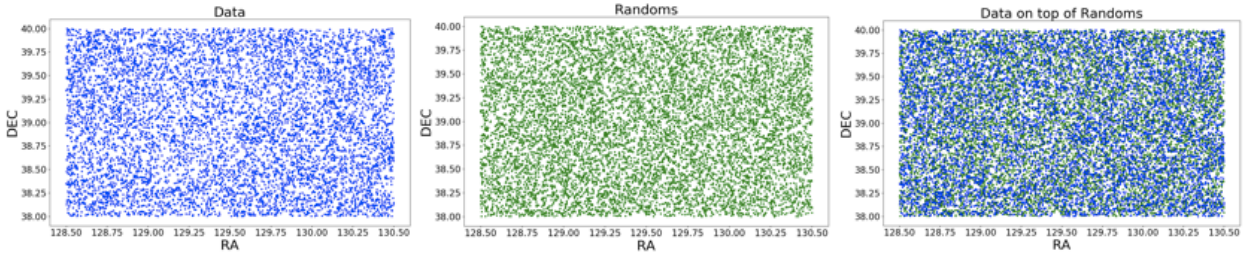

Figure 1.5: Distributions of data and random points used to calculate the two point correlation function. The left plot shows the coordinates of data points used to calculate $DD(r)$, the middle plot shows the coordinates of random points used to calculate $RR(r)$, and the right plot shows the coordinates of data on top of random points, used to calculate $DR(r)$.

Each data point used in Figure 1.5 represents the distance to an individual galaxy. This distance can be found by calculating the angular diameter distance using Equation 1.26. In this equation, we can use the BAO feature to calculate the comoving distance D_M, defined as

$$D_M = \frac{c}{H_0} \int_0^z \frac{dz'}{E(z')} \tag{1.33}$$

for a flat universe with no spatial curvature, as is currently observed [35]. In this equation, $E(z)$ is represented by

$$E(z) \equiv \sqrt{\Omega_M (1+z)^3 + \Omega_k (1+z)^2 + \Omega_\Lambda}, \tag{1.34}$$

describing the matter, curvature, and energy densities used to establish distances. By evaluating this BAO feature at various redshifts, one can infer the angular diameter distance D_A and thus the Hubble expansion at each redshift, $H(z)$.

1.7. Thesis Outline

This thesis is organized as follows. Chapter 2 describes the ROTSE and DESI experiments, in which SNe and BAO studies will be performed, respectively. It will specifically

discuss an overview of each experiment and the methods used to collect the respective data. Chapter 3 gives an overview of photometry and spectroscopy and describes the photometric data sample for ROTSE and the spectroscopic data sample for DESI. Chapter 4 discusses the data reduction processes for each experiment, with an emphasis on my work on the DESI online pipeline. In Chapter 5, I present extensive analysis of photometry and spectroscopy for SN 2007gr in order to apply the EPM to calculate the distance to its host galaxy. Chapter 6 describes my analysis for SN 2010kd, a superluminous Type Ic SN and a calculation of the Hubble constant using the ROTSE SNe IIP sample. Chapter 7 discusses a BAO analysis, in which I specifically focus on the effects of radial observational systematics on redshift and clustering measurements. Finally, Chapter 8 includes conclusions, discussing the overall implications on cosmology from the ROTSE and DESI results.

Chapter 2

Experimental Setup

To approach the challenges described in Chapter 1, I employ the use of the Robotic Optical Transient Search Experiment (ROTSE) to obtain photometric images and the Hobby Eberly Telescope (HET) to obtain spectroscopic images for SNe in the low z, local universe. These observations are used to calculate the distances to host galaxies of supernovae in local galaxy clusters [36]. The ROTSE experiment consists of 4 telescopes in Australia, West Texas, Namibia, and Turkey. I have spent an extensive amount of time working on the ROTSE-IIIb hardware, where the bulk of this work is laid out in Section 2.1.4.

This work also uses spectroscopic images obtained by the Dark Energy Spectroscopic Instrument (DESI) and photometric images obtained by the Dark Energy Camera Legacy Survey (DECaLS), Beijing-Arizona Sky Survey (BASS), and MOSAIC z-band Legacy Survey (MzLS) surveys of galaxies and quasars in the high z universe. These observations are used to examine the effects of radial observational systematics on galaxy clustering measurements. The ultimate goal of the DESI experiment is to chart the expansion history of the universe out to 11 billion light years away. With respect to the aspects of DESI described in this chapter, I contributed to testing of the instrument control system (ICS) described in Section 2.2.1.

2.1. ROTSE-III

Each ROTSE instrument is fully robotic and fully automated, using a Cassegrain system with a 45 cm f/1.8, spherical primary mirror and a flat secondary mirror to observe optical wavelengths from approximately 3,000 – 10,000 Å [36]. An all-refracting field corrector

provides a final focal length of 85 cm, with the final focus located $\sim$ 7.5 cm in front of the primary mirror vertex. This arrangement yields a field of view of 1.8 x 1.8 degrees, with a typical limiting magnitude of 18.5.

The experiment was initially deigned to observe gamma ray bursts (GRBs), which are highly energetic, short lived explosions observed in distant galaxies. There are two types of observed GRBs, short burst and long burst, distinguished by a duration of less than or greater than 2 seconds. Due to the brief duration of the GRBs, ROTSE-III is optimized to rapidly slew and observe these events. The bulk of this analysis uses observations from the ROTSE-IIIb telescope located at McDonald Observatory in West Texas.

2.1.1. CCD Imaging

Employing a thermally cooled charged coupled device (CCD) for imaging with adjustable focus, the ROTSE-III telescopes are able to patrol a large portion of the sky, taking hundreds of images per night when conditions are sufficient. Each telescope possesses a 2045 $\times$ 2049 Macroni CCD with 13.5 μm pixels to its corners [36]. A passband of 0.4-0.9 μm was chosen, although the observable passband for ROTSE extends past these limits. The quantum efficiency of the ROTSE CCD is shown in Figure 2.1. Ultimately, the image quality goal was to receive 70% or more of the light incident on the CCD inside the diameter of each pixel at all pointing angles of the telescope and all wavelengths without refocus.

To collect an adequate signal to noise ratio (SNR) for objects in a given image, thermal noise must be reduced as much as possible. This is achieved by a collection of devices, most notably a thermoelectric cooler (TEC) that can cool the CCD to a temperature of -40°C. The cooling occurs via a heat transfer loop, where a solution of glycol and water recirculates from the TEC to the camera. If not properly cooled, images become rapidly saturated, obscuring any objects contained in the FOV. This cooler is accompanied by an air pump

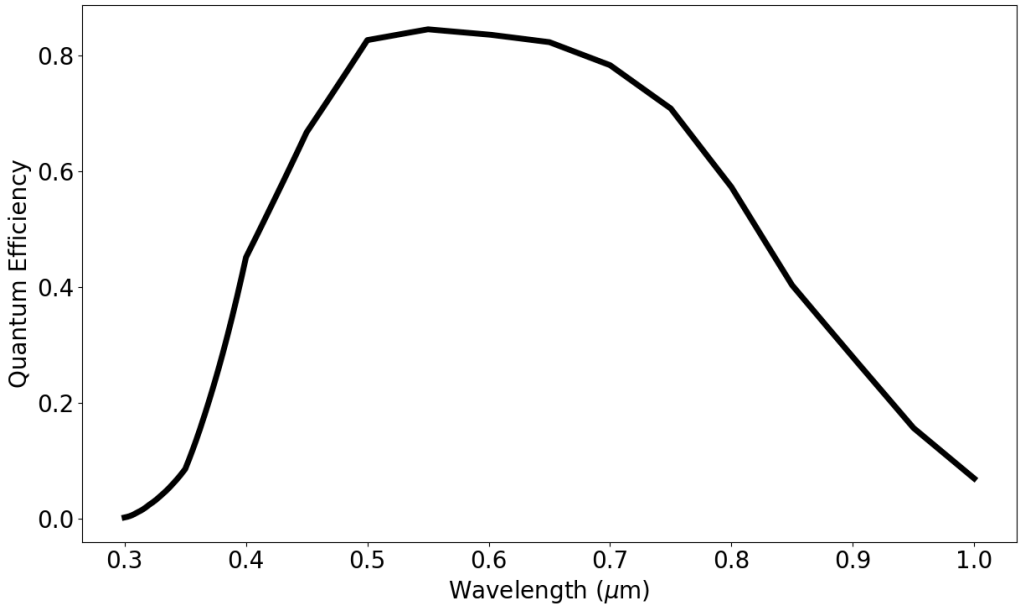

Figure 2.1: The observable passband for ROTSE-III telescopes, ranging from 0.3-1.0 μm.

that serves as a vacuum that keeps the camera lens from fogging. The camera readout noise is less than $8e^-$ and sky background is $\sim 15e^-$, so image noise becomes dominated by the sky after ~ 5 seconds.

2.1.2. Telescope Mount

In order to observe the sky, each telescope must have the ability to point to an accessible region of the sky. To mount each instrument, ROTSE-III uses a modified Centurion 18 fork mount made of sheet steel, ideal for rapid slewing [36]. The modifications made to each mount were done to improve the slew speed and mechanical tolerances of this movement, while maintaining the ability to precisely track astronomical objects. The fork mount attaches to the optical tube assembly (OTA) containing the optical system and CCD, as shown in Figure 2.2.

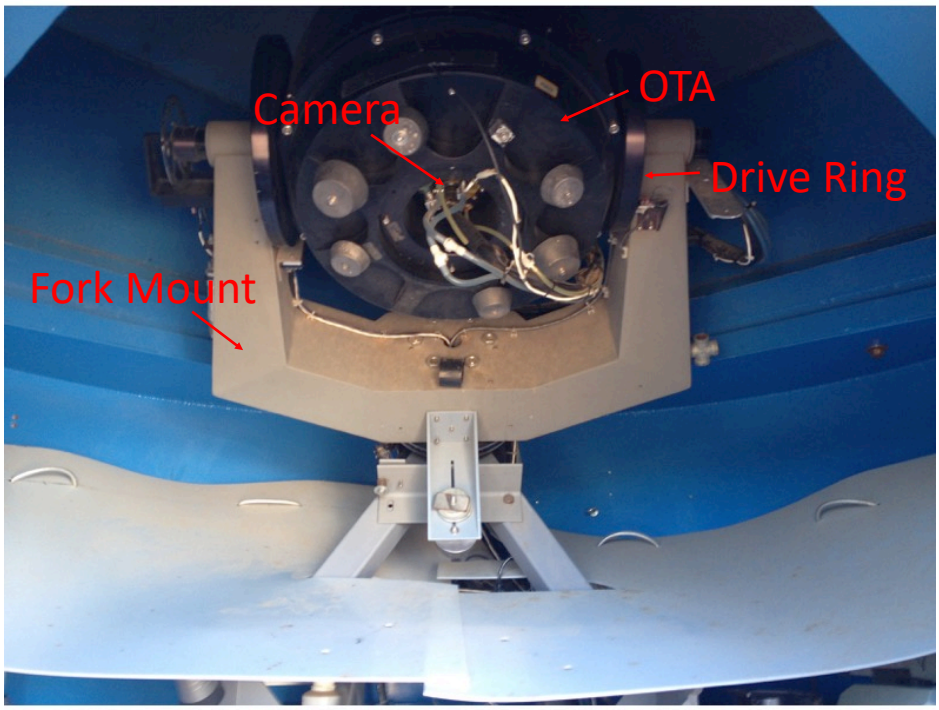

Figure 2.2: The ROTSE fork mount connected to the optical tube assembly inside the ROTSE-IIIb enclosure.

To point to a desired region of the sky, ROTSE uses the equatorial system which uses two measurements, right ascension (RA) and declination (DEC), to map the location of an astrophysical object onto the celestial sphere. Along each axis, a drive ring is attached to the OTA so that the telescope is able to observe the entirety of the sky that is accessible given the geographic location of each telescope. The drive ring assembly along the RA axis is shown in Figure 2.3. Each of these drive rings are powered by cylindrical motors, where the angular velocity applied to a small capstan enables the rotation of each ring. This small steel cylinder is encased in a rubber coating that comes into contact with each drive ring, delivering the torque necessary for telescope slews. This must be configured with the proper tension to allow for proper slewing.

While the drive rings power the movement of the OTA, an encoder system along each axis enables the correct pointing of the telescope. Along each drive ring is a thin strip of reflective, gold plated steel encoder tape, periodically micro-etched to be mapped to coordinates on the

sky. An encoder read head with the ability to process slews up to 10 m/s is symmetrically aligned at an optimal distance of 0.2 mm above each strip of encoder tape. These read heads record position information based on the etched tape as each axis rotates, which is then computationally converted to coordinates on the sky.

2.1.3. Observing Strategy and Operations

The fully robotic nature of this telescope also allows for remote observation and systematic scheduling, optimizing the observing strategy. Science images taken by ROTSE-III telescopes are of varying exposure length, typically 60 seconds for a supernova field.

ROTSE-IIIb first collected supernova data for the Texas Supernova Search program (TSS) from 2003 to 2007, discovering approximately 30 SNe in the first two years. Observations of supernovae involved both discovery and follow-up observations, with follow-up optical spectroscopic imaging coming from the 9.2 m Hobby-Eberly Telescope (HET), just down the mountain from ROTSE-IIIb. TSS observations were typically in the Coma, Virgo, Ursa Major, Perseus, and multiple Abell galaxy clusters and super-clusters. This project resulted in the discovery of a new type of supernova called superluminous-supernovae (SLSNe) [37] [38] [39], $\sim$2 magnitudes brighter than typical core collapse supernovae. In particular, ROTSE was involved in the discovery of SLSNe through observations of SN 2005ap, where this rare type is more luminous than any other type of observed supernova [40].

After TSS, the ROTSE Supernova Verification Project (RSVP) began, this time involving all four ROTSE-III telescopes, collecting data from 2007 to 2012. RSVP incorporated the same fields as TSS, but allowed for much additional sky coverage for much longer durations, particularly with the addition of two telescopes in the southern hemisphere, with ROTSE-IIIb and ROTSE-IIId as the predominant first observers.

In 2012, SMU acquired the ROTSE-IIIb telescope and operations of the ROTSE web server. From 2012 to 2016, ROTSE was involved in the Texas Supernova Spectroscopic Survey (TSSS), providing target supernovae to be spectroscopically observed by the HET. This meant daily monitoring of the nightly images, constantly verifying transient candidates. Under SMU management, approximately 10 supernovae have been discovered by ROTSE-IIIb, with many more getting follow-up observations. Although operations have been temporarily halted due to the mechanical faults and the COVID-19 pandemic, observations are planned to resume in the near future.

2.1.4. Reassembly of the Optical Tube Assembly

Precise slewing requires smooth contact between the capstan and drive ring to prevent over or under slewing, so that the mapping of encoder coordinates to celestial coordinates remains stable and to prevent damage to any parts of the mechanical system. Due to the fact that ROTSE-IIIb was designed for rapid slews to view GRBs, which are typically short in duration, the OTA accrued wear and tear that built up along the drive ring of the RA axis as seen in Figure 2.3. The arrow in the top right corner of the image points to excessive wear along the drive ring, which caused significant slipping of the capstan during active slewing of the telescope. This eventually led to failures of the mount when trying to slew along the RA axis, as frequent as multiple times per hour. The frequency of these failures made it impossible to obtain a full night of observations, resulting in the decision to cease operations in spring 2016 to refurbish the telescope. I have been involved in the entire refurbishment process, improving many aspects of the telescope with the help of the McDonald Observatory staff.

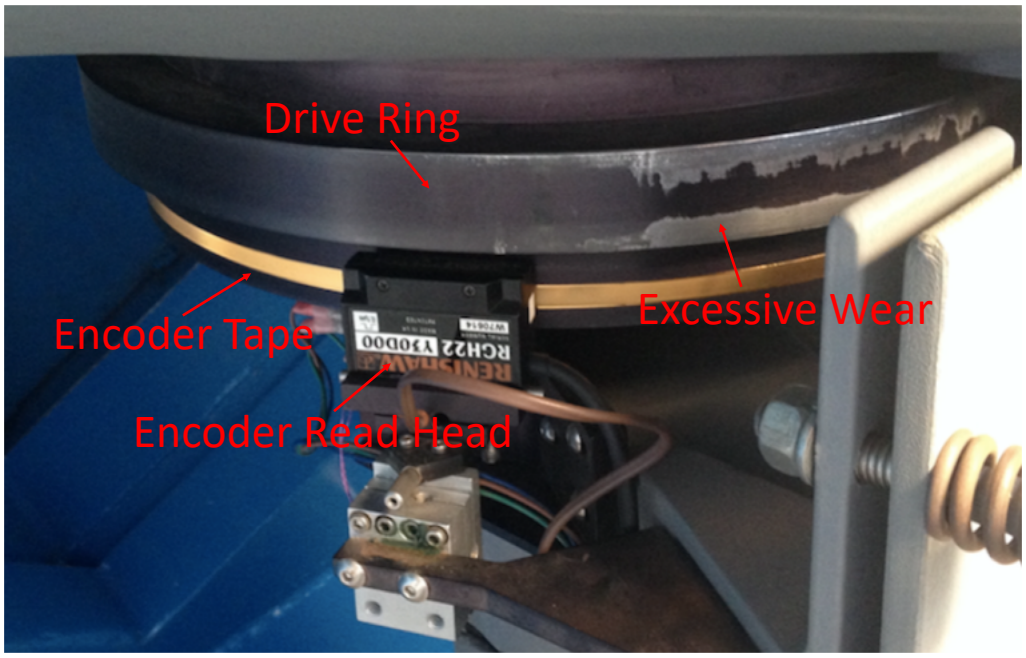

Figure 2.3: The ROTSE drive ring and encoder assembly along the RA axis. Updating this assembly was required to improve the stability of OTA movement.

2.1.4.1. Cleaning the Optics

While in the lab, the primary and secondary mirrors were thoroughly cleaned with compressed carbon dioxide and optical cleaning wipes. Additional cleaning of the entire OTA was done, as the lab setup allowed for better access to all of its components. The delicacy of the aluminum coating on the secondary mirror limited the ability to remove all debris, but the primary mirror and lens were returned to pristine condition.

2.1.4.2. Mount Refurbishment

In order to perform the necessary fixes, the OTA was detached from its setup in the enclosure, where a crane attached to a fork lift was used to lift the OTA out of the enclosure, moving it to a laboratory setting for maintenance. The removal process is shown in Figure

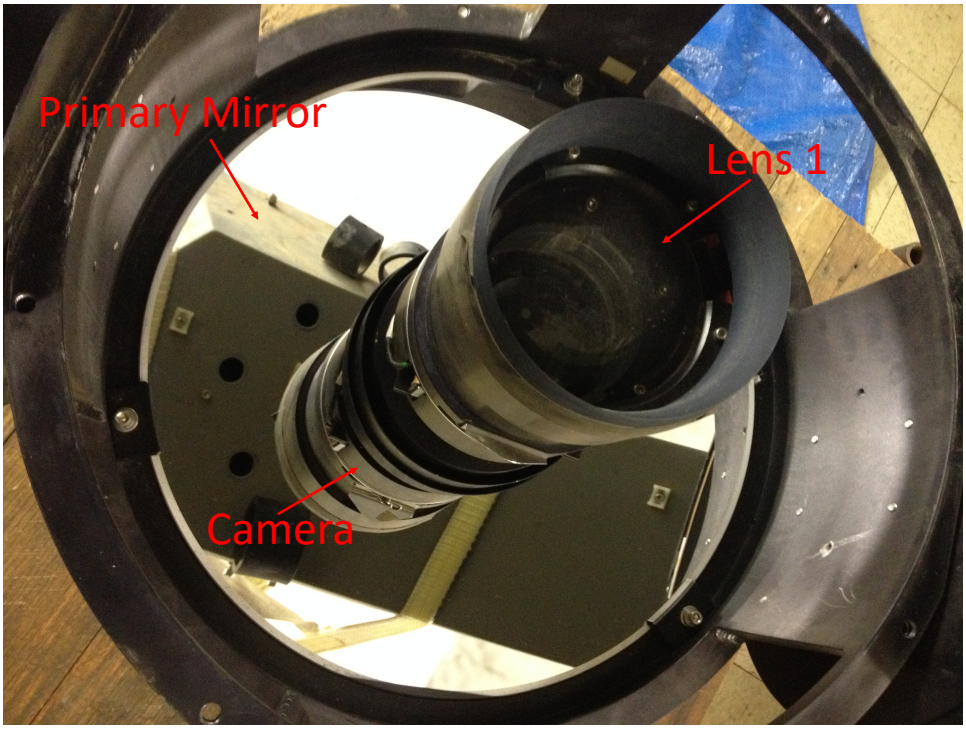

Figure 2.4: The ROTSE-IIIb optical assembly. The arrows point to the first lens of 4 leading to the CCD, the 45 cm, spherical primary mirror, and the CCD camera.

2.5. During the entirety of this process, the OTA was oriented to prevent damage to the optical components of the CCD.

Once the OTA was safely out of the enclosure, the RA drive ring was rotated by 180° so that the capstan would only be in contact with the previously unused portion of the drive ring. Fortunately, the encoder tape length and orientation was sufficient to not require its replacement. However, because the drive ring was rotated, the encoder had to be moved in order to fully access the proper amount of encoder tape. This involved detaching the encoder from the OTA foundation, and reattaching it to keep the encoder read head at a precise distance of 0.2 mm from the tape along the entire axis. Once its position was confirmed, limit switches were placed along the drive ring to optimize accessible slewing given limitations of the enclosure.

Figure 2.5: Removal of the ROTSE OTA from the enclosure. This removal was necessary to facilitate the refurbishments needed to return ROTSE-IIIb to on sky observing.

Unfortunately, in the process of reattaching the OTA to the fork mount, the encoder tape along the DEC axis was stripped from the drive ring, necessitating replacement. However, due to limited access to the drive ring with the OTA reattached to its foundation in the enclosure, the typical application process could not be used. Instead, it was necessary to apply the encoder tape to the drive ring very precisely by hand, as the applicator could not be used along the entire DEC axis. This involved slowly revolving the DEC drive ring, while carefully applying the encoder tape as parallel to the edges of the drive ring as possible, as any deviations larger than 0.1 mm from an entirely straight tape can lead to the inability of

the read head to properly determine its location along the tape. The encoder read head was then reattached, with the read head mounted similar to the read head along the RA axis, at an optimal distance of 0.2 mm away from the encoder tape. This is a precise endeavor as well, as the rotational tolerances of the read head with respect to the tape are $\pm 1^\circ$ roll, $\pm 1^\circ$ pitch, and $\pm 0.5^\circ$ yaw.

Once the OTA, drive motors, and encoders were all back in place, the tension and weighting had to be readjusted. This involves adding weights incrementally to either side of the fork mount until the OTA is balanced and tightening the tension screws that control the torque applied to the drive rings. Improper tension and an unbalanced OTA could cause severe damage to the capstans by wearing down their rubber coating and grinding down the steel shaft, putting excess stress on the drive motors. Once these factors were appropriately handled, the movement of the mount could then be tested. The motors are now functional, and the capstans are in appropriate contact with the drive rings, ensuring proper slewing.

2.1.4.3. Camera Refurbishment

Once proper slewing of the OTA was verified, the camera was tested. Noisy imaging and high temperature readouts indicated an internal failure of the camera and/or cooling system. Similar failures were seen using multiple cooling mechanisms, indicating an issue internal to the camera. It has since been seen that there is a leak in the casing of the camera, causing a high amount of thermal noise to enter the CCD. Once this problem has been alleviated, full testing of the ROTSE-IIIb assembly can be tested, with refocusing and coordinate adjustments necessary to return to fully functional operation. Figure 2.6 shows the CCD connected to a vacuum pump to try and remove excess moisture inside the camera enclosure.

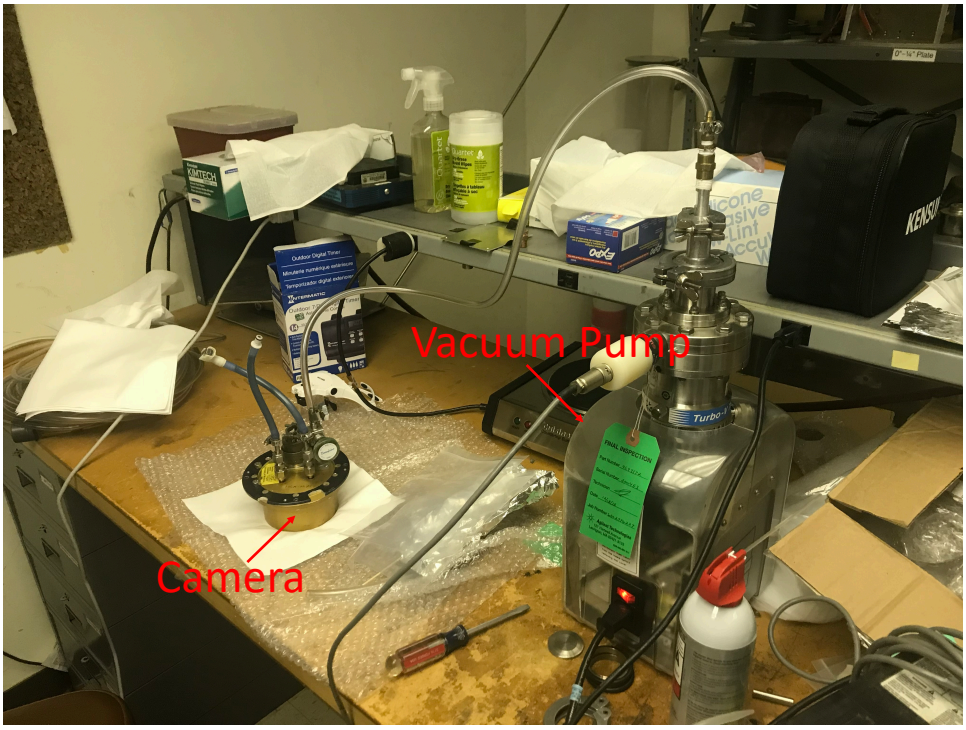

Figure 2.6: The ROTSE-IIIb CCD connected to a vacuum pump in attempt to remove excess moisture inside of the CCD enclosure.

2.1.4.4. Commissioning

In order to test the proper cooling of the CCD, both calibration and science images were taken in the fall of 2017. Figure 2.7 shows an example science image of a supernova field on the left and a dark calibration image containing only noise due to the internal electronics on the right, taken with the camera shutter closed. The science image was observed with an exposure time of 0.1 s and the dark calibration image was taken with an exposure time of 60 s. It can be seen that even with an exposure time as short as 0.1 s, much of the image contains saturated pixels. The dark calibration image is highly saturated, with pixels containing up to 30,000 counts, where a typical dark calibration image taken with an exposure time of 60 s contains pixels with approximately 3,000 to 4,000 counts. The small circles in the science image are stars, which is a promising sign that ROTSE-IIIb will be able to properly observe once the camera is properly cooled.

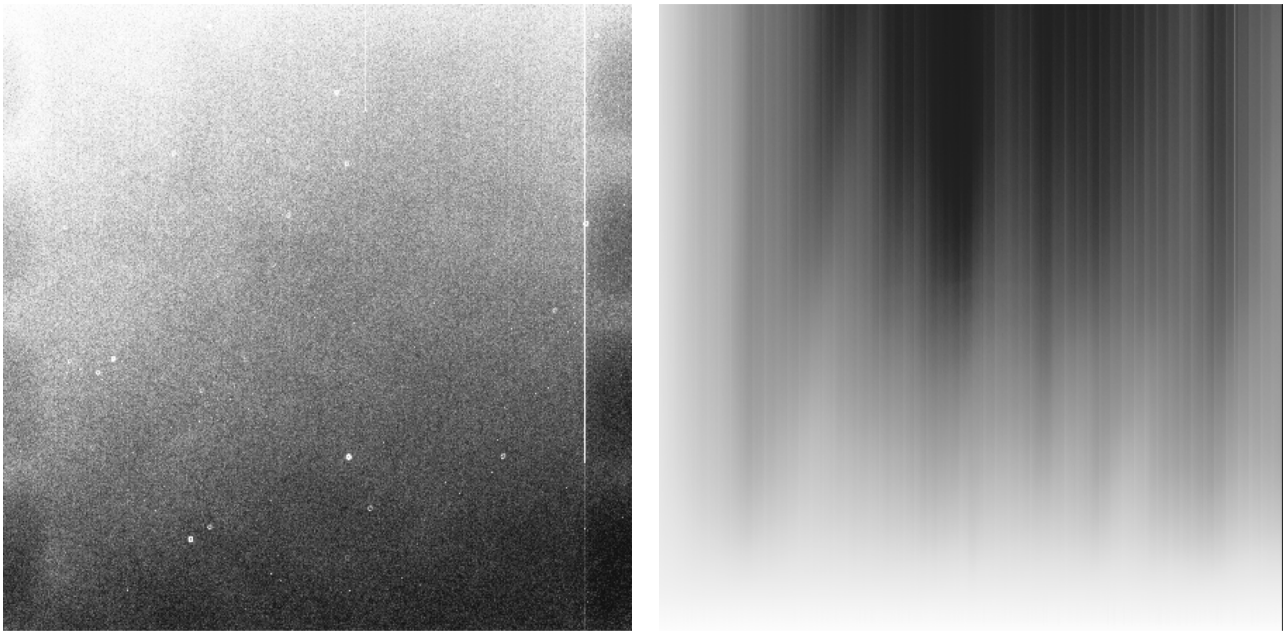

Figure 2.7: Two commissioning images taken by ROTSE-IIIb to test the CCD functionality. The left image shows a science image with an exposure time of 0.1 s, where the small circles are stars and the saturation is due to improper cooling of the CCD. The right image shows a saturated dark calibration image taken with the camera shutter closed with an exposure time of 60 s.

2.1.5. Hobby Eberly Telescope

The Hobby Eberly Telescope located at McDonald Observatory on the same peak as ROTSE-IIIb, is a 9.2 m optical, spectroscopic instrument used for follow up observations of ROTSE SNe. It is the most commonly used instrument for ROTSE follow up spectroscopy. The HET contains three spectrographs of low, medium, and high resolution, but the low resolution spectrograph (LRS) [41] suffices for the purposes of SNe follow up observations. The LRS is a high throughput optical grism spectrograph with a resolving power of $R = \frac{\lambda}{\Delta\lambda}$ ranging from 600 to 3,000.

2.2. Dark Energy Spectroscopic Instrument

The Dark Energy Spectroscopic Instrument (DESI) aims to measure the expansion history and large scale structure of the universe out to a distance of approximately 10 billion light years away [42]. Through observations of more than 30 million galaxies and quasars over a five year period, DESI will map the sky to unprecedented levels using state of the art equipment. The baseline survey for DESI covers 9,000° of the sky, with a goal of observing 14,000°, about one third of the entire sky. DESI will use the 3.8 m Mayall telescope at Kitt Peak National Observatory (KPNO) in Arizona to collect spectroscopic observations [43]. The previous photometric configuration of the Mayall telescope has been updated to incorporate a spectrograph system spanning 360 - 980 nm, with 5,000 optical fibers across the entire focal plane. Figure 2.8 shows a simple model of the new design of the Mayall used for DESI.

2.2.1. Instrument Control System

The DESI instrument control system (ICS) is constructed to perform all control and monitor functions required for successful operations [45]. The ICS involves the movement of both the telescope and optical fibers, ensuring optimal positioning in preparation for the next exposure, monitoring all components of the instrument. The DESI online system connects with the Mayall telescope control system (TCS) to send new pointing coordinates. In turn, the TCS provides current pointing and status information to ensure proper slewing to the following exposure. The ICS also receives telemetry information such as weather using a database operated by KPNO. Weather conditions can decrease the spectroscopic data quality, so the DESI ICS uses an exposure time calculator (ETC) to dynamically update exposure times. In the summer of 2018, I participated in mock observing that helped ensure the functionality of the ICS, where the online pipeline that I helped develop provides status

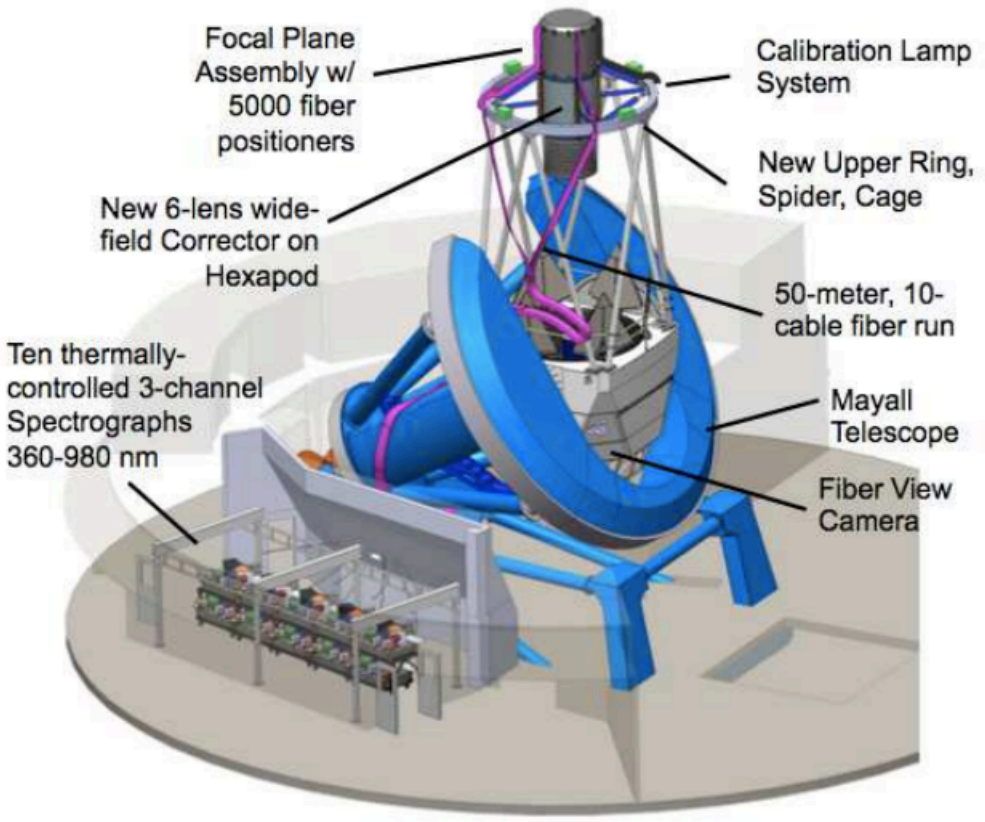

Figure 2.8: Model of the Mayall telescope used for DESI operations. Light enters the fibers at the focal plane and travels down to the spectrographs to be recorded by a CCD [44].

information to the ETC about the current exposure. More detail is given in Section 4.3.5 on specific results.

2.2.2. Optical System

DESI uses a Cassegrain system possessing a parabolic primary mirror and hyperbolic secondary mirror. This setup uses the existing Mayall primary mirror, with a newly developed prime focus corrector that allows the 5,000 optical fibers to be arranged over 8 square degrees of the sky. The primary mirror is 3.8 m in diameter, has a radius of curvature of 21.3 m, and a focal length of 10.7 m. This configuration yields an 8 square degree field of

view. The corrector system is composed of six corrector elements, with lenses ranging from 80 to 114 cm in size. The optical corrector elements are shown in Figure 2.9.

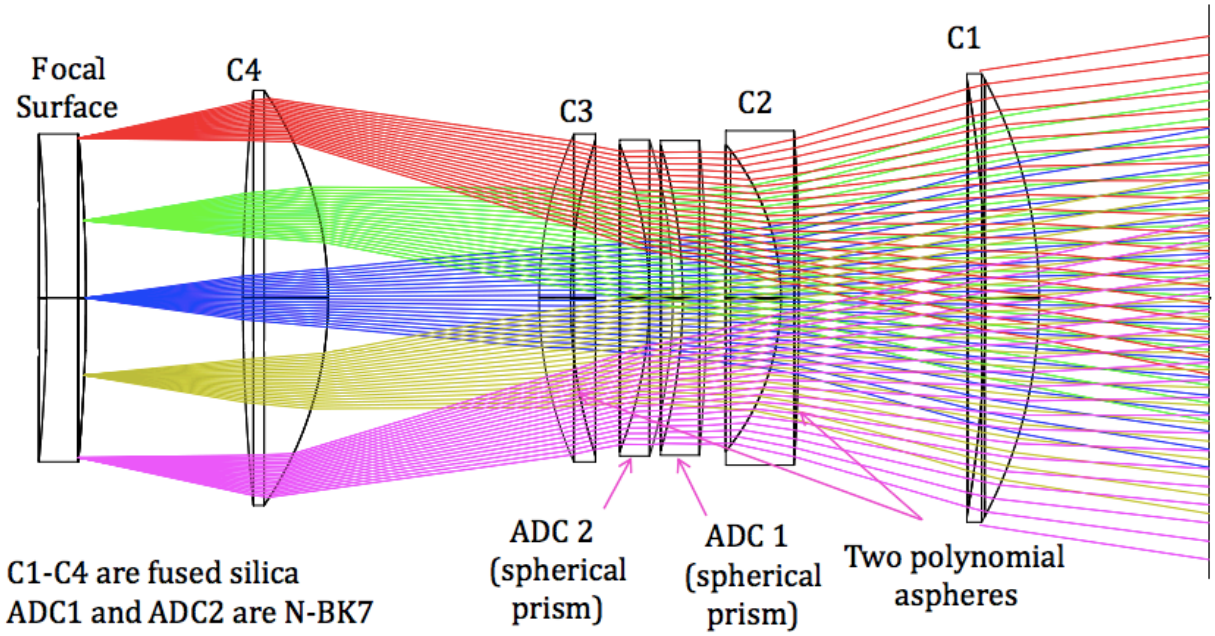

Figure 2.9: The DESI optical corrector system. This system is composed of 6 corrector lens, 4 of which are made of fused silica, and the other 2 made of borosilicate crown glass [43].

2.2.3. Focal Plane Assembly

To operate, light from an individual target will enter the tip of one of the 5,000 optical fibers on the focal plane. This light is then transmitted to the spectrograph by passing the information along the length of the optical fiber. The light is collimated using a collimating mirror, and then split using dichroic filters as beam splitters, ultimately reaching the CCDs as shown in Figure 2.12.

The focal plane system (FPS) comprises three functional components: fiber positioners that place each fiber on a unique science target for each exposure, field fiducial cameras that that provide point light sources as references throughout the FOV, and Guide, Focus, and Alignment (GFA) sensors that measure the pointing and tilt of the focal surface. The

fiber positioners are fully robotic, with 120 illuminated fiducial cameras and 10 GFA cameras. Figure 2.10 shows the completed DESI focal plane, with all 5,000 fibers and cameras installed.

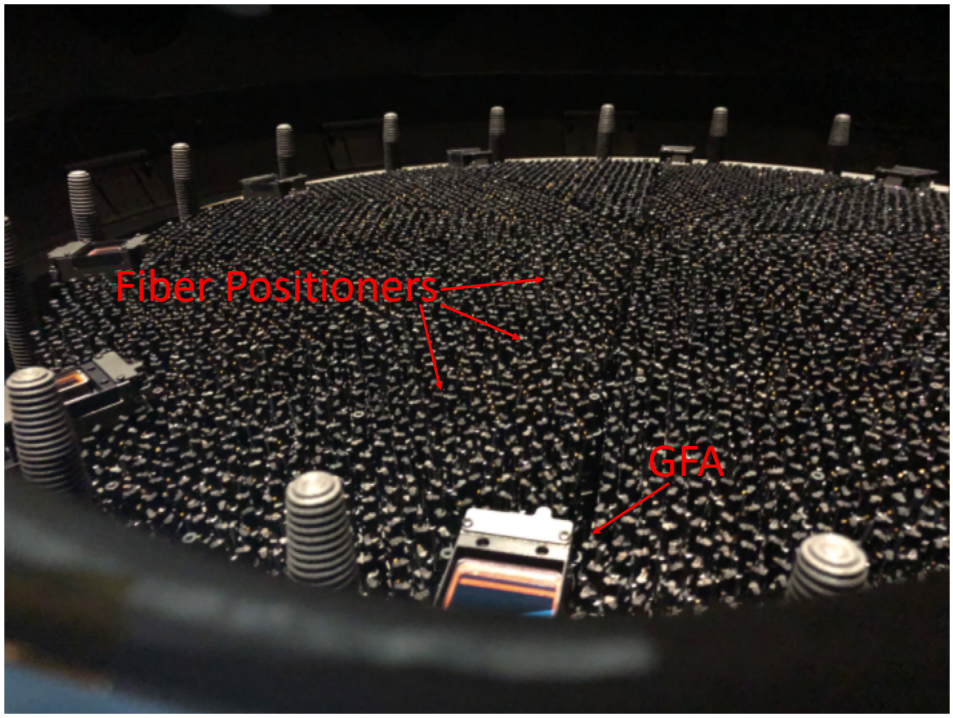

Figure 2.10: The completed DESI focal plane, now installed on the Mayall [46]. Arrows point to the FPS components, where fiber positioners contain both science fibers and illuminated fiducial fibers.

2.2.3.1. Optical Fiber System

The function of each optical fiber is to transmit the light from an observed science target from the focal plane to the spectrograph input, as shown in Figure 2.11. Each fiber has a 107 μm diameter, mounted in a single fiber positioner. The fibers are collected into ten groups of 500, where each fiber group spans 49.5 m from the focal plane to the spectrograph room.

The fibers used by DESI are Polymicro FBP, low OH fused silica fibers, optimal for broadband transmission without the spectral absorption features found in high OH, UV enhanced fibers [43]. The bulk throughput of the fiber system ranges from 55.5% at 360

nm to 93.7% at 980 nm. The FBP fibers experience low focal ratio degradation (FRD) due to their uniform cladding thickness and stress-relieved polyimide jackets. The fibers have a lifetime of 376,000 movements, well within the DESI range, where 185,000 total movements are predicted for an individual fiber over the five year survey.

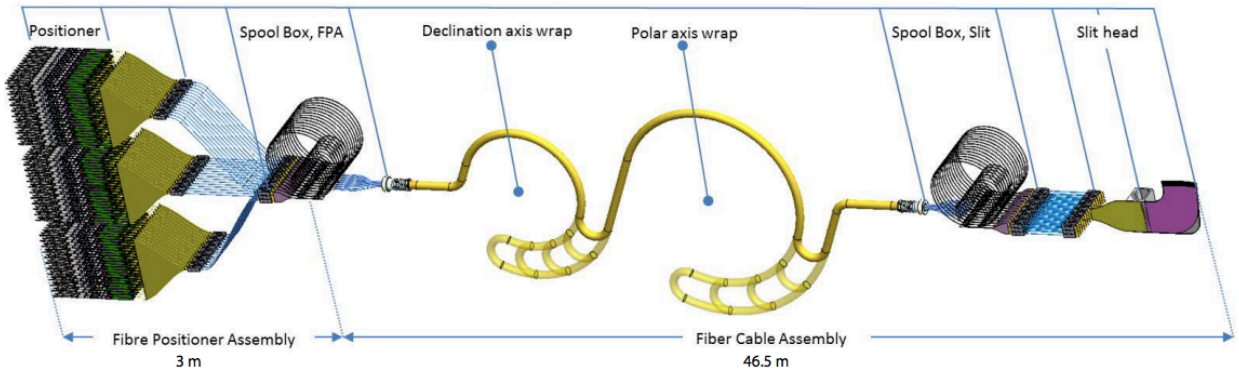

Figure 2.11: A schematic of the DESI optical fiber system. Light from an extragalactic target enters each fiber, then travels 49.5 m until it reaches the input of the spectrograph [43].

2.2.4. Spectrographs

Each of the fiber groups possessing 500 optical fibers leads to a spectrograph, where DESI employs ten identical spectrographs. Each spectrograph collects light from three wavelength channels (blue, red, and near-infrared) recorded by an individual CCD, for a total of 30 CCDs. Each of the channels has an optimized resolution range to optimize throughput and spectral coverage, at 2,000 - 3,000, 3,500 - 4,500, and 4,000 - 5,500, respectively. A schematic of the spectrograph system is shown in Figure 2.12.

Light that enters the DESI spectrograph first passes through a fiber slit. The slithead consists of a thin, stiff plate with a curved edge radius of 468 mm with one fiber group of 500 fibers. The fibers are mounted in bundles of 25, with 20 total bundles attached to the slithead.

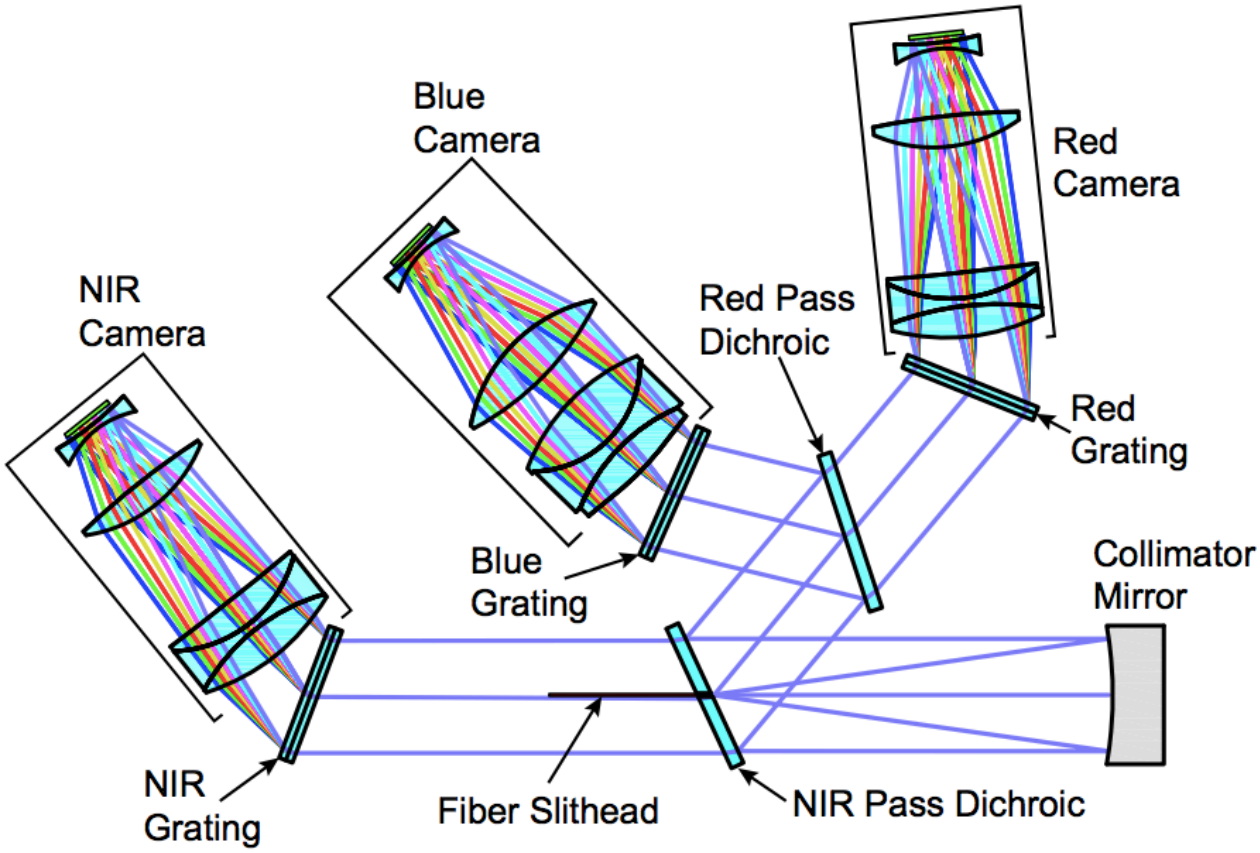

Figure 2.12: A schematic model of the DESI spectrograph and optical beam path [43].

After passing through the slithead, light is collimated using a spherical collimator mirror with reflective optics. The collimated light then passes through two dichroic filters to split the light into the three constituent channels. These filters are made of fused silica, coated with the dichroic on one side and an antireflection coating on the other. The observable channels can detect wavelength ranges of 360 - 590 nm, 566 - 772 nm, and 747 - 980 nm for the blue (b), red (r), and near-infrared (z) channels respectively. After splitting into constituent channels, the light then passes through a holographic grating to produce spectra. The light then enters the CCD, where DESI CCDs are composed of $4,000 \times 4,000$ pixel arrays with 15 μm pixels. The blue channel uses the ITL STA4150A camera provided by the University of Arizona Imaging Technologies lab and the red and near-infrared channels use the LBNL

$4,000 \times 4,000$, 250 μm thick CCD to optimize quantum efficiency [43]. Each camera records an image of 500 spectra, resulting in 30 total images for a single DESI exposure.

2.2.5. DESI Targets and Redshift Measurements

Redshift surveys such as the Dark Energy Spectroscopic Instrument (DESI) are designed to measure galactic redshifts in order to calculate the 2PCF to chart the large scale structure and expansion history of the universe [42]. The redshift of galaxies are determined by using chemical features seen in their spectra, where the wavelengths have been stretched, and thus redshifted, due to cosmological expansion. DESI aims to observe targets over a redshift range of $0 < z < 3.5$. In order to satisfy this goal, DESI will observe several different classes of galaxies and quasars in order to construct a large scale redshift catalog, with the target types and observing statistics shown in Table 2.1.

Table 2.1: Projected Observation Statistics of DESI Science Targets

Galaxy Type	Redshift range	Targets per deg^2	Exposures per deg^2	Baseline sample
LRG	0.3-1.0	610	610	7.7 M
ELG	0.6-1.6	2400	1870	17.1 M
QSO (tracers)	<2.1	170	170	1.7 M
QSO (Ly-α)	>2.1	90	240	0.7 M
BGS	0.05-0.4	800	740	9.9 M
BGS-Faint	0.05-0.4	600	460	6.0 M

2.2.5.1. Luminous Red Galaxies

Luminous red galaxies (LRGs) display high luminosity and appear red in optical wavelengths. Their redness is due to lack of star formation and high stellar mass. Spectra of LRGs show a distinct, prominent break in their spectral energy distribution (SED) around 4,000 Å caused by the accumulation of a large number of metal lines [47]. This feature can

be used to find their associated redshift in the same amount of observing time despite a lower signal to noise ratio [48]. An example LRG spectrum is shown in Figure 2.13.

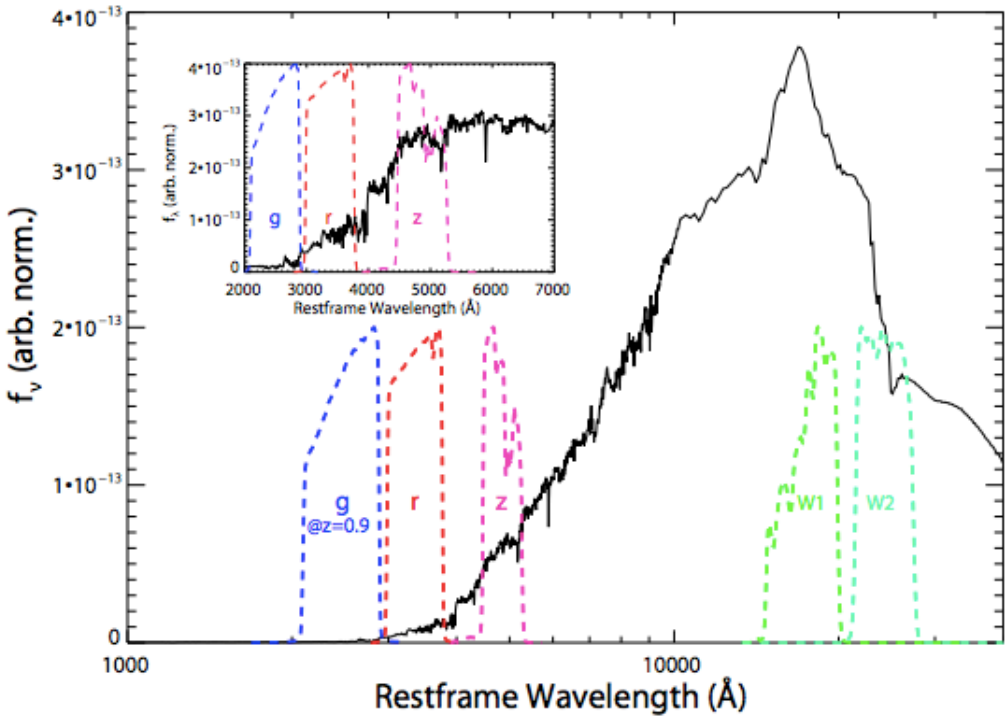

Figure 2.13: An LRG spectrum, with the passband of the DESI imaging survey filters laid on top. The top left of the image is zoomed in on the spectral feature of interest used to calculate its redshift [42].

2.2.5.2. Quasi-Stellar Objects

Quasi-stellar objects (QSOs) are galaxies with active nuclei, that appear to be extremely luminous stellar like objects. They are observed at the farthest distances, and can therefore be used to probe the dynamics of earlier epochs of the cosmos. At redshifts of $z < 2.1$, chemical features such as Ly-α, CIV, CIII, and MgII will be used to find their redshifts, as seen in Figure 2.14. To find the redshift to QSOs at $z > 2.1$, spectra will be re-observed to obtain adequate signal to noise to distinguish the Ly-α feature. This is due to the intervening mass overdensities along the line of sight potentially masking this feature, where

neutral hydrogen is sufficient to absorb the ionizing photons [49], showing up as extinction features in the quasar spectra.

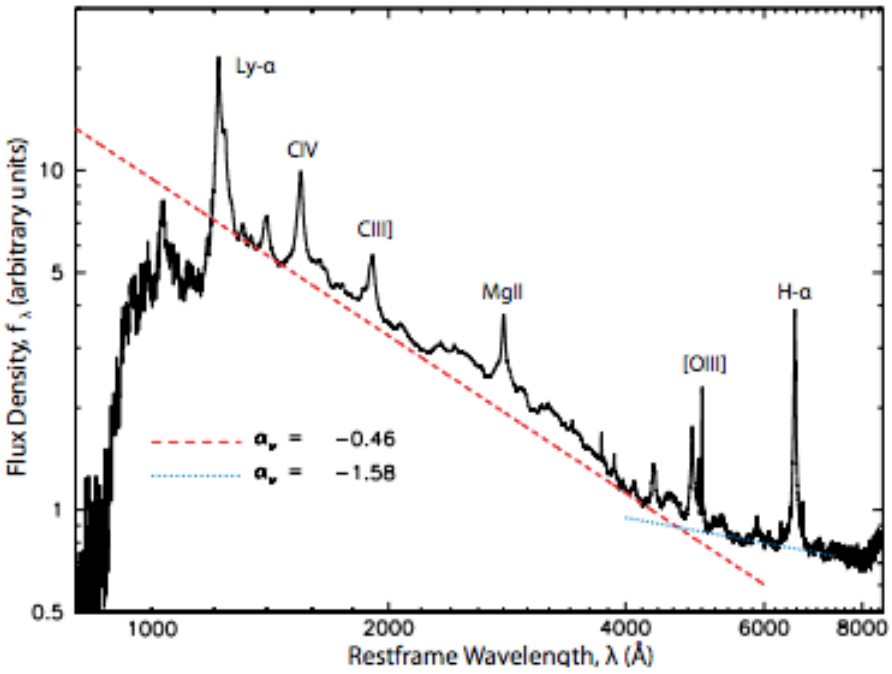

Figure 2.14: A QSO spectrum showing the chemical features of interest used to find its redshift [42].

2.2.5.3. Emission Line Galaxies

Emission line galaxies (ELGs) are typically late-type spiral galaxies, with sufficiently high star forming rates. They are largely comprised of short-lived, bright and massive stars, exhibiting strong emission features [50]. They are generally bluer than LRGs, as their color is dominated by the high forming rate of massive stars. ELGs are crucial targets to observe, as their redshift range spans that of the onset of the observed accelerated expansion of the universe. Prominent spectral features used to determine redshift include Hβ at 4,861 Å and OIII at 5,007 Å, although these features are only observable by DESI out to a redshift of $z < 1$. The main spectral feature used to find the redshift of ELGs is the OII doublet seen at

rest wavelengths of 3,727 Å and 3,729 Å, because of its bluer wavelength and unique profile, as can be seen in Figure 2.15.

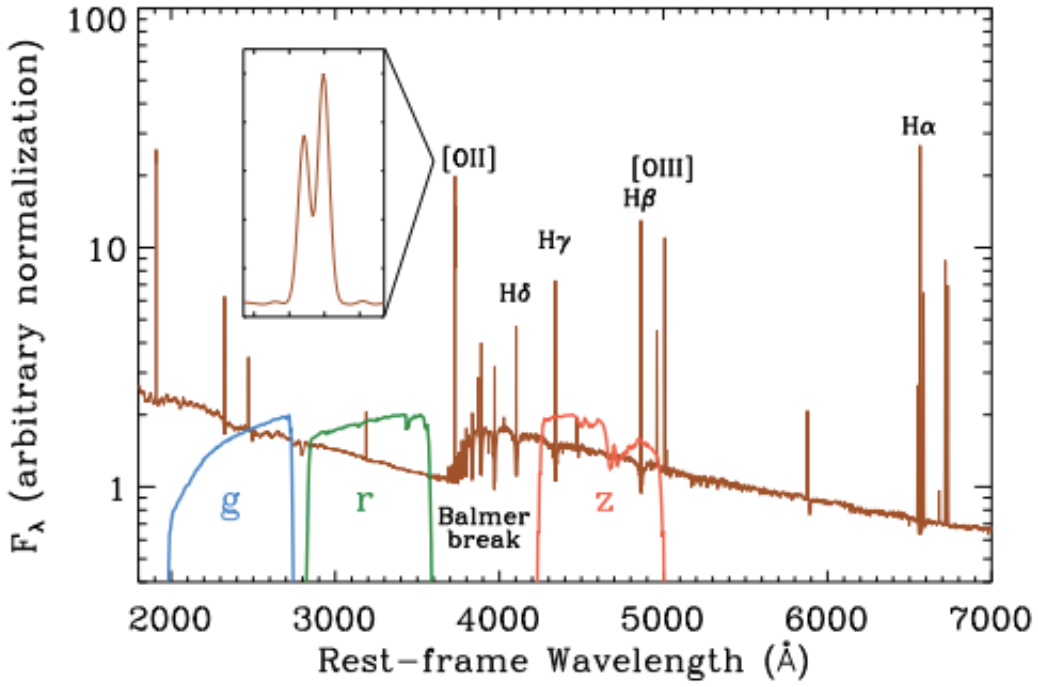

Figure 2.15: An ELG spectrum showing the chemical features of interest used to find its redshift. The main feature of interest, the OII doublet, is shown in the zoomed in image [42].

All of these objects will be observed during dark time conditions, when the moon contributes little to no excess noise to the spectroscopic images. ELGs will also be observed during gray time, when the moon contributes a non-negligible amount of noise to the images. However, at certain times, the moon conditions will be such that spectra for all of these target types would be too overwhelmed by photometric noise for scientific purposes. During these bright time epochs, the closest bright galaxies at $z < 0.4$ and Milky Way stars will be observed.

Chapter 3

Data Samples, Simulations, and Telescope Operations

Both ROTSE and DESI optimize their data collection strategy by continuously observing the night sky when weather permits. While ROTSE takes photometric images by searching for optical transient events, DESI will spectroscopically observe galaxies and quasars out to a redshift of $z \sim 4$.

Following data collection, both experiments send their respective images through processing pipelines specific to the experiments that allows scientific analysis to be performed. These processes are discussed in detail in Chapter 4, but it is necessary to at least define both photometry and spectroscopy before describing the data collected by both experiments.

For both experiments, I have participated in data collection. I was involved in the collection of ROTSE data described in Section 3.2.2 for three years, until the refurbishment process began. Although DESI has only recently started to collect spectroscopic data, I participated in an imaging survey described in Section 3.3 to be used for acquiring sources for the spectroscopic survey.

3.1. Photometry

Photometry is the process of measuring the amount of light or flux radiated from an astronomical object through a telescope. Modern photometry measures flux by connecting this telescope to a photometer, most commonly a CCD that converts flux to ADC counts, or detected electrons.

Flux coming from each individual source into the CCD will often span multiple pixels in both x and y. When it comes from a point source such as a star, the amount of light in pixel space across the CCD can be described by the system's point spread function (PSF). The PSF is a function in (x, y) of light deposited in nearby pixels in an image from a given point source, caused by effects due to the optics of the instrument and the atmosphere. So, each point source seen in an image is thus the convolution of the source itself and the PSF, as seen in Figure 3.1. This function may vary across the image, so knowing the PSF over the entire CCD is necessary to deconvolve the object from the imaging system. This deconvolution process, where one would like to accurately extract the signal from an astrophysical source, S_{source}, can be described by

$$S_{observed} = S_{source} \times f_{distortion} + \epsilon. \tag{3.1}$$

In Equation 3.1, $S_{observed}$ is the signal observed by the telescope, $f_{distortion}$ describes the distortion of S_{source} due to instrumental effects, and ϵ represents noise is the image, where each of these measurements is a function of (x, y).

However, light extracted from the pixels containing a given source does not only come from the object itself. Other prominent sources of excess light include noise due to the sky and electronics, which must be accounted for when determining that object's flux. The excess light from the sky comes from scattering and interactions of light in the atmosphere, where the full sky subtraction and noise reduction processes are described in Chapter 4.

Once the raw flux measured in detected CCD counts of an object has been determined, this value must be converted to a meaningful physical quantity. This quantity is called a magnitude, as described in Section 1.4.1. Each instrument will produce measurements specific to the device, which must be calibrated to put all measurements on equal footing.

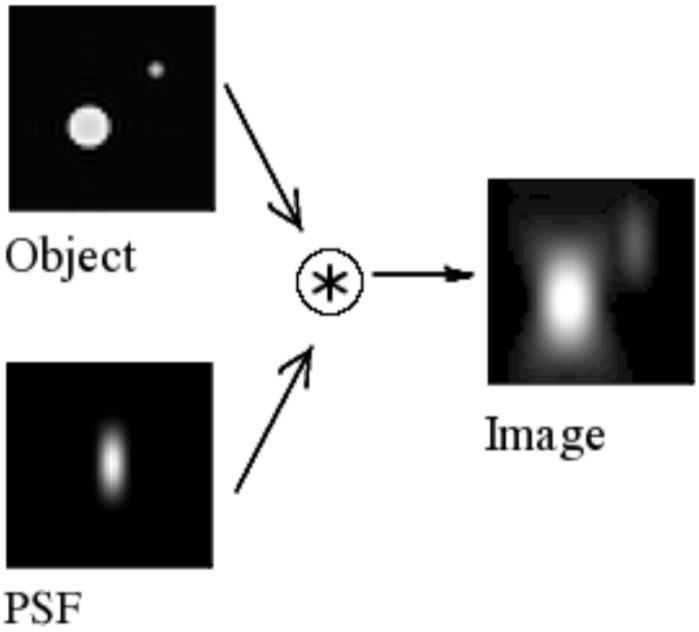

Figure 3.1: Example convolution of a point source and imaging system PSF to produce an output CCD image.

The end results is an apparent magnitude, or brightness of an object as observed by the telescope.

There are three basic ways in which this is typically done: absolute, differential, and relative photometry. Absolute photometry requires using a standard photometric system with a well defined passband, or wavelength range, where differences between instrumental observations and the standard system are used to determine observed magnitudes. Differential photometry compares the observed counts of a known reference object, typically a star, to the observed counts of a transient event in the same image, and uses this difference or ratio to calculate a differential magnitude for the transient event. This is the simplest method, and is of particular interest for transient events like variable stars, where one wants to know the change in brightness of an object over time.

In relative photometry, the observed magnitude of a well observed object, such as a star whose brightness does not change over time, is compared to the known magnitude of that

object, and this difference is used to correct the observed magnitude of a transient event such as a supernova whose brightness varies over time. Many expansive stellar/galactic catalogs exist and ROTSE can take any of these catalogs as input, but uses the USNO-B catalog [51] as default. This calibrated magnitude is then corrected for atmospheric extinction, which is the reduction of light as it passes through Earth's atmosphere. This correction comes from estimating the reddening of light due to dust emission in the space between the Milky Way and the host galaxy of the observed object [52].

Each telescope can detect photons within a specific wavelength range. As mentioned in Section 2.1, ROTSE has significant quantum efficiency from 3,000 - 10,000 Å. This is broader than typical photometry, where telescopes often use filters that limit the detectable wavelength range to some standard range. The Johnson-Cousins system [53] uses five filters - U, B, V, R, and I, or $UBVRI$ - that each cover a subset of the ROTSE wavelength range, as shown in Figure 3.2. This has the advantage of measuring color, or differences between magnitudes observed by sequential filters, and being able to describe attributes such as temperature evolution that require knowledge of the flux observed at different wavelengths. However, because of the finite quantum efficiency of these filters, photons between each passband are lost, necessitating the use of unfiltered telescopes such as ROTSE. The expansive wavelength range of ROTSE allows it to be used as a bolometer, covering almost the entire optical wavelength range.

There are numerous filter systems, but here $UBVRI$ system is of most relevance. Most stellar sources including SNe, however, emit light well outside the optical range, from X-rays to infrared. This information is important when trying to perform many calculations such as EPM described in Section 1.5.3.2. The $UBVRI$ system can be extended to the NIR region with filters such as the 2MASS [54] JHK_s filters, that extend all the way out to approximately 2.4 μm.

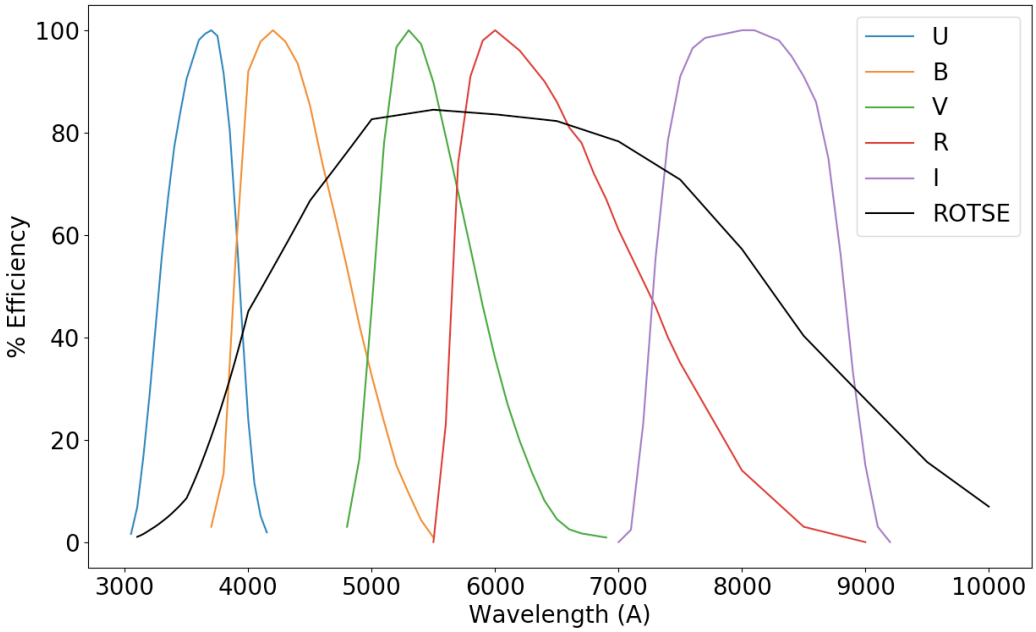

Figure 3.2: Comparison of the ROTSE transmission to that of the Johnson-Cousins UBVRI system.

While one can calibrate objects seen by a telescope to standard catalogs, there must still be a system that defines what a "standard" brightness actually is. This is done by defining what is called a zero-point magnitude for each filter and photometric system,

$$m_x = -2.5 \log_{10}(f_x) + ZP_x, \tag{3.2}$$

where m_x is the magnitude for a given filter x, f_x is the flux detected by the telescope passing through the filter, and ZP_x is the zero point magnitude of the filter. The Johnson-Cousins system uses the star Vega to calculate zero point magnitudes [53], where all colors are set to zero, meaning all $UBVRI$ magnitudes have the same value. In this system, Vega has a magnitude of 0.03 in all bands. ROTSE typically calibrates magnitudes using either Johnson V or R band zero points. Final, calibrated magnitudes are used to construct light curves, which show the brightness of an object over time. For this analysis, I use modified Julian dates (MJD) to define the date of observation [55].

3.2. ROTSE Data Collection

Since the inception of ROTSE-III in 2003 [36], the four telescopes comprising the ROTSE-III experiment have amassed approximately 40 TB of photometric data. The collection of data can be broken down into three surveys, The Texas Supernova Search (TSS) from 2003-2007, the ROTSE Supernova Verification Project (RSVP) from 2007-2012, and the Texas Supernova Spectroscopic Survey (TSSS) from 2012-2016. During operations, this data collection occurs on a nightly basis, assuming the weather conditions for observing are appropriate. These images are then calibrated and reduced in order to extract the relevant information for scientific analysis. I was involved in the data collection from 2013-2016, helping to identify transient candidates and process the data once transients were confirmed. I also helped to maintain the rotse OS in addition to the hardware tasks discussed in Chapter 2.

3.2.1. ROTSE Operations

All of the ROTSE-III telescopes are fully robotic and fully automated by default. This automation is designed to facilitate rapid GRB observations. NASA's *Swift* satellite detects gamma rays [56], and once it observes a GRB, it immediately sends a notification to all relevant telescopes, including ROTSE. Specifically, the *Swift* Burst Alert Telescope (BAT), which searches the sky for new GRBs [57], sends autonomous messages to any telescope connected to the Gamma-Ray Coordinates Network (GCN) [58]. Upon receipt of a GCN alert, ROTSE is able to immediately slew to the new GRB to provide follow-up observations of the optical after glow of the GRB. A manual mode is also available, where the user controls the movement of the OTA and exposures, but this is not typically employed. In general, full automation is used, where the ROTSE Operations System (rotse OS) controls the functionality of the telescope. The rotse OS is composed of multiple, interconnected daemon interfaces, each serving a particular function, shown schematically in Figure 3.3.

The rotse OS is comprised of three computers that control the data acquisition, movement of the OTA, and processing of data to be viewed by observers. The central computer hosts the rotse daemons and their interactions and controls the data acquisition, interacting with the main rotse daemon, rotsed, via the camera daemon, camerad. The mount computer controls the slewing of the telescope, interacting with rotsed via the schierd daemon. The third computer takes data from the camera computer, sending it through the data reduction pipeline described in Chapter 4. The clamd and spotd daemons control the mechanics of the enclosure and handling of any mechanical failures, respectively. The alertd daemon interacts with the GCN to receive information about ongoing GRBs and weathd daemon uses local weather conditions to determine if the conditions are safe for observing. The userd daemon allows users to control the telescope via the ROTSE user shell (rush). Table 3.1 more explicitly defines the use of each rotse daemon

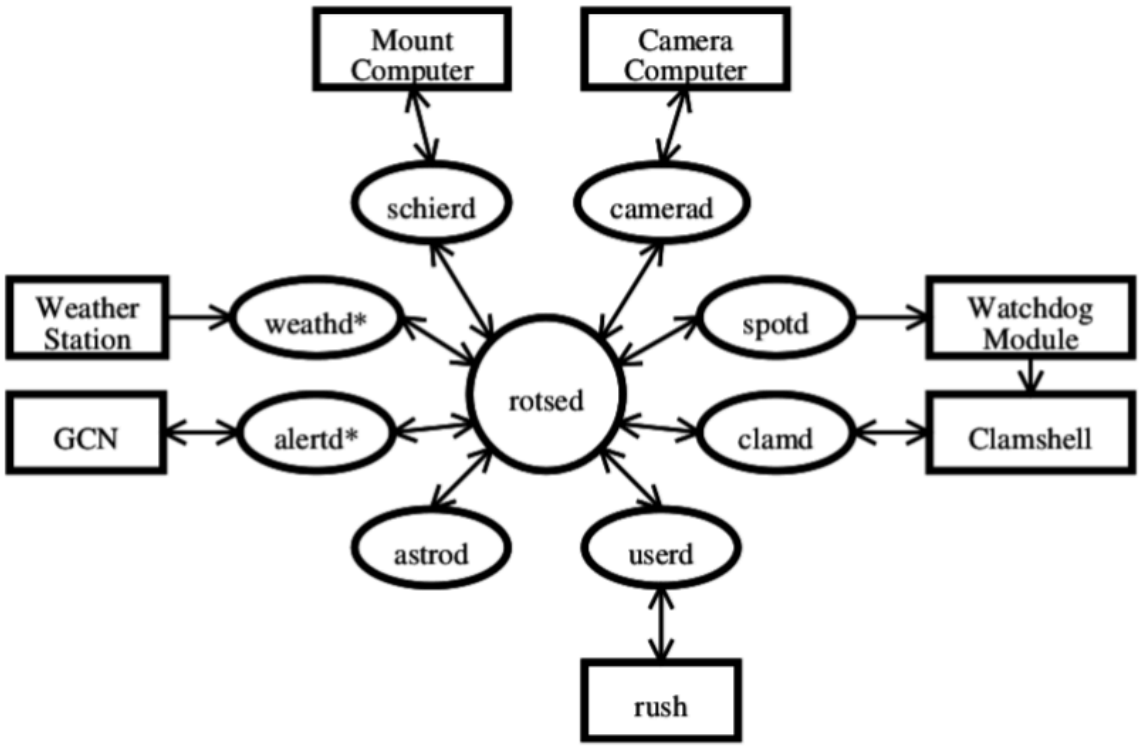

Figure 3.3: A schematic representation of the ROTSE Operations System [36].

Table 3.1: ROTSE Daemon Functionality

Daemon	Functionality
rotsed	central daemon handling the coordinated interaction of all ROTSE daemons
camerad	controls the camera functionality and exposure settings
schierd	interacts with the mount computer to control the movement of the telescope
weathd	keeps track of weather conditions and dictates when to shut the ROTSE enclosure
alertd	alerts the central daemon of a GCN alert, facilitating the observation of a current GRB
astrod	keeps track of the scheduling of observations
clamd	controls the opening and closing of the ROTSE enclosure
spotd	alerts the system of any mechanic failures, so that the clamshell will shut necessarily
userd	facilitates manual use of the telescope via use of the ROTSE user shell (rush)

Inside the ROTSE-IIIb enclosure, the central computer hosts the rotse OS daemons and their interactions. This includes interacting with the daemon that talks to the mount computer that controls the movement of the OTA, and obtaining weather and GRB information. Additional daemons control operation of the clamshell and the camera, telling the enclosure when to open and close and the camera when to take an exposure. Recorded images are passed along to a third computer, which processes the data to be used for subsequent analysis. Thumbnails are sent to the ROTSE web server, so that they can be viewed by users in near real time for both GRB and SNe searches.

3.2.2. ROTSE Data Sample

In addition to images of the sky taken on a nightly basis, described here as science images, calibration images are taken during the evening before the sun passes below the horizon, in order to maximize observing time.

3.2.2.1. Science Images

During a typical night of observing, ROTSE is configured for a particular scientific imaging strategy. Target coordinates and priorities are specified to determine the observing schedule for the night. In real time, these can be compared to target coordinates coming from a GCN alert to reprioritize the observing strategy. Due to the brevity of GRB events, any given GRB takes immediate priority. Due to the scientific importance of SNe for the ROTSE surveys, follow up observations of these events take subsequent priority. Supernova fields are then patrolled throughout the night, to facilitate the discovery of new transient events.

If a GRB occurs in an accessible region of the sky, the OTA immediately slews to observe this event. Upon receipt of a GRB notification, ROTSE takes successive $5 - 60$ second exposures for the entire duration of the GRB, which ranges from minutes to hours depending on its progenitor. Initial exposures are 5 seconds so that information is not lost while the explosion is rapidly changing, with later exposures extending to 60 seconds.

Exposures of supernova survey fields are generally 60 seconds, and are observed multiple times per night to improve the overall signal to noise ratio (SNR) for that region of the sky. Typically, supernovae to be followed up are observed up to 16 times per night. Supernova survey fields are observed up to 8 times per night, where in both cases the frequency of observation depends on adequate weather conditions.

3.2.2.2. Calibration Images

When the CCD is collecting photons for a science exposure, there is inherent thermal noise in the electronics, and additional photons from sky background. These must be accounted for when trying to extract the amount of light in these pixels solely due to astrophysical objects. There is also a systematic charge collection, dark current, that builds up over time in each pixel, that must be accounted for as well. This is done by taking "dark" exposures without opening the camera shutter. Sets of dark exposures are taken with exposures times of 5, 20, and 60 seconds to match those of science images, so that the dark current can be subtracted from science exposures during the data reduction process. This is done by tabulating N dark exposures and taking a median value per pixel to produce a calibration frame.

In addition to thermal noise that builds up across the entire CCD, there can be variations across the field of view of the CCD, yielding different light deposition. For instance, imaging effects such as vignetting, which reduces the light absorbed as one moves radially from the center of the FOV due to the angle of light after passing through the camera lens, can cause these types of variations. Also, individual pixels will have modestly varying gains. These effects are accounted for by taking "flat" images during evening twilight, so that the entire CCD is uniformly illuminated. Ultimately, the corrected image is defined by

$$Corr(x, y) = Flat(x, y) \times (Image(x, y) - Dark(x, y)), \tag{3.3}$$

where $Image(x, y)$ is the observed image, $Dark(x, y)$ is the dark image, and $Flat(x, y)$ is the flattened image.

3.2.3. Complementary Photometric Observations

In addition to ROTSE observations, the use of complementary photometry is valuable in fully describing transient events. Many telescopes with broadband filters observe the same SNe observed by ROTSE, and obtaining this data not only helps to validate ROTSE detection and measurement, but also supplements ROTSE epochs when observation by ROTSE is not possible. Additionally, these extra observations help calibrate ROTSE as a bolometer to be used for evolution of characteristics such as temperature and photospheric velocity evolution [25].

In addition to GRB detection, NASA's $Swift$ satellite is crucial for achieving ROTSE's scientific goals regarding supernova observation. For SNe discovered or followed up by ROTSE, the $UVOT$ instrument onboard the $Swift$ satellite provides complementary optical u, b, and v data and supplemental ultraviolet data via the use of their $uvw1$, $uvm2$, and $uvw2$ filters [59].

For additional optical photometry, several main sources include, but are not limited to the Konkoly and Lick Observatory telescopes. In particular, the 0.6 m, 0.9 m, and 1.8 m Schmidt telescopes [60] and the 0.76 m Katzman Automatic Imaging Telescope (KAIT) [61] have provided many complementary observations. The Konkoly telescopes and KAIT provide broadband photometry comparable to that of ROTSE, allowing direct comparisons of these measurements, while additional $UBVRI$ photometry provided by KAIT allows the comparison of ROTSE data to filtered photometry.

Additional instruments must be used to acquire NIR observations. If data can be collected across the entire spectrum for individual SNe where ROTSE data exists, it can be used to calibrate ROTSE broadband photometry to bolometric luminosity, which describes the amount of light from an object across all wavelengths. This calibration process is important, as it allows ROTSE to be used as a bolometer when optical or NIR data is missing, as

described in more detail in Chapters 5 and 6. Table 3.2 shows the observable wavelength range of photometric passbands that I use for analysis in this thesis.

Table 3.2: Photometric Observations per Passband

Photometric System	Filter	Observed λ (nm)	Object(s)
ROTSE	Unfiltered	300 - 1,000	SNe IIP, SN 2007gr, SN2010kd
Jonhson	U	300 - 420	SN 2007gr, SN 2010kd
Jonhson	B	360 - 560	SN2007gr, SN2010kd
Jonhson	V	460 - 740	SN2007gr, SN2010kd
Jonhson	R	520 - 960	SN2010kd
Jonhson	I	680 - 1,200	SN2010kd
DECam	g	385 - 556	DESI targets
DECam	r	531 - 734	DESI targets
DECam	z	800 - 1,029	DESI targets
SDSS	r'	533 - 772	SN2007gr
SDSS	i'	652 - 901	SN2007gr
2MASS	J	1,066 - 1,442	SN 2007gr
2MASS	H	1,440 - 1,818	SN 2007gr
2MASS	K_s	1,934 - 2,384	SN 2007gr

3.3. Preliminary Photometric Observations for DESI

Although DESI is a spectroscopic instrument, the use of photometry is important for this experiment as well. Knowing where to point the optical fibers for each exposure requires knowledge of the targets to be observed and where they are in the sky. Additionally, the imaging magnitudes provide the ability to make color cuts for each target type so that the observing strategy of each sample is well defined before observing begins. These color cuts are described in further detail in Section 3.5.2.1.

Acquiring this knowledge for DESI was done over a several year period, using ground-based telescopes for optical photometry and the *WISE* satellite for NIR photometry [62]. The observing schedule for these surveys is summarized in Table 3.3. The ground based

photometry comes from three telescopes - the Blanco 4 m telescope at Cerro Tololo through the Dark Energy Camera Legacy Survey (DECaLS), and the Bok 2.3 m and Mayall 4 m telescopes at KPNO through the Beijing-Arizona Sky Survey (BASS) and MOSAIC z-band Legacy Survey (MzLS) surveys respectively [63]. For the latter, MzLS, I contributed 10 nights of observations. The imaging footprint of these surveys, with additional targets from the Dark Energy Survey (DES) is shown in Figure 3.4.

In addition to supplying DESI with the necessary targets for fiber assignment, having imaging magnitudes from these surveys allows the DESI simulations to more accurately reflect what will be seen in the data. In particular, the g, r, and z band imaging magnitudes coming from the Dark Energy Camera (DECam), which was the most efficient option for obtaining optical photometry, allow DESI to adequately simulate properties of targets corresponding to its b, r, and z spectroscopic bands, respectively.

Table 3.3: DESI Imaging Survey Schedule [63]

Survey	Telescope	Nights	Start	Finish	Passbands
DECaLS	Blanco	145	2014 Aug	2019 Mar	g, r, z
BASS	Bok	250	2015 Jan	2019 Mar	g, r
MzLS	Mayall	383	2016 Feb	2018 Feb	z

3.4. Spectroscopy

Spectroscopy is the process of measuring the amount of flux per wavelength radiated from an observed source. Because the measured flux is per unit wavelength, light from the telescope must be focused through a slit or fiber so that the CCD obtains only light from the source of interest. To avoid excess dispersion, the light must also pass through a collimator. In order to see light as a function of wavelength, it must also pass through a diffraction grating before entering the CCD. A schematic representation of the DESI beam path shown in Figure 2.12. An example of an observed spectrum across the CCD is shown in figure 3.5,

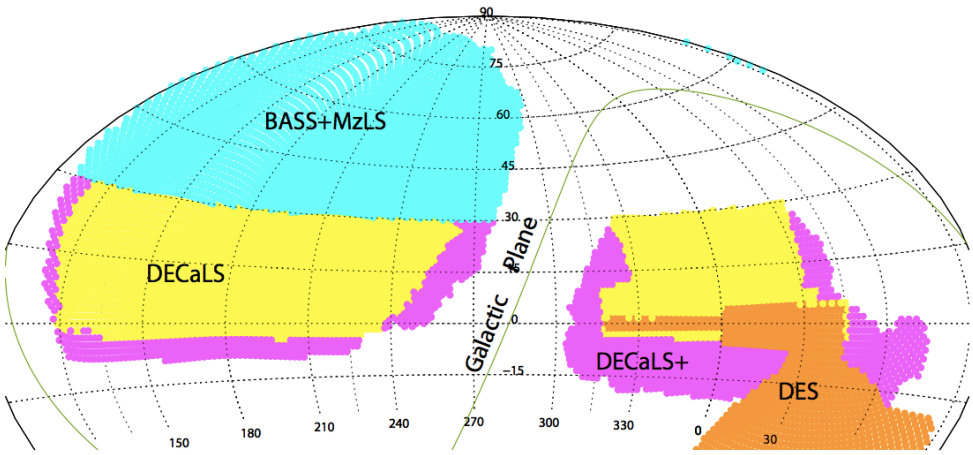

Figure 3.4: The primary imaging surveys used for acquiring DESI science targets. The cyan region shows the area of the sky covered by the BASS and MzLS surveys, the yellow and magenta regions show sky coverage of the DECaLS survey, and the orange region shows sky coverage of the DES survey [42].

where the gray horizontal line is the spectrum, and the bright ellipses show atomic emission lines due to elements in the atmosphere.

Figure 3.5: An example of a zoomed in galactic spectrum. The gray horizontal line is due to light coming from the source per unit wavelength, and the bright ellipses are discrete emission lines from the chemicals present in the atmosphere.

Once spectra are obtained in CCD images, they must be extracted and converted into meaningful physical quantities. Spectral extraction involves counting the detected electrons in pixels along the spectrum corresponding to some predefined wavelength bin. The minimum size of these wavelength bins is limited by the spectral resolution of the instrument's

diffraction grating, defined as

$$R = \frac{\lambda}{\Delta\lambda}, \tag{3.4}$$

where $\Delta\lambda$ is the smallest difference in wavelength that can be distinguished for a given wavelength, λ.

To extract a spectrum, it must be located in the image. This requires mapping the trace of the spectrum as a function of (x, y), as the spectrum may not lie in a straight line along the length of the image. Once the spectrum is located, counts along the spectrum in each wavelength bin must be counted. Initially, this was done by simply summing the counts over the pixel space for each bin. Unfortunately, this approach suffers from a degradation of SNR along the spectrum, so "optimal extraction" was proposed [64]. This method weights each point by its inverse variance, increasing the SNR along the spectrum and resulting in statistically uncorrelated values in each bin. Better still, is the method of "spectro-perfectionism," which is the method of spectral extraction used by DESI [65]. Spectro-perfectionism accounts for the fact that the PSF along a spectrum is not a separable function of pixels in (x, y), to be explained in further detail in Chapter 4.

Extracted Spectra must be calibrated for fiber to fiber variations across the CCD. This is done using continuum lamp calibration images taken earlier in the day, where each fiber is fully illuminated to show differences in flux along the fiber. Excess flux from the sky must be subtracted so that only flux from the astrophysical source remains. For fiber-fed spectrographs such as DESI, individual sky spectra are observed across the image and subtracting from science spectra. An example of an ELG spectrum before and after sky subtraction is shown in figure 3.6.

Extracted counts must be converted to a meaningful physical quantity via flux calibration. Spectroscopic flux calibration requires the inclusion of standard stars in each image. The stellar spectra from these objects are fit to stellar templates, then scaled to their imaging

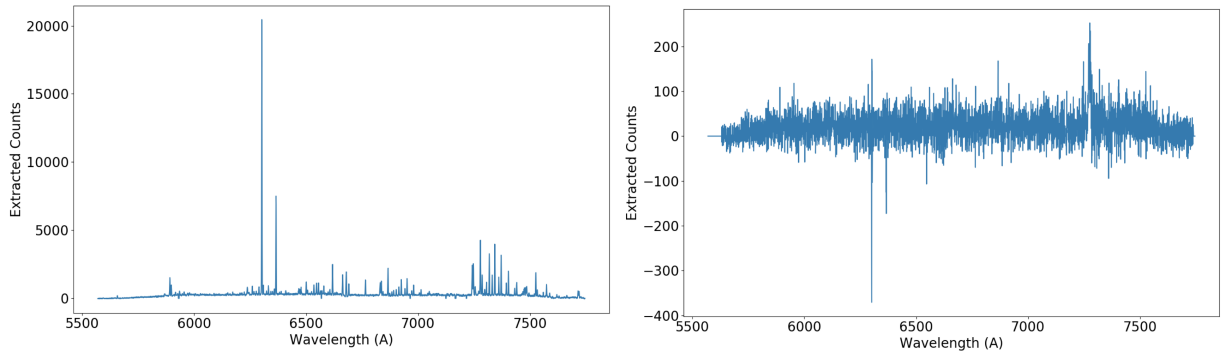

Figure 3.6: An ELG spectrum before and after sky subtraction. The spectrum on the left is before sky subtraction, with most of the visible emission lines due to the atmosphere. The spectrum on the right contains flux from only the ELG.

magnitudes from preliminary photometric imaging. From this scaling, a calibration vector is constructed and applied to science spectra.

3.5. DESI Data Collection

Beginning in 2020, DESI will begin collecting data and will continue to observe galaxies and quasars over a five year period. In total, more than 30 million science targets will be observed, from the local universe to over ten billion lightyears away. DESI will take science exposures on a nightly basis, given appropriate weather conditions for observing. Once these exposures are taken, they are passed through the DESI spectroscopic pipeline to be processed for analysis, described in full in Chapter 4.

3.5.1. DESI Operations

The Mayall telescope is fully robotic, but requires observers to monitor the proceedings throughout the entire night. An online data quality assessment pipeline will be used by these observers to make sure data quality is at the level required to obtain accurate redshifts for each target type, described in more detail in Chapter 4. The time between exposures will be less than 120 seconds [43], but this is enough time to process the data via the online pipeline, allowing the dynamic exposure time calculator (ETC) to update exposure lengths

in near real time. Precise exposure times are necessary to achieve high enough SNR to distinguish crucial spectral features, without wasting precious observing time. In addition to real time data quality assessment, the DESI data acquisition system (DAQ) must use complex algorithms to rapidly convert RA and DEC for targets in the FOV of a subsquent exposure to non-colliding fiber positions on the focal plane.

3.5.2. DESI Data Sample

The DESI data sample is comprised of science and calibration images. Calibration images including dark, bias, pixel flat, arc lamp, and continuum lamp exposures taken in the afternoon, when the dome is closed and no artificial light is present. Science exposures are taken for the duration of the night assuming adequate conditions, from the time that the Sun sets ten degrees below the horizon to the time it rises to ten degrees below the horizon.

3.5.2.1. Science Images

To measure the imprint of BAO on the large scale structure of the universe, DESI will make spectroscopic observations of four distinct classes of extragalactic sources - LRGs, ELGs, and QSOs as described in Section 2.2.5, and low redshift galaxies apart of the bright galaxy survey (BGS). To determine which objects will be observed spectroscopically, DESI uses the observed magnitudes of the preliminary photometric surveys to define color cuts and the results of prior spectroscopic surveys [42].

Although DESI data collection has been delayed due to complications from COVID-19, the color cuts for the survey validation observations have been defined. For BGS, the brightest galaxies where $r < 19.5$ and low quality galaxies where $r < 20.1$ will be observed. To observe LRGs in the desired redshift range, the color cuts $g - W1 > 2.6$, $g - r > 1.4$, and $r - W1 > 1.8$ are applied. The $W1$ filter is used by the Wide-Infrared Survey Explorer

(WISE), with an observable wavelength range of approximately $2,620 - 3,960$ Å [66]. For ELGs, color cuts of $r - z < 0.3$ and other sliding cuts in g will be applied. QSOs will be observed with an r band limit of $r = 22.7$ for high z objects, with an r band cut of $22.7 < r < 23.5$ for fainter objects.

During a typical night of observing, DESI will take approximately 40 exposures per night, with exposure times of approximately 1000 seconds. However, this number can increase or decrease depending exposure times which are adjusted based on observing conditions, discussed in further detail in Chapter 4. The observing strategy for DESI will be broken into three regimes based on moon conditions. These conditions include the phase of the moon and its angular position with respect to the coordinates of the current observation. The three regimes are the dark time, gray time, and bright surveys.

The dark and bright time surveys will cover the same 14,000 square degree footprint, but will differ in terms of target types observed. Dark time targets include ELGs, LRGs, and QSOs, while bright time targets will include BGS targets, Milky Way survey stars (MWS), and white dwarves (WD). Gray time observations will occur during times with intermediate moon brightness, where ELGs will be the dominant target type for these exposures. Table 2.1 shows the density of targets per exposure and projected baseline sample for the dark time and bright time surveys.

An example of a DESI dark time science exposure is shown in figure 3.7. This is a survey validation (SV) exposure, taken in June 2020, for a z band camera containing mostly ELGs.

3.5.2.2. Calibration Images

Spectroscopic analysis must account for bias and dark current. Here, we take a bias image to account for the innate noise in the electronics and atmosphere, and we take a dark

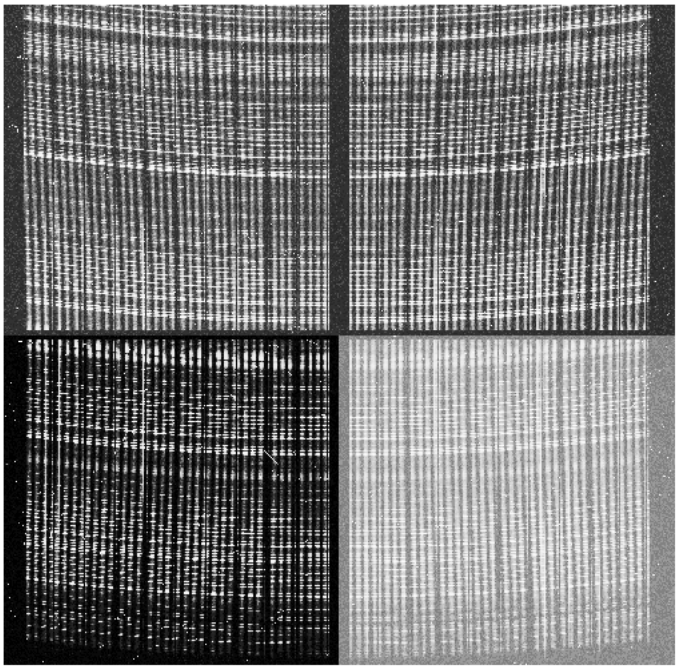

Figure 3.7: A DESI dark time science exposure, where vertical lines represent science targets, calibration targets, and empty regions of the sky. This was taken in June 2020 as a part SV for camera $z2$, containing mostly ELGs.

image to account for the building of excess noise over time. Because the length of a science exposure may vary, dark exposures are taken for one second, where the dark current per second is scaled to the length of the exposure during preprocessing. An additional pixel flat image is taken, to account for pixel to pixel variations across the entire CCD.

For spectroscopy, additional calibration images must be taken to account for spectrum to spectrum variations and to ensure that both the emission lines and continuua are adequately calibrated. One such calibration, taken by exposing the entire CCD to continuum lamps, is performed so that each fiber receives a similar amount of flux. This allows fiber to fiber variations to be accounted for through a fiber flattening calibration process. An example of a DESI flat exposure is shown in figure 3.8. The vertical lines seen in the continuum lamp exposure show fully illuminated fibers.

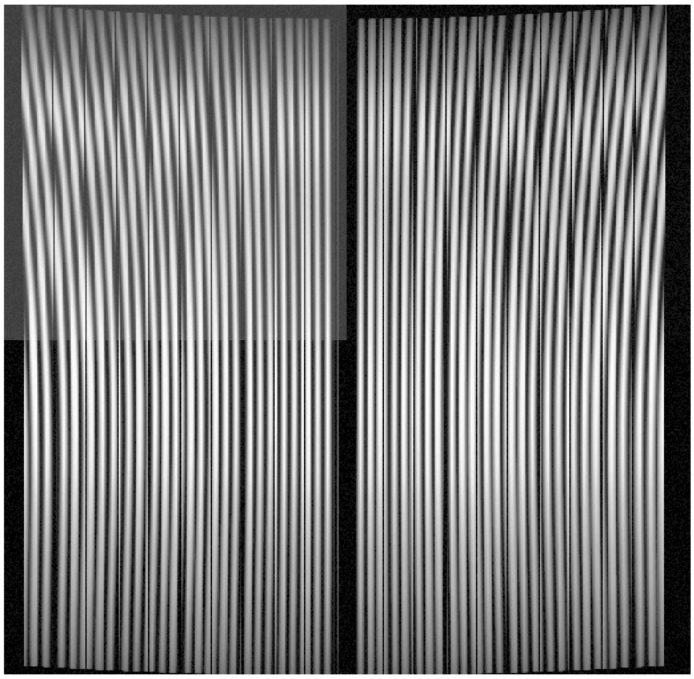

Figure 3.8: A DESI continuum lamp exposure, where vertical white lines show fully illuminated fibers. Large gaps between spectra indicate the separation of fiber bundles of 25 fibers each. The large separation in the middle divides the CCD amplifiers.

Because we ultimately need to map longitudinal y coordinates to wavelength values along a spectrum, we expose each fiber to arc lamps to illuminate the CCD. This exposes each fiber to a series of discrete atomic lines, with well defined wavelengths. The discrete nature of these emission lines allows the PSF to be properly calculated across the image, allowing an accurate y to wavelength solution to be found. An example of a DESI arc exposure is shown in figure 3.9. The spots seen in the arc lamp exposure show discrete atomic emission lines.

3.5.3. DESI Spectroscopic Simulations

Before DESI began data collection in late 2019, the spectroscopic pipeline and other DESI software had to be tested using simulated spectroscopic images. While these simulated

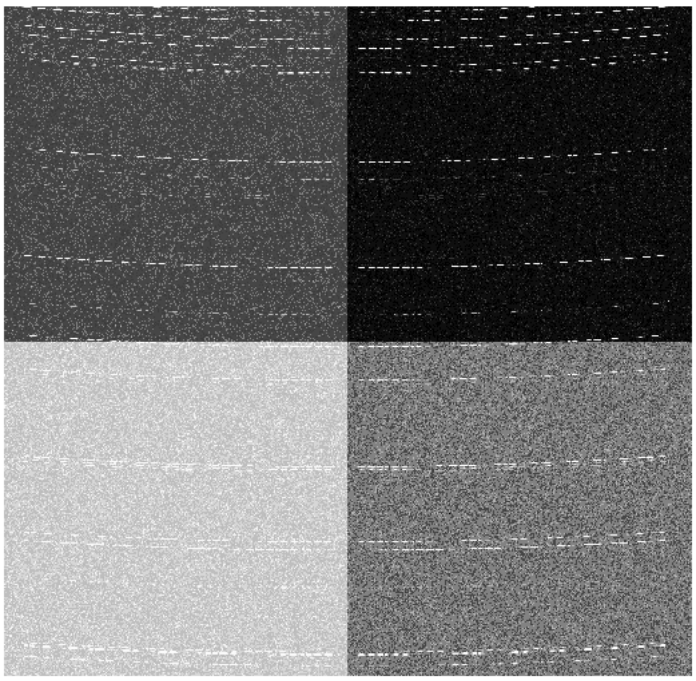

Figure 3.9: A DESI arc lamp exposure, where white spots show atomic emission lines based on the chemical present in each arc lamp. The four distinct sections of the image correspond to the 4 CCD amplifiers.

images reflect many, if not most, of the properties that will be seen in the DESI survey, it must be noted that only a limited amount of real spectroscopic data is available.

3.5.3.1. DESI Simulated Images

The targets to be included in spectroscopic simulations are initially generated using an N-body simulation, with a given input cosmology to provide RA, DEC, and redshift for each target. Spectral templates are matched to the magnitudes and colors of targets in the preliminary imaging surveys, so that each target possesses a simulated spectrum similar to what will be observed in the survey. These template spectra are based on previous spectroscopic surveys, for example the DEEP2 survey that provides template ELG spectra

for simulated ELGs [67]. A more detailed description of the target generation process is discussed in Chapter 7.

Once all targets possess simulated spectra, their coordinates on the sky are combined with observing conditions coming from models of KPNO weather, to populate exposures with spectra. Additional elements such as cosmic rays and fiber flexure are also simulated, so that the spectroscopic pipeline can test what it will see with data as realistically as possible. Once all input characteristics have been simulated, the spectra are projected onto the CCD in 2-D pixel space, with the observed spectrum by each fiber spanning the x direction and wavelength range of each spectrum roughly corresponding to the y direction.

3.5.3.2. DESI Simulated Spectra

While DESI simulated images are useful in testing the spectroscopic pipeline used to fully reduce DESI data, going through the computational steps to produce 1-D science spectra from these 2-D images takes a lot of time and computer power. Many forms of preliminary analysis used to predict or forecast clustering measurements and cosmology to be observed by DESI require the production of many science spectra in small amounts of time. One such method is via the use of the QuickGen pipeline, which quickly generates 1-D simulated spectra in minutes rather than hours [68]. For this pipeline, I implemented the simulation of bright and gray time objects, observing conditions such as moon brightness, and a more accurate flux calibration. In addition, I was responsible for keeping this pipeline up to date with the evolving DESI software and simulations, and ensuring that its outputs were on par with those of the offline spectroscopic pipeline. To ensure this, I ran the offline spectroscopic pipeline to generate results for the same target inputs, and then compared the final spectra, as shown in Figure 3.10.

This pipeline takes as input the same simulated spectra and observing conditions described in the previous section. However, generating outputs becomes much faster by skipping the projection of spectra onto the CCD and subsequent spectral extraction. Instead, QuickGen parametrically models the effects of observational systematics and the DESI spectrographs to go directly from the raw image and spectral template inputs to simulated 1-D extracted spectra.

Calibration spectra such as arc and flat exposures are similarly simulated to be used for calibrating science spectra. Once the extracted 1-D science spectra are simulated, they are fiber flattened and sky subtracted using the sky spectra in the image. Spectra are flux calibrated using standard star spectra in the image, with these processes described in full detail in Chapter 4. For consistency, outputs from the QuickGen pipeline mirror those of the offline spectroscopic pipeline.

Outputs from this pipeline were used in various DESI data challenges, as well as studies involving systematic and clustering measurements. An example comparison of QuickGen output to that of the offline spectroscopic pipeline is shown for a single ELG spectrum before and after sky subtraction in Figure 3.10, where the discrepancy seen in flux along the continuum was noted in a study I performed to place the output of both pipelines on the same footing. The large residuals seen in the right plot are due to emission lines from the observed galaxy.

3.6. Spectroscopic Follow-up Observations for ROTSE

Similar to the use of photometric surveys to supplement the DESI survey, ROTSE uses spectroscopic observations to supplement its imaging data.The 9.2 m HET is the most commonly used spectroscopic instrument for supplemental data. Other instruments must be used to obtain UV and IR spectra, and instruments other than the HET are also used to

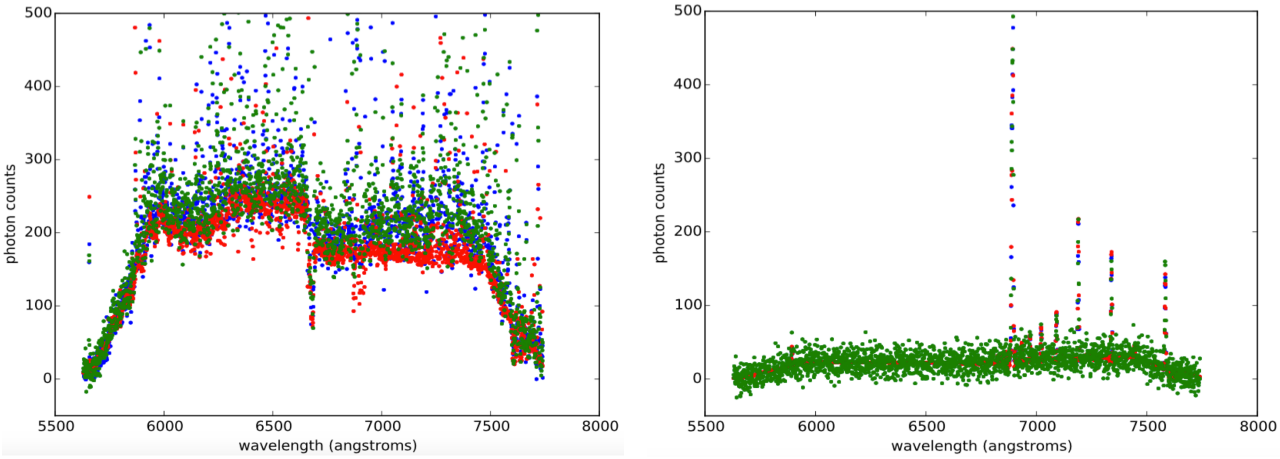

Figure 3.10: Comparison of an output ELG spectrum for the QuickGen pipeline and the offline spectroscopic pipeline. The red points indicate the input spectrum, the green points indicate Quickgen output, and the blue points indicate output from the offline spectroscopic pipeline.

collect optical spectra such as the Lick 3m [61] and Keck-1 10m [69]. For objects where HET spectra are unavailable, the WISeREP repository of SNe spectra is used [70].

Only a single spectroscopic observation is necessary for confirmation of a supernova and its chemical composition, but subsequent observations throughout the duration of the explosion show how the chemical composition and depth of ejecta evolve over time. This can be used to determine important properties of the supernova such as ejecta velocities, nickel mass, and temperature evolution. Table 3.4 shows the available spectra and instruments used for the SNe spectroscopically analyzed in this thesis.

Table 3.4: Optical SNe Spectra Summary

Object	Instrument(s)	Number of Spectra
SN 2007gr	Lick 3m, Keck-I 10m	10
SN 2008in	Lick 3m, HET 9m, IGO 2m, BTA-6 6m	13
SN 2010kd	HET 9m, Keck-I 10m	9

Chapter 4

Data Reduction

Once the ROTSE and DESI experiments have collected data, it must be properly reduced for scientific analysis. For ROTSE, this involves reducing photometric data to ultimately produce astrophysically meaningful flux measurements. For spectroscopic data, we must produce flux calibrated, extra-galactic spectra suitable for redshift fitting, determination of chemical composition, temperature evolution, and velocity measurements.

The ROTSE photometric pipeline was already in place by the time of this thesis and I used it to generate all of the ROTSE photometric results shown here and in the following chapters. While I did not write this code, I have developed a wrapper to quickly perform the image differencing described in Section 4.1.1 for all available images for a given object. Photometric results shown for other passbands were obtained using previous publications and the Open Supernova Catalog [71]. However, all other analysis of SNe observed by ROTSE was performed using software that I wrote, including bolometry and the evolution of temperature and velocities.

I was integrally involved in the development of the DESI online spectroscopic pipeline described in depth in Section 4.3. I also helped in the development of some aspects of the offline spectroscopic pipeline described in Section 4.2, so I focus on these pipelines in this chapter.

4.1. ROTSE Data Reduction Pipeline

Once ROTSE science images are taken, they are reduced to be ready for analyses. We first preprocess each image using calibration images taken earlier in the day. Preprocessing

involves removing the bias and dark current by subtracting the appropriate dark calibration exposures given the exposure length of the science image. The result is then divided by the appropriate flat calibration image. The corrected images are stored and the raw images are removed from disc.

In addition, an object file associated with each image is stored. This object file contains a list of astronomical sources identified by sextractor [72]. Calibrated magnitudes for each individual source are determined using magnitudes of sources in the USNO-B catalog [51] that appear in the image. This process involves matching triplets of stars to map celestial coordinates to the projection of the CCD onto the sky. These object files also contain information regarding read noise, sky noise, and PSF, to be used for image differencing as will be described in more detail below.

To find a newly occurring supernova, preprocessed images of the same fields must be coadded to improve the SNR around a potential supernova candidate. Coaddition aligns multiple images of a given region, rebinning subsequent images on the pixel grid of the first image and adding the counts to form a single coadded image on that grid. Because the light from a supernova can be overwhelmed by light from its host galaxy, particularly if the supernova is close to the nucleus of the galaxy, an image differencing technique is necessary. For this thesis, I use the ImageDiff software developed by Dhungana (2016) [68] [25], where the methodology is described in Section 4.1.1. For each supernova field that ROTSE observes, there is a coadded template image containing approximately 30-40 preprocessed images, taken when no transient events were taking place. The images are trimmed down to show only the region containing the transient event, with enough surrounding reference stars to be used for photometric calibrations. The size of this smaller image, or subimage, is often taken to be a 280×280 pixel region, so that the entire image does not have to be fully reduced.

Once subimages are created for both the survey images containing the potential supernova and the template image from prior observations, the template image, rebinned in (x, y) to the

same grid as the survey image, is subtracted from the survey image, so that only residual light from the transient event is left. Figure 4.1 shows an example of this process. Any region of the subtracted image containing excess light, $\geq 5\sigma$ above noise, is transmitted to the web server to be analyzed by ROTSE observers the following morning. These detections are often asteroids, bright star artifacts, cosmic rays, variable stars, or high proper motion stars, but if the light is not due to an identifiable astrophysical source, it is subjected to offline processing and follow up observation in order to determine if a new supernova has been discovered. Offline processing for SN 2007gr is described fully in Chapter 5. If a supernova has been observed, spectroscopic follow up occurs so that it can be confirmed and categorized.

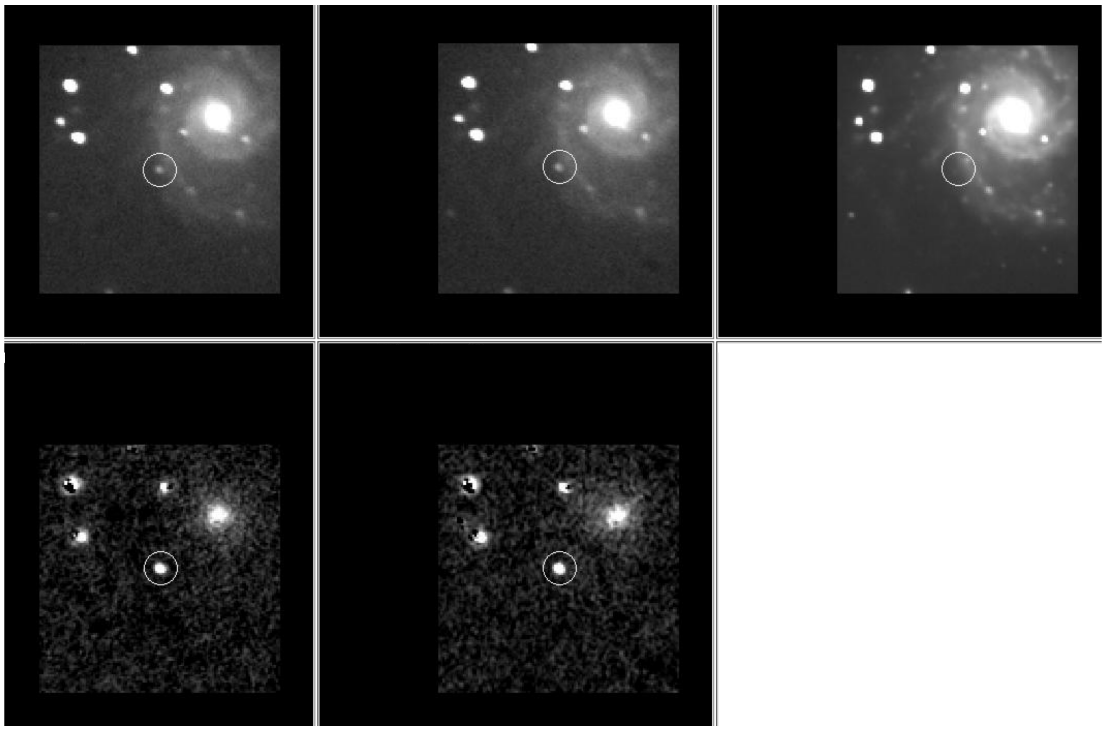

Figure 4.1: An example of the ROTSE online image differencing process. The top left two images show the science image, the bottom two left images show subtracted images containing only residual light due to a transient candidate, and the top right image shows the template image. This set of images is showing ROTSE detection of SN2013ej, where the circle in the middle of each image shows where the supernova is located.

4.1.1. Image Differencing

In general, image differencing seeks to isolate the flux from an individual supernova from any background emission such as that from a host galaxy. Although a bright supernova can outshine its host galaxy, it is still difficult to accurately extract light from only the transient object. Observing conditions can also be a large cause of noise around the transient event, which is why a proper template image observed many times in nominal conditions is crucial for precise image differencing.

To perform the subtraction, we utilize kernel based PSF modeling [68]. We represent a survey image $S(x, y)$ containing a supernova as the convolution of a template image $T(x, y)$ without the supernova, a kernel based PSF model, $K(u, v)$, and a noise term, $\epsilon(x, y)$, as

$$S = (K \otimes T)(x, y) + \epsilon(x, y). \tag{4.1}$$

Here, (x, y) are the coordinates in pixel space and (u, v) are the kernel coordinates. I have found the most success isolating the supernova flux using a delta function basis for the PSF kernel, where the kernel is defined as

$$K(u, v) = \sum_i c_i k_i(u, v). \tag{4.2}$$

It is therefore a linear problem to solve for the coefficients c_i, using

$$S = \sum_i A_i c_i + \epsilon, \tag{4.3}$$

where $A_i = k_i \otimes T$. The final differenced image in (x, y) is then represented by

$$D(x, y) = S(x, y) - \left(\sum_i A_i c_i \right)(x, y). \tag{4.4}$$

An example of this image differencing process is shown for a single observed epoch of SN 2008in, a type IIP supernova. The left plot shows the template image, the middle plot shows the survey image, and the right plot shows the differenced image. It is worth noting that SN 2008in is located in a very bright galaxy. As can be seen in the right plot, image differencing successfully subtracts the light from the host galaxy and surrounding background.

Figure 4.2: Image differencing for a single epoch of SN2008in. The left plot shows the template image without the supernova, the middle plot shows the science image, and the right plot shows the differenced image. The red arrow in the right plot points to SN2008in, without excess light contributions from its host galaxy, NGC 4303.

4.1.2. ROTSE Photometry

After image differencing, we extract the counts from the supernova and convert these counts into a magnitude for each observed epoch. We take reference stars from the pre-subtracted science image surrounding the supernova, but not too close to the host galaxy, so that the flux in the image from the supernova can be compared to the flux of stars with known magnitudes. Table 4.1 shows the epochs used for SNe extensively analyzed in this thesis. An example of this selection process is shown in Figure 4.3, where stars inside of the

yellow circles are chosen to be reference stars. The image shown is the template image for SN 2008in, centered around the region of sky where the supernova occurred.

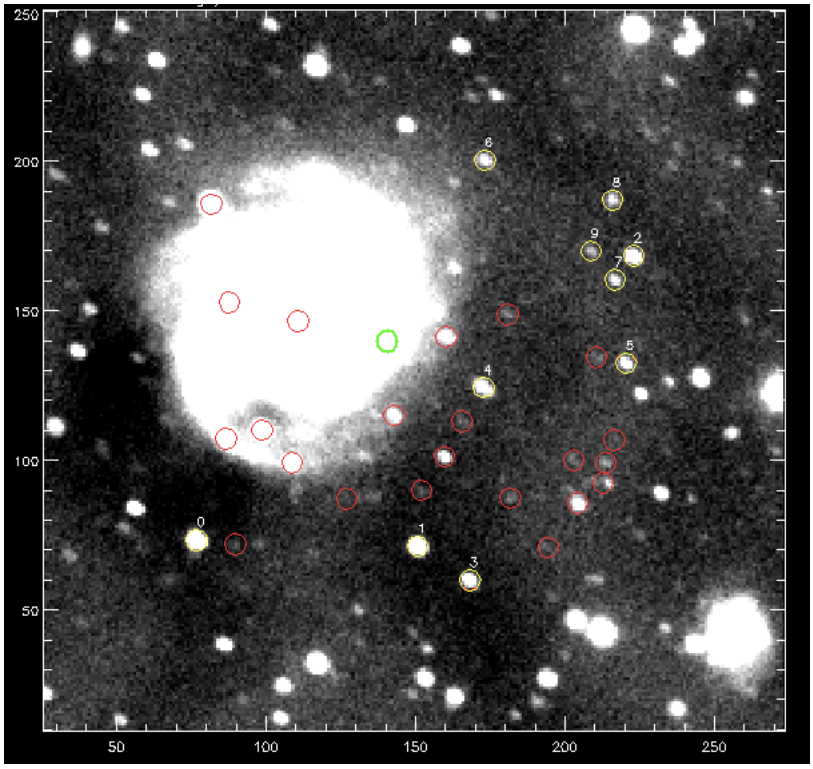

Figure 4.3: A ROTSE subimage showing the reference star selection process for SN 2008in. The green circle in the center is the region of the sky where the supernova occurred, and objects in the yellow circles are chosen to be reference stars. Objects inside of the red circles are potential reference star candidates based on their SNR and distance in arcminutes from the supernova. The numbers along the x and y axes represent pixel number.

The reference stars are then located in the images for each observed epoch. Because the subtracted images contain only light from the supernova, aperture photometry is now possible. This is done using the FWHM of the PSF, calculated by fitting a Gaussian profile to the observed supernova in the differenced image.

Now that the counts from the supernova have been extracted and scaled to a physical quantity for each epoch, these quantities are converted to magnitudes. Typically, ROTSE magnitudes are calibrated to either V or R band magnitudes using known magnitudes of

Table 4.1: ROTSE SNe Templates

Object	Template Date	First ROTSE Epoch
SN 2007gr	February 6, 2009	August 10, 2007
SN 2008in	March 12, 2008	December 30, 2008
SN 2010kd	February 26, 2006	November 14, 2010

stellar catalogs. For the SNe analyzed here, I use the AAVSO Photometric All Sky Survey (APASS) catalog [73] to calibrate to R band magnitudes. Photometric light curves are constructed using these results, where a final ROTSE light curve for SN2008in is shown in Figure 4.4.

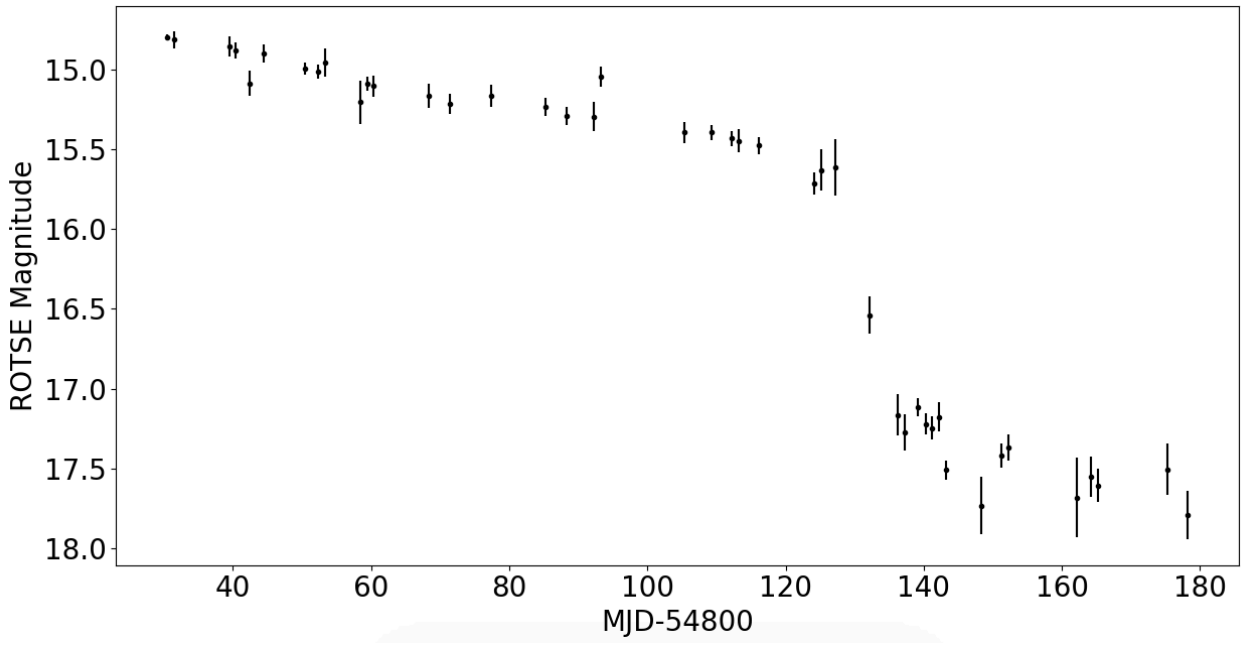

Figure 4.4: The optical light curve for type IIP SN2008in. This is the final result of the data reduction process for ROTSE photometric imaging of SNe. The x axis shows the observed date in MJD and the y axis shows the brightness of the object in ROTSE magnitudes.

4.2. DESI Data Reduction Pipeline

For spectroscopic reduction, I first focus on the DESI spectroscopic pipeline, before describing the online QuickLook pipeline. The first step of the DESI spectroscopic pipeline involves preprocessing images, to essentially remove excess noise so that the image is ready for spectral extraction. The counts in each pixel, scaled by the gain of the exposure, from an appropriate bias image are subtracted from counts in each pixel of the raw science image. Read noise is estimated using counts in the overscan region of the image, where no spectra are observed. The dark current is scaled by the exposure time and gain of the science exposure and subtracted from the image. The pixel flat accounts for pixel to pixel variations across the image. This is done by dividing the counts per pixel across the science image by the counts per pixel across the pixel flat image. Finally, cosmic rays present in the science image are located and removed by finding spikes in the spectra that are narrower than the PSF. The final preprocessed image can be represented by

$$Preprocessed = \frac{(Image - bias - noise) \times gain}{flat}, \tag{4.5}$$

where $Preprocessed$ is the preprocessed image, $Image$ is the raw image, and $flat$ is the correction from the pixel flat calibration.

Due to temperature variations across the focal plane, flexure can occur in the optical fibers, leading to changes in how spectra are projected onto the CCD. Fiber flexure can affect the effective fiber throughput and projected PSF. This then affects the PSF model and thus the ability to accurately perform sky subtraction and flux calibration [43]. We use Legendre polynomials to perform least square fits for each spectrum to find the trace of each fiber and account for these effects. This step also calculates PSF information, where the PSF is modeled using two central Gauss-Hermite cores with wings modeled using a power law. Using the coefficients from the Legendre polynomial fits to find the spectra in the image, this

process also finds a wavelength solution so that emission lines can be adequately modeled and pixels can be converted to wavelength bins during extraction.

To extract spectra from the image, the method of spectro-perfectionism is used [65]. Rather than using row-wise extraction methods, spectro-perfectionism uses a two-dimensional model of the spectroscopic data that more accurately reflects how an input spectrum translates into photon counts on the CCD image [65]. Using the trace information, PSF models, and wavelength solution found in the previous step, encompassed in the sparse matrix A_{il}, each spectrum f_l can be extracted from each CCD pixel vector p_i using

$$p_i = (\Sigma_l A_{il} f_l) + n_i, \tag{4.6}$$

where n_i is a noise vector corresponding to each pixel vecor p_i. A comparison of spectral extraction via spectro-perfectionism vs. optimal extraction, described in Chapter 3, is shown in Figure 4.5. In this image, the left plot shows discrete emission lines of a single spectrum, shown as red ellipses with yellow outlines. The middle plot shows how spectro-perfectionism models these emission lines and the right plot shows how optimal extraction models these emission lines. It can be seen that the middle plot closely models the spectrum, while many artifacts arise in the plot on the right. This indicates the accuracy of spectro-perfectionism and the advantage of using this method to model spectral features observed in 2-D pixel space.

Extracted spectra must be corrected for fiber-to-fiber throughput variations using a fiber flat calibration. We calculate a fiber flattening correction for each fiber by averaging all flat spectra from continuum lamp exposures, then divide each fiber's flux by this average spectrum. This requires that the fiber flat calibration spectra are on the same wavelength grid as the science spectra. Then, each wavelength bin of the science spectra is divided by

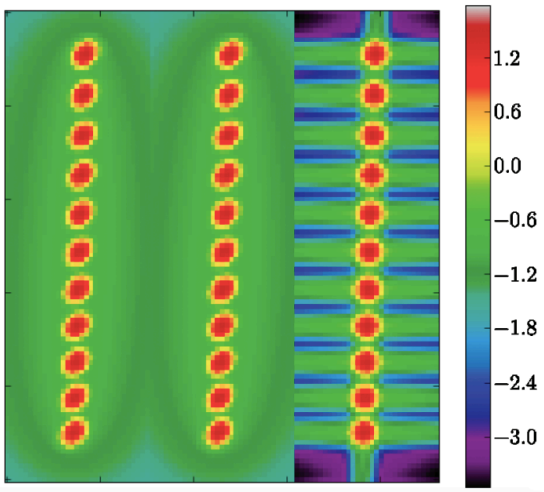

Figure 4.5: Comparison of spectral extraction using spectro-perfectionism vs. the conventional method of optimal extraction. The left section shows a spectroscopic image containing a single spectrum of only discrete emission lines. The middle section shows how spectro-perfectionism models this spectrum and the right section shows how optimal extraction models this spectrum [65]. The middle image almost exactly reflects the properties of the spectrum on the left, while many discrepancies arise in the right plot, indicating the advantages of using spectro-perfectionism.

corresponding wavelength bin of the fiber flat spectra, leaving science spectra that have been flat calibrated.

In order to see the underlying science spectra, sky background must be subtracted. Emission features from the atmosphere can mask emission lines from the science targets, depending on the redshift of the objects. For DESI, each petal of the focal plane, comprised of 500 fibers that all feed into a single CCD, allocates approximately 40 fibers to only sky regions for each exposure. Because the sky flux in one fiber may be different from the sky flux in another fiber, as they are pointing to different regions of the sky, a sky model is computed for each petal. DESI uses Cholesky decomposition to form an average sky model to be applied to each science fiber. This is done by first deconvolving sky spectra with their respective resolution matrices and then convolving the average of all sky spectra with the resolution of each fiber. This produces an accurate model of sky for each fiber across the image. This

modeled sky flux is then subtracted from all fibers, leaving no flux for sky fibers, and only the flux from science targets for science fibers, as seen in Figure 3.6.

After sky subtraction, the flux in the spectra are still in terms of extracted counts, which must be converted to meaningful physical units. The convention used by DESI is to convert flux to units of ergs/s/cm^2/Å. Target selection for DESI not only involves choosing science targets and empty regions of the sky, but also standard stars to be used as calibration sources. The primary source of spectrophotometric standard stars will be main sequence F type stars [42]. These stars have well defined properties and atmospheres, making them optimal candidates for spectrophotometric calibration over the optical wavelength range [74]. The fiber flattened, sky subtracted stellar spectra from all three channels, b, r, and z, are combined to form a single spectrum for each star. These spectra are then fit to a best matching stellar spectrum template, where the many templates used for DESI come from the spectroscopic results of Gaia, SDSS, and eBOSS [75] [76] [77]. Stellar templates with appropriate temperature, surface gravity, and metallicity are chosen, where I implemented the ability for these properties to be included in spectral fitting. Flux from these spectra is then scaled to the well defined imaging magnitudes from the preliminary imaging surveys described in Chapter 3. This scaling process allows a flux calibration vector to be constructed, which can then be applied to the science spectra, leaving sky subtracted, flux calibrated spectra. Figure 4.6 shows a final flux calibrated standard star spectrum to be used for calculating a flux calibration vector, with an example flux calibration vector shown in Figure 4.7.

Flux calibrated spectra are sent through a spectral redshift fitter, to determine the classification and spectroscopic redshift for each observed target. The redshift fitter uses galaxy and quasar spectral templates with known redshifts to fit each observed spectrum. For all spectra, a range of trial galaxy redshifts is explored. At each trial redshift, the galaxy eigenbasis is shifted, and a χ^2 minimization is performed. This information is stored, and the

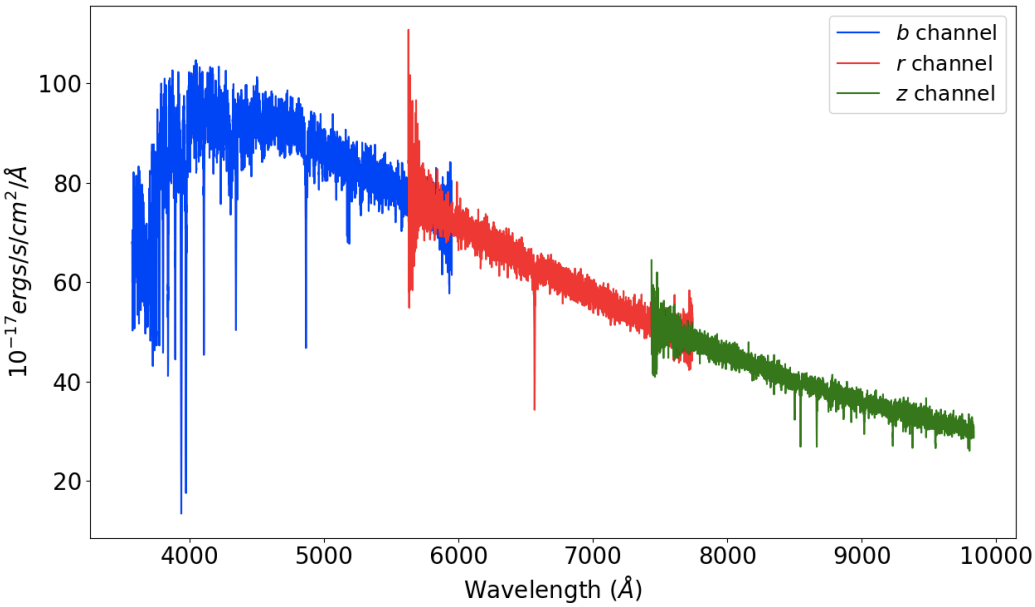

Figure 4.6: A fiber flattened, sky subtracted standard star spectrum to be used for flux calibration. The spectrum shown consists of all three optical wavelength regions observed by DESI.

process repeats for the next trial redshift. Multiple templates are used, and the combination of template type and redshift that yields the lowest reduced χ^2 value is used as the spectroscopic pipeline redshift measurement and classification of the spectrum.

4.3. Real-time Spectroscopic Reduction & Quality Assessment

In order to ensure that DESI data is of high enough quality to produce the redshift and clustering measurements necessary for scientific analysis, it must be spectroscopically reduced and analyzed in real-time. The results must be continuously during operations. The QuickLook pipeline (QL) was written to perform this task, rapidly reducing spectroscopic images to produce sky-subtracted, flux-calibrated spectra in near real time.

DESI uses an exposure time calculator (ETC) to maximize the efficiency of the DESI observing strategy, and ultimately it is the job of QuickLook to ensure that exposure times are achieving projected the signal to noise ratio (SNR) from the ETC to discern the chemical

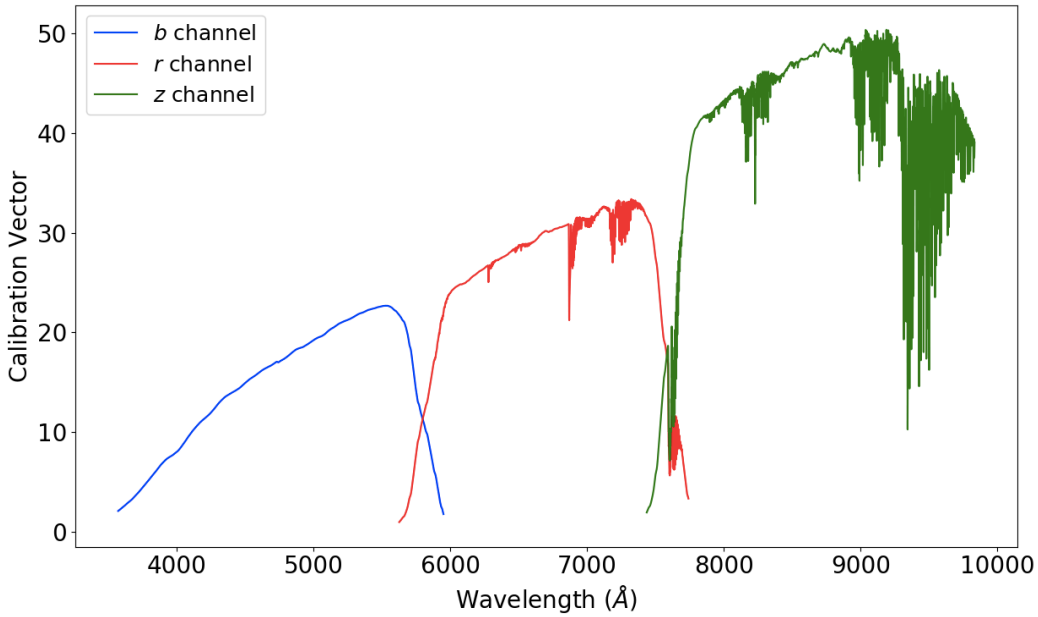

Figure 4.7: An example flux calibration vector for all three optical wavelength regions observed by DESI to be applied to an LRG spectrum. This vector is used to calibrate extracted counts to meaningful physical units.

features seen in stellar and galactic spectra. The ETC dynamically uses real-time observing conditions from the Guide, Focus, and Alignment (GFA) sensors to adjust exposure times to reach the fiducial SNR for a canonical galaxy. Using a model that describes the effects of observing conditions on SNR, the ETC continuously updates the currently achieved SNR throughout integration of the spectrographs. The results of QL indicate whether the ETC is providing sufficient exposure times. Based on these results, it is up to the observer to determine if action should be taken.

Proper exposure times are crucial for DESI, as the large sample size requires millions of exposures over a five year period. An exposure time that is too short could end up in an image with insufficient signal to noise, and therefore an inability to calculate spectral redshift due to noisy features seen in the spectra. An exposure time that is too long wastes precious observing time.

Observing conditions taken into account by the ETC because of their affect on the overall signal to noise include:

- Airmass: the amount of atmosphere that light from an astrophysical object passes through before it reaches Earth, where an increased angle from the zenith amounts to increased airmass,
- Seeing: the amount that light is blurred or smeared out due to interaction with the atmosphere,
- Transparency: the fraction of light passing through the atmosphere, where a value of 1.0 indicates a fully transparent atmosphere,
- Extinction: the amount of light from an object that is absorbed by its host galaxy or the Milky Way,
- Moon Fraction: the fraction of the moon that is illuminated,
- Moon Altitude: the altitude of the moon with respect to the horizon,
- Moon Separation: the distance between the moon and the object being observed.

The full offline spectroscopic pipeline is temporally and computationally expensive, taking more than an hour to reduce a single exposure. The online QuickLook pipeline must return reduced spectra within 2 minutes. This ensures that an assessment of DESI performance can occur before the next exposure begins. This assessment provides timely feedback to gauge ETC performance and whether adjustments should be made. Figure 4.8 shows a schematic representation of how QuickLook fits into the DESI data systems. QL uses fast and robust pipeline algorithms (PAs) to rapidly reduce spectra, with quality assessment algorithms (QAs) to analyze data quality after each PA, as seen schematically in Figure 4.9. Each QA provides results that tell users the status of data quality, with an alarm sounded if any metric is seen to be outside of a predetermined threshold.

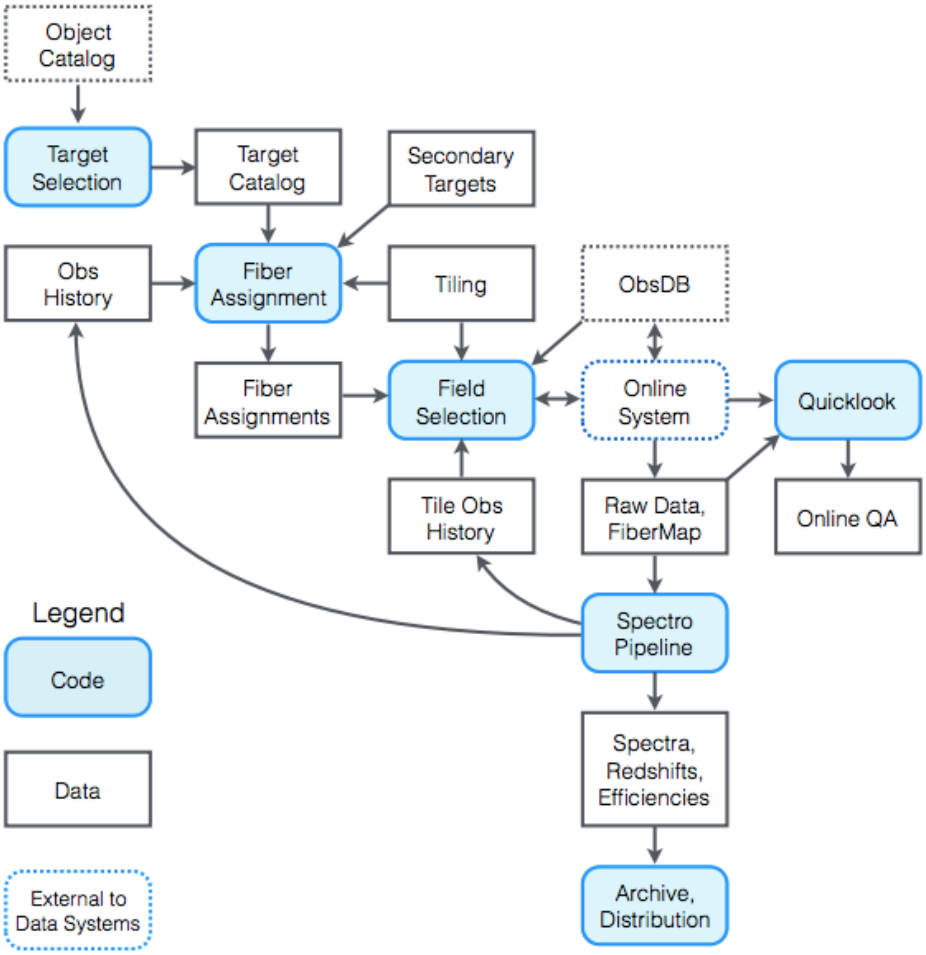

Figure 4.8: A block diagram of the DESI data system [43]. QuickLook obtains raw data directly and can operate in the online system to produce viewable results for the observer.

4.3.1. Data Reduction Algorithms: Science Exposures

Each reduction algorithm is a processing step that takes the input data one step closer to becoming output spectra. QL can process science or calibration data, so there are several sets of PAs depending on the type of data it takes as input. These steps are defined in the configuration files that allow the user to easily define inputs to be taken in by QL. This section describes the necessary PAs for scientific data reduction, with calibration data

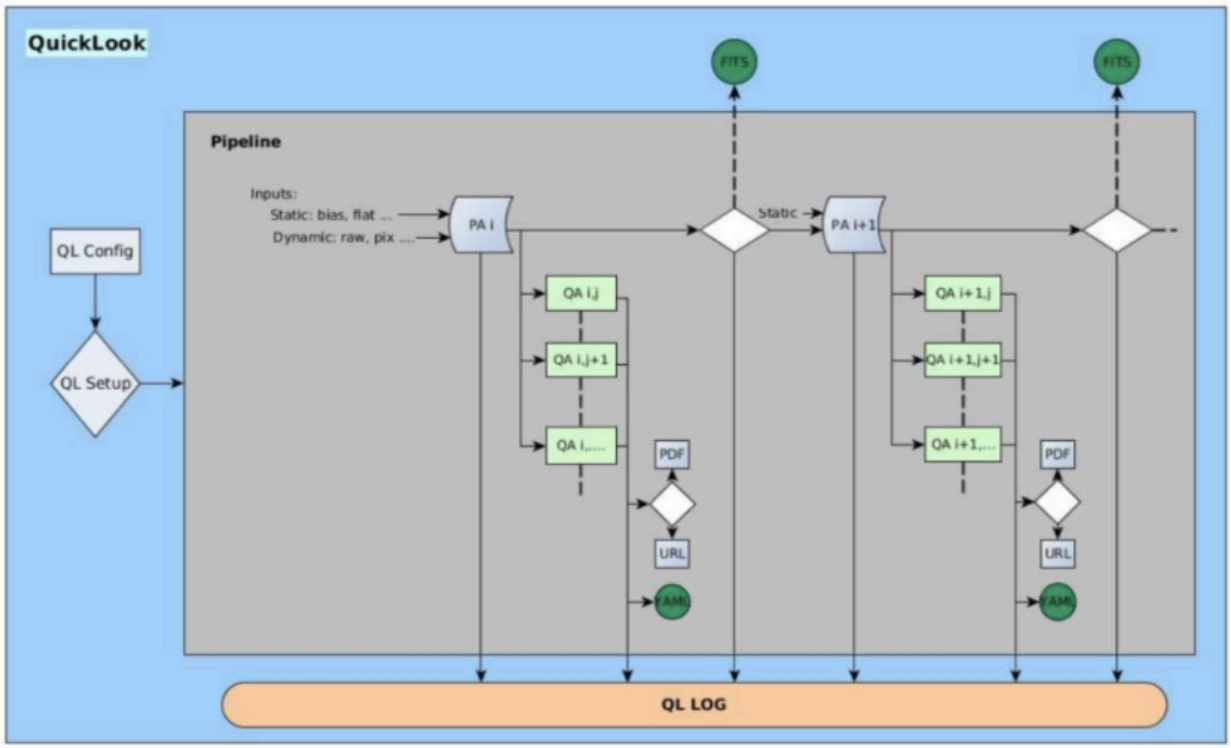

Figure 4.9: A schematic representation of the QuickLook work flow.

reduction steps in the following section. For science exposures, QL must be able to run on all types of data, including each of the dark time, gray time, and bright time surveys. I wrote the flux calibration reduction algorithm and integrated the offline flexure algorithm, and had a significant role in maintaining and updating all of the algorithms.

4.3.1.1. Initialization

Before any data reduction is performed, the first step of any QL run is to make sure that all relevant information is available to the pipeline and that all files are in the correct place and of the correct format. QL science runs require an input image file, a fibermap file that defines all information about the fibers contained in the image, and calibration files used locate the PSF across the image and ensure that each fiber is properly illuminated. Once

QL makes sure all necessary information is accessible, it moves on to the actual processing algorithms.

4.3.1.2. Preprocessing

A preprocessing algorithm takes a raw DESI image and sets it up for spectral extraction by removing excess bias, dark current, and cosmic rays. Preprocessing raw DESI exposures is not temporally expensive, so QL uses the same preprocessing algorithm as the offline spectroscopic pipeline. For more details on this step, see Section 4.2.

4.3.1.3. Accounting for Fiber Flexure

Flexure of the CCD and spectrograph slit can alter fiber orientation, thus affecting the effective throughput, spectral trace along the CCD, and PSF stability [43]. This can be caused by temperature variations over time. It is an important issue to take into consideration as it can affect the proper mapping of pixels to wavelength, thus affecting spectral extraction, sky subtraction, and flux calibration if improperly dealt with. This can be handled by measuring the trace along the fiber before spectral extraction, so that the proper pixels containing spectral information are used for extraction. Similar to the preprocessing algorithm, QL integrates the offline flexure algorithm described in Section 4.2.

4.3.1.4. Spectral Extraction

Because QL must fully reduce raw data in near real time, it cannot use the method of spectro-perfectionism, which is computationally expensive. Therefore, a much quicker and more robust boxcar method of extraction is used. First, the user must define the boxcar width in pixels to be extracted along each spectrum. QL uses 2.5 pixels as the default width of a boxcar. Using the trace information from the previous step to find where the spectra lie in the image, this pixel width defines how many pixels per row will be used to extract flux for each spectrum. Too small of a box width omits flux from each spectrum being extracted, while too large of a box width integrates more noise with no additional flux and risks containing flux from adjacent spectra.

Once pixels are mapped to spectra over the entire image, extraction is performed. For this extraction, one bin of flux is taken to be one row of pixels in a boxcar, where the counts in n pixels defined by the box width are summed to define the flux in that bin. This is repeated for all boxcars associated with each spectrum, to return spectra in extracted counts vs. y pixel value. The pixel values are then converted to wavelength values in Angstroms using the wavelength solution, with the flux divided by the gradient of the wavelength range to return flux per Angstrom. Finally, the flux is resampled into wavelength bins supplied by the user, with extracted spectra ready for calibration and sky subtraction.

4.3.1.5. Fiber Flattening Calibration

QL handles fiber to fiber variations using fiber flat calibration files generated by the offline pipeline. Computing these fiber flat corrections is described below in Section 4.3.2.2. To alleviate these variations, it is first necessary to ensure that the science spectra and fiber flat spectra are on the same wavelength grid. Then, each flux bin in each spectrum is simply divided by the flat correction in the corresponding bin. This very simple algorithm

is adequate in placing all fibers on the same footing, while saving a lot of processing time compared to the offline algorithm.

4.3.1.6. Computing a Sky Model

If a sky file or sky model is not provided as input to QL, a sky model must be derived in order to perform sky subtraction. This is done using the sky fibers in the image to compute a weighted average for the entire image. Typically, there are approximately 40 sky fibers per science exposure to compute this model. The weights are taken to be the inverse variance, and then the flux in each wavelength bin is averaged using these weights. Once there is a single sky model along the entire spectrum, it is convoluted with the PSF information to allow subtraction for each spectrum.

4.3.1.7. Sky Subtraction

As with fiber flattening, for sky subtraction, the science spectra and sky model must be on the same wavelength grid. Similarly, sky subtraction can add processing time that QL cannot afford. QL simply takes the flux in each science spectrum and subtracts the sky model without accounting for a throughput correction. This leaves only the flux from the science target in each spectrum.

4.3.1.8. Flux Calibration

In a similar manner to the offline pipeline, extracted counts are converted to physical units of ergs/cm^2/s/Å. However, unlike the offline pipeline, QL uses a precomputed average flux calibration vector to save computing time. A calibration exists for each spectrograph, applicable for each of the 3 corresponding wavelength dependent cameras. These files include a range of calibration vectors corresponding to a variety of potential observing conditions.

A calibration vector is chosen to match the seeing and airmass values of the current exposure. Then, for each spectrum the calibration value for each bin is put on the same wavelength grid and scaled by the exposure time. Finally, the flux in each bin is multiplied by the corresponding calibration value, leaving the final flux calibrated spectra. Examples of spectra reduced by the QuickLook pipeline for camera $r0$ are shown in Figure 4.10 for an ELG and QSO.

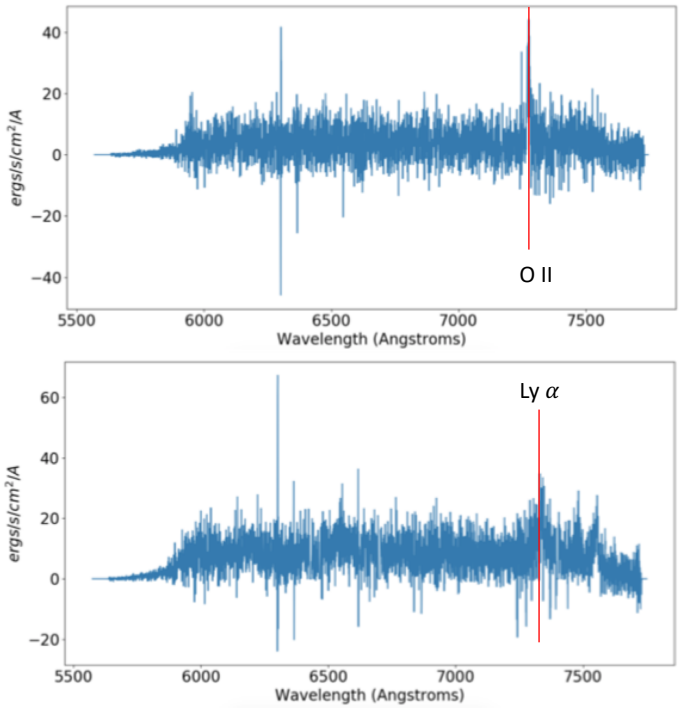

Figure 4.10: Science spectra fully reduced by the QuickLook Pipeline. The top plot shows an ELG spectrum with the red line indicating the observed OII doublet. The bottom plot shows a QSO spectrum with the red line indicating the observed Lyman alpha feature.

4.3.2. Data Reduction Algorithms: Calibration Exposures

In addition to science data, QL must be able to process raw calibration data. Most of the algorithms used for calibration data reduction through extraction are the same as described above. The algorithms described below are those specific to the processing of arc lamp and continuum lamp exposures. I worked on maintenance of the arc lamp calibration algorithm and the development of the continuum lamp calibration algorithm.

4.3.2.1. Arc Lamp Resolution Fitting

The purpose of this algorithm for arc lamp processing is to return a PSF file that provides an initial wavelength solution and resolution information for spectral extraction and sky subtraction in science exposures. It takes as input extracted arc lamp spectra and returns trace and PSF information along the x and y axes. This PSF information comes from fitting Gaussian profiles to the arc lines along each spectrum. While PSF information comes from this algorithm, the trace and wavelength solution are gathered during the step calculating fiber flexure.

The list of arc lamp emission lines included in the image must first be provided. Once the lines are found in pixel space, a Gaussian is fit to each line and the σ values are returned. A Legendre polynomial is then fit to these σ values vs. wavelength for each fiber. This fit provides the resolution information along each fiber, which is passed to the final output PSF file.

4.3.2.2. Computing Fiber Flattening Corrections

This algorithm is used to calculate the fiber flattening corrections used to alleviate fiber to fiber variations in science exposures. This is done using extracted spectra from a continuum lamp exposure as input. After the flux from each fiber is deconvolved from the resolution information, it is summed in each wavelength bin, resulting in a single spectrum containing all of the continuum amp flux. This is then divided by the total number of fibers to return an average flat lamp spectrum. The average spectrum is then reconvolved with the resolution information for each fiber and passed to the output fiber flat file.

4.3.3. Quality Assessment Algorithms

Attached to each PA is one or more algorithm(s) to assess the quality of data after that pipeline step has been performed. So, QAs following the preprocessing algorithm examine the pixel level quality of the image itself, QAs following extraction examine the quality of spectra in the image, QAs following sky subtraction examine the quality of subtracted science spectra, etc. Upon finishing, each algorithm returns a set of metrics, as well as useful plots, that indicate the quality of data and whether it meets the threshold ultimately required for redshift fitting of the objects in the image.

Within the metrics for each QA, a single metric is designated as the most crucial, indicating to the user in real time whether the data is sufficient after that pipeline step. Predetermined values and thresholds are determined for this metric, chosen by examining the nominal value of this metric over many comparable exposures. If the value of this metric for a given exposure is within the "normal" threshold, then the data for this QA are deemed NORMAL, and no further action is required. If the value of this metric is outside of the normal threshold, but within the "warning" threshold, then a WARNING is flagged. For these warnings, no particular action is necessarily required, but the metric should be further monitored to see if this is a persistent issue that must be addressed. If the value of this metric is outside of the warning threshold, then an ALARM is indicated, and the issue must be addressed. This could mean excess noise in an amplifier of the CCD, overheating of the spectrograph, etc., but action must now be taken to understand the poor data quality.

The following list briefly describes each QA and how they are useful in assessing DESI spectrographic data quality. The subsequent sections describe in depth three QAs that I wrote that are of particular importance. Overall, I was responsible for updating and maintaining all of the QAs used by the QL pipeline. The QAs that I wrote from scratch are Trace_Shifts, Get_RMS, Calc_XWSigma, and Sky_Peaks. I also rewrote to completion and substantially improved the algorithms for Integrate_Spec and Calculate_SNR.

- Check_HDUs: Verify that all of the necessary information is available in the header of the raw image file.
- Bias_From_Overscan: Record the bias level across the image.
- Get_RMS: Record the read noise across the image.
- Count_Pixels: compute the number of pixels receiving light above a certain threshold to confirm that there is an appropriate level of light in the image.
- Calc_XWSigma: Calculate the resolution of spectral features by fitting Gaussian profiles to sky emission lines.
- Trace_Shifts: Record the fiber flexure in x and y directions.
- CountSpectralBins: Count the flux in each spectral bin after extraction.
- Sky_Continuum: Calculate the amount of sky flux in wavelength regions of sky spectra containing no emission lines.
- Sky_Peaks: Sum the sky flux for sky fibers in regions containing high flux emission lines.
- Calculate_SNR: Calculate the signal to noise ratio for all science targets.
- Integrate _Spec: Integrate the flux calibrated spectra to provide spectrum based magnitudes that can be directly compared to imaging magnitudes.

4.3.3.1. Calc_XWSigma

Running on the 2-D spectroscopic image after the preprocessing algorithm is finished, we attempt to ensure that the PSF is stable across the image in both x and y directions. To begin, well defined sky emission lines are chosen in each of the three spectrograph arms. Lines

are chosen with high flux and no neighboring flux, also requiring enough lines to be located in each amp of the CCD, typically 2-3. The total number of lines for each fiber is between 4 and 6, based on the number of available features in each spectrograph arm meeting the requirements. Figure 4.11 shows an example sky emission line to be fit for camera $r0$. The vertical lines represent individual spectra and ellipses along these lines represent emission features. The red ellipses show a sky feature that will be fit to ensure PSF stability across the image.

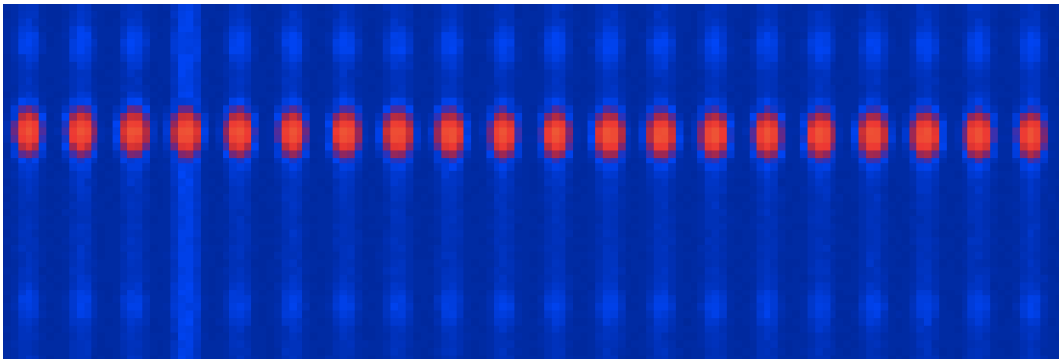

Figure 4.11: A zoomed in portion of a DESI preprocessed image. The vertical lines represent individual spectra and ellipses show emission lines in each spectra. The red ellipses show a sky feature to be fit in the QA XWSigma.

These spectral features are then found in the image by converting the fiber and wavelength information from the input PSF file to x and y pixel space. Once the features are found, rows and columns of n pixels each are isolated around the central pixel of each feature, where n is defined by the user. This value is typically taken to be 7 pixels, as more pixels in the x direction would run into adjacent fibers, more pixels in the y direction would run into adjacent spectral features, and less pixels in both directions does not allow adequate fitting of the spectral profile.

Next, a 1-D Gaussian profile is fit to each spectral feature in x and y, with σ values returned in both the x and y directions. The sigma values are averaged along each fiber and

within each amp, so that the resolution characteristics can be examined. If sigma values are too high for a particular fiber, amp, or across the entire image, this could indicate issues with the focus of the camera and PSF stability or some underlying electronics issue.

Figure 4.12 shows the result for this algorithm, where the top plots show the average σ values in the x and y directions, and the bottom plots similarly show the average σ values per amplifier. These values indicate expected results, where the information displayed is what one would expect for a typical exposure.

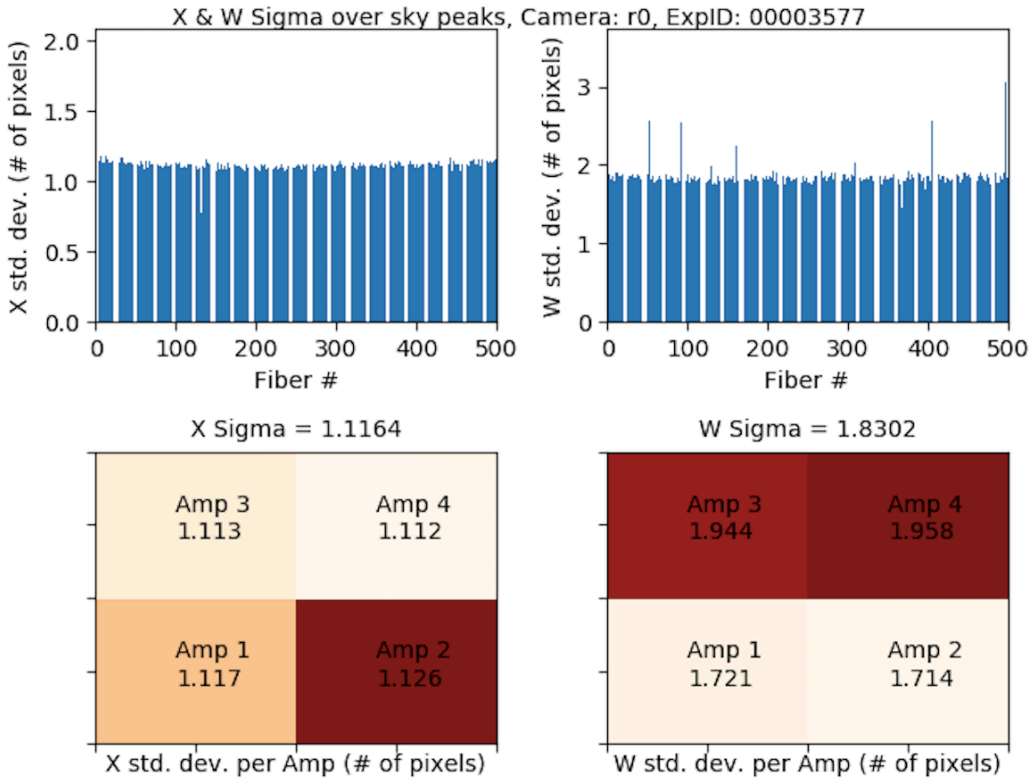

Figure 4.12: The output png of the Calc_XWSigma QA. The top plots show the average σ values resulting from Gaussian fits of sky emission lines per fiber, where the left plot shows the x values and the right plot shows the y values. The bottom plots show respective σ values averaged over each amp of the CCD. Darker colors in these plots represent increased dispersion of light in the X and W directions, although these plots display typical X and W sigma values per amplifier.

4.3.3.2. Calculate_SNR

This QA is run on extracted science spectra after fiber flattening and sky subtraction have been performed. In order to accurately determine the redshift of galaxies that DESI will observe, the chemical features in their spectra need to have enough signal to be found and properly fit. This requires observing each target long enough to improve the signal to noise ratio above a certain threshold. For instance, DESI requires an overall SNR of 7 for ELGs so that, in particular, the [OII] doublet present in their spectra can be satisfactorily discerned for redshift fitting.

To calculate the SNR for each target, the flux along each spectrum is multiplied by the square root of the inverse variance. The median SNR value for each target is then taken, to be used in determining the overall SNR distribution per target type in the current exposure.

Once the flux information from imaging magnitudes per target type is obtained, median SNR vs. flux is fit using [78]

$$SNR = \frac{af_x t_{exp}}{\sqrt{t_{exp}(af_x + b)}}, \tag{4.7}$$

where f_x is the flux for a given wavelength band x, t_{exp} is the exposure time, a is a fit parameter representing throughput, and b is a fit parameter representing noise.

For each target, f_x is converted to a magnitude using Equation 3.3, as typical astronomical SNR plots show SNR vs. magnitude rather than flux. The zero point for this equation is 22.5, as DESI uses the system put in place by the Sloan Digital Sky Survey (SDSS) for calculating fluxes and magnitudes [79].

Normalized residuals from the difference of fit SNR and observed SNR are then taken. While QL only runs on a single camera at a time, residuals from all cameras in an exposure can show potential SNR patterns across the entire focal plane as seen in Figure 4.13. The three plots represent the three spectrograph arms, where blue points indicate targets with

signal to noise higher than the fit and red points indicate targets with signal to noise lower than the fit. The slightly redder region around the edge of the plots, seen most clearly in the left most plot, indicate an SNR focal plane dependence, where the edge of the focal plane produces lower SNR due to effects such as vignetting.

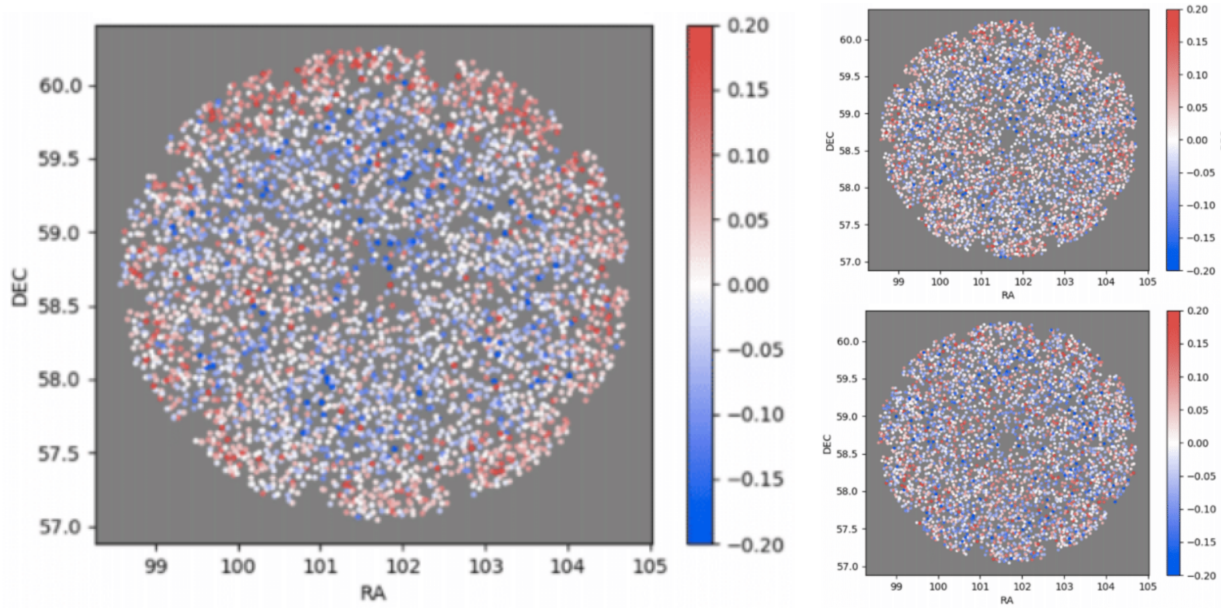

Figure 4.13: SNR vs. focal plane dependence for a gray time exposure. Blue points indicate targets with higher SNR than the fit and red points indicate targets with lower SNR than the fit. The left plot shows the b spectrograph channel, the top right plot shows the r spectrograph channel, and the bottom right plot shows the z spectrograph channel.

An example plot of the SNR output is shown in Figure 4.14. The top left plot shows the median SNR for each fiber, the top right plot shows the residual SNR plot for the focal plane petal being currently processed, and the bottom four plots show SNR^2 vs. magnitude for each target type in the exposure. This example is for a dark time exposure containing ELGs, LRGs, QSOs, and standard stars.

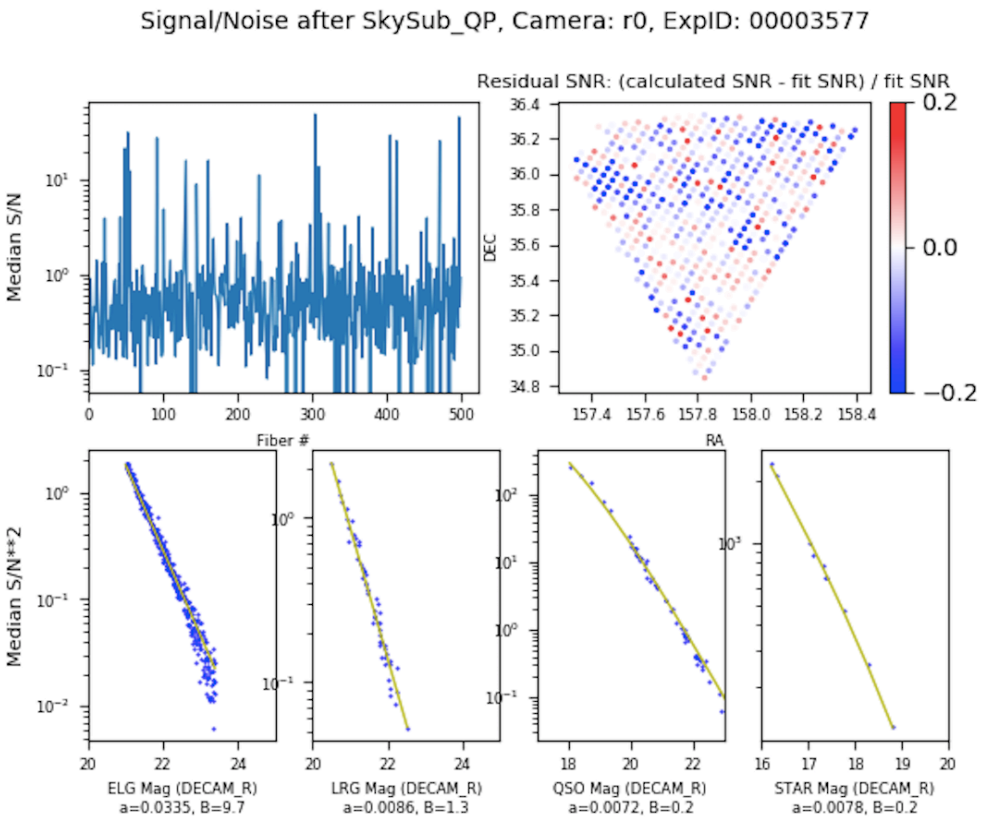

Figure 4.14: The top left plot shows the median SNR values per fiber. The top right plot shows the residual SNR values after fitting SNR vs. magnitude for each target type, shown vs. the on sky coordinates, RA and DEC. The bottom four plots show the fits of SNR vs. magnitude for each target type during a dark time science exposure.

4.3.3.3. Integrate_Spec

This QA is run on the flux calibrated science spectra. To make sure the final spectra have been adequately reduced, the flux contained in each spectrum is converted to a fiber magnitude and compared to the respective imaging magnitude from the photometric surveys used to acquire DESI targets. Fiber magnitudes are calculated using the flux present in the final flux calibrated spectra. Because the light from each fiber passes through a dichroic filter before reaching the CCD, the flux must be convolved with the transmission efficiency of the filter. The filters used for the b, r, and z spectrograph channels for DESI correspond to the g, r, and z DECAM filters used in the photometric imaging surveys, where their respective quantum efficiencies are shown in Figure 4.15.

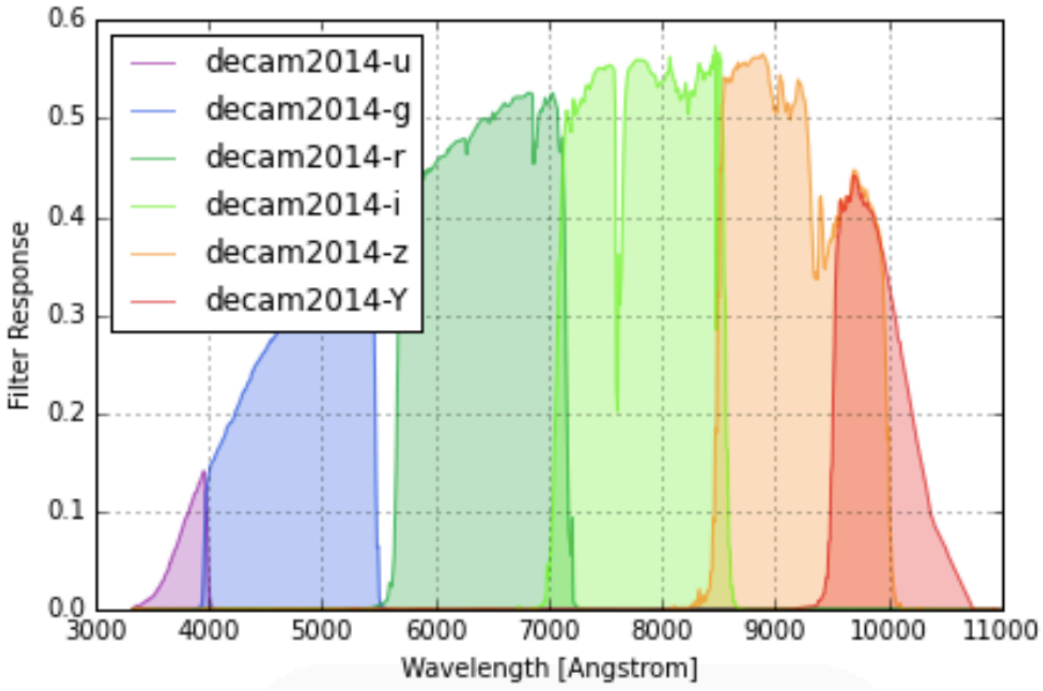

Figure 4.15: The transmission efficiency for the *ugrizY* DECAM filters. The g, r, and z filters were used for the preliminary imaging survey, and correspond to the b, r, and z filters used by DESI.

Once fiber magnitudes are calculated, their difference with respect to imaging magnitudes represents the difference in flux seen before and after the data reduction process. Any large discrepancies could primarily indicate a significant loss in throughput. Figure 4.16 shows the differences between imaging and fiber magnitudes for a single exposure for cameras $b0$, $r0$, and $z0$. An example output plot showing the fiber magnitudes calculated by QL is shown in Figure 4.17.

4.3.4. Running QuickLook

A single QuickLook run involves processing the raw data from a single camera from a single exposure at a time. In order to find the correct raw image to be reduced, the night of observation, exposure ID, and camera must be specified via command line arguments. For a science run, the raw science image is required, as well as a PSF and fiber flat calibration

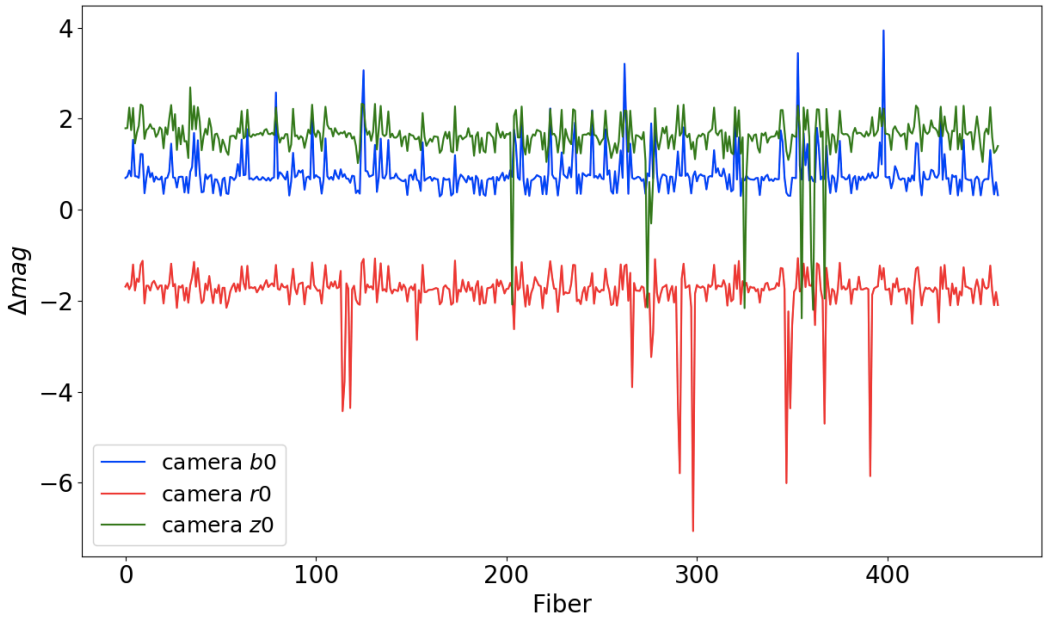

Figure 4.16: The difference between imaging and fiber magnitudes for cameras $b0$, $r0$, and $z0$ vs. fiber number.

files. I worked to continuously maintain this pipeline, adding necessary algorithms and simplifications for the developers and observers when necessary.

To setup the QL pipeline, a configuration file is also a required command line argument. This configuration file determines which PAs and underlying QAs will be run. Within each QA, it specifies the reference values and ranges that will be used to determine if a QA will be given a description of NORMAL, WARNING, or ALARM. Once information from the configuration is passed to the pipeline, a configuration object is created containing dictionaries for each PA and QA. These dictionaries provide the pipeline with relevant parameters for each step and indicate where all outputs should be placed, passed to the algorithms via the configuration object.

Once the pipeline has all of the necessary information, the steps described in Section 4.3.1 are sequentially run. After all PAs and QAs are complete, the pipeline merges all of the calculated metrics into a merged JSON file to be analyzed by observers if necessary.

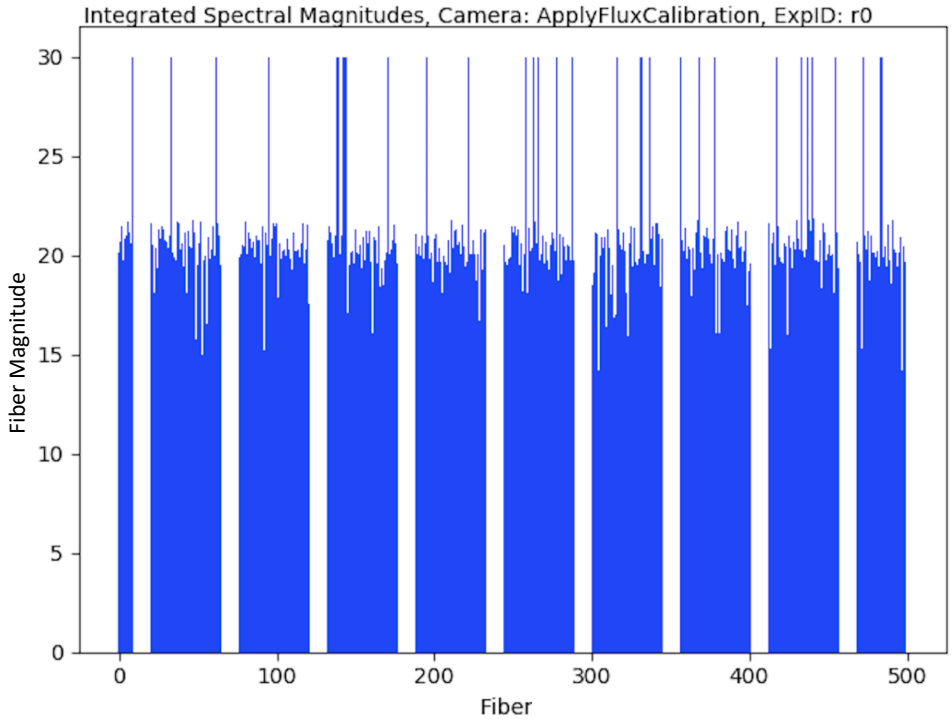

Figure 4.17: Example output of the quality assessment algorithm displaying fiber magnitudes vs. fiber number. This plot shows the spectral magnitudes for all science fibers in a dark time image.

While QL has the capacity to output files for each step of the pipeline, the required outputs are this merged JSON file, a psf file containing updated trace information, and a FITS file containing the final spectra and all information pertaining to the targets in the exposure. The output QA plots shown above are optional. An additional algorithm that I wrote provides the observer the capability to see any plot that may be of use given any of the output QA metrics. Finally, QL outputs are passed to the web interface QuickLook Framework (QLF), which allows observers to see the status of each QA and example spectra in real time.

4.3.5. Mock Observing

To ensure the overall functionality of the instrument control system (ICS) and QuickLook pipeline and its ability to be fully integrated into the DESI data acquisition system and online web interface, a week long commissioning exercise was conducted. I contributed to many

aspects of the tests performed. This program facilitated the full commissioning of QuickLook before data collection began, using a full night of simulated calibration and science exposures to do so. Mock observing occurred on site at Kitt Peak National Observatory inside the Mayall telescope control room, newly reconfigured for DESI.

In total, 20 exposures were simulated for all 30 cameras, including 3 arc lamp exposures, 3 continuum lamp exposures, and 14 science exposures comprising 4 bright, 4 gray, and 5 dark time exposures. These exposures were loaded into the data area on the desi-1 computer which must be accessed through the National Optical Astronomy Observatory (NOAO) network. The desi-1 computer acts as the central DESI computer, collecting spectroscopic images and passing them along to the National Energy Research Scientific Computing Center (NERSC) at Lawrence Berkeley Laboratory (LBL) for full reduction and analysis.

It was first necessary to properly setup the computing environment with QuickLook and other necessary DESI software packages, so that desi-1 could access the QuickLook pipeline and subsequently find and reduce the simulated exposures. This involved establishing proper environment variables in order to send the appropriate exposures through the pipeline and allow for easily accessible results to be displayed by the online interface and viewed by observers.

Once the environment was appropriately setup, several tests were performed to ensure proper functionality. Most importantly, it was verified that QuickLook could independently process data from not only the staged simulation area containing the 20 simulated exposures, but also data as written by the ICS mimicking what would be seen in actual spectroscopic data collection. This was verified for all exposure types, calibration and science, under all observing conditions. It was also necessary to verify QuickLook functionality as incorporated through QLF. This verification involved testing the simultaneous running of QuickLook on all 30 cameras of a single exposure and examining whether proper results including QA metrics and plots were being displayed online.

Figure 4.18 shows an example webpage accessible to observers for a single science exposure. Each of the three rows of focal plane petals represents the cameras corresponding to each of the b, r, and z spectrograph channels. Each of the three columns represents QuickLook results after a particular step of the pipeline, where we first check viability of the CCDs, then fibers, and finally spectra. Petals shown in green represent those receiving NORMAL values, petals in yellow represent those receiving a WARNING value, and petals in red (not seen here) represent petals receiving an ALARM value. The petals in yellow indicated the necessity to further fine tune QA reference values and ranges, so that QuickLook could improve its ability to properly assess the data quality after each pipeline step. Observers wishing to look into more descriptive results could simply click on a petal to access QuickLook plots such as those seen in Figures 4.12, 4.14, and 4.17.

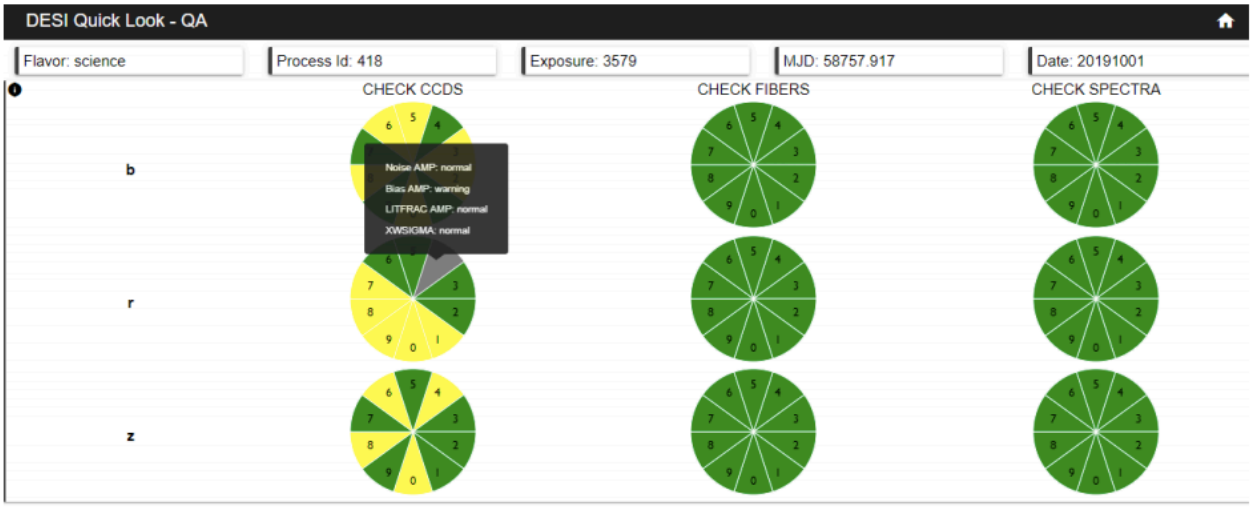

Figure 4.18: An example online display of the QuickLook pipeline results for a single science exposure. Petals shown in green represent those obtaining a NORMAL status and petals in yellow represent those obtaining a WARNING status.

Overall, the mock observing program was a successful experience. Upon updates that I provided regarding the QuickLook configuration file and ability for the pipeline to properly access and load ICS written data files, it was indeed verified that the QuickLook pipeline

could successfully run as required by the DESI data systems team. Based on the results of this commissioning phase, QuickLook was further optimized based disk space available on the desi-1 machine. Due to the high volume of QuickLook results given the number of cameras and exposures to be processed over a single night, outputs were limited to a single file containing merged results from all QAs. This reduction of outputs also provided the optional, rather than default, ability to generate plots and other files such as the large files containing preprocessed images. Commissioning also verified QuickLook's capability of running on a single camera in under the required time of 2 minutes on desi-1. Timing results for each exposure type are shown in Table 4.2. This timing requirement helps to ensure the ability of the ETC to adequately update exposure times based on the results provided by QuickLook.

Table 4.2: QuickLook Run Times

Exposure Type	Run Time (minutes:seconds)
Science	1:35.5
Arc Lamp	1:53.4
Continuum Lamp	1:21.1

Chapter 5

Extensive Photometric and Spectroscopic Analysis of SN 2007gr

The analysis discussed in this chapter focuses on a stripped envelope, core collapse supernova, SN 2007gr. While the EPM distance measurements described in Chapter 1 are typically applied to SNe IIP, it is always useful to have cross checks using different classes of supernovae. Different types of CCSNe display different properties, leading to different systematics regarding the characteristics needed for EPM. Although stripped envelope supernovae may not possess the optically thick ejecta required by EPM, they still possess an expanding photosphere that can be used to estimate distances to their host galaxies. To be sure that EPM can be applied to the full sample of stripped envelope SNe observed by ROTSE, I focus on SN 2007gr, a well observed SN Ic. This chapter includes extensive photometric and spectroscopic analysis I performed on SN 2007gr in order to calculate the distance to its host galaxy.

SN 2007gr was a Type Ic supernova (SN Ic) in the bright spiral galaxy NGC 1058, first detected by ROTSE-IIIb on August 10, 2007, but officially discovered by KAIT on August 15 [80]. It is a stripped envelope supernova, meaning its progenitor star lost its hydrogen envelope before it collapsed into a core collapse supernova, presumably due to massive ejections. As a SN Ic, it also lost its helium envelope before exploding. A more in depth spectroscopic analysis leading to its classification as a SN Ic is provided in Section 5.3. Stripped envelope CCSNe display a variety of properties depending on the physical parameters of the progenitors [81]. Precursor observations from the Hubble Space Telescope (HST) near the explosion indicate that the progenitor of SN 2007gr is most likely a post main sequence supergiant star [82]. While Paragi et al. associate a relativistic jet with

the ejecta of SN 2007gr [83], radio observations from the Very Large Array (VLA) and X-ray observations from the *Chandra X-ray Observatory* of this event indicate an ordinary, non-relativistic explosion [84].

At a distance of approximately 10 Mpc [81] [85] [86] [87], SN 2007gr is a nearby Type Ic event, exploding near the nucleus of its host galaxy, NGC 1058. Because of this, extensive photometric and spectroscopic observations are available. The optical and NIR data used for this analysis is summarized in Table 5.1. Although EPM it not typically applied to stripped envelope SNe, this analysis uses the photometric and spectroscopic properties from the many observed epochs of SN 2007gr to determine the distance to NGC 1058.

Table 5.1: SN 2007gr Optical and NIR Data

Passband	Type	Instrument	Number of Epochs
Optical	Photometric	ROTSE-IIIb 0.45m	106
U	Photometric	FLWO 1.2m	54
B	Photometric	FLWO 1.2m	128
V	Photometric	FLWO 1.2m	129
r'	Photometric	FLWO 1.2m	51
i'	Photometric	FLWO 1.2m	52
J	Photometric	Peters 1.3m	68
H	Photometric	Peters 1.3m	66
K_s	Photometric	Peters 1.3m	62
Optical	Spectroscopic	Keck-I 10m	4
Optical	Spectroscopic	Lick 3m	3
Optical	Spectroscopic	FLWO 1.5m	5

5.1. Photometry

This analysis uses broadband optical data from ROTSE and filtered optical data from the Fred L Whipple Observatory (FLWO) 1.2 m telescope spanning more than 200 days [88]. NIR data over a period of more than 150 days was obtained with the Peters Automated 1.3 m telescope [88].

5.1.1. ROTSE Photometry

SN 2007gr was initially observed by ROTSE on August 10, 2007, or 54322.4 MJD, at RA 2:43:27.98, DEC 37:20:44.7, with a ROTSE magnitude of 15.9. This is the earliest detection of this event. The coadded ROTSE image for August 10 is shown in Figure 5.1. ROTSE observed this event from $t = -14$ d to $t = 130$ d from peak brightness, as measured in B magnitude. The peak observed ROTSE magnitude is 12.6 on 54340.5 MJD. From the distance modulus of 29.84, galactic extinction of 0.062 [52], and host galaxy extinction of 0.03 [81], this apparent magnitude yields a peak absolute ROTSE magnitude of $m_{ROTSE} = -17.3$. This is consistent with the peak R absolute magnitude.

The rise time to peak R magnitude is typically taken to be 14 - 18 days for SN 2007gr due to a lack of detection from the KAIT telescope on August 10, with a limiting absolute R band magnitude of $m_R > -12$ [89] [90] [81]. However, because of the ROTSE detection on this date, my analysis indicates that this rise time approaches or even exceeds this upper limit of 18 days. Figure 5.2 shows the optical ROTSE photometry calibrated to R band photometry.

5.1.2. Optical and NIR Photometry

This analysis includes UBV data from the FLWO 1.2 m telescope using Johnson filters. This telescope also obtained $r'i'$ data using SDSS filters. Although the $r'i'$ data is only

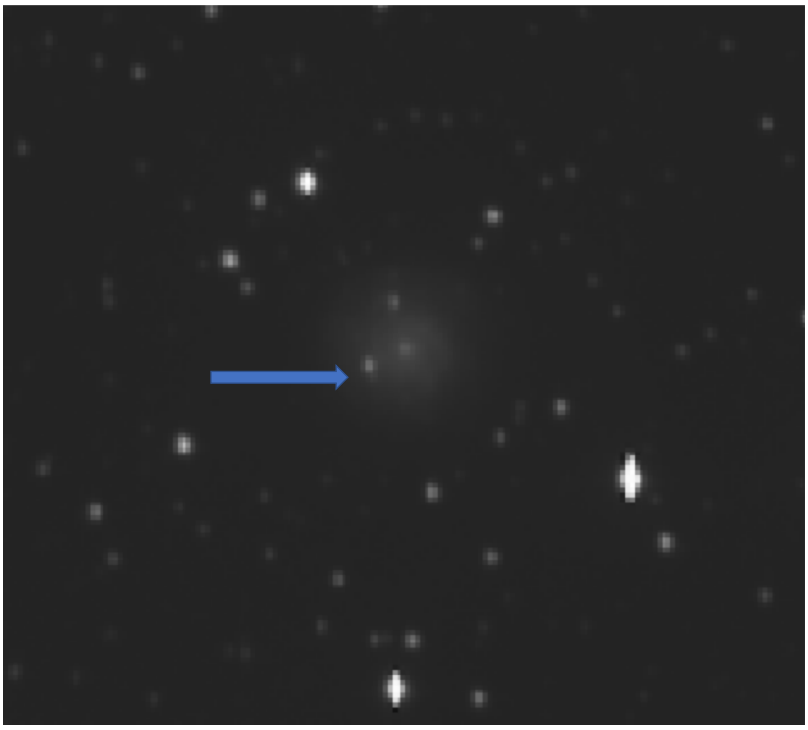

Figure 5.1: This coadded image shows the first ROTSE observation of SN 2007gr on August 10, 2007. These observations occurred before detection by any other instrument. The arrow indicates where the event occurred in its host galaxy, NGC 1058. Note that the bright source close to where the arrow points is a foreground star, as the supernova lies beneath this point.

obtained after peak magnitude, this is sufficient for EPM analysis. NIR data obtained by the Peters Automated 1.3 m telescope used 2MASS JHK_s filters. Figure 5.3 compares the observed magnitudes from each of these filters and ROTSE over time. It is evident from this plot that a significant amount of flux from SN 2007gr lies in the NIR region, where the peak JHK_s magnitudes occur 10 - 15 days after peak optical magnitudes. It can also be seen that less flux is emitted towards the UV end of the spectrum, in particular for UB magnitudes, after 30 days from B maximum.

5.2. Bolometry

Bolometric flux represents flux from an object across its entire spectrum. Photometric magnitudes can be converted to flux densities using Equation 3.3, which can then be converted to total flux for each filter using the filter information such as the transmission

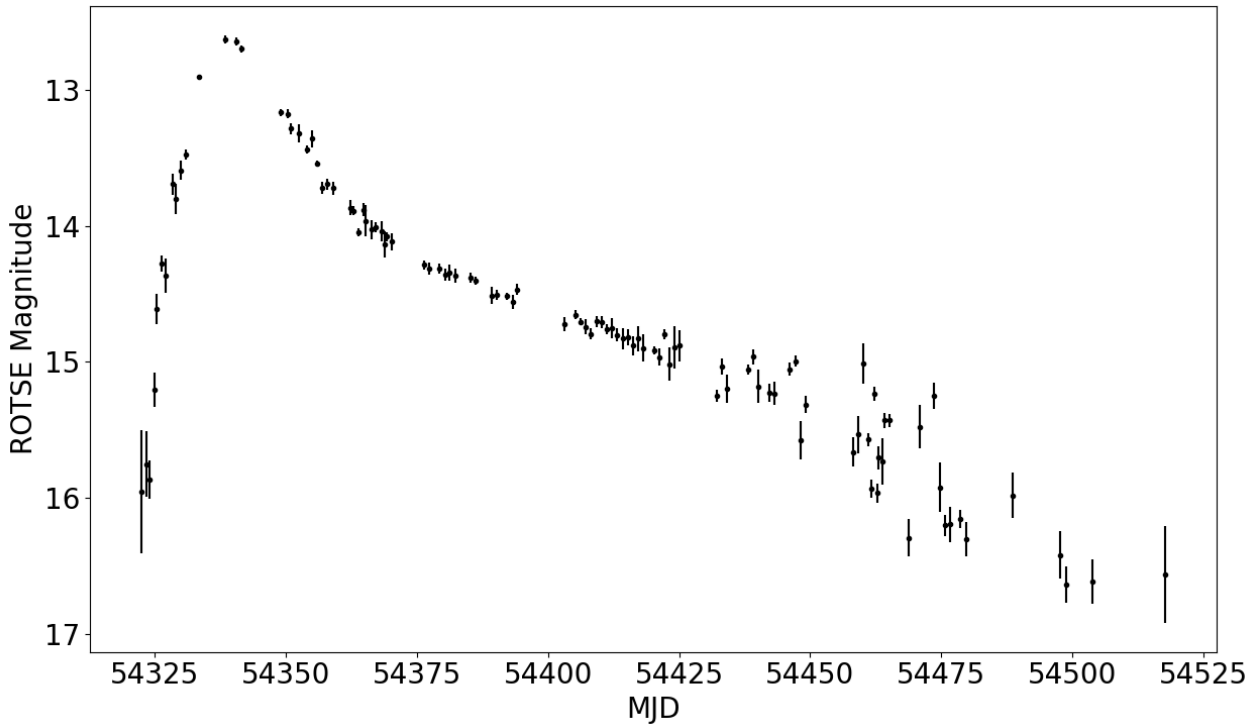

Figure 5.2: ROTSE light curve for SN 2007gr. This photometric light curve is calibrated to R band data, with a peak magnitude of 12.6.

efficiency curves seen in Figure 3.2 and Figure 4.15. Combining the total flux from each filter will give the quasi-bolometric flux from the object, as radio, sub millimeter, and X-ray data is not included.

5.2.1. Bolometric Luminosity

Before converting the observed magnitudes for SN 2007gr to flux densities, they are corrected for reddening to due Milky Way and host galaxy extinction using the values indicated in Section 5.1.1. To obtain total flux from these magnitudes, filter transmission information is integrated and multiplied by the flux density obtained using Equation 3.3, with appropriate zero point values applied for each filter. Once total fluxes are calculated, they can be

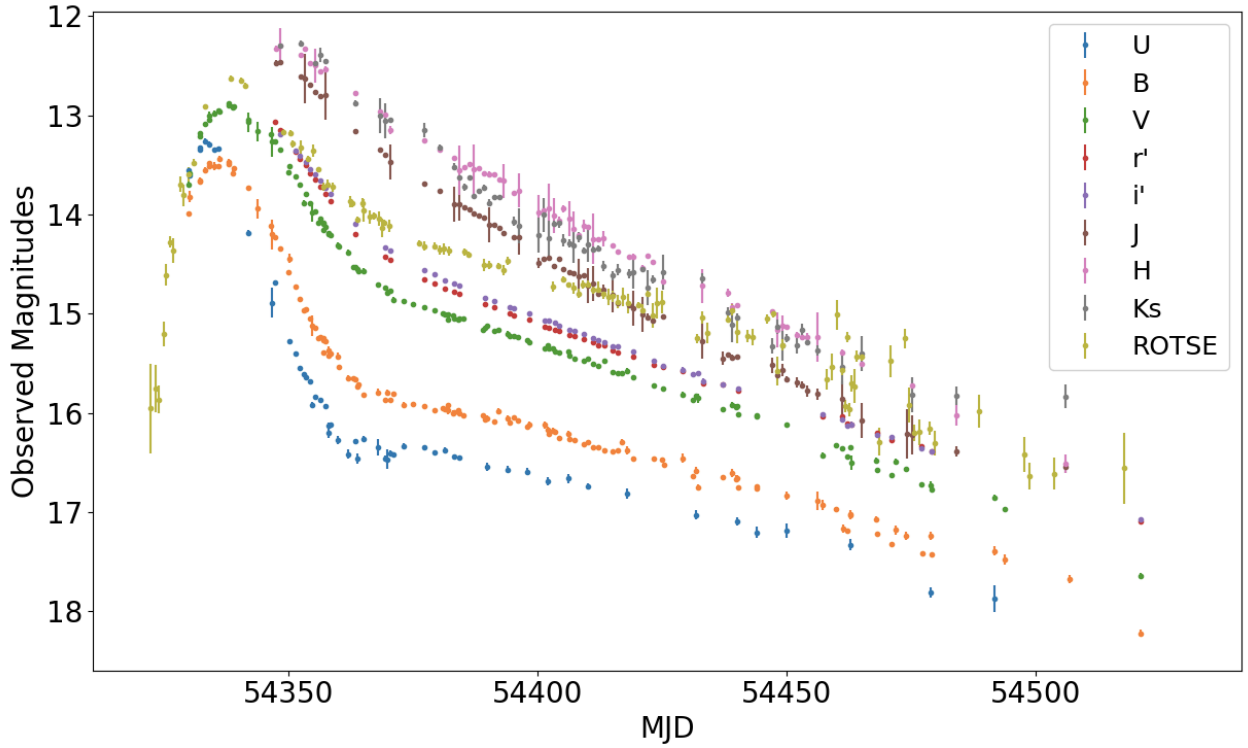

Figure 5.3: Optical and NIR photometry for SN 2007gr. The legend in the top right corner indicates the filter corresponding to the observed magnitudes, where ROTSE magnitudes are shown in yellow. Optical $UBVr'i'$ data was obtained using the FLWO 1.2 m telescope, and NIR data was obtained using the Peters Automated 1.3 m telescope.

converted to luminosities using

$$L = 4\pi r^2 F, \tag{5.1}$$

where L is the luminosity, F is the total flux, and r is the distance to the object. The distance to NGC 1058 chosen here is 10.6 Mpc, determined using Cepheid variable stars [82]. EPM analysis requires only fluxes, not luminosities, so no prior knowledge of the distance to NGC 1058 is used for the following EPM analysis. Figure 5.4 shows the observed luminosities for ROTSE and $UBVr'i'JHK_s$ filters. The data points have been interpolated so that they are on the same MJD grid for calculating bolometric luminosities. The ROTSE luminosities are much higher than all other filters due to its broadband coverage.

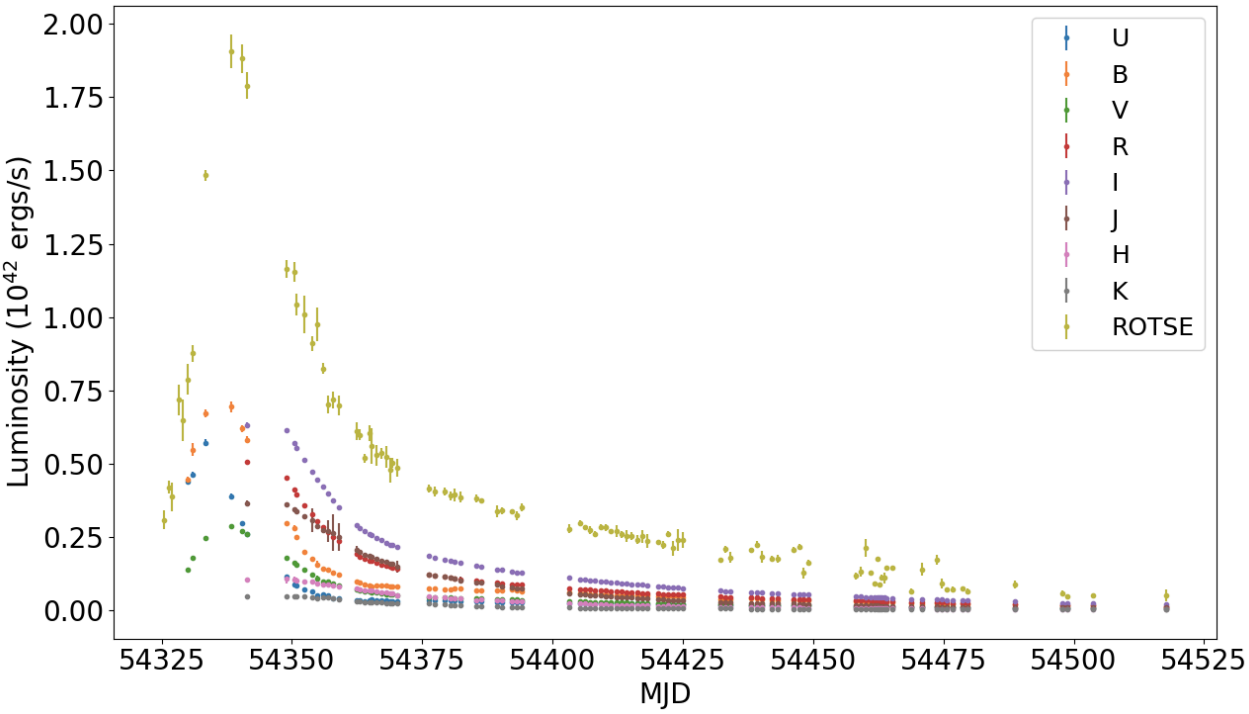

Figure 5.4: Optical and NIR luminosities for SN 2007gr. The legend in the top right corner indicates the filter corresponding to the observed luminosities, where ROTSE luminosities are shown in yellow. The ROTSE luminosities are considerably higher due to its broad wavelength coverage.

Once luminosities are derived for each filter, they can be summed to determine the bolometric luminosity. Figure 5.5 shows the bolometric luminosities for SN 2007gr. The three curves shown indicate the optical, optical and NIR, and total luminosities for this object, described as $UBVRI$, $UBVRIJHK$, and $UBVRIJHK+$, respectively. For $UBVRIJHK+$ luminosities, the $+$ represents flux in between optical and NIR filters. Linear interpolation between filters is used to determine each additional source of flux. Although no ultraviolet photometry is available, temperature evolution suggests that most of the flux comes from the optical and infrared regions, with little ultraviolet contribution. There is considerable flux between the i' and J filters, so a simple linear interpolation is used to add flux in this region.

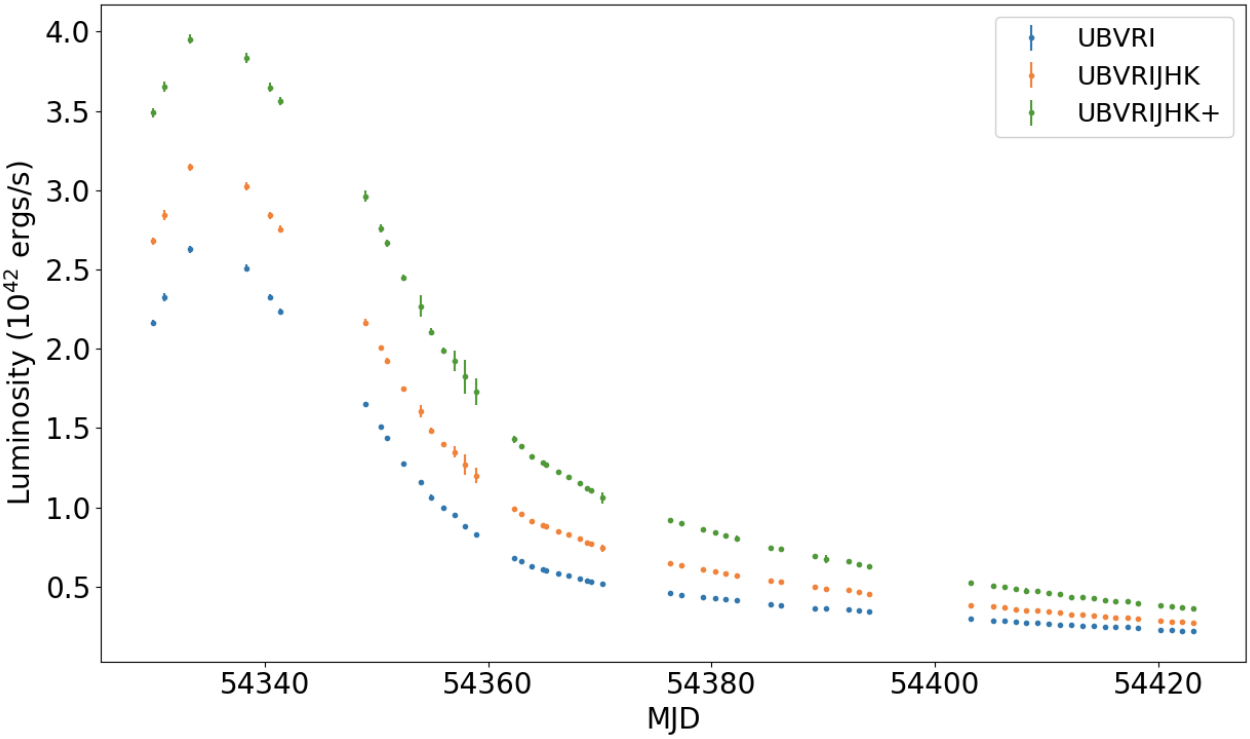

Figure 5.5: Bolometric luminosities for SN 2007gr. The legend in the top right indicates the filters used to derive the respective luminosities. The $UBVRI$ points represent the total optical luminosities from the $UBVr'i'$ data. The $UBVRIJHK$ points represent the total optical and NIR luminosities from the $UBVr'i'JHK_s$ data. The $UBVRIJHK+$ points represent the bolometric luminosities.

5.2.2. Bolometric Calibration

Fortunately, there is ample optical and NIR photometry available for SN 2007gr to be used to calculate the necessary quantities for EPM. However, this is not always the case. Therefore, I use this object to derive a bolometric calibration that can be applied to other SNe Ic with ROTSE data, when there is insufficient photometry to calculate bolometric fluxes. It will take more SNe Ic to establish a more rigorous calibration, but this object was sufficient to be applied to another SN Ic, SN 2010kd [91]. This calibration has been previously performed for a larger sample of SNe IIP [25] [68].

The open CCD transmission of ROTSE is broad, covering a wavelength range similar to that of $UBVRI$. We first establish a calibration of ROTSE data to filtered $UBVRI$ data. Then, noting that the ratio of ROTSE luminosity to $UBVRI$ luminosity follows a linear relationship with respect to $B-V$ color [25],

$$log_{10}\left(\frac{L_{ROTSE}}{L_{UBVRI}}\right) = a(B-V)+b, \tag{5.2}$$

is used to perform the calibration, where a and b are the slope and intercept to be solved for and then applied to ROTSE luminosity values. A similar calibration is used to calibrate $UBVRI$ data to $UBVRIJHK$ data. Finally, $UBVRIJHK$ data is calibrated to quasi-bolometric, $UBVRIJHK+$ luminosities. These calibrations are taken from $t = 0$ d to $t = 100$ d with respective to peak ROTSE magnitude, and the relationships for SN 2007gr are shown in figure 5.6.

Using these relationships, ROTSE luminosity can be calibrated first to $UBVRI$ luminosity, then to $UBVRIJHK$ luminosity, and finally to bolometric luminosity. Figure 5.7 compares the ROTSE luminosities to the respective luminosities after each of these calibrations, as well as the ROTSE luminosity after these calibrations for all observed ROTSE epochs.

5.3. Spectroscopy

Optical spectra for SN 2007gr were obtained by the Shane 3 m telescope at the Lick Observatory, the Keck-I 10 m telescope at the Keck Observatory, and the FLWO 1.5 m telescope. SN 2007gr was initially spectroscopically classified as generic SN I b/c [92] due to lack of clarity regarding the possible helium line at 6350 Å [81]. However, spectral evolution does not indicate the presence of any helium, thus SN 2007gr is typically described as a SN Ic. Figure 5.8 shows the evolution of the SN 2007gr spectrum over time, with the identifiable

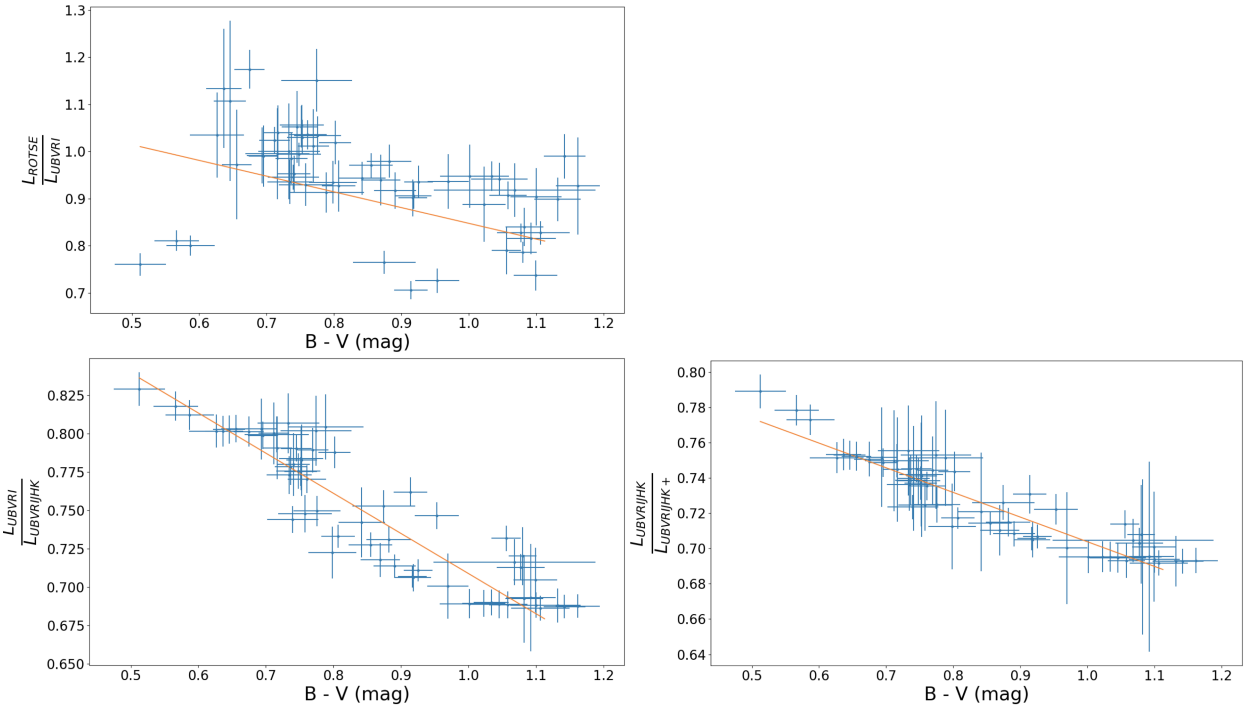

Figure 5.6: Bolometric calibration of SN 2007gr. Each of these plots shows the linear relationship and fit of a luminosity ratio versus $B - V$ color. The top left plot shows this for the ratio between ROTSE and $UBVRI$, the bottom left plot shows this for the ratio between $UBVRI$ and $UBVRIJHK$, and the bottom right plot shows this for the ratio between $UBVRIJHK$ and bolometric luminosity. These calibrations are determined using data from $t = 0$ d to $t = 100$ d with respective to peak ROTSE magnitude.

chemical elements labeled at the top of the plot, and temporal markers indicating the number of days from B maximum.

Overall, optical spectra of SN 2007gr show an abundance of intermediate mass elements. The earliest spectrum shown in figure 5.8 at $t = -8$ d from B maximum exhibits moderate P Cygni absorption profiles from Ca II H and K and MG II lines at 3964 Å, 3964 Å, and 4481 Å respectively, where a P Cygni profile describes chemical features with the presence of both absorption and emission from the same spectral line. Weak Na I D (blended), Si II, and O I features are also present, at 5891 Å, 5897 Å, 6355 Å, and 7774 Å respectively, as well as the Fe II triplet at 4924 Å, 5018 Å, and 5169 Å. The Fe II triplet lines are relatively unblended, which is atypical for SNe Ic [81]. From peak light to approximately two weeks

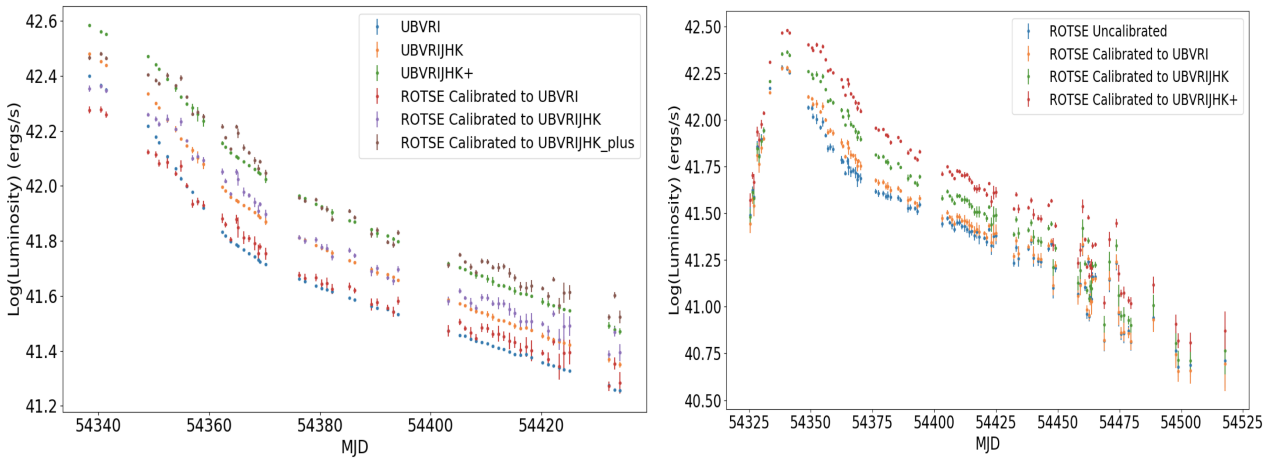

Figure 5.7: Bolometric calibration of ROTSE luminosities for SN 2007gr. The left plot shows ROTSE luminosities compared to the respective luminosities indicated in the legend after calibration. The right plot shows ROTSE luminosities before and after each of these calibrations for all observed ROTSE epochs.

after peak light, these intermediate mass features become increasingly prominent, with the silicon feature fading from spectra after this point [89]. These epochs also exhibit a strong NIR Ca II triplet (8498 Å, 8542 Å and 8662 Å) [89] and a moderate C I feature at 9094 Å, although this feature is not visible in many of the spectra due to the limiting wavelength coverage seen in figure 5.8.

Although the feature at 6350 Å was initially classified as He I [92], typical SNe Ib show an increase in the intensity of helium features with time [81], counter to what is seen in the spectral evolution of SN 2007gr. Valenti et al. indicate that a more likely candidate for this feature is C II, due to the other prominent carbon features present in the optical and NIR spectra [81]. As noted, this results in the spectroscopic classification of SN 2007gr as a SN Ic.

5.4. Ejecta Velocities

The ejecta velocities for several elements present in the SN 2007gr spectra were calculated by fitting a Gaussian profile to the absorption features of the P Cygni profile of each element. The mean of each Gaussian profile is taken to be the ejecta velocity, indicating the blueshift

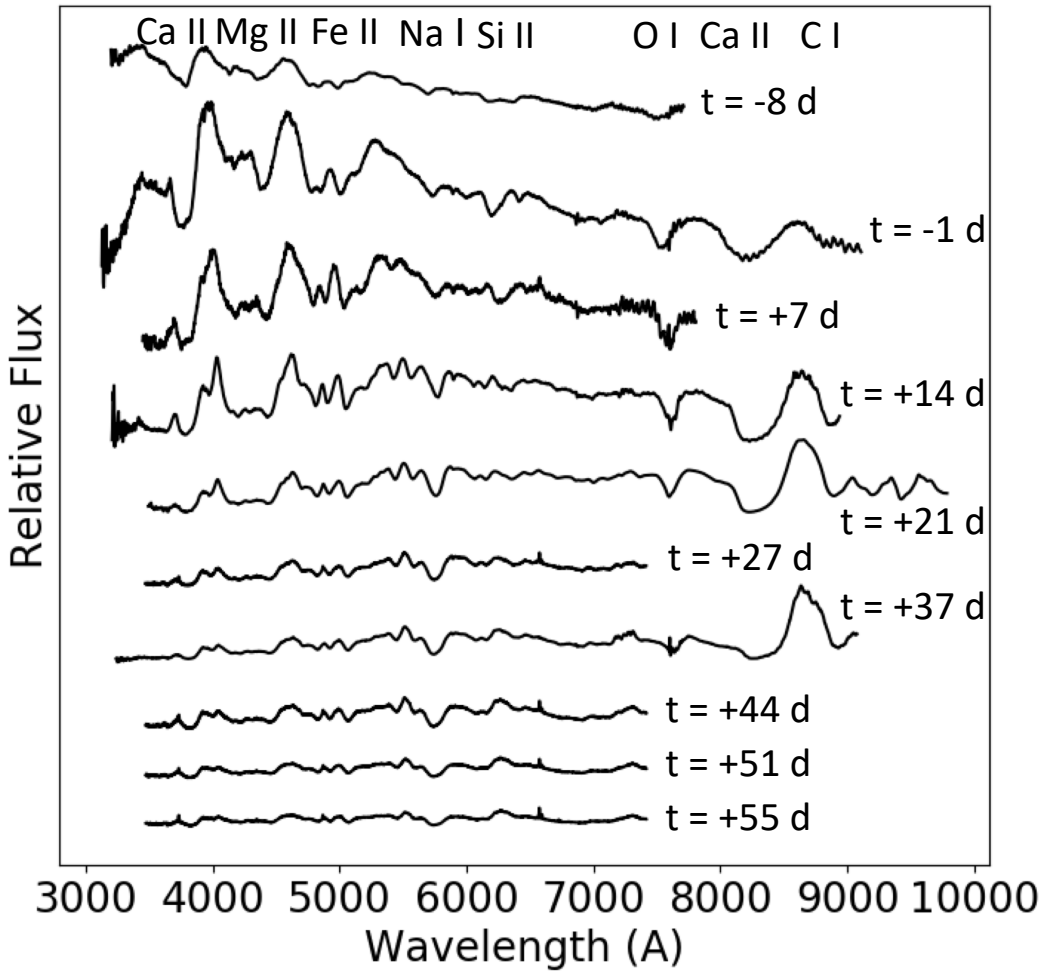

Figure 5.8: Time evolution of SN 2007gr spectra. The chemical features visible are labeled at the top, indicating an abundance of intermediate mass elements. The temporal markers indicate the number of days from B maximum.These spectra were obtained using the Lick 3 m Shane telescope and the Keck-I 10 m telescope.

of each element in the spectrum. Using the estimation of ejecta velocities allows for the examination of the distribution of elements in each layer where the respective lines form. [89]. Figure 5.9 shows the ejecta velocity over time for the Ca II H and K, Mg II, Na I, Fe II, and O I features, where average velocities are taken for chemical features with multiple lines present.

Ca II features show the highest velocities, indicating the presence of calcium in the outermost layers of ejecta. Mg II features show the lowest velocities, indicating the presence

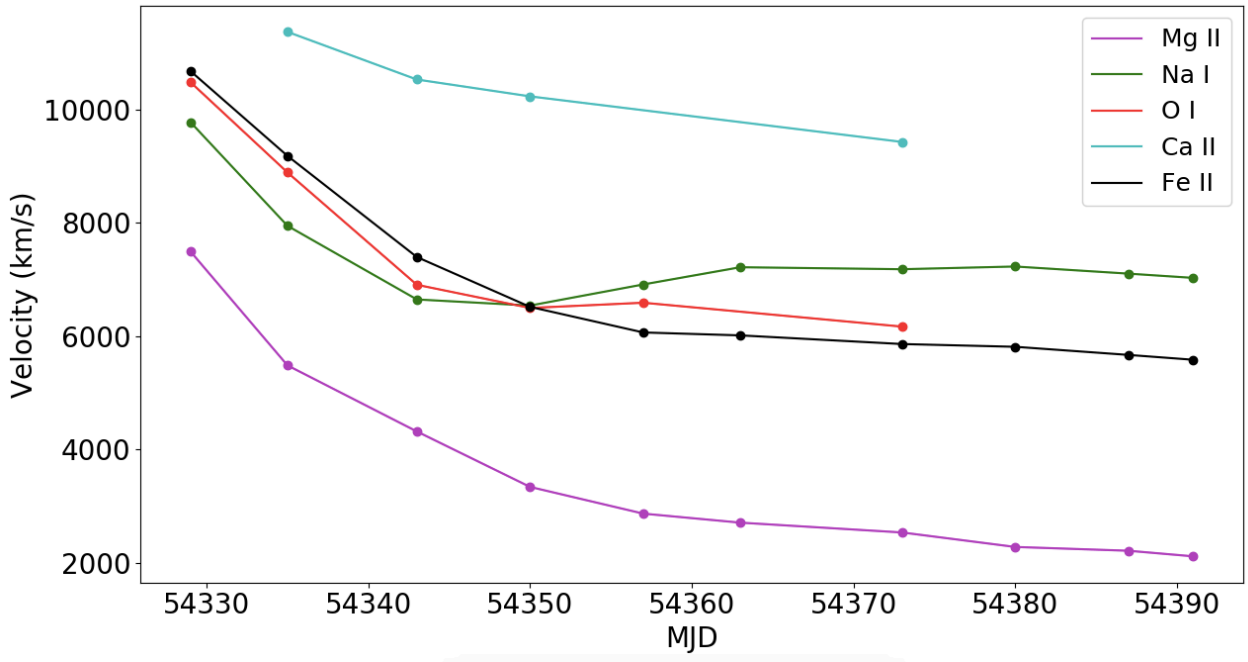

Figure 5.9: Ejecta velocities for SN 2007gr. Ca II features show the highest velocity, indicating the presence of Ca II in the outermost layers of ejecta. Fe II, Na I, and O I all show similar velocity evolution, indicating that these elements are all present in the inner layers of ejecta. Mg II features display the lowest velocities, indicating the presence of Mg II in the innermost layers of ejecta.

of magnesium in the innermost layers of ejecta. Fe II, Na I, and O I all show similar velocity evolution, indicating their presence in the innermost layers of ejecta. The increase in Na I velocity at 2 weeks after B maximum is most likely due to the recombination of the two lines at 5891 Å and 5897 Å.

5.5. Photospheric Velocity

The features present in SN 2007gr spectra are narrower than other SNe Ic, which is most likely related to the slow evolution of the ejecta and photospheric velocities [81] [82] [90]. For this analysis, I use the expansion velocities of intermediate mass elements present in the photosphere to estimate its velocity.

Using this method, the photospheric velocity at maximum light is 9,200 km/s, declining to 6,000 km/s at 30 days after maximum light. This is consistent with previous results, although these values vary based on the methods used to determine photospheric velocity. Using C I lines, the photospheric velocity is seen to be 11,000 km/s one week after explosion, declining to 4,800 km/s at 50 days after explosion [81]. Although the decline is steeper using this method, the values close to the time of explosion and during the photospheric phase are similar. Using Si II lines as an approximation, 6,700 km/s is seen to be the photospheric velocity at B maximum, declining to 4,000 km/s ten days later [89].

There are several estimates for the duration of the photospheric phase of this event, found to be between 20 [90] and 30 days [89] past explosion. However, it has also been noted that SN 2007gr remained optically thick inside 5,000 km/s at 50 days post explosion [81]. Figure 5.10 shows the evolution of photospheric velocities over time, where this analysis examines velocities from maximum light to $t < 30$ d after maximum light.

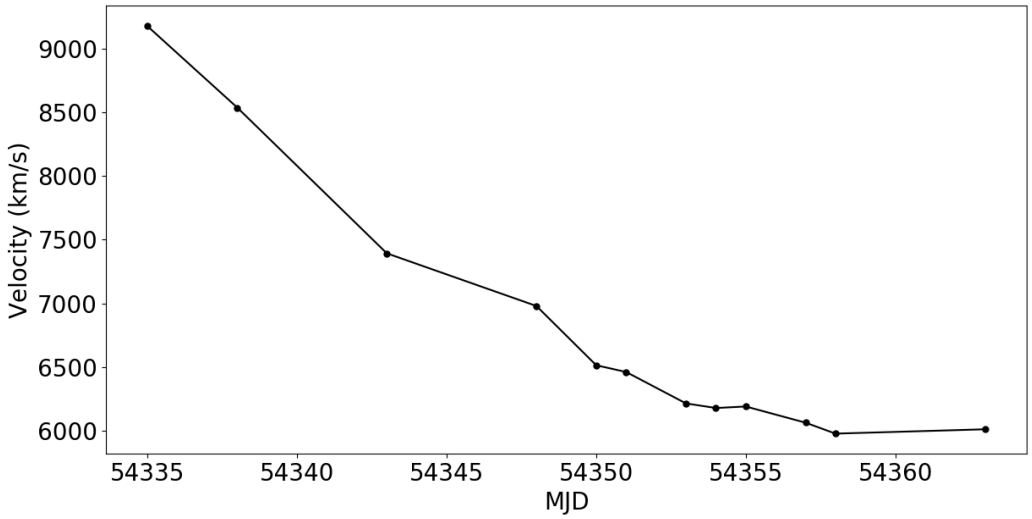

Figure 5.10: Time evolution of photospheric velocity for SN 2007gr. The photospheric phase for this event lasts until approximately 30 days post explosion, where the velocity at maximum light is 9,200 km/s.

5.6. Temperature Evolution

Due to the composition of SN 2007gr, it is difficult to fully approximate the temperature evolution of this event. Based on the early appearance of CO, the CO emitting region of SN 2007gr is estimated to be greater than 2,000 K [90]. To estimate the iron mass present in SN 2007gr, Hunter et al. [89] use the fact that forbidden lines, or spectral lines not visible in spectra of the same gases on Earth, are excited at temperatures of approximately 6,500 K, also placing a constraint of the temperature of certain layers of SN 2007gr.

For this analysis, temperatures of SN 2007gr were determined by fitting a Planck function to observed photometry. To derive flux values used for this fit, observed magnitudes were converted to flux densities, which were then evaluated at the effective wavelength of each filter. At approximately one week before maximum light, the temperature is seen to be 8,600 K, dropping to 5,700 K one week after maximum light, and 4,800 K at 50 days after maximum light. Figure 5.11 shows the temperature evolution over time of SN 2007gr.

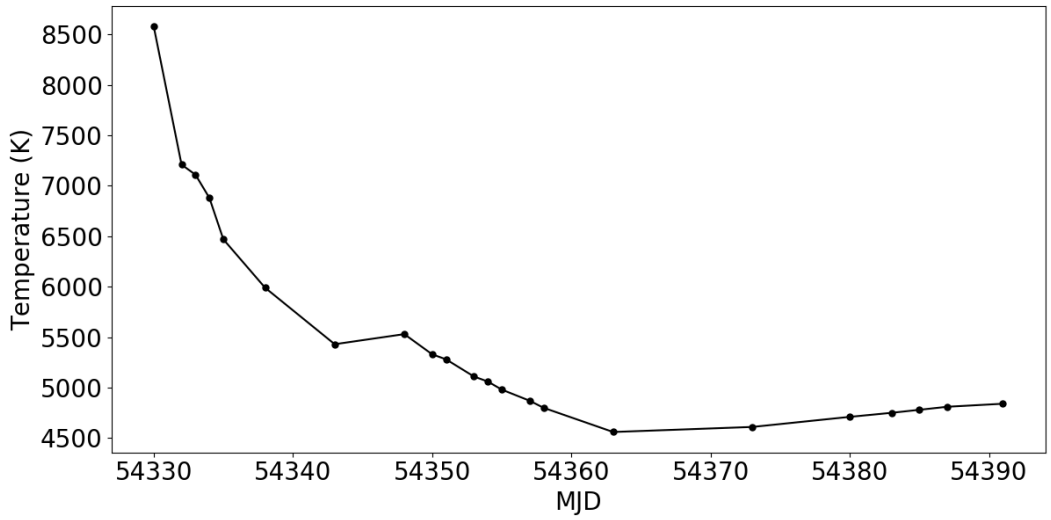

Figure 5.11: Temperature evolution of SN 2007gr. The temperature is seen to approximately 8,600 K one week after explosion, dropping to approximately 4,600 K 50 days after explosion.

5.7. Distance Measurement

The distance to the host galaxy of SN 2007gr, NGC 1058, was estimated using the expanding photosphere method. As described in Section 1.5.3.2, this requires knowledge of the photospheric velocity and radius of the supernova, seen explicitly in Equation 1.34. This linear relationship allows not only the distance to the host galaxy to be estimated, but also the time of explosion. The distance to NGC 1058 was found to be 9.5 ± 0.9 Mpc and the time of explosion was found to be -13.7 d from B maximum.

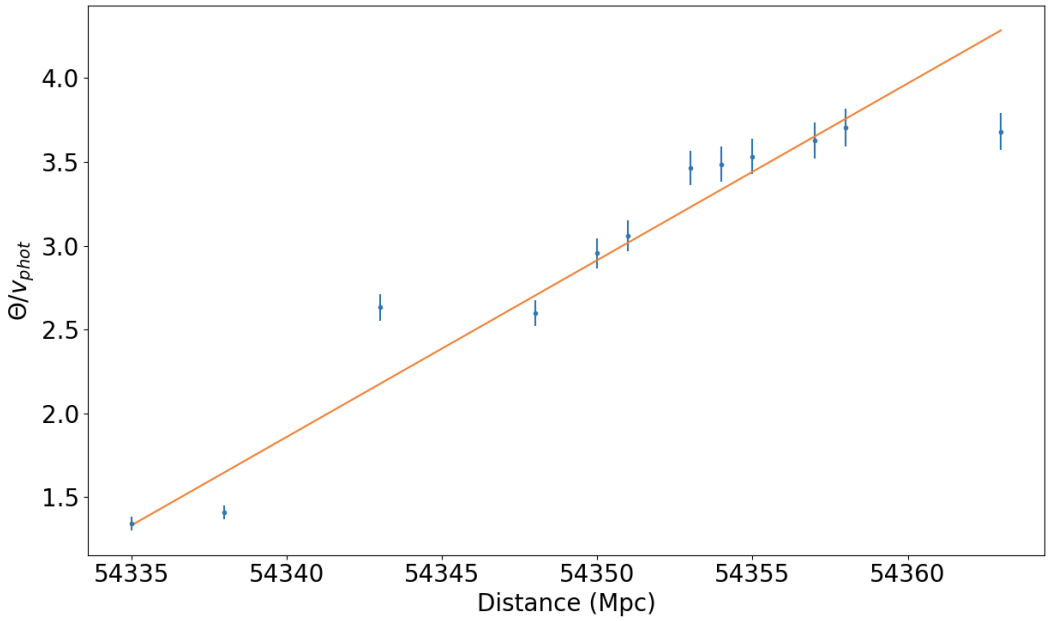

Figure 5.12: The linear fit of photospheric radius over photospheric velocity for SN 2007gr vs. time. The slope of this fit represents the distance to the host galaxy of NGC 1058, and the intercept represents the time of explosion. The distance to NGC 1058 is estimated to be 9.5 ± 0.9 Mpc, and the estimated time of explosion is $t = -13.7$ d from B maximum.

Previous analysis suggests that the distance to NGC 1058 is anywhere between 9.3 and 10.6 Mpc, consistent with this result. Using Cepheid variable stars, Silbermann et al. [85] find the distance to NGC 925, a member of a group of galaxies to which NGC 1058 belongs. This distance of 9.3 ± 0.7 Mpc is therefore adopted for the host galaxy of SN 2007gr [84] [89] [81]. Using the Tully-Fisher relation, Terry et al. [87] calculated this distance to be 10.6 ± 1.3 Mpc [89] [81] [82] [83]. Another supernova, SN 1969L, was also observed in NGC 1058,

where the surface brightness fluctuation (SBF) was used to calculate this distance to be 10.0 ± 1.0 Mpc [86]. Table 5.2 summarizes these distance measurements to NGC 1058.

It is worth noting that although this distance measurement is comparable to previous measurements of its host galaxy, SN 2007gr may not meet the requirements of EPM described in Section 1.5.3.2. Because it is a stripped envelope supernova, it is difficult to define the photospheric phase and depth. Additionally, its multiple layers make it difficult to define the photospheric temperature using available photometry and whether the bolometric flux, also calculated using this photometry, can be appropriately applied to flux solely due to the photosphere of SN 2007gr. There is an additional factor used in EPM, the dilution factor in Equation 1.30, that describes the effect of the surrounding atmosphere on the ability to accurately calculate of the photopheric radius. This is well defined using models of hydrogen that can be applied to SNe IIP [26], but it is not well defined for other types of CCSNe, where additional elements may be present in the atmosphere. Thus, the dilution factor is set to 1 for this analysis, but may have an impact on calculating the photospheric radius, and therefore the distance to SN 2007gr and its host galaxy NGC 1058.

Table 5.2: NGC 1058 Distance Measurements

Method	Distance (Mpc)
Cepheid Variable Stars	9.3 ± 0.7
Expanding Photosphere Method (this analysis)	$\mathbf{9.5 \pm 0.9}$
Surface Brightness Fluctuation	10.0 ± 1.0
Tully-Fisher Relation	10.6 ± 1.3

Chapter 6

Cosmology with ROTSE Core Collapse SNe

As mentioned at the beginning of Chapter 5, ROTSE has played a role in a number of supernova projects. This chapter describes contributions that I made to two analyses involving a superluminous supernova, SN 2010kd [91], and a calculation of the Hubble flow of the local universe using type IIP CCSNe [68]. For SN 2010kd, I contributed to the photometry described in Section 6.1.1.2 and the bolometry described in Section 6.1.2. For the SNe IIP analysis, I calculated H_0 using the process described in Section 6.2.3.

6.1. SN 2010kd

SN 2010kd is a SLSN discovered by the ROTSE Supernova Verification Project (RSVP) in a metal poor dwarf galaxy [91]. SLSNe are incredibly rare, comprising only approximately 0.01% of CCSNe [38]. As described in Chapter 2, the time of discovery and observation of SLSNe began with the ROTSE discovery of SN 2005ap [40], where the mean absolute magnitude of a superluminous supernova is -21.7 [93] [38] [91].

SN 2010kd supernova was discovered by ROTSE on November 14, 2010 [94] at a magnitude of approximately 17.2 at RA 02:08:01:11 and DEC 49:13:31. A ROTSE observation of this supernova can be seen in Figure 6.1. Similar to ordinary, luminous supernovae, SLSNe are further defined by their hydrogen content [93], either hydrogen rich or hydrogen poor, where SN 2010kd spectra show that it is hydrogen poor (SLSNe I), ultimately classified as a Type Ic SN. SLSNe I are thought to be a subclass of SNe Ic [91], where spectral features of this type of superluminous supernova are similar to that of typical SNe Ic [95].

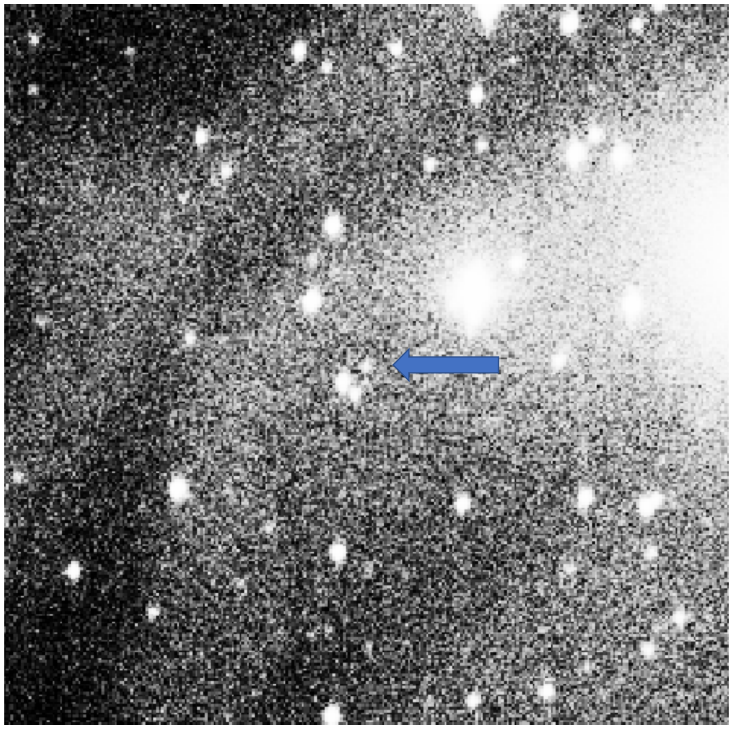

Figure 6.1: An optical ROTSE image of SN 2010kd. This supernova is superluminous, located in a metal poor dwarf galaxy, where the blue arrow points to SN 2010kd.

6.1.1. Photometry

SN 2010kd was photometrically observed in UV and optical bands by the UVOT instrument onboard the *Swift* satellite [59] during early-time, allowing peak brightness to be constrained in several UV and optical bands [91]. ROTSE broadband photometry is available out to more than 100 days past B maximum. $UBVRI$ photometry is also available from the Sampurnanand 1.04 m telescope located at the Aryabhatta Research Institute of Observational Sciences (ARIES) [96]. Table 6.1 summarizes the available data for SN 2010kd.

Table 6.1: SN 2010kd Optical and UV Data

Passband	Type	Instrument	Number of Epochs
Optical	Photometric	ROTSE-IIIb 0.45m	60
$UVW2$	Photometric	$Swift$-UVOT 0.3m	6
$UVM2$	Photometric	$Swift$-UVOT 0.3m	6
$UVM1$	Photometric	$Swift$-UVOT 0.3m	6
u	Photometric	$Swift$-UVOT 0.3m	6
b	Photometric	$Swift$-UVOT 0.3m	6
v	Photometric	$Swift$-UVOT 0.3m	6
U	Photometric	Sampurnanand 1.04m	15
B	Photometric	Sampurnanand 1.04m	19
V	Photometric	Sampurnanand 1.04m	17
R	Photometric	Sampurnanand 1.04m	19
I	Photometric	Sampurnanand 1.04m	18
Optical	Spectroscopic	HET 9.2m	7
Optical	Spectroscopic	Keck-I 10m	2

6.1.1.1. Optical and UV Photometry

Figure 6.2 shows UV and optical light curves for SN 2010kd. Absolute magnitudes for SN 2010kd are calculated using

$$M = m - 5\,log(D_L/10\,\mathrm{pc}) + 2.5\,log(1+z), \tag{6.1}$$

where these magnitudes are first corrected for galactic extinction. In addition to the $UBVRI$ photometry from the Sampurnanand telescope, $Swift$-UVOT data was collected using the $UVW2$, $UVM2$, and $UVW1$ UV filters, and u, b, and v optical filters. Unfortunately, this data is not extensively available, but does occur pre and post peak brightness, allowing important constraints such as peak B brightness to be placed on SN 2010kd. To calculate B maximum, $Swift$ b magnitudes were converted to Johnson B magnitudes using the transformation equations decribed by Poole et al. [97]. The peak B brightness was then calculated

to be -21.80 ± 0.02 magnitude, where a third order spline function was fit to absolute B magnitudes over a period of approximately $-20 < t < 20$ days surrounding B maximum.

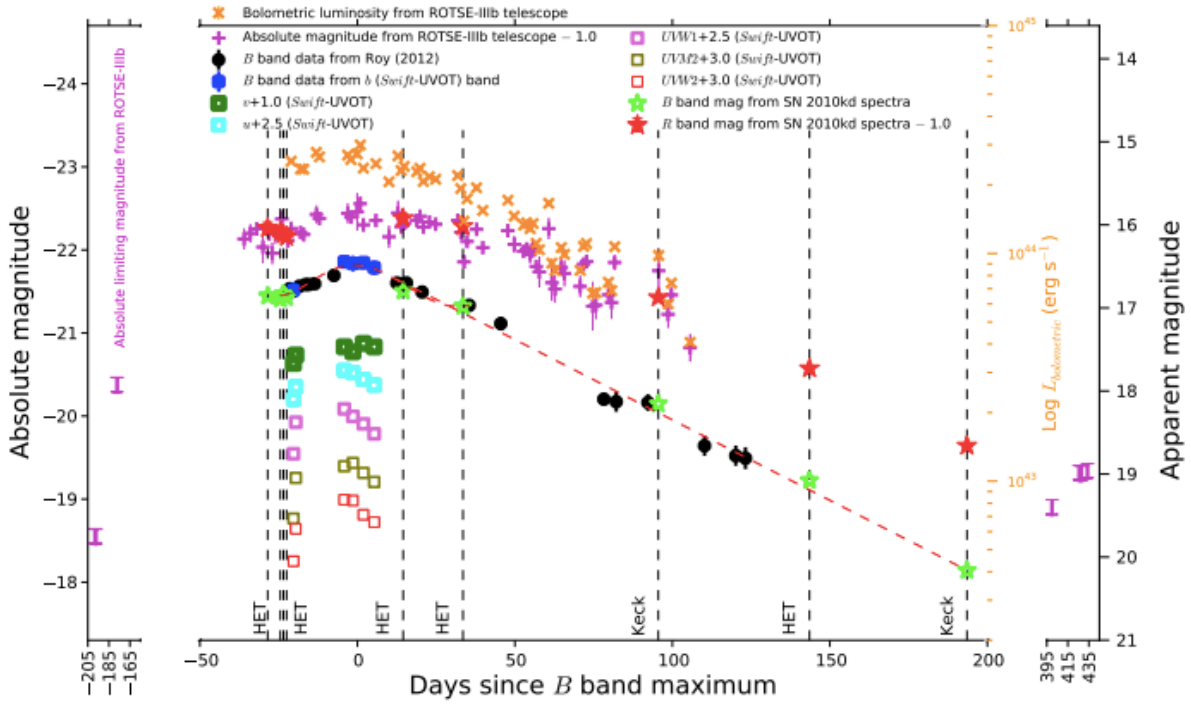

Figure 6.2: UV and optical light curves for SN 2010kd [91]. The *Swift*-UVOT instrument provides early time UV and optical data, while ROTSE provides ample broadband coverage pre and post peak brightness. Additional $UBVRI$ band data is also available [96]. Vertical dashed lines indicate epochs where spectroscopy is available.

Using B photometry, SLSNe I are broken into two subgroups, fast decaying and slow decaying, where typical decay rates are ~ 0.06 and ~ 0.02 mag per day respectively [91]. Kumar et al. [91] find the decay rate of B photometry for SN 2010kd to be ~ 0.19 mag per day, similar to that of typical slow decaying SLSNe I.

6.1.1.2. ROTSE Photometry

SN 2010kd was discovered by ROTSE-IIIb as a part of its RSVP mission to observe as many SNe as possible, at an apparent magnitude of approximately 17.2 [94] [91]. In addition

to first discovery, ROTSE provides the most extensive photometric data for SN 2010kd, ranging from approximately 35 days prior to B maximum, out to more than 100 days post B maximum.

The photometric analysis I performed on this object calibrates ROTSE magnitudes to R magnitudes [53]. This can be seen in Figure 6.2, where the magenta plus signs represent ROTSE absolute magnitudes, similar in value to the red stars which indicate R magnitudes derived from integrating optical spectra. Figure 6.3 explicitly shows the observed ROTSE light curve for SN 2010kd.

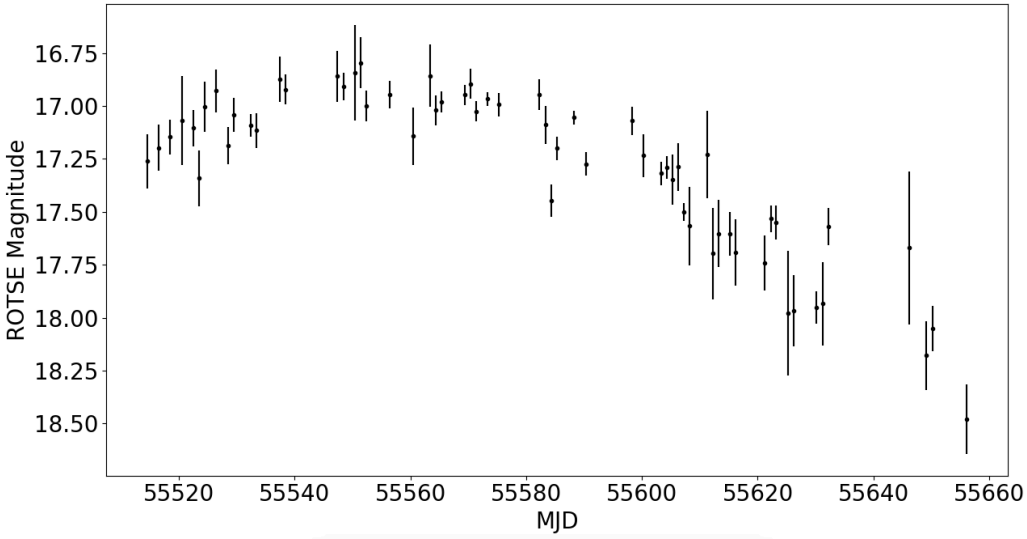

Figure 6.3: ROTSE photometry for SN 2010kd. The ROTSE-IIIb telescope extensively observed this transient event, with data ranging from $t = -35$ days to $t = +105$ days from B maximum

6.1.2. Bolometry

To obtain a bolometric light curve, I adopt a similar strategy to the one described in Section 5.2, where ROTSE broadband photometry is calibrated to bolometry using the available optical photometry for SN 2010kd. Although there is no NIR data available, it can be seen that the UV contribution from SN 2010kd is comparable to that of the

NIR contribution from SN 2007gr, making this calibration strategy plausible. I used this calibration strategy in Kumar et al. [91], which extensively examines the photometry and spectroscopy of SN 2010kd.

To perform this calibration, the broadband coverage of the ROTSE open CCD is used, establishing a relationship between ROTSE luminosity and $UBVRI$ luminosity from Sampurnanand photometry. Comparison of ROTSE photometry to $UBVRI$ photometry is shown in Figure 6.4. Common epochs were derived using a linear interpolation, converting $UBVRI$ photometry to the observed epochs of ROTSE photometry. Fluxes, and subsequently luminosities, were derived for ROTSE and $UBVRI$ photometries as described in Section 5.2.1. Using Equation 5.2, it is possible to calibrate ROTSE luminosities to $UBVRI$ luminosities, using the linear relationship between the ratio of these luminosities and $B-V$ color, as seen in Figure 6.5.

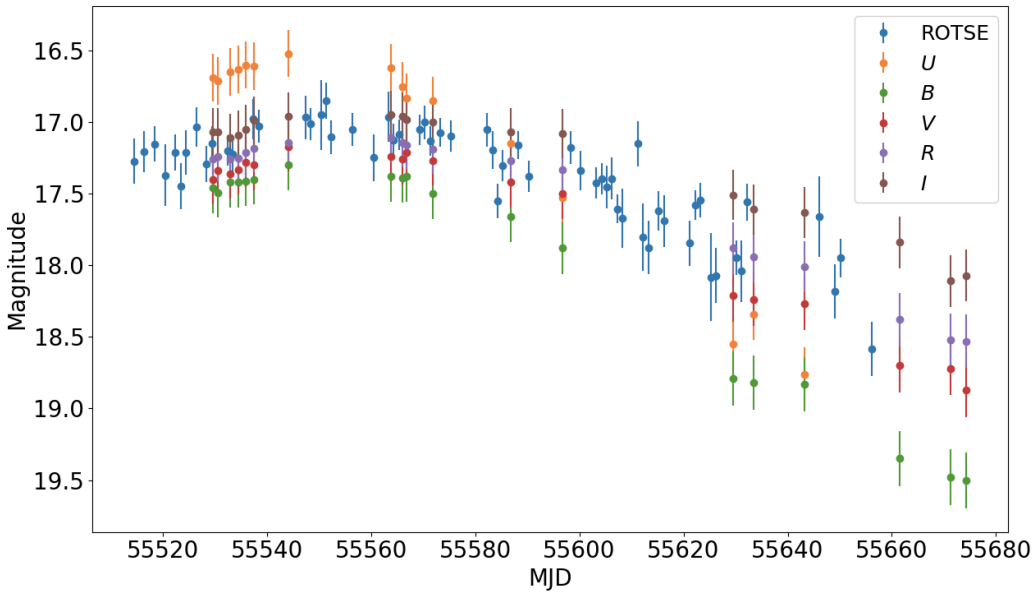

Figure 6.4: Comparison of ROTSE photometry to $UBVRI$ photometry for SN 2010kd. The $UBVRI$ magnitudes are used to calibrate ROTSE photometry to ultimately derive bolometric luminosities.

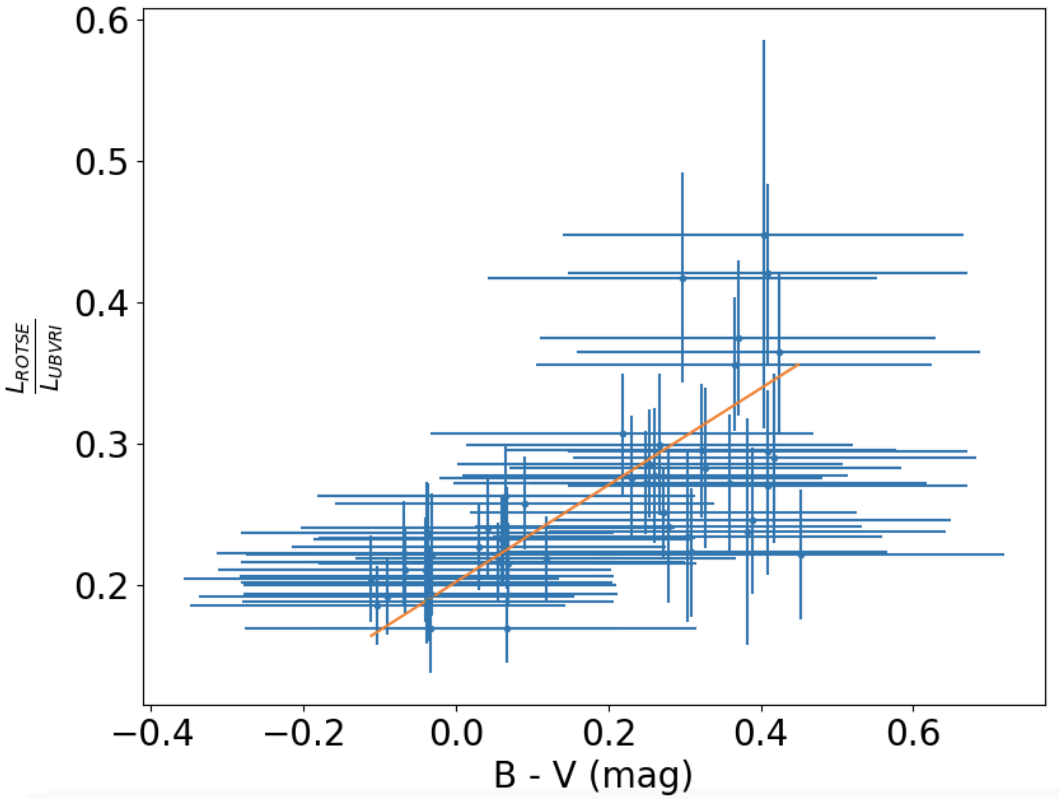

Figure 6.5: The linear relationship between the ratio of ROTSE luminosities and $UBVRI$ luminosities, and $B-V$ color for SN 2010kd. The linear fit of this relationship can be used to calibrate ROTSE photometry to $UBVRI$ optical photometry, allowing a pseudo-bolometric light curve to be established using ROTSE broadband photometry.

Extensive photometric data across its entire spectrum is not available for SN 2010kd, so the calibration of ROTSE luminosities to $UBVRIJHK$ data for SN 2007gr is applied to this event. This is justified by the fact that both objects are SNe Ic and show similar amounts of flux outside of the optical region. Similarly, ROTSE photometry is calibrated to bolometric flux using the linear interpolation between I and J filters described in Section 5.2.1. Figure 6.6 shows ROTSE luminosities after each calibration, including the final bolometric luminosities, displayed as bolometric magnitudes in Figure 6.2. Using this strategy, the final peak bolometric luminosity is $\sim 2.67 \pm 0.20 \times 10^{44}$ ergs/s.

It is worth noting that the behavior of SN 2010kd luminosity vs. $B-V$ is different than that of SN 2007gr. This is due to the fact that the superluminous SN 2010kd is a

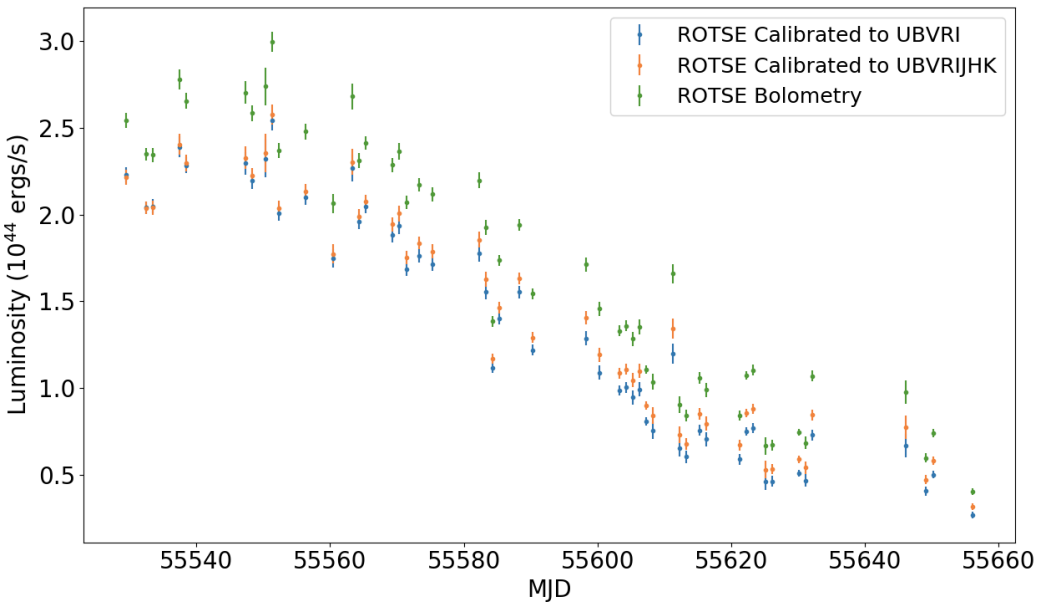

Figure 6.6: ROTSE broadband photometry converted to luminosities after each calibration for SN 2010kd. The blue points indicate ROTSE photometry calibrated to $UBVRI$ data, the orange points indicate ROTSE photometry calibrated to $UBVRIJHK$ data, and the green points indicate ROTSE photometry calibrated to bolometric luminosities. Calibration to $UBVRI$ was performed using optical data for SN 2010kd, while the subsequent calibrations are performed using the calibration information for SN 2007gr.

hotter object, with higher contributions in the ultraviolet range, rather than NIR and higher wavelength regions. The behavior of SN 2007gr is similar to the SNe IIP sample described in Dhungana et al. [25], although a larger ROTSE observed SNe Ic sample is necessary to facilitate a full SNe Ic calibration. Therefore, further analysis is needed to test SN 2010kd as a viable EPM candidate. If it seen that this supernova can provide an accurate distance to its host galaxy, it would be a very useful object for ROTSE CCSNe cosmology due to its redshift of $z \sim 0.1$.

6.1.3. Spectroscopy

Optical spectra for SN 2010kd were obtained using the LRS on the HET [41] and the Low Resolution Imaging Spectrometer (LRIS) on the Keck-I 10 m telescope [69], from $t = -28$ to $t = +194$ days with respect to B maximum. Due to a lack of observed hydrogen and helium in its spectra, SN 2010kd is spectroscopically classified as a Type Ic SN, as is typical for SLSNe Ic [95]. Figure 6.7 shows the temporal evolution of SN 2010kd spectra.

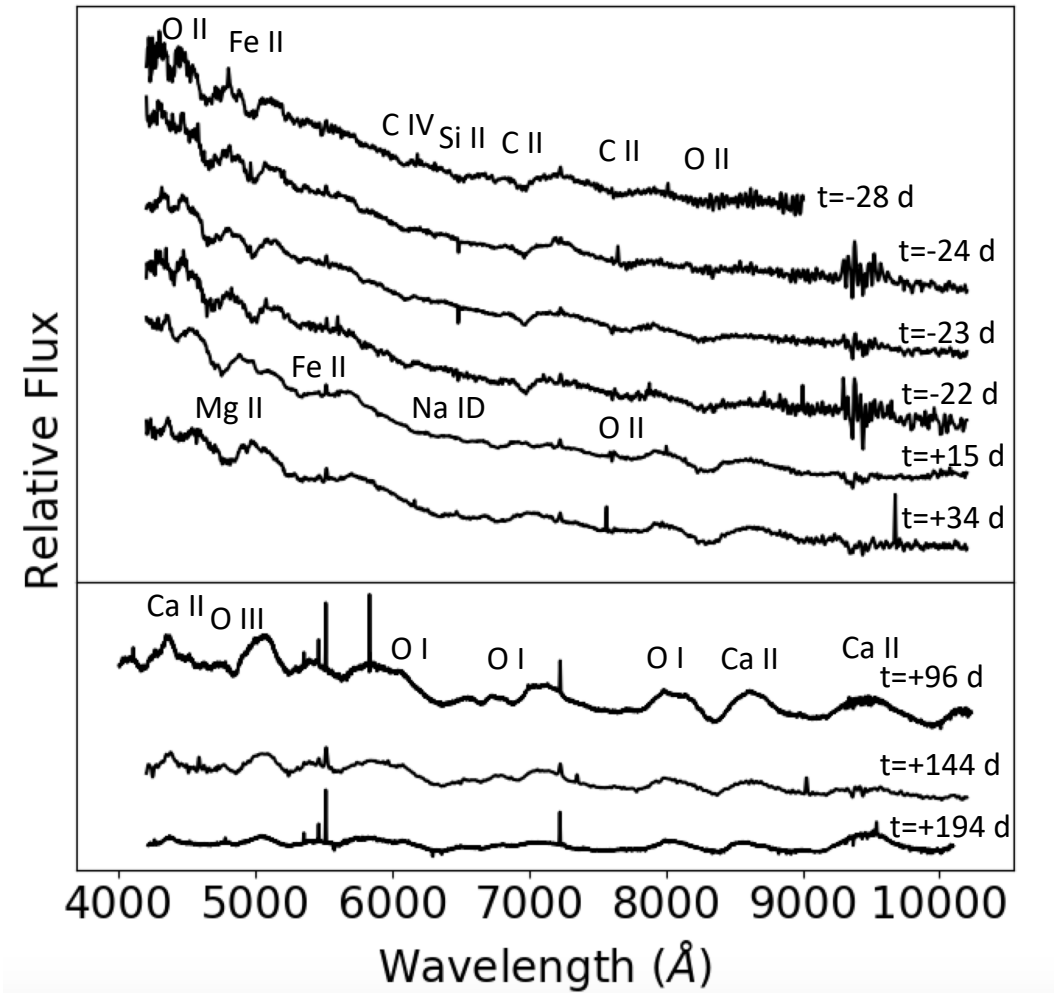

Figure 6.7: The temporal evolution of SN 2010kd optical spectra from $t = -28$ d to $t = +194$ d from peak light. The top plot shows spectra observed during the hotter, photospheric phase and the bottom plot shows spectra observed during the cooler, nebular phase.

During its photospheric phase, SN 2010kd spectra appear to be dominated by the blue continuum, exhibiting temperatures between 10,000 - 20,000 K, obtained by fitting spectra to the Planck blackbody function [91]. The spectra during this phase display prominent intermediate mass features, including O II, C IV, Si II, CII, and O I [91] before B maximum. After B maximum, Mg II, Fe II, and Na I also appear. The appearance of these features is backed up by well fit spectra using the SYNAPPS spectral fitting software [98].

As the supernova expands and cools over time, the ejecta become transparent and the object enters the nebular phase. For SN 2010kd, this occurs much later than typical SNe Ic, due to the massive amount of ejecta involved in a SLSN I [99]. Prominent features during this phase include absorption features due to Ca II, OII, Na I, Fe II, and OIII [91].

Comparisons of SN 2010kd spectra to other SLSNe I spectra indicate that it evolves similarly to other slow decaying SLSNe I. Additionally, comparisons to broad lined, type Ic SNe (SNe Ic-BL) show that it evolves similarly in the nebular phase to these events, with comparable features but with varying intensities [91].

6.2. SNe IIP Cosmology

Although the vast majority of supernova cosmology has happened with the use of SNe Ia as standardizable candles for distance measurements to their host galaxies, SNe IIP have become increasingly popular due to their photospheric properties. As described in Section 1.5.3.2 and performed in Chapter 5, these properties can be applied to EPM to calculate the distance to the host galaxies of CCSNe.

Due to the opacity of the photospheres of SNe IIP during the plateau phase of their light curves, as seen in each plot of Figure 6.8 showing ROTSE photometry that I measured for several ROTSE SNe IIP, this type of core collapse supernova has been used to perform these distance calculations [23] [24] [25] [28]. Applying this method to calculate the distances

to the host galaxies of the entire ROTSE sample of SNe IIP, the Hubble flow of the local universe can be calculated [68].

6.2.1. ROTSE SNe IIP

The ROTSE sample of SNe IIP consists of 12 individual supernovae out to a redshift of $z \sim 0.06$. Table 6.2 shows the list of available SNe IIP in this sample, including their respective host galaxies, redshift, and the number of spectra used for analysis.

6.2.1.1. Photometry

Photometric reduction for the SNe IIP sample is performed as described in Section 4.1. ROTSE magnitudes for this study are calibrated to APASS V magnitudes using the APASS DR9 catalog [73], as opposed to the typical R band calibration. This is done to avoid the strong hydrogen alpha feature in typical SNe IIP spectra and to build consistency with the dilution parameter described in Equation 1.30 [68]. The photometry used for this analysis was performed by Dhungana [68], but Figure 6.8 shows the photometry I used to cross check these results for 4 of the SNe IIP in this sample.

6.2.1.2. Spectroscopy

The majority of spectra obtained for the SNe IIP sample were from the LRS on the HET [41]. For events without available HET spectra, they are obtained from open sources such as WISeREP [70] or the Open Supernova Catalog [71], or from the literature [68]. Table 6.2 includes the number of spectra for each object used in this analysis. HET spectra were reduced using standard spectroscopic reduction techniques [100] [25] [68]. Spectra from the literature and open sources were obtained in fully reduced forms. All spectra were K-corrected and corrected for extinction [68]. Figure 6.9 shows some of the spectral evolution

Table 6.2: ROTSE SNe IIP Sample

Supernova	Host Galaxy	Redshift	Spectra Used
SN 2004gy	NGP9	0.02690 ± 0.00100	1
SN 2005ay	NGC 3938	0.00270 ± 0.00001	3
SN 2006bp	NGC 3953	0.00351 ± 0.00001	4
SN 2006bj	Anonymous	0.03770 ± 0.00100	1
SN 2008bj	MCG +08-22-20	0.01896 ± 0.00011	1
SN 2008gd	SDSS J012044.48+144139.6	0.059096 ± 0.000053	1
SN 2008in	NGC 4303	0.00522 ± 0.00001	3
SN 2009dd	NGC 4088	0.00252 ± 0.00001	3
PTF10gva	SDSS J122355.39+103448.9	0.02753 ± 0.00012	1
SN 2013ab	NGC 5669	0.00456 ± 0.00001	2
SN 2013bu	NGC 7331	0.002722 ± 0.000004	1
SN 2013ej	NGC 0628/M74	0.00219 ± 0.000003	5

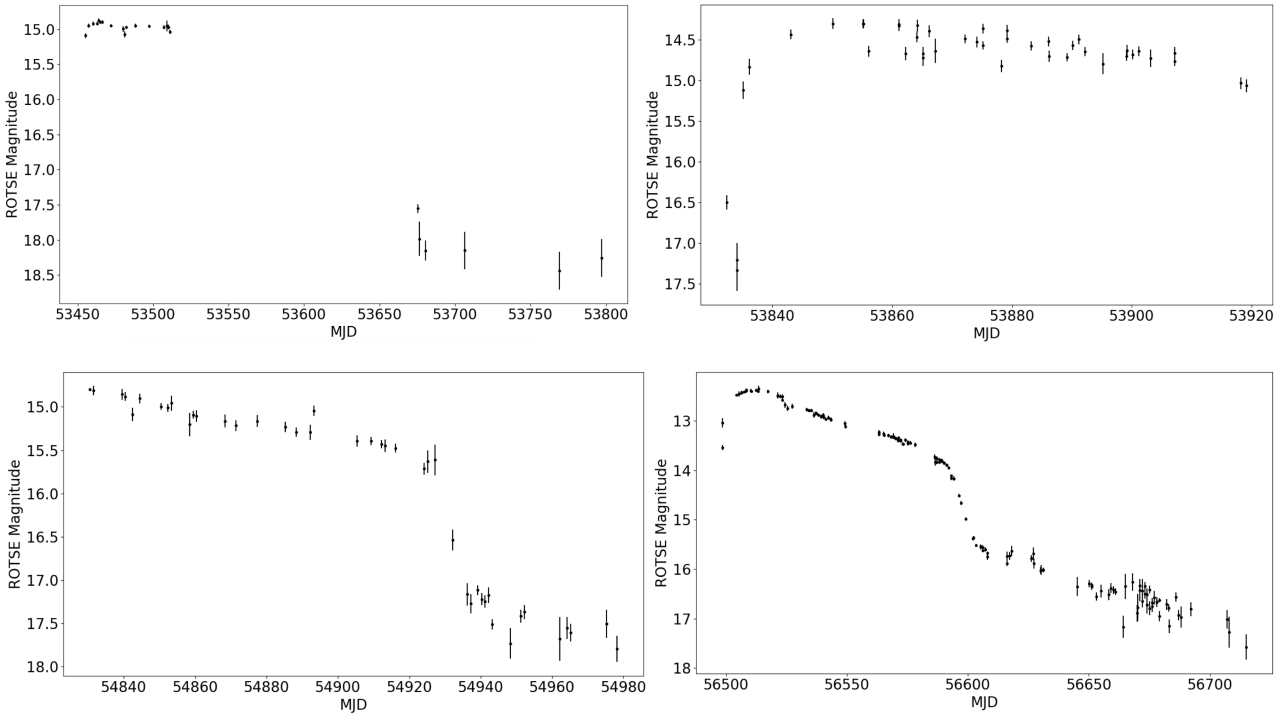

Figure 6.8: ROTSE light curves for 4 SNe IIP. The top left plot shows the light curve for SN 2005ay, the top right plot shows the light curve for SN 2006bp, the bottom left plot shows the light curve for SN 2008in, and the bottom right plot shows the light curve for SN 2013ej.

for the same 4 objects shown in Figure 6.8. The hydrogen and helium features are noted in these plots to show that these objects possess the opaque envelope needed for EPM distance measurements.

6.2.2. EPM Distance Measurements

Using the equations described in Section 1.5.3.2, the distances to the host galaxies of the SNe IIP sample were estimated. The quantities necessary to fulfill this equation are photospheric temperature, photospheric velocity, and bolometric flux. Estimates of the dilution factor are derived using models of SNe IIP atmospheres from Dessart et al. [26].

6.2.2.1. Bolometric Flux

Because many of the objects in this sample lack the necessary photometric observations in the UV, optical, and NIR regions, the effective blackbody flux is derived by convolving the filter response function using

$$b_\lambda(T) = \int_0^\infty R_\lambda(\lambda^{'})\pi B(\lambda^{'}, T)d\lambda^{'}, \tag{6.2}$$

where $R_\lambda(\lambda^{'})$ is the response function and $B(\lambda^{'}, T)$ is the Planck function [68]. While the observed flux is treated as K-corrected flux, the quantity described here, $b_\lambda(T)$, is in the supernova rest frame [68].

6.2.2.2. Temperature Evolution

Temperatures for the SNe IIP sample are derived by fitting the spectral energy distribution (SED) constructed from optical BVI photometry to the Planck function [68]. However, because this information is not abundantly available for all events in this sample, a model

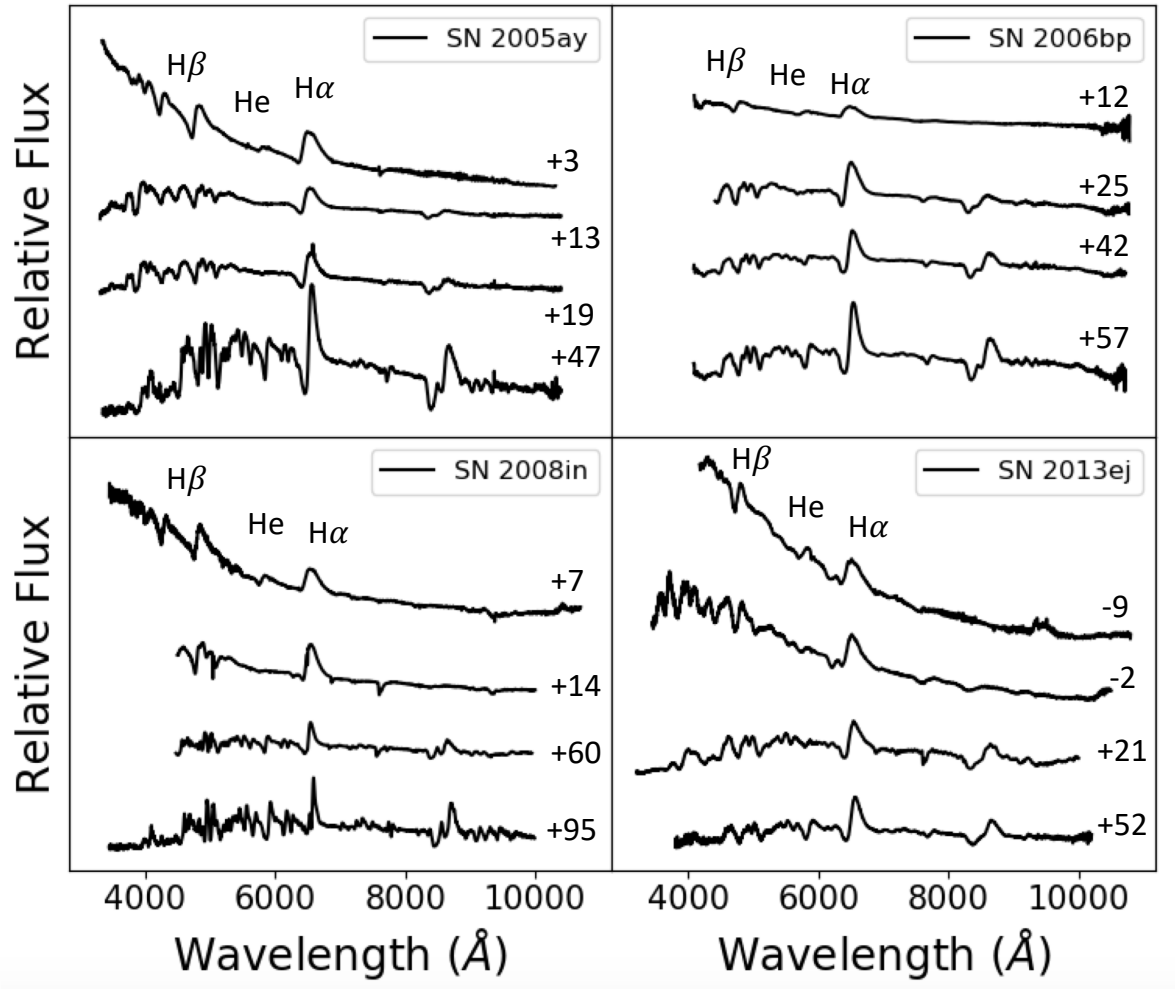

Figure 6.9: Spectral evolution of 4 SNe IIP in the ROTSE sample. The top left plot shows spectra for SN 2005ay, the top right plot shows spectra for SN 2006bp, the bottom left plot shows spectra for SN 2008in, and the bottom right plot shows spectra for SN 2013ej. The numbers next to each spectrum indicate the days before or after peak brightness. The H and He features are noted to show that spectra for these objects possess the opaque outer layer necessary for EPM.

for the temperature evolution is derived using

$$\frac{T(t)}{T(50)} = a + be^{c(\frac{t}{50})}. \tag{6.3}$$

The coefficients in this model are found using the temperature evolution of well observed SNe IIP over a 50 day period during the photospheric phase.

6.2.2.3. Photospheric Velocities

Photospheric velocities for these events were calculated using the profiles of weak chemical features such as the Fe II triplet. When this information is masked or unseen in the spectra, H and He lines can be used to calibrate the effective photospheric velocity, particularly during earlier epochs when the hydrogen envelope surrounding SNe IIP is prominent.

To calculate these velocities, a Gaussian profile is fit to the absorption profile of each feature [68]. Once these are calculated for the available spectroscopic epochs, these values are extrapolated to photospheric epochs using power law models [101]. This allows the photospheric velocities to be found at more epochs, as photometric data are typically more abundant than spectroscopic data for this SNe IIP sample.

6.2.2.4. Distance Measurements

Inserting the information found in the previous three sections into the equations in Section 1.5.3.2, distances were calculated to the host galaxies of the SNe IIP. This information displays a linear relationship, where the slope of the fit represents the distance to the host galaxy, and the intercept represents the time of explosion of the supernova. Table 6.3 shows the results of the fits. The uncertainties shown for the distances and times of explosion in Table 6.3 include both systematic and statistical uncertainties. Systematic errors for the

EPM study include uncertainties due to temperature and velocity modeling, extinction and k-corrections, and time of explosion.

The distance results show that this sample happens to be divided into two groups, where 7 SNe are at a distance of $d < 25$ Mpc and 5 SNe are at a distance of $d > 85$ Mpc. The closest supernova is SN 2013ej at a distance of $8.9 \pm 0.2 \pm 0.2$ Mpc and the farthest supernova is SN 2008gd at a distance of $200.5 \pm 20.5 \pm 50.3$ Mpc.

6.2.3. Low z Hubble Constant

Once distances to the host galaxies are found for the SNe IIP sample, they can be used to calculate the Hubble flow of the local universe out to a redshift of $z \sim 0.06$. For this analysis, I calculate the Hubble constant by fitting $v = H_0 d$ for the derived distances and observed redshifts. However, the effects of peculiar velocities on the observed redshifts can be large for the closer galaxies in this sample, so I first employ a simulation strategy to try and mitigate these effects.

As galaxies recede due to cosmological expansion, recessional velocity is not the only component of each galaxy's total velocity. Due to the gravitational potential of galaxy clusters and superclusters, local motion is also experienced by galaxies, where this excess contribution is called peculiar velocity. While this peculiar motion is negligible compared to the Hubble velocity outside of the local universe, it can vastly affect the observed velocity of galaxies visible to ROTSE-IIIb.

Calculating the peculiar velocity of an individual galaxy requires knowledge of its distance [102]. Because the distances to all host galaxies found by this analysis were derived using total observed velocities, peculiar motion cannot be isolated from recessional motion. A simulation strategy must be used to mitigate this effect when calculating the Hubble constant for this SNe sample.

Table 6.3: SNe IIP EPM Results

Supernova	Distance (Mpc)	t_0 (MJD)
SN 2004gy	$115.5 \pm 7.9 \pm 14.9$	$53360.2 \pm 1.6 \pm 2.5$
SN 2005ay	$21.6 \pm 0.4 \pm 4.1$	$53453.3 \pm 0.4 \pm 4.0$
SN 2006bp	$136.9 \pm 8.2 \pm 38.0$	$53812.7 \pm 1.1 \pm 4.0$
SN 2006bj	$19.4 \pm 0.4 \pm 3.4$	$53834.20.6 \pm 2.0$
SN 2008bj	$89.3 \pm 3.6 \pm 15.8$	$54337.6 \pm 0.8 \pm 2.5$
SN 2008gd	$200.5 \pm 20.5 \pm 50.3$	$54724.1 \pm 2.5 \pm 3.5$
SN 2008in	$15.3 \pm 0.2 \pm 2.9$	$54825.3 \pm 0.4 \pm 2.1$
SN 2009dd	$14.3 \pm 0.3 \pm 1.4$	$54926.7 \pm 0.5 \pm 1.3$
PTF10gva	$148.6 \pm 8.5 \pm 22.5$	$55319.1 \pm 1.5 \pm 0.9$
SN 2013ab	$24.2 \pm 0.5 \pm 2.9$	$56339.1 \pm 0.5 \pm 1.0$
SN 2013bu	$17.0 \pm 0.7 \pm 2.0$	$56401.1 \pm 0.8 \pm 1.0$
SN 2013ej	$8.9 \pm 0.2 \pm 0.2$	$56497.0 \pm 0.4 \pm 0.3$

6.2.3.1. Simulation Strategy

The simulation strategy used here breaks the SNe sample into two groups based on distance. This first group of 7 SNe, where $5 < d < 25$ Mpc, will be largely affected by peculiar velocities, while the second group of 5 SNe, where $85 < d < 205$ Mpc, will not be. To model peculiar velocities, we start by simulating 10,000 sets of 7 galaxies with random distances of 5–30 Mpc to reflect the sample size and distances of the closer SNe data sample and 10,000 sets of 5 galaxies with random distances of 7–260 Mpc to reflect the sample size and distances of the farther SNe data sample. While the entire sample of 12 SNe is located in the very low redshift universe, these two subsamples are deemed "low z" and "high z" to avoid confusion. An example simulation for each sample is shown in Figure 6.10. This process is repeated for input cosmologies of $50 < H_0 < 90$ km/s/Mpc at 5 km/s/Mpc intervals, where the velocity of each galaxy is determined by $v = H_0 d$.

Peculiar motion is modeled for each galaxy by adding a random velocity component from a Gaussian distribution. The results of Graziani et al. [103], which model our lack

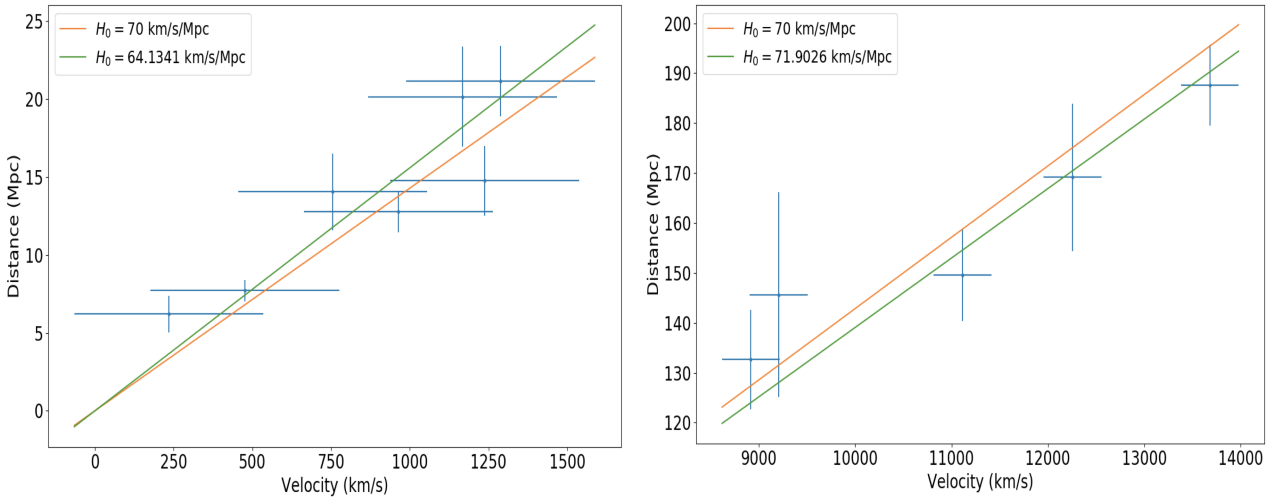

Figure 6.10: Example simulations of the low z, where $5 < d < 25$ Mpc, and high z, where $85 < d < 205$ Mpc, SNe samples. The left plot shows one example of the low z sample and the right plot shows one example of the high z sample. The linear fits shown in each plot represent the initial cosmology, in this case for $H_0 = 70$ km/s/Mpc, and the fit cosmology given the simulated characteristics of each SNe sample.

of knowledge of the non-linear component of the velocity field, show an average value of 280 ± 35 km/s for galaxies out to $z \sim 0.054$. So, we add an additional component to the simulated velocities to reflect this, choosing a random value from a Gaussian distribution centered at 280 km/s, with a standard deviation of 35 km/s. This value is multiplied by a random value between -1 and 1 to reflect the fact that peculiar velocities can be observed at any direction along the line of sight.

Once the distances and velocities for each of the 10,000 pseudo-experiments are simulated, values of H_0 are fit for each set of simulated galaxies. Orthogonal distance regression is used to perform these fits, where errors in distance are chosen to reflect the data sample, and errors in velocity are chosen to be 300 km/s, as is typically used for peculiar velocity errors [104] [105] [106]. After all simulations have been fit for each input value of H_0, the values are averaged so that a calibration can be performed to mitigate the effects of peculiar velocity, where a line is fit to average fit H_0 values vs. true H_0 values. Figure 6.11 shows the difference between fit H_0 values and true H_0 values vs. true H_0 values for the low z and

high z samples before calibration, and the combined sample after calibration. It can be seen in this plot that the mitigation strategy effectively accounts for deviations from the true H_0 values. Table 6.4 explicitly shows this, where the final calibrated slope and intercept are very close to 1 and 0, respectively.

The errors on the H_0 fits are corrected for the pull of the distribution, where a constant is fit to the normalized difference between the RMS of the H_0 values and the average error of the fit vs. the average error of the fit. The simulations are then repeated after applying the calibrations for $H_0 = 60$, 70, and 80 km/s/Mpc to verify the simulation strategy, with the final distributions of the fit H_0 values and associated errors shown in Figure 6.12.

6.2.3.2. Final Calibration of H_0 for the IIP Data Sample

Finally, the low z SNe sample is fit for H_0, with the calibration vectors applied to account for the unknown peculiar motion of the data sample, with the final results shown in Figure 6.13. This process is repeated for the high z SNe sample, also shown in Figure 6.13. The final H_0 value for the low z sample is seen to be 64.6 ± 10.9, while the final H_0 value for the high z sample is seen to be 70.7 ± 5.4. The combined, weighted average of the entire sample yields a final H_0 value of $69.5 \pm 4.8(stat) \pm 0.3(sys)$ km/s/Mpc. With these results, it can be seen that the errors on H_0 are dominated by statistical variations. By including the ROTSE SNe Ib, Ic, and Ib/c samples, I look to improve the statistical error on H_0.

Table 6.4: Fit Parameters for Simulated H_0 values vs. true H_0 values

Sample	Slope	Intercept
Low z (Before Calibration)	1.0008 ± 0.0012	0.0169 ± 0.0863
High z (Before Calibration)	1.0013 ± 0.0011	0.0832 ± 0.0762
Combined (After Calibration)	0.9999 ± 0.0004	0.0055 ± 0.0304

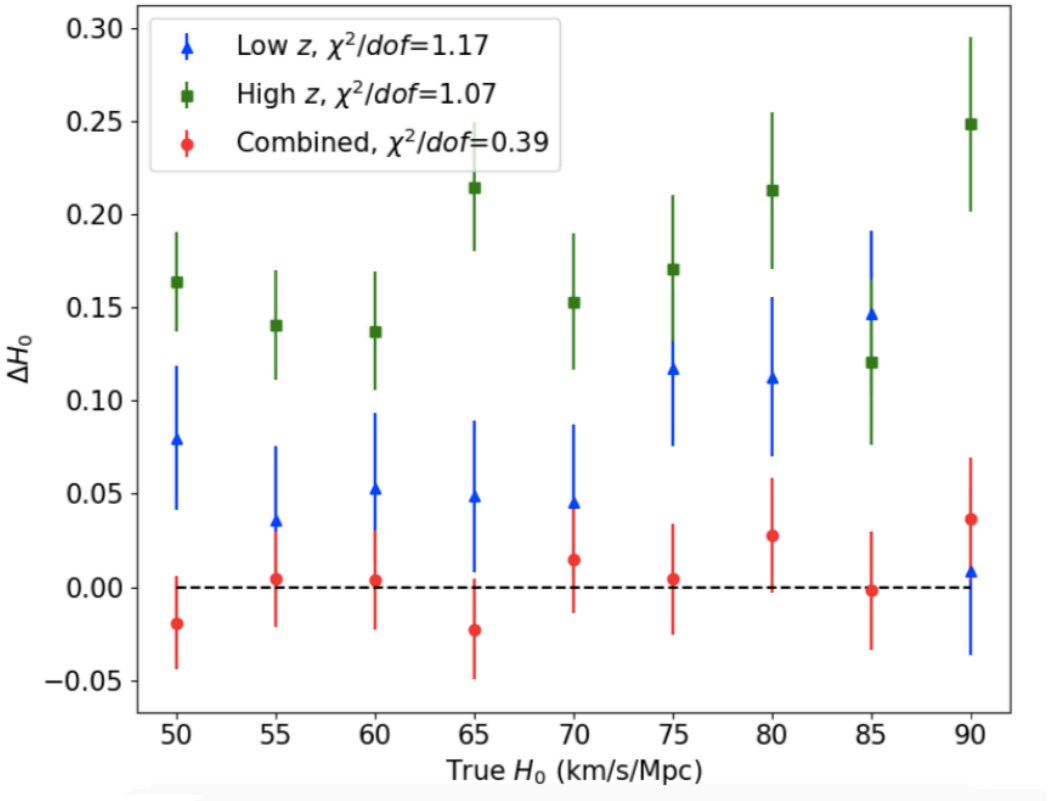

Figure 6.11: Residuals of the average fit H_0 values - true H_0 values before and after calibrating the samples to account for the effects of peculiar motion. The blue triangles represent the low z sample before calibration, the green squares represent the high z sample before calibration, and the red circles represent the combined sample after calibration. It can be seen that while the samples before calibration deviate from $\Delta H_0 = 0$, represented by the dashed black line, the combined sample after calibration falls along the horizontal line of $\Delta H_0 = 0$.

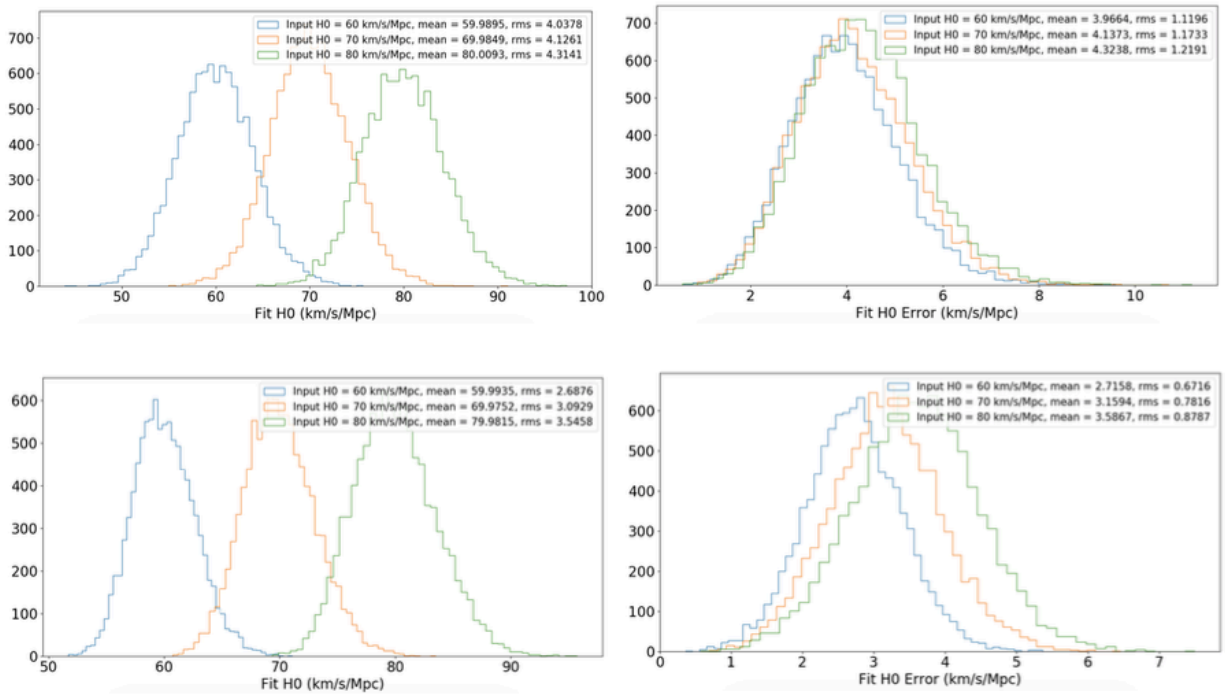

Figure 6.12: The low z and high z H_0 distributions for $H_0 = 60$, 70, and 80 km/s/Mpc after calibration. The top left plot shows the H_0 distributions for low z sample, with the associated H_0 errors shown in the top right plot. The bottom left plot shows the H_0 distributions for high z sample, with the associated H_0 errors shown in the bottom right plot.

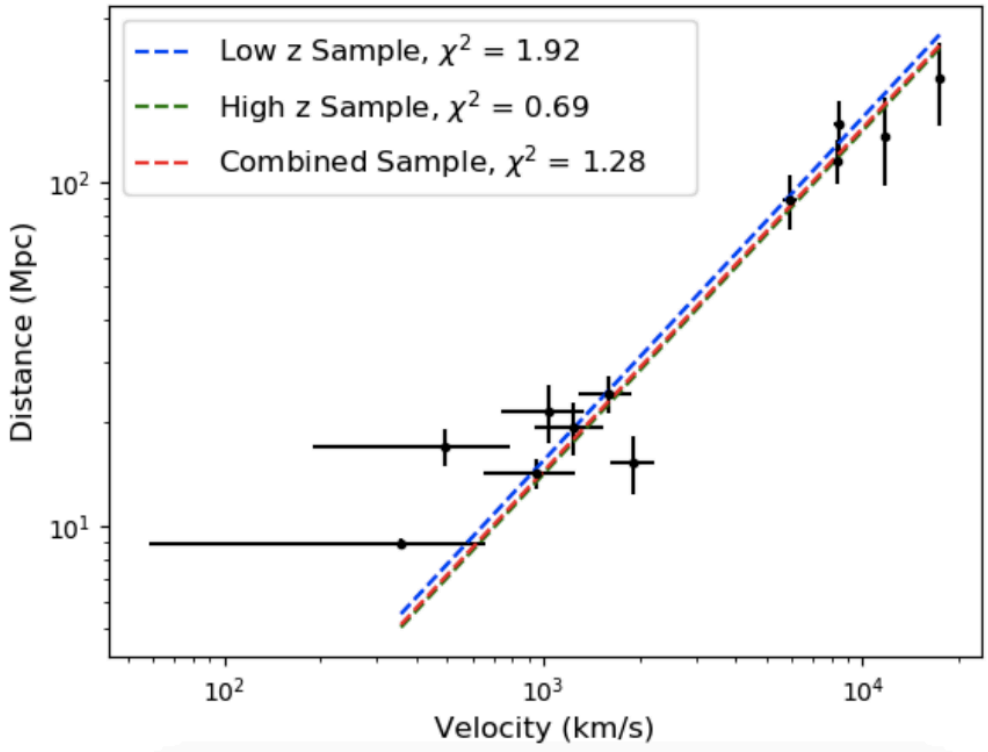

Figure 6.13: The best fit Hubble constant values for the ROTSE SNe IIP sample after correcting for the effects of peculiar velocities. The blue dashed line represents the linear fit of the low z SNe sample, yielding an H_0 value of 64.6 ± 10.9. The green dashed line represents the linear fit of the high z SNe sample, yielding an H_0 value of 70.7 ± 5.4. The red dashed line represents the linear fit of the combined sample, yielding a final H_0 value of $69.5 \pm 4.8(stat) \pm 0.3(sys)$.

Chapter 7

Effects of Radial Observational Systematics on DESI Cosmology

With the discovery of baryon acoustic oscillations (BAO), a new realm of cosmology is now accessible. While the the role of using SNe Ia to constrain dark energy is well known, the observable redshift range of these objects is limited. The ability to measure the BAO feature seen in Figure 1.4 in various bins of redshift out to the farthest observable galaxies reveals the expansion history of the universe, constraining the cosmological parameters used to describe it. Observing this BAO peak requires calculating the two point correlation function (2PCF) defined by Equation 1.32, which requires a precise three-dimensional map of the universe.

DESI will measure the 3-D universe using RA, DEC, and redshift, with redshift providing the radial coordinate of each galaxy. Due to the DESI cosmological error budget of 0.1%, it is necessary for spectroscopic redshift measurements to be extremely accurate. However, many sources of systematic error can potentially hinder these measurements. Here, I focus on the effects of radial observational properties that impact redshift measurements, and ultimately DESI's measure of the BAO feature. These systematics include airmass, seeing, transparency, extinction, and moon conditions, as described by List 4.3 in Section 4.3.

Because this analysis occurs before data collection, simulations such as those described in Section 3.5.3 must be used. For this analysis, I generate a mock galaxy catalog with simulated spectra for more than 25 million objects and five years of simulated exposures. However, the full reduction of even a single DESI exposure can be computationally and temporally expensive. So, I provide a forecast for the entire dark time DESI survey by modeling the redshift efficiency of the offline spectroscopic pipeline to quickly generate a redshift catalog for the full DESI footprint. I pursue a cosmological analysis of this catalog

with and without observational effects to estimate how these systematic properties impact DESI's ability to constrain cosmological parameters, where I focus in particular on H_0.

7.1. Simulation Strategy

In order to generate a simulated redshift catalog, a mock catalog of science targets must first be generated. KPNO observing conditions are modeled so that simulated exposures can be populated with both targets and observational properties. Once fibers are assigned to galaxies, quasars, standard stars, and sky, we use this information in QuickCat, which I have helped to develop and maintain. The methodology is described below, enabling the ability to rapidly generate simulated large scale redshift catalogs in minutes, as opposed to hours or even days.

7.1.1. Generating Science Targets

Generating a mock galaxy catalog requires using an N-body simulation with a given cosmology to populate a simulated universe with dark matter halos and subhalos. Individual targets are generated with RA and DEC, and redshift values with and without the effects of redshift space distortion (RSD) due to the surrounding dark matter halos. Characteristics of science targets acquired from imaging surveys are used to give extragalactic properties to the simulated galaxies and quasars in order to simulate spectra to be inserted into simulated DESI exposures.

7.1.1.1. N-Body Simulation

For this analysis, the Dark Sky N-body simulation is used to essentially generate particles in a box for the DESI dark time survey [107]. The Dark Sky simulations aim to provide an accessible model of the evolution of the large scale structure of the universe by simulating the nonlinear structure formation of galaxy filaments and halos. The data release used

here simulated $10{,}240^3$ particles in a volume spanning 8 Gpc/h across, with observational constraints used as inputs from large scale structure surveys such as Planck, BOSS, and BICEP2 [108]. The cosmology used for simulations in this thesis assumed a matter density of $\Omega_m = 0.295$, with $h = 0.688$, where $h = \frac{H_0}{100 \text{ km/s/Mpc}}$. Particles are given a mass of $3.9 \times 10^{10} h^{-1}$ solar masses, evolving from an initial time of $z = 93$ to present day. These parameters can be varied to simulate different cosmologies to test which cosmology best matches the data, but because DESI has only recently begun to collect data, it is not currently possible to perform this test with DESI data. Figure 7.1 shows a projection of the particle density for a simulated lightcone in the redshift range $0.9 < z < 1.0$.

Particles must be simulated at the halo and subhalo level due to the computational limitations of simulating the time evolution of $10{,}240^3$ particles. To identify halos, the Dark Sky simulations use the ROCKSTAR algorithm which employs an adaptive friends-of-friends halo finding approach in both position and velocity [109] [107]. To populate halos, galaxies are placed in the simulation using a simple time evolving halo occupation distribution (HOD), assuming a spherical, Navarro–Frenk–White (NFW) profile. An HOD describes the bias between galaxies and dark matter by specifying the probability that a given galaxy lies in a given halo and the relative spatial distribution of galaxies and dark matter [110]. The HOD used here is adjusted to match the small scale clustering measured in previous surveys such as SDSS, BOSS, and DEEP2. Using these cosmological inputs, the simulations ultimately output RA, DEC, and redshift containing RSD information for each target.

7.1.1.2. DESI Target Generation

To simulate the morphological properties of the galaxies and quasars, DESI uses the photometric properties such as color and magnitude of the data sample from preliminary surveys such as the MzLS, DECaLS, and BASS surveys described in Section 3.3. These properties are fit to spectral templates per observed Hierarchical Equal Area isoLatitude

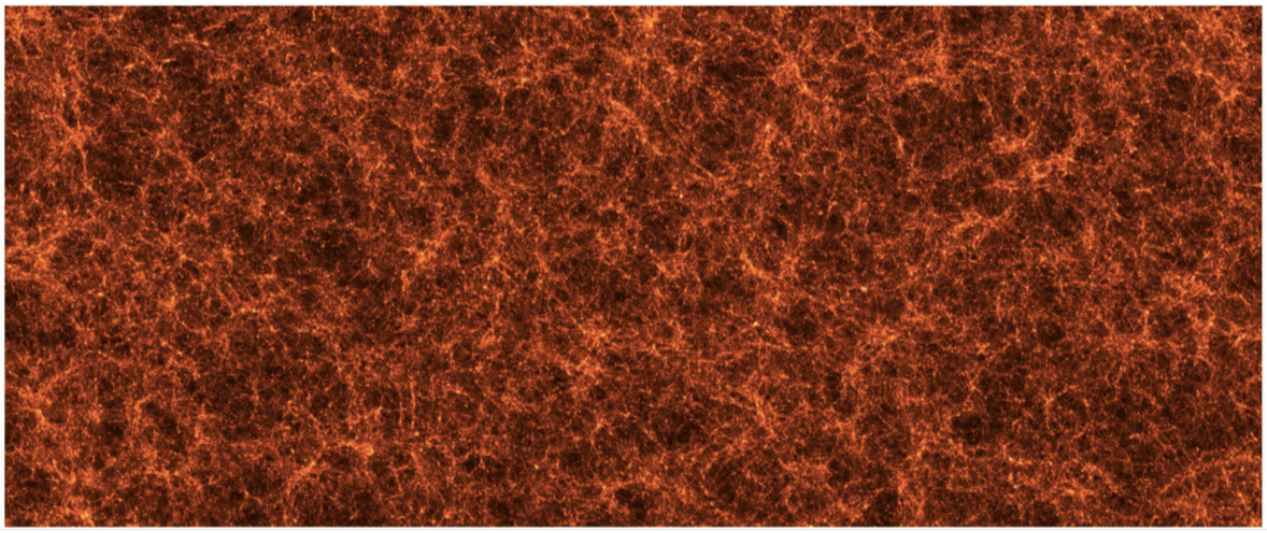

Figure 7.1: The projected mass density of the Dark Sky N-body simulation for a lightcone in the redshift range $0.9 < z < 1.0$ [107]. This image represents 1/10,000 of the total simulation volume.

Pixelization, or healpixel [111], generating a simulated spectrum for each target. Healpixels in this context represent the pixelization of the two-dimensional celestial sphere.

Although the spectra themselves are not needed directly for this analysis, r band flux for LRGs, ELG, and QSOs and OII flux for ELGs are extracted from the spectral features to be used for simulating redshift efficiency. The fully simulated catalog comprises more than 27 million total targets, including more than 20 million ELGs, 4.5 million LRGs, and 2 million QSOs. Figure 7.2 shows the projection of these simulated galaxies and quasars onto the celestial sphere.

7.1.2. Generating Science Exposures

This analysis uses these targets to populate more than 15,000 exposures that will be taken during the 5 year DESI dark time survey, covering more than 14,000 square degrees, as seen in Figure 7.2.

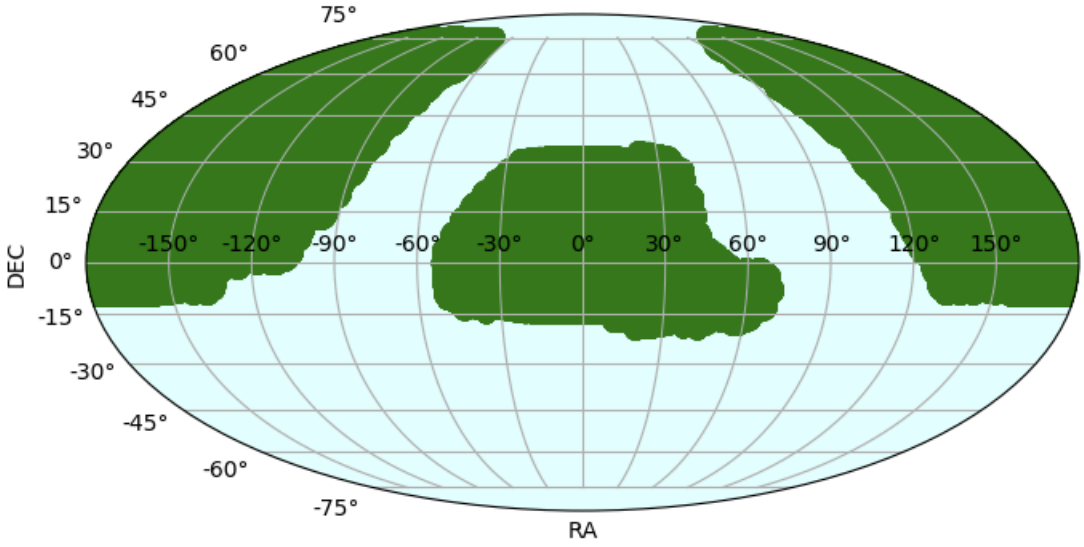

Figure 7.2: The simulated footprint for the 5 year DESI dark time survey shown as the projection of simulated galaxies and quasars on the 2-D celestial sphere with science targets shown in green. This footprint covers approximately 14,000 square degrees, one third of the entire sky.

7.1.2.1. Modeling Observing Conditions

While the full DESI survey will include bright and gray time observations, this analysis is restricted to dark time conditions. Thus, it does not look into the effects of moon conditions on redshift measurements. The observational properties included here are airmass, seeing, transparency, and extinction, similar to previous BOSS analyses [112]. The distributions of these observing conditions for all 15,000 exposures are shown in Figure 7.3.

The exposures are simulated as a sequence of tile observations from December 1, 2019 to November 30, 2024, the originally scheduled survey. The exposures are stochastically simulated with randomly generated weather conditions from previous KPNO observations, taking into account the physical observing conditions as well as the effects of the pressure and temperature of the atmosphere given the latitude, longitude, and elevation of the Mayall telescope.

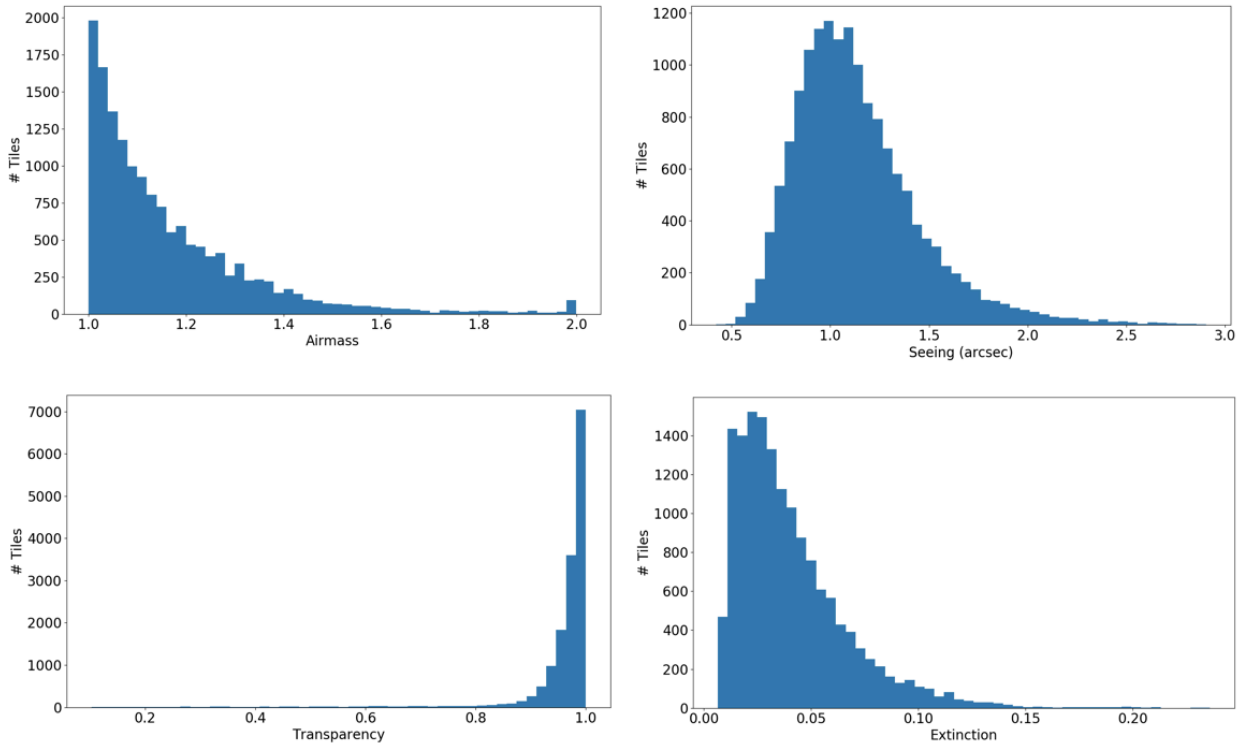

Figure 7.3: The distributions of observing conditions in the set of simulated exposures for this analysis. The top two plots show the distributions of airmass (left) and seeing (right) and the bottom two plots show the distributions of transparency (left) and extinction (right).

7.1.2.2. Fiber Assignment

Given the tile and target locations, as well as observing priorities per target, DESI assigns fibers dynamically to place them on targets accessible to the focal plane of each tile. For every tile to be observed, there are more than 5,000 accessible targets in the focal plane, so observing priorities are used to determine which targets are observed. Additional priorities are based on the number of necessary sky and standard star fibers in the image.

Well designed fiber assignment is a necessity, as the dominant source of target loss is fiber assignment inefficiency [42]. Lower redshift galaxies display higher angular clustering due to their proximity, so LRGs will often have priority during dark time observations. ELGs will also be observed during the gray time survey, so they are often assigned with lower priority

in dark time. Tiles will be observed in 5 passes throughout the entire survey to ensure that the required completeness is met.

7.1.3. Simulating Redshift Catalogs

Once exposures are populated with observing conditions and fiber assigned targets, a 3-D redshift catalog is simulated using the QuickCat software. In order to simulate the redshift measurements and efficiency of a large number of science targets, QuickCat parametrically models the results of the offline reduction pipeline and redshift fitter described in Section 4.2. Using this method, QuickCat is able to account for all of the effects of the detector and data reduction through redshift fitting. The spectroscopic redshifts of less than 100,000 objects can be used to simulate the full DESI footprint rather than having to send all 27 million targets through the spectroscopic pipeline, as a sample of 100,000 objects is more than enough to adequately display the redshift distribution and efficiency of redshift measurements for each target type.

7.1.3.1. Simulating Redshift Measurements

The error on each redshift measurement is defined as

$$z_{error} = \frac{a}{f^b}(1 + z_{true}), \tag{7.1}$$

where z_{true} is the true redshift of the object containing both RSD and Hubble expansion effects, f is the OII flux for ELGs and r band flux for LRGs and QSOs, and a and b are fitted parameters. The fitted parameters are different for each target type, where the models for LRGs, ELGs, and QSOs are shown in Figure 7.4. Using these fits, QuickCat generates redshifts by shifting the true redshift value of each object by a random value from a Gaussian distribution scaled to the redshift error for each target type. More explicitly, the simulated,

or measured, redshift is simply

$$z_{measured} = z_{true} + \epsilon, \tag{7.2}$$

where ϵ is scaled to z_{error}. Due to the fact that QuickCat models the measured DESI redshifts, this simple formalism accounts for all of the effects of the spectrographs and data reduction pipeline, to the extent that deviations are known and Gaussian.

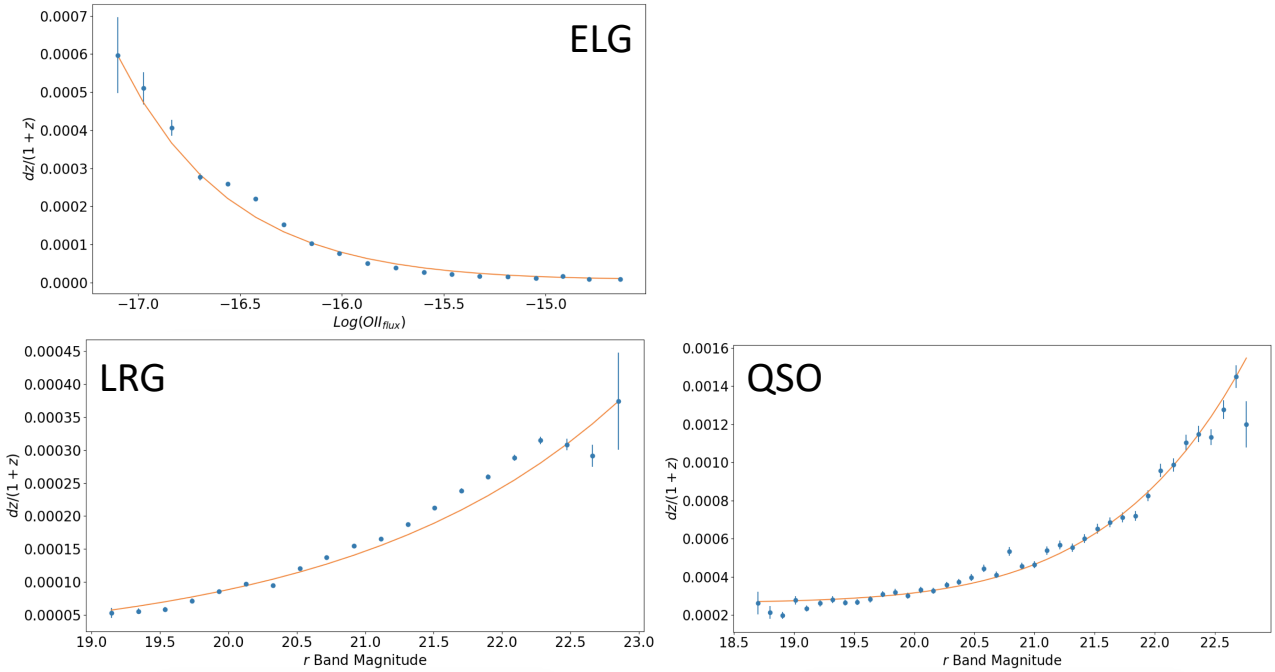

Figure 7.4: Fits of the redshift error vs. r band magnitude for LRGs (bottom left), ELGs (top), and QSOs (bottom right). The parametric fits shown here are used by QuickCat to produce simulated redshift measurements.

7.1.3.2. Simulating Redshift Efficiency

Redshift fit results are simulated by QuickCat by providing a binary value for whether or not a given target has an accurate redshift. The spectroscopic pipeline and redshift fitter may produce an inaccurate outcome such as a missed OII doublet or a misallocated fiber. These are simulated via a binary prescription sufficient to provide an accurate model of redshift efficiency. To provide these binary values, the probability of obtaining an accurate redshift is

modeled for each target type as shown in Figure 7.5. Then, based on the probability for each target, a simple Monte Carlo simulation is performed to determine if the redshift for that target receives a "good" or "bad" value. This is to mimic the redshift efficiency of the offline pipeline, where a "good" redshift represents an accurately fit redshift and a "bad" redshift represents an inaccurate fit. Inaccuracies in redshift fitting can arise due to the inability to find the OII doublet, a misallocated fiber, a broken fiber, etc.

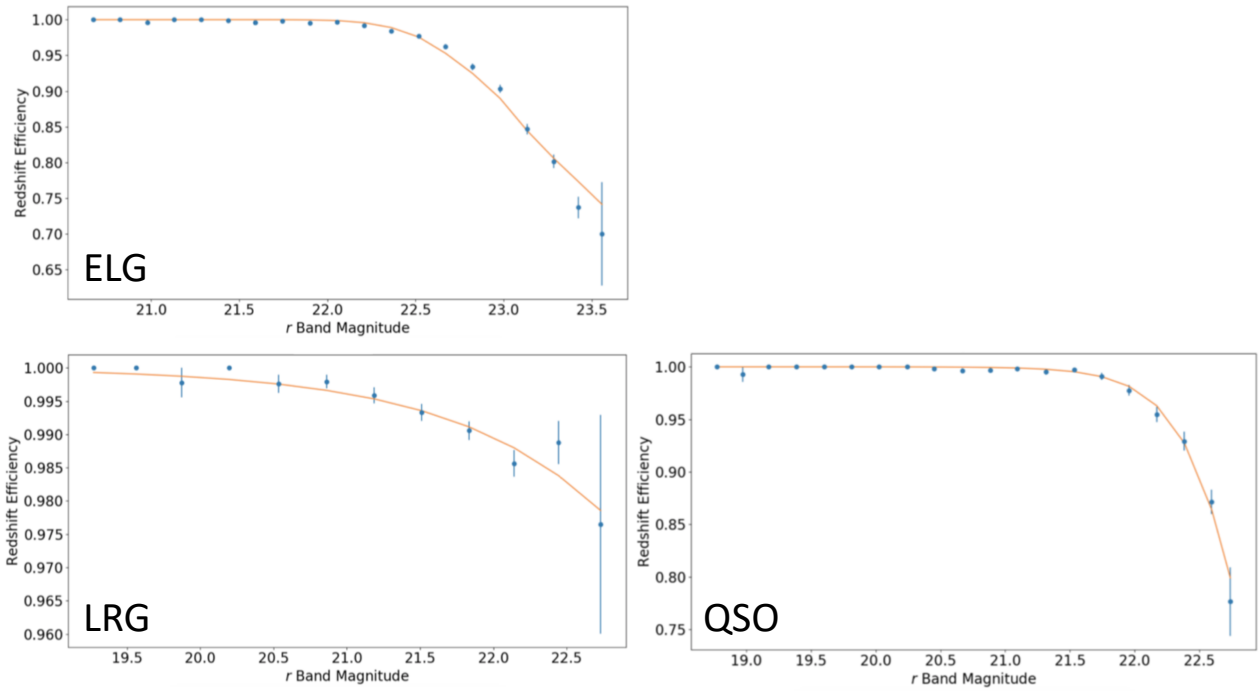

Figure 7.5: Fits of the redshift efficiency vs. r band magnitude for LRGs (bottom left), ELGs (top), and QSOs (bottom right). The parametric fits shown here are used by QuickCat to produce simulated redshift efficiency.

The probability of obtaining an accurate redshift for any target depends on both flux from the target and observing conditions during the exposure. The total probability of obtaining an accurate redshift is therefore

$$P_{total} = P_{target} \times P_{obs}, \tag{7.3}$$

where P_{target} comes from the contribution due to flux and P_{obs} is the contribution due to observing conditions.

For ELGs, we assume that the probability of obtaining an accurate target redshift, P_{ELG} is a function of its SNR in emission lines and the continuum, given by

$$P_{ELG} = \frac{1}{2}\left(1 + erf\left(\frac{SNR}{c\sqrt{2}}\right)\right). \tag{7.4}$$

The coefficient c in this equation is a fitted parameter included in case this probability is not 100% correlated with SNR. The total SNR is defined as

$$SNR = \sqrt{(a \times 7 \times \frac{f_{OII}}{f_{OIIthresh}})^2 + (b \times f_r)^2}, \tag{7.5}$$

where the SNR due to emission lines is approximated using OII flux and the SNR due to the continuum is approximated using r band flux, f_r. The a and b coefficients are fitted parameters representing emission line and continuum normalizations, respectively. DESI aims to achieve an overall SNR of 7 for each ELG after 5 passes are complete, so the $\frac{7}{f_{OIIthresh}}$ seen in Equation 7.5 is a scaling factor representing the number of times above the OII flux threshold a given ELG is, where the OII flux threshold is defined in Figure 7.6.

For LRGs and QSOs, we assume that the probability of obtaining an accurate redshift, P_{LQ} is a function of r band magnitude, given by

$$P_{LQ} = \frac{1}{1 + e^{\frac{m_r - a}{b}}}, \tag{7.6}$$

where m_r is the r band magnitude and a and b are fitted parameters.

The probability due to observing conditions is

$$P_{obs} = \Pi_i p_i + \epsilon, \tag{7.7}$$

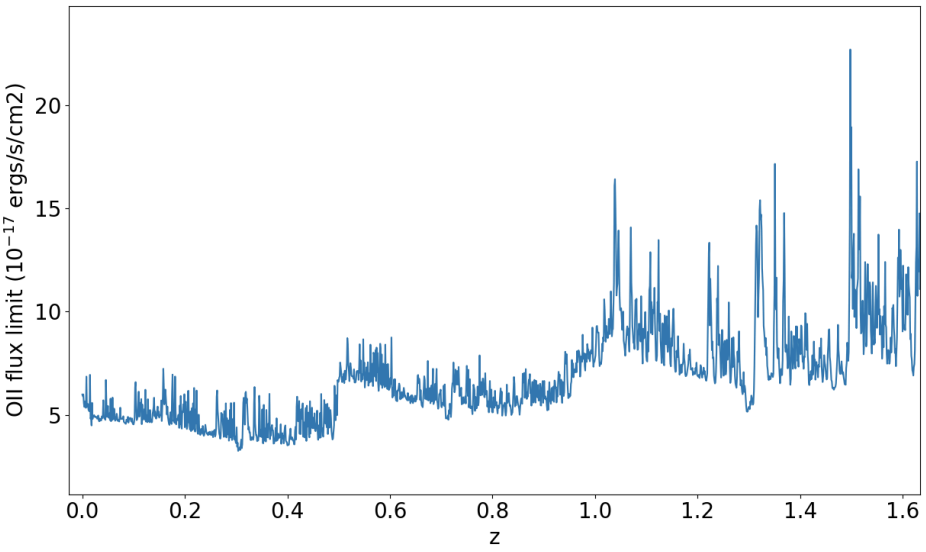

Figure 7.6: The redshift dependency of OII flux required for DESI to obtain an accurate redshift for ELGs.

where p_i is the individual contribution of each observational systematic,

$$p_i = c_0 + c_1 v + c_2(v^2 - \langle v \rangle^2), \tag{7.8}$$

ϵ is a noise term, and the coeffecients c_i are fitted parameters. A random value between 0 and 1 is then assigned to each target. If P_{total} is above this random value, then the redshift measurement for that target is deemed successful. If P_{total} is below the random value, then the redshift measurement is deemed unsuccessful. The simulated redshift efficiency, ε_z, is then defined as the ratio between the number of successful redshift measurements, n_{goodz}, and the total number of objects n_{total}, or

$$\varepsilon_z = \frac{n_{goodz}}{n_{total}}. \tag{7.9}$$

7.2. Redshift Catalogs Under Survey vs. Nominal Conditions

To observe the systematic effects of observing conditions on redshift efficiency, redshift catalogs for the full survey are generated with two different sets of observing conditions. First, a redshift catalog is generated where all exposures are taken under Nominal observing conditions, where values of airmass, seeing, transparency, and extinction are all given values of 1.0. A second redshift catalog is generated under the dark time Survey conditions shown in Figure 7.3.

7.2.1. Simulated Redshift Catalogs

Comparisons of the overall true redshift and simulated redshift distributions for both Nominal and Survey conditions are shown in Figure 7.7. For Nominal and Survey conditions, only redshifts deemed accurate by the binary prescription described at the end of Section 7.1.3.2 are included in order to show the effects of observing conditions and the spectrograph on the overall measured redshift distributions. To zeroth order, the closer the measured redshift distributions are to the true redshifts, the higher the redshift efficiency. It can be seen in these histograms that for LRGs and QSOs, the redshift distributions are all quite similar, while the ELG redshift distributions for Nominal and Survey conditions are lower than the true redshift distribution. The important point for this analysis, however, is that for all target types the correlation between Nominal and Survey conditions is high.

Figure 7.8 provides the correlation between measured redshifts under Survey conditions, $z_{measured}$, and true redshifts, z_{true}, in the top row, and the correlation between redshifts under Survey conditions and Nominal conditions in the bottom row. Extreme deviations from the diagonal in these plots represent redshift measurements deemed catastrophic failures.

Table 7.1 shows the overall redshift efficiencies for each target type under Nominal and Survey conditions. For all target types, the cumulative efficiencies are very similar under

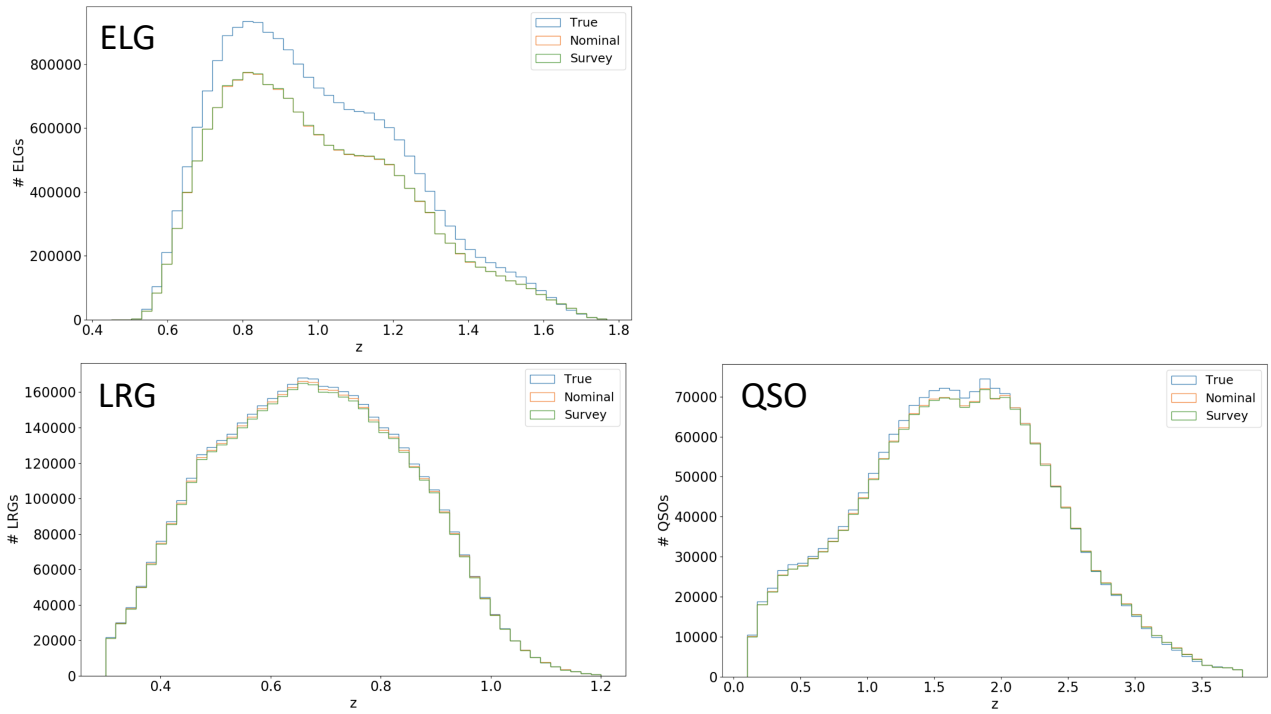

Figure 7.7: The simulated redshift distributions of the 5 year DESI dark time survey for ELGs (top), LRGs, (bottom left), and QSOs (bottom right). The histograms show the distributions of true redshifts, redshifts under Nominal conditions, and redshifts under Survey conditions.

both Nominal and Survey conditions. LRGs and QSOs exhibit high redshift efficiency, close to 100% for the entire dark time survey. ELG redshift efficiency is much lower than LRGs and QSOs, reflecting the lower spectral fitting efficiency of the spectroscopic pipeline for ELGs in the simulated sample used for this analysis.

Table 7.1: Redshift Efficiency for DESI dark time Science Targets

Target Type	Redshift Efficiency (Nominal)	Redshift Efficiency (Survey)
LRGs	98.9%	98.2%
ELGs	81.4%	81.5%
QSOs	98.4%	98.0%
All	85.5%	85.4%

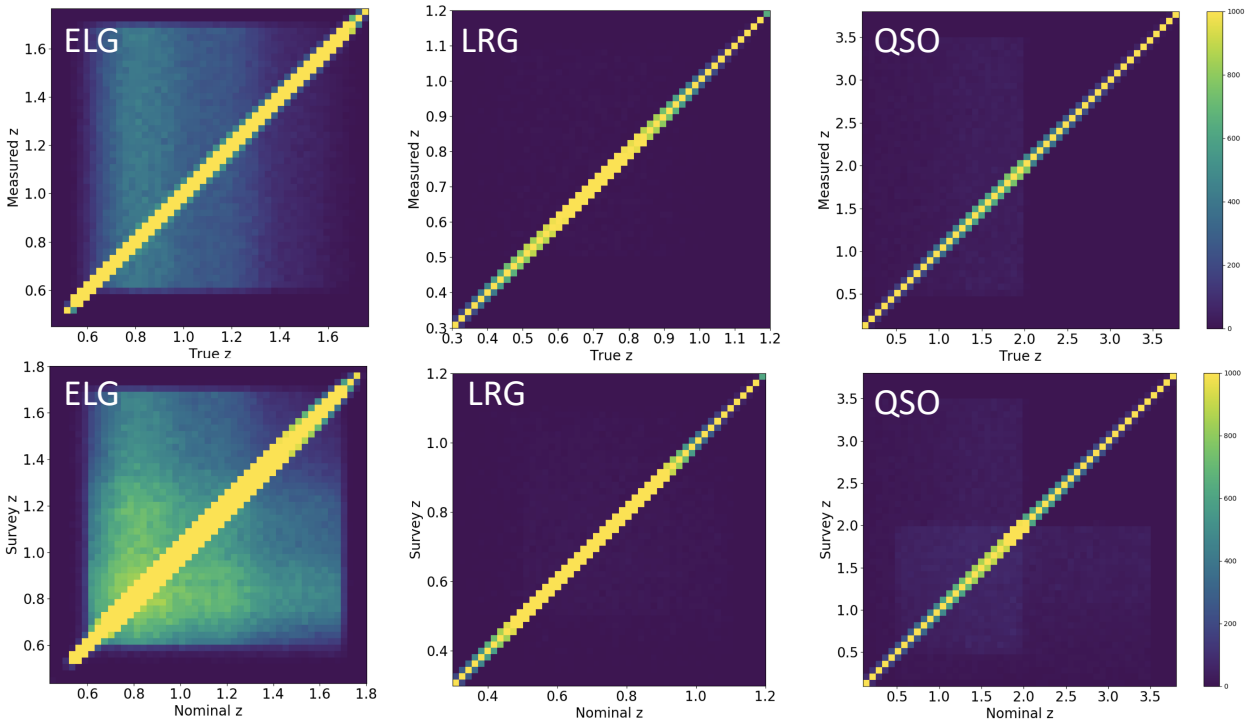

Figure 7.8: The top plots show redshifts under Survey conditions vs. true redshifts for ELGs (left), LRGs (middle), and QSOs (right). The bottom plots show redshifts under Survey conditions vs. Nominal conditions for ELGs (left), LRGs (middle), and QSOs (right).

7.2.2. Effects of Individual Observing Conditions

Previous experiments such as DES and BOSS can be largely affected by observing conditions [113] [112]. With a fixed exposure time, poor weather conditions can have a significant impact on the ability to resolve spectroscopic features, particularly affecting higher redshift objects. In discrete redshift bins, number densities of galaxies are seen to be highly impacted by observational parameters. This can subsequently affect cosmological measurements as the pair counts needed to calculate the 2PCF become biased with changing galaxy densities.

The ETC is DESI's attempt to mitigate these biases and obtain a higher completeness of redshift measurements, interacting with the instrument control system described in Chapter 2. To examine the effects of individual observing conditions on redshift efficiency for DESI, I take the ratio of accurate redshifts and total objects for each target type as described in

Equation 7.9, binned in values of airmass, seeing, transparency and extinction. Figure 7.9 indicates the dependence of redshift efficiencies on each of these properties.

Airmass has the highest impact on ε_z for LRGs and ELGs. However, QSOs are significantly impacted by seeing, while LRGs and ELGs are not. These affects could potentially be explained by the brightness of QSOs compared to LRGs and ELGs being less affected by airmass, while their point like stellar appearance becomes more affected by seeing and degradation of the PSF. Transparency has a negligible effect on LRGs and QSOs, with significant impact on ELGs. Extinction has the smallest effect on all target types, but even deviations of $< 5\%$ impact the overall completeness of the redshift catalog.

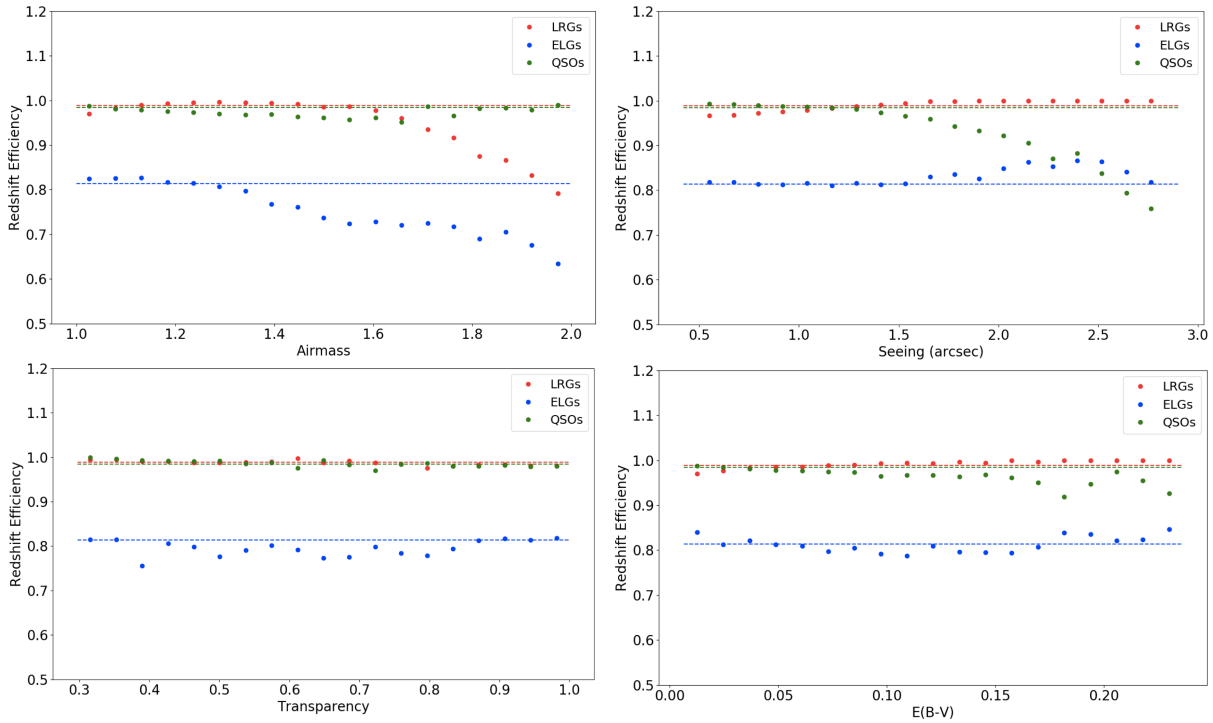

Figure 7.9: Redshift efficiency after utilization of the ETC vs. airmass (top left), seeing (top right), transparency (bottom left), and extinction (bottom right) for all target types. LRGs are shown in red, ELGs are shown in blue, and QSOs are shown in green. The corresponding dashed lines represent the redshift efficiency of each target type during Nominal conditions.

These results show that the models used by the ETC adequately compensate for transparency and extinction in LRGs, but not ELGs and QSOs. Airmass and seeing have a

significant impact on all target types. Although the effects of these conditions on imaging quality are to an extent intertwined and not fully separable, the models used by the ETC describe the effects of each condition individually. While more sophisticated models may be needed to fully compensate for the deviations from nominal observing conditions seen in Figure 7.9, the impact of these effects may also be due to the fact that simulations, rather than data, are used for this analysis. DESI has only recently begun data collection. A more complete catalog will allow QuickCat to model data rather than simulations. Not only will this provide a more realistic forecast of the DESI survey, but also a means of testing various cosmological models against DESI spectroscopic observations and redshift measurements. With the current implementation, QuickCat has the capability of examining the effectiveness of the ETC and the ability for DESI spectroscopic simulations to produce cosmological results, without having to spectroscopically simulate the entire survey.

7.3. Clustering Measurements

To quantify correlations in the spatial distribution of galaxies and quasars, we use the Landy-Szalay estimator described in Chapter 1 to calculate the 2PCF, expressed as

$$\xi(r) = 1 + \left(\frac{N_r}{N}\right)^2 \frac{DD(r)}{RR(r)} - 2\left(\frac{N_r}{N}\right)\frac{DR(r)}{RR(r)}, \tag{7.10}$$

where N_r is the number of random data points and N is the number of data points. This requires finding the correlation between data and random catalogs. Figure 1.5 shows an expanded view of the data and random catalogs, where distances between adjacent points are used to determine the clustering of galaxies by measuring the excess probability in data of finding pairs separated by a given distance.

For this analysis, I use the Corrfunc software to measure the 2PCF. Corrfunc is a suite of high performance clustering routines with the ability to compute the Landy-Szalay calculations for spatial correlation functions in a Cartesian geometry necessary for this analysis [114].

The correlation function presented here is in real space, not redshift space, necessitating distance calculations to the extragalactic sources in the sample. The distances to these sources are outside of the local universe, so a cosmological model must be used. The Planck results are used here, where $\Omega_m = 0.308 \pm 0.012$ and $H_0 = 67.8 \pm 0.9$ km/s/Mpc [115]. This process is repeated for each target type under both Survey and Nominal conditions to compare the BAO feature in both cases. Errors on the correlation function are approximated using the prescription of Peebles et al. [87] [116].

Once the 2PCF has been calculated, it must be fit to examine where the BAO feature is actually observed. To fit the 2PCF feature, I use

$$\xi(r) = \left(\frac{r}{r_0}\right)^{-\gamma} + \frac{N}{\sqrt{2\sigma^2}} e^{-\frac{(r-r_m)^2}{2\sigma^2}} + \frac{a_1}{r^2} + \frac{a_2}{r} + a_3, \tag{7.11}$$

where r_0 and γ account for the power law distribution seen in the correlation function, and N, σ, and r_m are parameters of the Gaussian fit of the BAO feature. The parameter r_m indicates the mean of the Gaussian, which is used as the estimation of the location of the BAO feature. The final three terms include nuisance parameters a_1, a_2, and a_3 that help to marginalize the underlying signal in the correlation function [117].

In order to better find the BAO feature, an optimization of the fitting strategy was performed to best isolate the 2PCF distribution due to non-BAO clustering. This was done by first fitting the low r region to a power law over an optimal range of points given the χ^2/dof of the fits. The same process was repeated for the high r region by fitting these points to a second degree polynomial. The results of both of these fits were then provided as initial conditions to fit the full 2PCF distribution, excluding the BAO region. Upon fitting this distribution, the fitted parameters were applied to Equation 1.1, so that the final fit only involved fitting a Gaussian profile to the BAO feature. Figure 7.10 shows this process for a single ELG fit. It is worth noting that the small χ^2/dof values are due to the limited

number of points being fit. This process was applied to each target type for all redshift bins under both Nominal and Survey conditions. The blue points and blue dashed line show the power law fit to the low r region, and the green points and green dashed line show the quadratic fit to the high r region. The red dashed line shows the full fit of the background. Using this strategy, the following sections show the results of the Gaussian fit of the BAO feature.

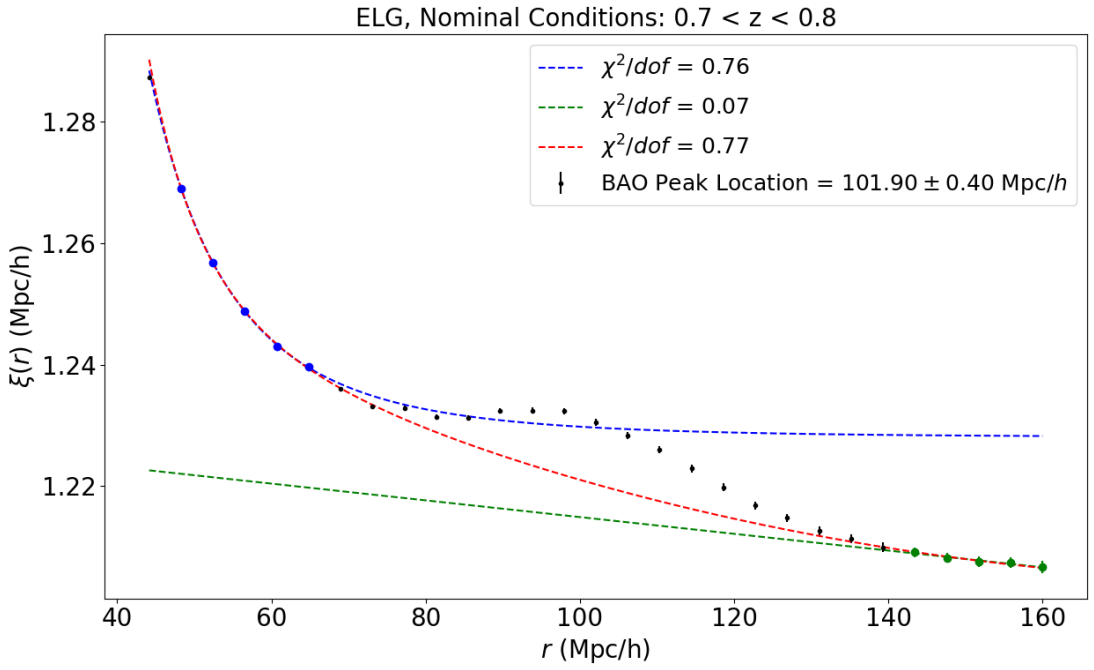

Figure 7.10: An example fit of the ELG 2PCF distribution excluding the BAO region for $0.7 < z < 0.8$ under Nominal conditions. The blue points and blue dashed line show the power law fit to the low r region, the green points and green dashed line show the quadratic fit to the high r region, and the red dashed line shows the full fit of the 2PCF without BAO. These fits are then applied to the fit of the 2PCF including the BAO region as seen in the following sections.

7.3.1. LRG Clustering Measurements

Figures 7.14 and 7.15 show the 2PCF for LRGs over a redshift range of $0.3 < z < 0.9$ in bins of $\Delta z = 0.1$ for both Nominal and Survey conditions. The BAO feature is clearly seen in both samples. Table 1.1 shows the results of fitting a Gaussian profile to the BAO feature of both samples where it can be seen that the difference between the location of the BAO peak is consistently low. The high χ^2/dof values for the redshift range $0.3 < z < 0.4$ can be attributed to the atypical 2PCF measurements for this distribution of LRGs. With a minimal BAO feature, Equation 1.1 cannot accurately find the BAO peak, leading to a poor fit of the 2PCF. This indicates that an alternative BAO fitting strategy may be necessary to accurately measure BAO for this distribution, such as a template fitting strategy of the power spectrum that can then be applied to the 2PCF through a Fourier transform [117].

Table 7.2: LRG Two point Correlation Function Results

Redshift Range	BAO Peak (Mpc/h) (Nominal)	χ^2/dof	BAO Peak (Mpc/h) (Survey)	χ^2/dof
$0.3 < z < 0.4$	107.20 ± 0.36	41.76	107.16 ± 0.36	26.92
$0.4 < z < 0.5$	109.24 ± 0.51	3.56	108.59 ± 0.40	3.21
$0.5 < z < 0.6$	105.98 ± 0.36	2.20	106.26 ± 0.40	2.24
$0.6 < z < 0.7$	108.27 ± 0.65	4.63	108.56 ± 0.68	2.94
$0.7 < z < 0.8$	104.54 ± 0.48	4.38	104.54 ± 0.51	4.59
$0.8 < z < 0.9$	104.29 ± 0.89	1.30	103.30 ± 0.71	2.49

7.3.2. ELG Clustering Measurements

Figures 7.16 and 7.17 show the 2PCF for ELGs over a redshift range of $0.7 < z < 1.5$. The BAO feature is prominent for both of these samples due to the high statistics given the large number of ELGs in this redshift range. Table 1.2 shows the results of fitting the BAO feature of both ELG samples. These results show that for both Nominal and Survey conditions, the BAO feature is found at approximately the same distance scale. The high

χ^2/dof values for the redshift ranges $1.3 < z < 1.4$ and $1.4 < z < 1.5$ can be attributed a lack of BAO feature and noisy BAO feature, respectively. Similar to the $0.3 < z < 0.4$ range for LRGs, these values indicate the potential necessity for an alternative BAO fitting approach.

Table 7.3: ELG Two point Correlation Function Results

Redshift Range	BAO Peak (Mpc/h) (Nominal)	χ^2/dof	BAO Peak (Mpc/h) (Survey)	χ^2/dof
$0.7 < z < 0.8$	101.43 ± 0.41	2.90	101.74 ± 0.41	2.28
$0.8 < z < 0.9$	105.30 ± 0.55	1.28	105.49 ± 0.65	1.47
$0.9 < z < 1.0$	104.58 ± 0.45	1.34	104.80 ± 0.46	1.43
$1.0 < z < 1.1$	107.55 ± 0.58	2.99	108.13 ± 0.56	2.71
$1.1 < z < 1.2$	112.80 ± 1.13	3.66	112.76 ± 1.05	3.34
$1.2 < z < 1.3$	104.14 ± 0.57	9.03	103.26 ± 0.66	5.63
$1.3 < z < 1.4$	104.57 ± 1.56	22.28	96.86 ± 1.10	11.21
$1.4 < z < 1.5$	102.94 ± 0.66	17.25	105.56 ± 0.89	21.61

7.3.3. QSO Clustering Measurements

Figures 7.18 and 7.19 show the 2PCF for QSOs over a redshift range of $1.5 < z < 2.5$ in bins of $\Delta z = 0.5$. A coarser redshift binning is necessary for QSOs due to the decreased number of targets. While the total QSO sample is comprised of approximately 2 million targets, it is spread over a redshift range of $0 < z < 3.5$, making the density of these targets very low compared to the LRG and ELG samples. This accounts for the noisy BAO feature seen in the Nominal and Survey samples. Table 1.3 shows the results of fitting the BAO feature of both QSO samples. Although there are only two redshift ranges that yield a prominent BAO feature, it can still be seen that the BAO peak is found at a similar distance scale for both samples.

These results are promising for the DESI dark time survey. The results shown here are similar to the results of BOSS, which consistently show this peak at $\sim$105 Mpc/h [118] [112].

Table 7.4: QSO Two point Correlation Function Results

Redshift Range	BAO Peak (Mpc/h) (Nominal)	χ^2/dof	BAO Peak (Mpc/h) (Survey)	χ^2/dof
$1.5 < z < 2.0$	102.65 ± 1.16	4.25	102.80 ± 1.53	1.90
$2.0 < z < 2.5$	106.88 ± 1.70	2.10	103.96 ± 1.44	8.66

Overall, the difference between this location for Nominal and Survey conditions is low. The LRG and ELG results are particularly promising, with measurements of the BAO feature over a large redshift range. Overall, the ability to perform cosmological analysis on these results is clear. Once DESI begins collecting data, this prescription will provide a valid means of forecasting DESI cosmology. Updated models to reflect the spectroscopic data will not only allow the further mitigation of observational systematics, but also the test of which cosmology best matches the observed universe.

This strategy shows that BAO can be consistently measured for all target types over multiple redshift ranges. However, this section only applies to a single mock catalog. For a full cosmological analysis, many mock catalogs are needed to isolate any systematic effect due to observing conditions and completely eliminate any statistical variance [117].

7.4. Effects of Observing Conditions on DESI Cosmology

The same 2PCF and fitting strategies are applied to examine the effects of observing conditions on the ability to extract cosmological parameters from DESI observations. Here, I focus in particular on measurement of the sound horizon, r_d, which represents the physical distance of the BAO scale at the time of recombination after the baryon drag epoch. Due to the limited statistics of the QSO sample and the computational requirements of generating many ELG samples, I focus this study on LRGs.

7.4.1. Measurement of the Sound Horizon

In order to determine whether there is any systematic bias in the measurement of r_d, I generate 200 mock LRG catalogs over 4,000 square degrees of sky. For a straightforward approach, I focus on a single redshift bin ($0.7 < z < 0.8$) with high LRG statistics. The increased number of mock catalogs attempts to reduce any statistical fluctuations that may be obscure comparison of r_d measurements under Survey vs. Nominal conditions. Shown in Table 7.5, the average fit peak BAO value for the ensemble of 200 mock catalogs is 104.40 ± 0.06 under Nominal conditions and 104.37 ± 0.06 under Survey conditions, where the errors are given by $\sigma = RMS/\sqrt{n}$ for each distribution. The average difference of Survey measurements - Nominal measurements is -0.04 Mpc/h. Figure 7.11 shows these distributions and the distributions of the associated estimated statistical errors on the BAO fits. Figures 7.20 and 7.21 show some example fits from the Nominal and Survey samples, respectively.

Table 7.5: LRG BAO Peak Measurements ($0.7 < z < 0.8$)

Observing Conditions	Mean (Mpc/h)	Median (Mpc/h)	RMS (Mpc/h)
Nominal	104.40	104.43	0.87
Survey	104.37	104.29	0.86

Once the BAO feature has been fit, r_d can be calculated using

$$r_d = \frac{r_{measured}}{h}, \tag{7.12}$$

where $r_{measured}$ is the measured BAO peak value coming from the fit and $h = 0.6774$ for the cosmology used here. Shown in Table 7.6, the median value of r_d is 154.12 ± 0.09 Mpc under Nominal conditions and 154.07 ± 0.09 under Survey conditions, where the errors are given by $\sigma = RMS/\sqrt{n}$ for each distribution. Figure 7.12 shows these distributions.

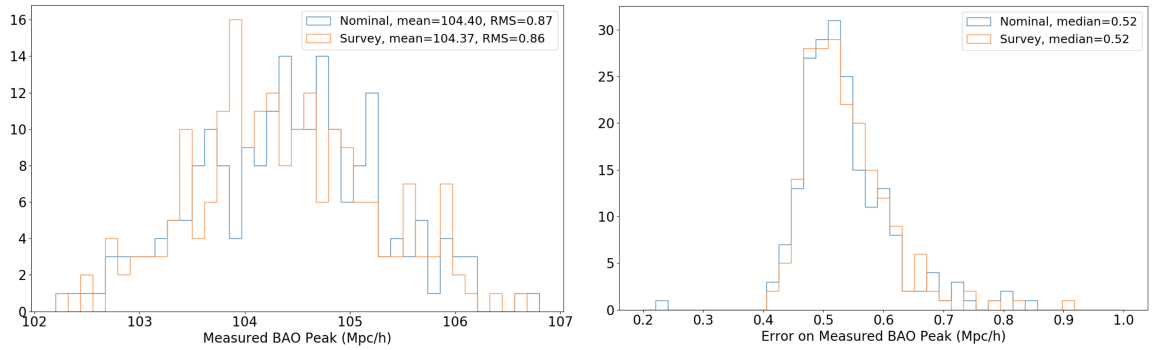

Figure 7.11: The left plot shows the distributions of the BAO peak measurements for the 200 mock LRG catalogs under Nominal and Survey conditions. The right plot shows the respective statistical errors on the BAO fits.

Table 7.6: LRG Sound Horizon Measurements ($0.7 < z < 0.8$)

Observing Conditions	Mean r_d (Mpc)
Nominal	154.12 ± 0.09
Survey	154.07 ± 0.09

7.4.2. Systematic Effect of Observing Conditions

The results of the previous section indicate a small, yet likely statistically significant, difference in measured r_d values under Nominal and Survey conditions. Figure 7.13 compares Survey and Nominal sound horizon measurements, with the left plot showing the measurements for each mock catalog and the right plot showing the difference between Survey and Nominal measurements. Overall, measured values for each mock catalog for each sample yield similar results. However, even a slight shift in r_d can produce different observed cosmologies. Although statistical variation becomes increasingly smaller with an increased number of mock catalogs, this strategy should provide a measurement of the systematic uncertainty. The results in Table 7.6 indicate a systematic error on r_d of -0.05 Mpc. The correlation coefficient between these two samples is 0.74. Using this, the error on the difference between

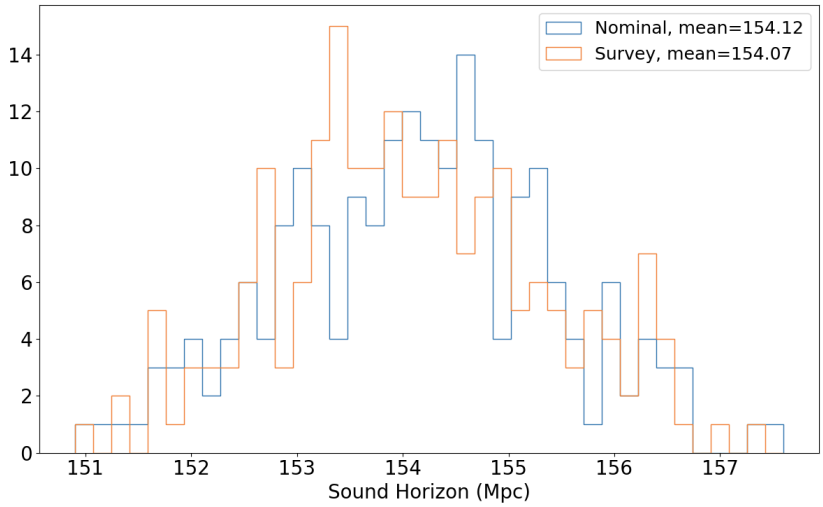

Figure 7.12: Distributions of the measured sound horizon, r_d, for the 200 mock LRG catalogs under Nominal and Survey conditions

the two means is 0.10. This does indicate the necessity for an increased number of mock catalogs to alleviate statistical error, but a systematic shift is seen nonetheless.

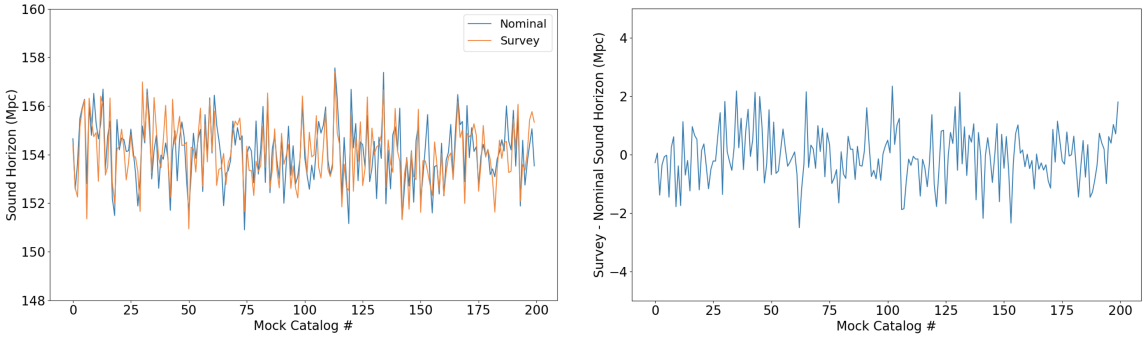

Figure 7.13: The left plot shows Nominal and Survey sound horizon measurements for each of the 200 mock catalogs. The right plot shows the difference between Survey and Nominal measurements for each mock catalog.

Using $cz = H(z)r_d$, a shift of -0.05 Mpc on r_d could propagate to an uncertainty on extracting the Hubble parameter $H(z)$ at the time of recombination of approximately 0.02 km/s/Mpc. This amounts to a fractional error on the order of 0.03%. Based on the DESI

systematic error budget due to the instrument and observational effects of 0.26% on $H(z)$ [131], this result is within that allowance. Given the discrepancies between current values of measured H_0, where $H_0 = 73.24 \pm 1.74$ km/s/Mpc using Type Ia SNe [119] and $H_0 = 67.66 \pm 0.42$ km/s/Mpc using CMB measurements [8], this is a promising result. This indicates that DESI will in fact be able to shed light on the H_0 controversy, assuming the error on measuring $H(z)$ at recombination is proportional to that on measuring H_0.

While this strategy only examines a single dark time target type, these results show that observing conditions should ultimately have little effect on DESI cosmology with respect to LRGs. This indicates effective use of the exposure time calculator, which appears to adequately mitigate the effects of observing conditions. At such an early state, this is promising for DESI as the observing strategy will only continue to improve throughout the entirety of the survey.

7.5. LRG, ELG, and QSO BAO Fits

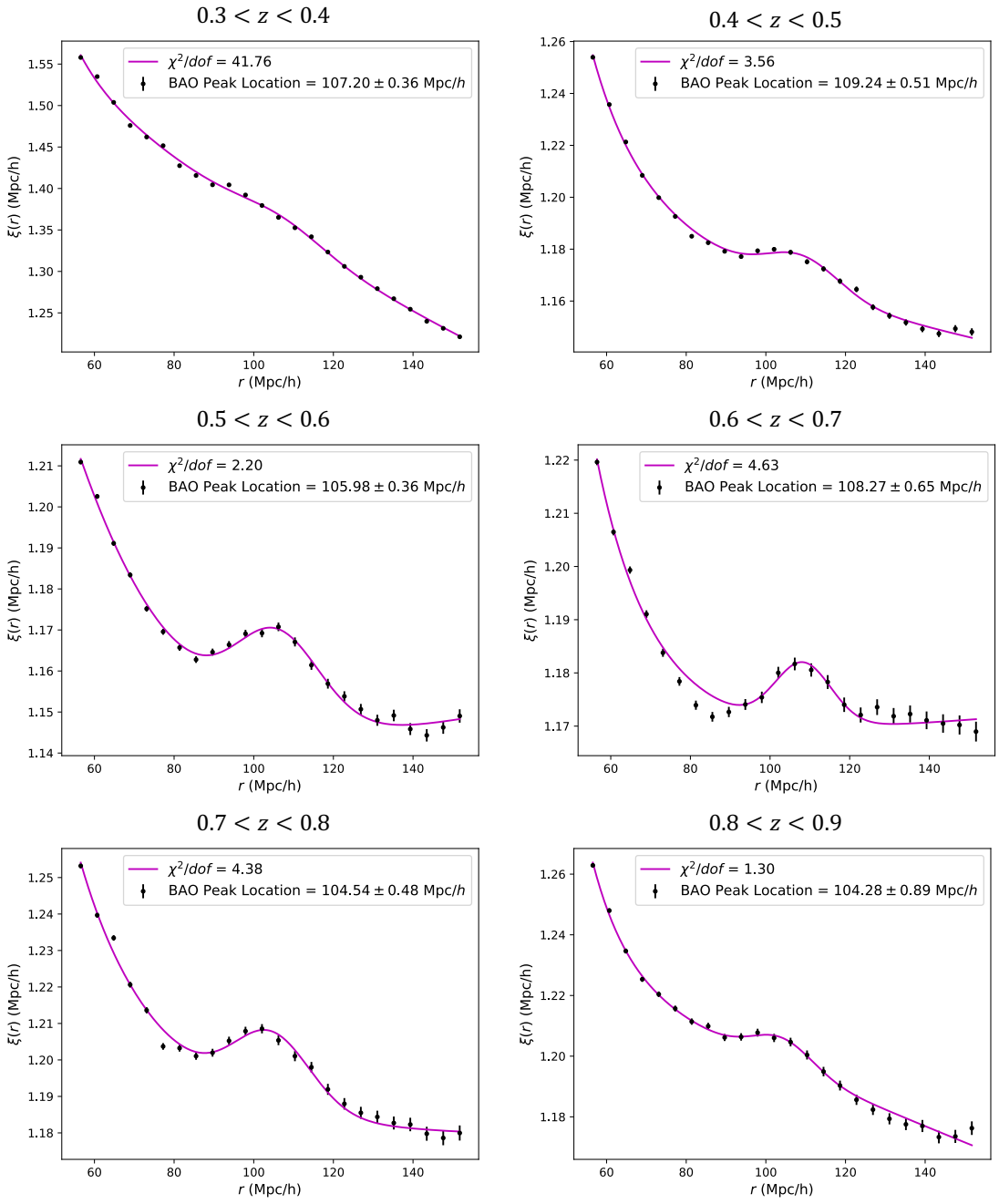

Figure 7.14: The measured 2PCF for LRGs under Nominal conditions. Each plot shows a redshift bin of $\Delta z = 0.1$, with the BAO feature fit using Equation 1.1.

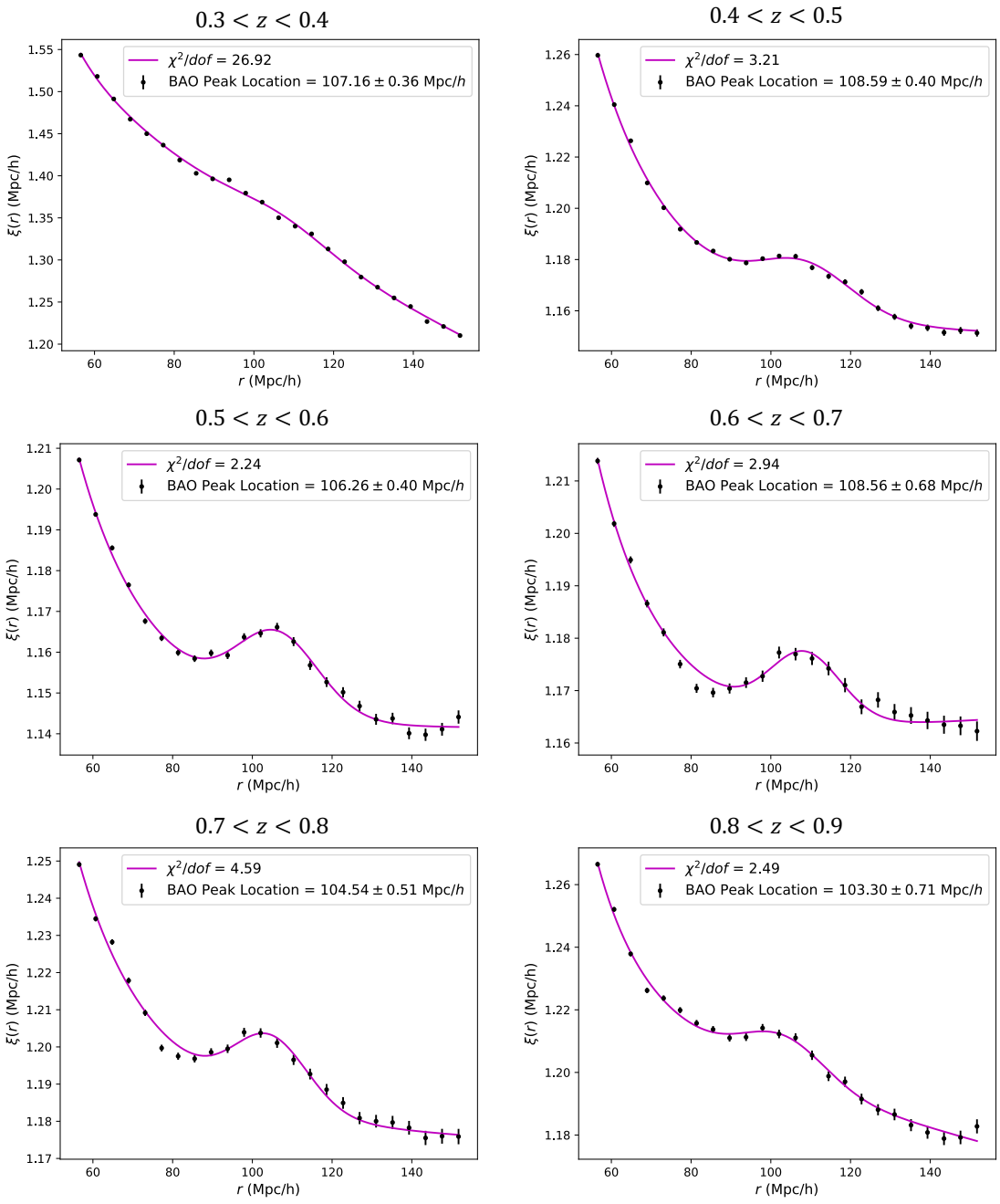

Figure 7.15: The measured 2PCF for LRGs under Survey conditions. Each plot shows a redshift bin of $\Delta z = 0.1$, with the BAO feature fit using Equation 1.1.

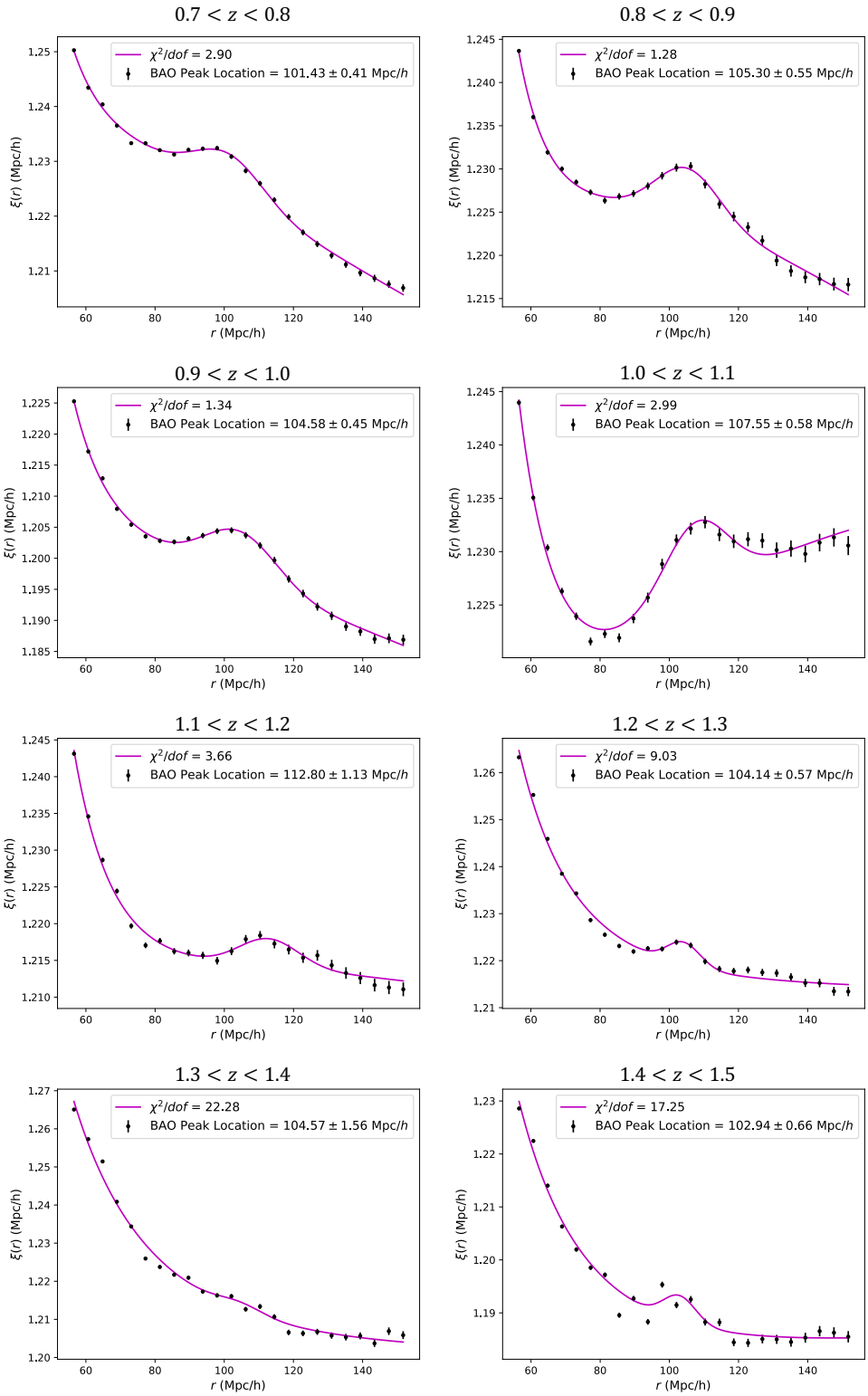

Figure 7.16: The measured 2PCF for ELGs under Nominal conditions. Each plot shows a redshift bin of $\Delta z = 0.1$, with the BAO feature fit using Equation 1.1.

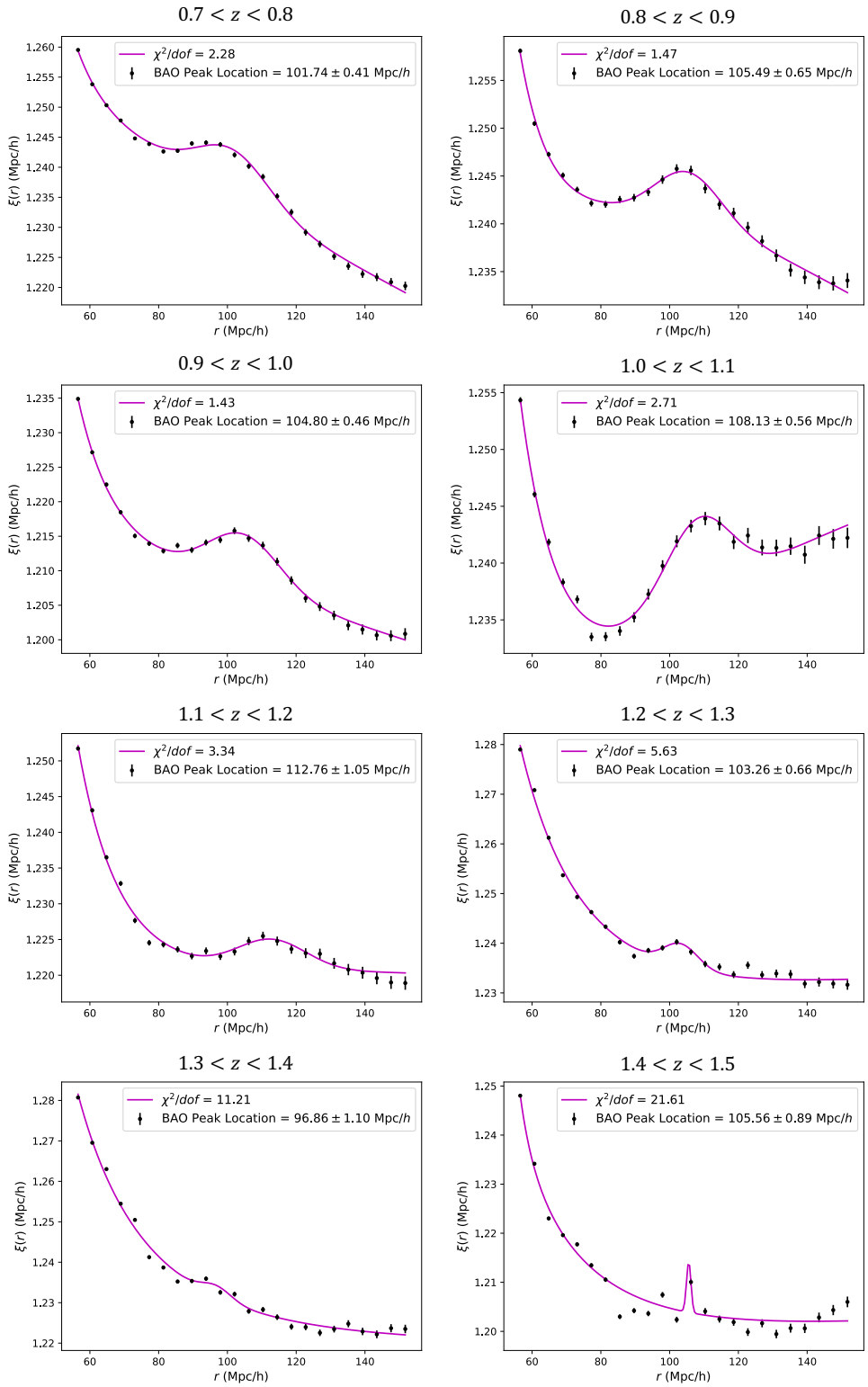

Figure 7.17: The measured 2PCF for ELGs under Survey conditions. Each plot shows a redshift bin of $\Delta z = 0.1$, with the BAO feature fit using Equation 1.1.

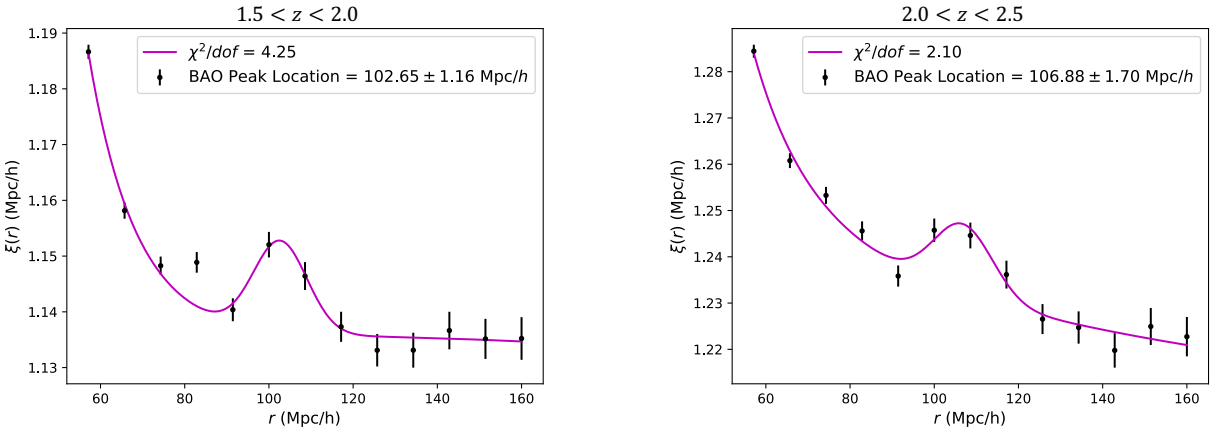

Figure 7.18: The measured 2PCF for QSOs under Nominal conditions. Each plot shows a redshift bin of $\Delta z = 0.5$, with the BAO feature fit using Equation 1.1.

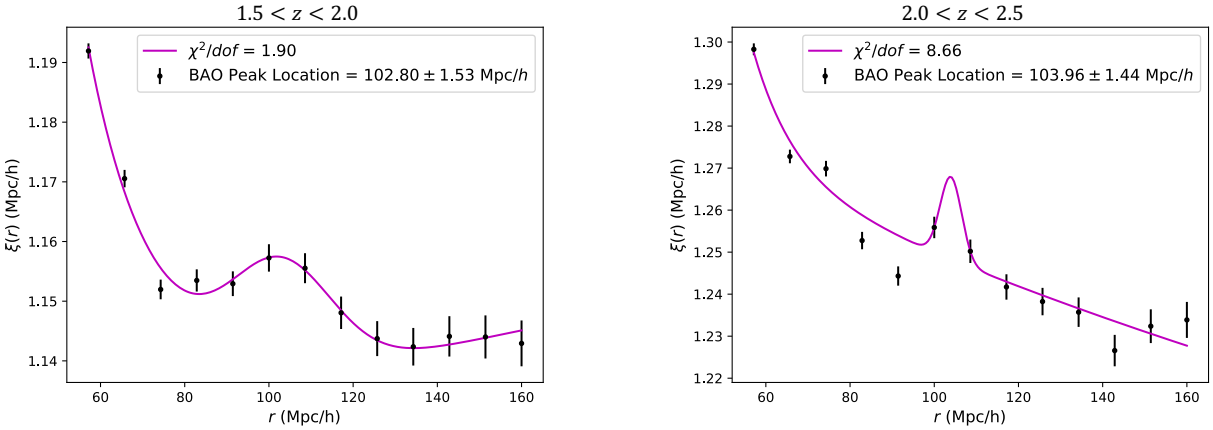

Figure 7.19: The measured 2PCF for QSOs under Survey conditions. Each plot shows a redshift bin of $\Delta z = 0.5$, with the BAO feature fit using Equation 1.1.

7.6. LRG BAO Fits Used to Measure the Sound Horizon

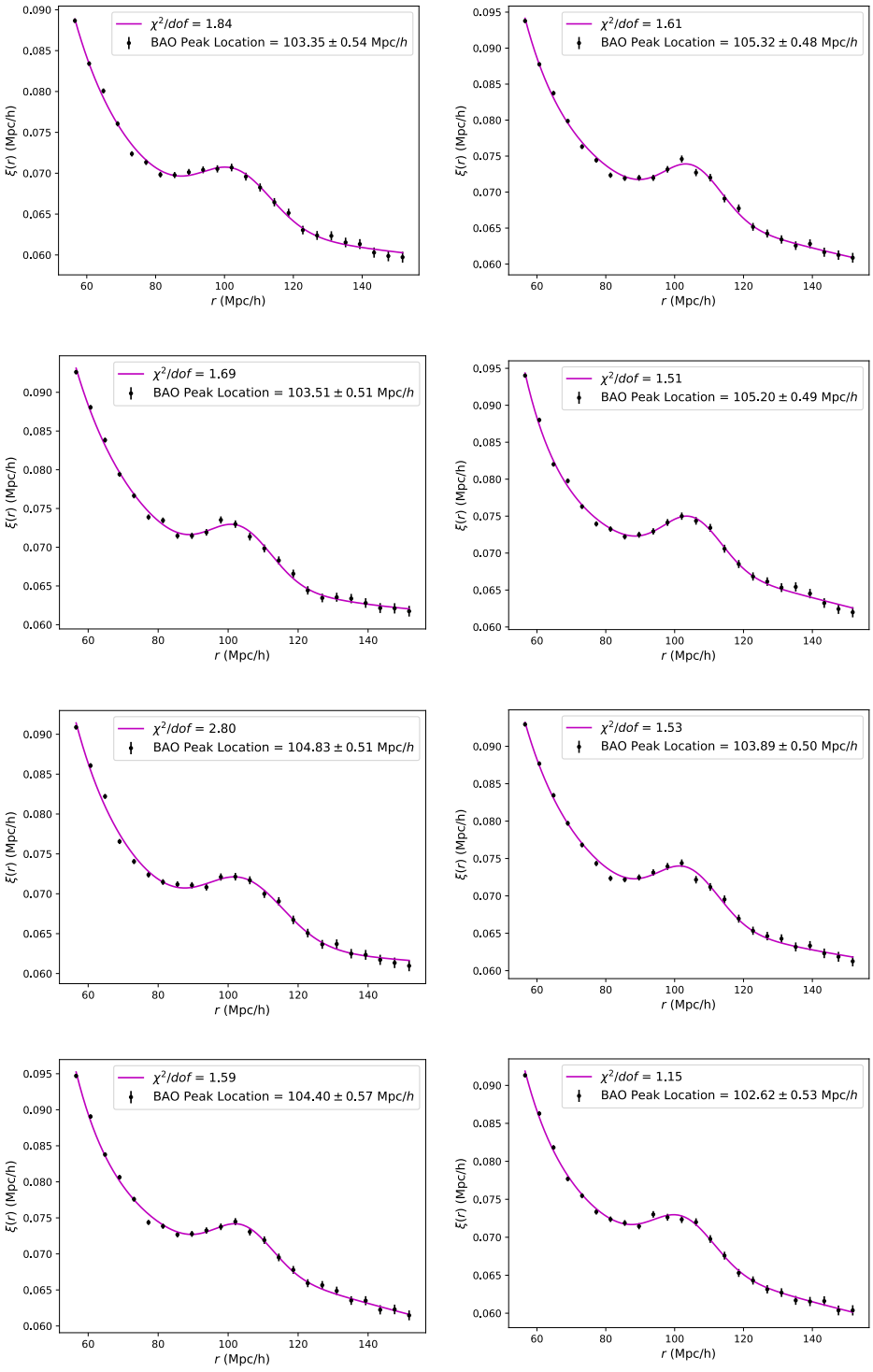

Figure 7.20: Eight example 2pcf fits for the mock LRG sample under Nominal conditions.

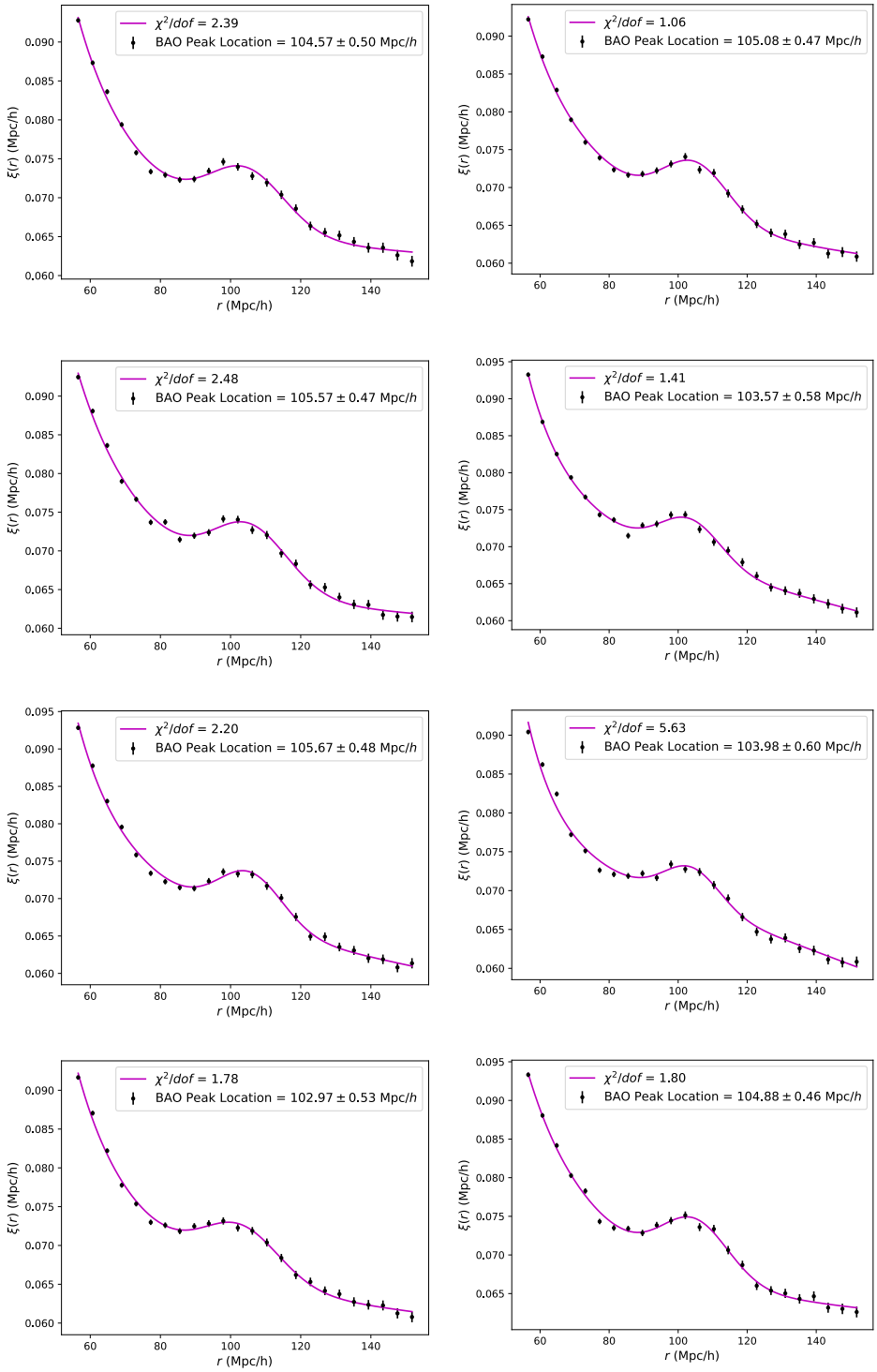

Figure 7.21: Eight example 2pcf fits for the mock LRG sample under Survey conditions.

Chapter 8

Conclusion

With current and upcoming experiments such as DESI and the Laser Interferometer Gravitational-Wave Observatory (LIGO), ROTSE has an opportunity to make important contributions to the forefront of astrophysics with its use in follow up optical observations. The methodology outlined in this thesis regarding the ROTSE-III experiment shows that it has been highly successful in terms of discovering SNe and providing extensive photometric observations even without first detection. The return of ROTSE-IIIb to imaging on sky is highly anticipated, as multi-messenger astronomy is an exciting new experimental probe of astrophysics with the discovery of gravitational waves.

The use of SNe IIP as cosmological probes also shows the ability of ROTSE to perform cosmological analysis with as little as a single spectrum for each event. With an updated mechanical system to support the movement of the telescope, the CCD remains as the only significant aspect of the instrument requiring refurbishment. Although the work to return to consistent nightly observing is not negligible, the possibility of continued observing is promising. Additional imaging facilitates the observation of more SNe IIP, allowing the determination of the local Hubble flow using ROTSE events to become more refined.

Analysis of SN 2007gr provides an intriguing new source of distance measurements to the host galaxies of other types of CCSNe. Applying EPM to Types Ib, Ib/c, and Ic SNe will greatly improve the statistics of measuring H_0. It can be seen for this object that a distance of 9.5 ± 0.9 Mpc is comparable to previous distance measurements to its host galaxy, NGC 1058, using other methods such as Cepheid variable stars and the Tully-Fisher relation.

Using the photometric analysis of SN 2010kd shown here, a distance measurement to its host galaxy only requires spectroscopic analysis and the application of these reductions to the quantities required by the EPM. As another Type Ic, this event will help in determining the validity of SNe Ic as candidates for the EPM. As a superluminous supernova at $z \sim 0.1$, this would be the farthest event in the ROTSE sample used for a distance calculation.

To probe the more distant universe, DESI will provide the largest map of the large scale universe out to $z \sim 4$. With 4 distinct target galaxy types, BGS, LRG, ELG, and QSO, observations of more than 30 million galaxies will allow this experiment to determine the Hubble flow from the local universe out to approximately 11 billion light years away.

Using an online spectroscopic pipeline to monitor observations, the efficiency of observing will be highly improved compared to previous spectroscopic surveys. With the employment of the ETC, the amount of excess observing time and poor quality images due to low SNR will be significantly reduced. The QuickLook pipeline described in this thesis shows the ability for this to occur, with the near real time reduction of spectroscopic images in less than 2 minutes.

In order to test the effects of observing conditions on DESI, a simulation strategy is defined here that provides a forecast of the entire dark time survey. By generating approximately 30 million targets using an N-body simulation with each galaxy halo populated using the clustering properties seen in previous surveys, one third of the entire sky is simulated. Instead of sending each of these targets through the full spectroscopic reduction process, the redshift efficiency of the offline spectroscopic pipeline is modeled, so that a redshift catalog can be simulated in minutes instead of hours or days.

The resulting catalog facilitates the measurement of the BAO signature that can be used as a standard cosmological ruler. By simulating this catalog under Nominal and Survey conditions, the effectiveness of the ETC can be tested. Comparing BAO measurements for

LRGs, ELGs, and QSOs in multiple redshift bins shows similar results under Nominal and Survey conditions. Although it is outside the scope of this thesis to fully extract cosmological parameters from the simulated galaxy catalogs, it is shown here that small deviations could be seen in the estimation of the sound horizon.

However, with the start of DESI observing and the increase of available spectroscopic redshifts from DESI data, this strategy will soon be able to be applied to data rather than simulations. The increase in observations not only improves the statistics, but also allows refinement of the fiber assignment and target selection strategies. This will allow models of redshift efficiency to be based on real data, vastly increasing the realism of this simulation strategy. The framework established in this thesis is promising as a means of forecasting the results of the DESI survey.

Appendix A

BAO Fitting Strategy (Alternative Approach)

In this alternative approach to fitting the 2PCF to measure the BAO peak, I use the equation

$$\xi(r) = A + Br + Cr^2 + Dr^E + Fe^{-\left(\frac{r-G}{H}\right)^2}, \tag{1.1}$$

where A represents the offset, B and C account for the linear and quadratic components of the tail, D and E account for the power law distribution, and F, G, and H are parameters of the Gaussian fit of the BAO feature. The parameter F indicates the mean of the Gaussian, which is used as the estimation of the location of the BAO feature.

A.0.1. LRG Clustering Measurements

Figure 1.1 shows the comparison of the 2PCF for LRGs over a redshift range of $0.3 < z < 0.9$ in bins of $\Delta z = 0.1$ for both Nominal and Survey conditions. The BAO feature is clearly seen in both samples. Table 1.1 shows the results of fitting a Gaussian profile to the BAO feature of both samples where it can be seen that the difference between the location of the BAO peak is consistently low.

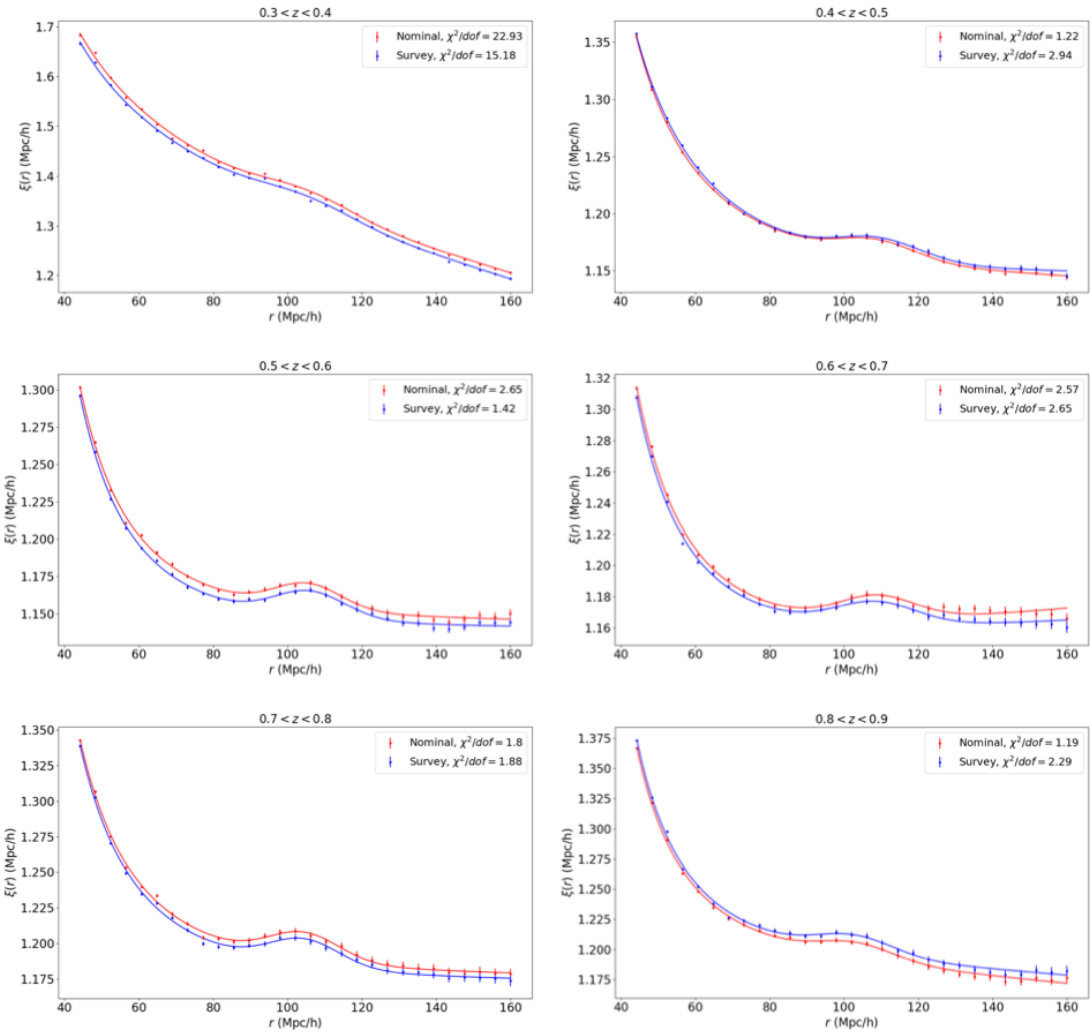

Figure 1.1: The measured 2PCF for LRGs under Nominal and Survey conditions. Each plot shows a redshift bin of $\Delta z = 0.1$, with the BAO feature fit using Equation 1.1.

Table 1.1: LRG Two point Correlation Function Results

Redshift Range	BAO Peak (Nominal) (Mpc/h)	BAO Peak (Survey) (Mpc/h)
$0.3 < z < 0.4$	105.8 ± 0.4	105.4 ± 0.5
$0.4 < z < 0.5$	108.8 ± 0.7	109.6 ± 0.7
$0.5 < z < 0.6$	105.5 ± 0.7	106.0 ± 0.7
$0.6 < z < 0.7$	108.9 ± 1.1	108.5 ± 1.1
$0.7 < z < 0.8$	104.4 ± 0.8	104.4 ± 0.8
$0.8 < z < 0.9$	103.3 ± 1.2	102.9 ± 1.1

A.0.2. ELG Clustering Measurements

Figure 1.2 shows the same comparison for ELGs over a redshift range of $0.7 < z < 1.5$. The BAO feature is prominent for both of these samples due to the high statistics given the large number of ELGs in this redshift range. Table 1.2 shows the results of fitting the BAO feature of both ELG samples. These results show that for both Nominal and Survey conditions, the BAO feature is found at approximately the same distance scale.

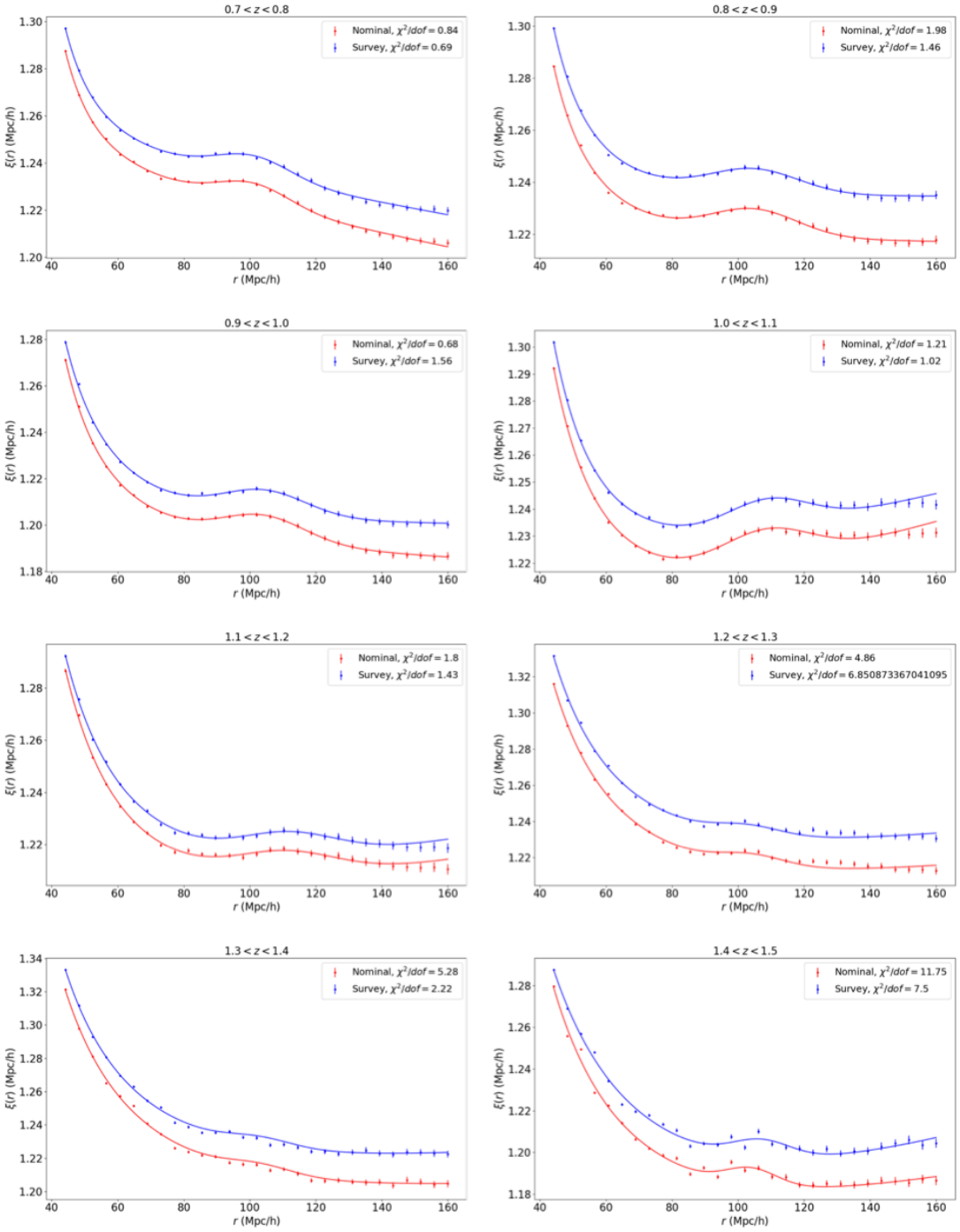

Figure 1.2: The measured 2PCF for ELGs under Nominal and Survey conditions. Each plot shows a redshift bin of $\Delta z = 0.1$, with the BAO feature fit using Equation 1.1.

Table 1.2: ELG Two point Correlation Function Results

Redshift Range	BAO Peak (Nominal) (Mpc/h)	BAO Peak (Survey) (Mpc/h)
$0.7 < z < 0.8$	101.2 ± 0.7	101.1 ± 0.7
$0.8 < z < 0.9$	104.8 ± 0.7	104.8 ± 0.8
$0.9 < z < 1.0$	104.8 ± 0.8	104.4 ± 0.7
$1.0 < z < 1.1$	108.6 ± 0.8	108.9 ± 0.9
$1.1 < z < 1.2$	110.7 ± 1.1	111.7 ± 1.2
$1.2 < z < 1.3$	104.1 ± 2.2	103.1 ± 2.3
$1.3 < z < 1.4$	102.9 ± 2.0	103.0 ± 1.9
$1.4 < z < 1.5$	104.0 ± 0.9	106.9 ± 1.0

A.0.3. QSO Clustering Measurements

Figure 1.3 shows this comparison for QSOs over a redshift range of $1.5 < z < 2.5$ in bins of $\Delta z = 0.5$. A coarser redshift binning is necessary for QSOs due to the decreased volume of targets. While the total QSO sample is comprised of approximately 2 million targets, it is spread over a redshift range of $0 < z < 3.5$, making the density of these targets very low compared to the LRG and ELG samples. This accounts for the noisy BAO feature seen in the Nominal and Survey samples, although it can still be seen in both 2PCFs. Table 1.3 shows the results of fitting the BAO feature of both QSO samples. Although there are only two redshift ranges that yield a prominent BAO feature, it can still be seen that the BAO peak is found at a similar distance scale for both samples.

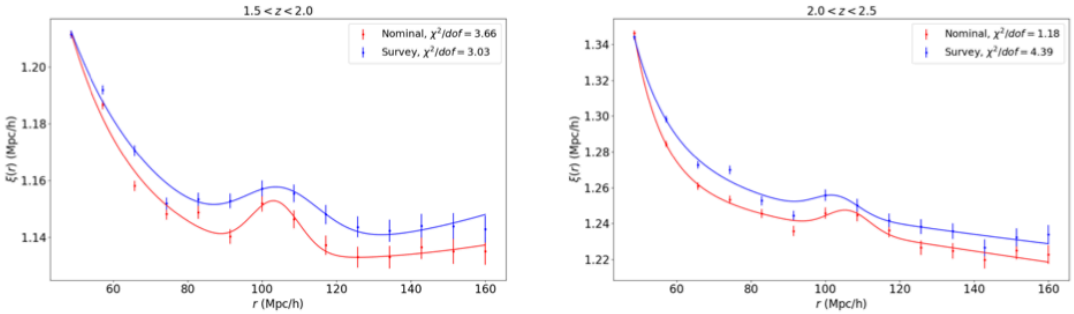

Figure 1.3: The measured 2PCF for QSOs under Nominal and Survey conditions. Each plot shows a redshift bin of $\Delta z = 0.5$, with the BAO feature fit using Equation 1.1.

Table 1.3: QSO Two point Correlation Function Results

Redshift Range	BAO Peak (Nominal) (Mpc/h)	BAO Peak (Survey) (Mpc/h)
$1.5 < z < 2.0$	103.6 ± 1.3	105.2 ± 1.9
$2.0 < z < 2.5$	106.2 ± 3.9	103.0 ± 1.6

Appendix B

Systematic Effects of Observing Conditions on DESI Cosmology (Alternative Approach)

B.1. Effects of Observing Conditions on H_0

The same fitting strategy used in Appendix A is applied to examine the effects of observing conditions on the ability to extract H_0 from DESI's cosmological observations. Here, I simulate distance measurements to calculate the 2PCF using five different cosmologies by using the same Planck results each time, but varying H_0 using $50 < H_0 < 90$ km/s/Mpc at 5 km/s/Mpc intervals. The comparison tables in each of the following sections quote different values of the h parameter, where $h = \frac{H_0}{100 \text{ km/s/Mpc}}$. I compare the resulting BAO peak locations for Nominal and Survey conditions to analyze any potential systematic effects that arise. This process is repeated for each redshift bin producing reliable BAO measurements for all target types. All of the final fits are shown below.

B.1.1. LRG BAO Peak Measurements vs. H_0

Table 2.1 shows the resulting BAO peak measurements for LRGs under Nominal conditions and Table 2.2 shows the same results under Survey conditions. The same redshift bins used in Section A.0.1 are used here. Figure 2.1 directly compares these values, showing the measurements of both scenarios for each cosmology.

B.1.2. ELG BAO Peak Measurements vs. H_0

Table 2.3 shows the resulting BAO peak measurements for ELGs under Nominal conditions and Table 2.4 shows the same results under Survey conditions. The redshift range

Table 2.1: LRG BAO Peak Locations under Nominal Conditions (Mpc/h)

Redshift Range	$h = 0.6$	$h = 0.65$	$h = 0.7$	$h = 0.75$	$h = 0.8$
$0.3 < z < 0.4$	105.1 ± 0.4	104.9 ± 0.5	104.8 ± 0.5	106.1 ± 0.5	104.7 ± 0.5
$0.4 < z < 0.5$	110.1 ± 1.0	110.1 ± 1.0	108.9 ± 1.0	110.0 ± 0.9	110.2 ± 1.1
$0.5 < z < 0.6$	106.3 ± 0.9	105.5 ± 0.9	105.7 ± 1.0	106.8 ± 0.9	106.7 ± 1.0
$1.6 < z < 0.7$	104.7 ± 1.8	101.3 ± 2.9	105.6 ± 1.7	105.4 ± 1.7	105.8 ± 1.7
$0.7 < z < 0.8$	103.7 ± 1.2	104.7 ± 1.3	103.7 ± 1.3	103.2 ± 1.2	104.1 ± 1.3
$0.8 < z < 0.9$	101.5 ± 1.3	102.5 ± 1.4	103.2 ± 1.4	102.0 ± 1.3	102.5 ± 1.5

Table 2.2: LRG BAO Peak Locations under Survey Conditions (Mpc/h)

Redshift Range	$h = 0.6$	$h = 0.65$	$h = 0.7$	$h = 0.75$	$h = 0.8$
$0.3 < z < 0.4$	103.9 ± 0.5	104.2 ± 0.6	105.1 ± 0.5	104.9 ± 0.5	105.2 ± 0.6
$0.4 < z < 0.5$	110.5 ± 1.1	111.1 ± 1.3	110.5 ± 1.3	109.9 ± 1.1	111.6 ± 1.2
$0.5 < z < 0.6$	105.9 ± 1.0	107.1 ± 1.0	106.2 ± 1.1	106.4 ± 1.0	105.7 ± 1.0
$1.6 < z < 0.7$	105.4 ± 1.7	106.2 ± 1.9	106.1 ± 1.8	106.0 ± 1.6	106.8 ± 1.8
$0.7 < z < 0.8$	103.9 ± 1.3	103.6 ± 1.3	103.8 ± 1.3	104.0 ± 1.3	104.0 ± 1.3
$0.8 < z < 0.9$	102.1 ± 1.2	100.9 ± 1.3	102.1 ± 1.2	101.8 ± 1.3	102.5 ± 1.2

included for ELGs is $0.7 < z < 1.5$, although there weren't sufficient results for $1.3 < z < 1.4$, so this bin was omitted. Figure 2.2 directly compares these values, showing the measurements of both scenarios for each cosmology.

B.1.3. QSO BAO Peak Measurements vs. H_0

Table 2.5 shows the resulting BAO peak measurements for QSOs under Nominal conditions and Table 2.6 shows the same results under Survey conditions. Only two redshift bins consistently yield sufficient BAO measurements, so $1.5 < z < 2.0$ and $2.0 < z < 2.5$ are the only bins shown for this sample. Figure 2.3 directly compares these values, showing the measurements of both scenarios for each cosmology.

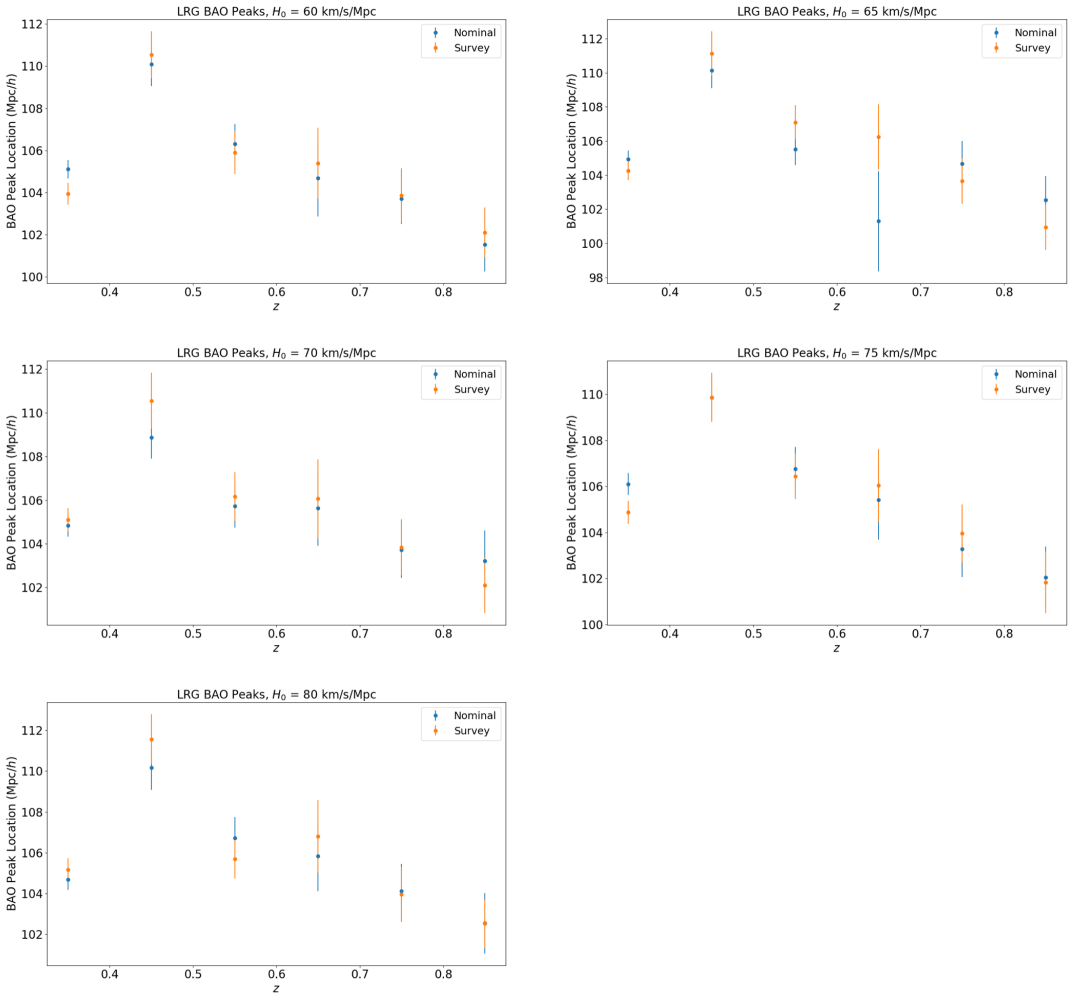

Figure 2.1: The measured BAO peak locations for LRGs under Nominal and Survey conditions. Each plot shows a cosmology with a different H_0 value, ranging from $50 < H_0 < 90$ km/s/Mpc at intervals of 5 km/s/Mpc.

The results of the previous sections indicate that although there are statistical shifts of the BAO measurement between various redshift bins, there is not a systematic shift of the BAO measurement in either direction under Nominal vs. Survey conditions. The various cosmologies of $50 < H_0 < 90$ km/s/Mpc also do not appear to show a systematic shift of the BAO feature. However, any discrepancy in this measurement can lead to improper cosmological implications, even if the deviations between nominal and survey conditions appear to be purely statistical. Thus, a systematic uncertainty based on the size of the

Table 2.3: ELG BAO Peak Locations under Nominal Conditions (Mpc/h)

Redshift Range	$h = 0.6$	$h = 0.65$	$h = 0.7$	$h = 0.75$	$h = 0.8$
$0.7 < z < 0.8$	102.2 ± 0.4	103.0 ± 0.4	101.3 ± 0.4	102.5 ± 0.4	101.9 ± 0.4
$0.8 < z < 0.9$	102.5 ± 0.4	102.6 ± 0.4	103.1 ± 0.4	103.5 ± 0.4	104.0 ± 0.4
$0.9 < z < 1.0$	103.3 ± 0.4	103.6 ± 0.4	103.4 ± 0.4	103.2 ± 0.4	103.0 ± 0.4
$1.0 < z < 1.1$	107.8 ± 0.7	107.7 ± 0.7	107.1 ± 0.7	106.9 ± 0.6	107.1 ± 0.6
$1.1 < z < 1.2$	107.2 ± 0.9	109.2 ± 1.0	107.2 ± 1.0	108.7 ± 1.0	107.7 ± 1.1
$1.2 < z < 1.3$	104.1 ± 0.8	104.0 ± 1.0	104.5 ± 1.0	104.8 ± 1.1	104.2 ± 0.8
$1.4 < z < 1.5$	105.2 ± 0.6	103.0 ± 0.7	108.6 ± 0.8	107.8 ± 0.7	101.7 ± 0.7

Table 2.4: ELG BAO Peak Locations under Survey Conditions (Mpc/h)

Redshift Range	$h = 0.6$	$h = 0.65$	$h = 0.7$	$h = 0.75$	$h = 0.8$
$0.7 < z < 0.8$	102.3 ± 0.4	101.2 ± 0.4	102.0 ± 0.4	101.5 ± 0.4	101.5 ± 0.4
$0.8 < z < 0.9$	102.6 ± 0.4	102.9 ± 0.5	103.4 ± 0.4	103.5 ± 0.4	103.1 ± 0.4
$0.9 < z < 1.0$	102.9 ± 0.5	103.7 ± 0.5	103.5 ± 0.5	103.8 ± 0.5	103.5 ± 0.5
$1.0 < z < 1.1$	107.0 ± 0.7	108.8 ± 0.7	107.7 ± 0.7	108.8 ± 0.7	109.0 ± 0.8
$1.1 < z < 1.2$	107.1 ± 1.0	111.7 ± 1.0	113.9 ± 1.1	111.6 ± 1.1	113.6 ± 1.2
$1.2 < z < 1.3$	108.8 ± 1.9	103.7 ± 0.9	104.9 ± 1.1	103.4 ± 1.0	101.7 ± 1.4
$1.4 < z < 1.5$	102.0 ± 0.6	103.2 ± 1.0	103.8 ± 0.9	106.4 ± 0.8	104.1 ± 0.7

deviation between these two scenarios is placed on the BAO measurement for each target type.

To calculate this uncertainty, the RMS of the difference between BAO measurements under Survey and Nominal conditions for LRGs, ELGs, and QSOs is taken. The difference of this RMS value and the average error on the BAO peak measurements is then taken to represent the systematic uncertainty. Table 2.7 shows the systematic error for each target type on the BAO measurement. Using a 0.5% upper limit for the systematic uncertainty based on these values, this could propagate to an error in measured H_0 by up to ± 0.4 km/s/Mpc.

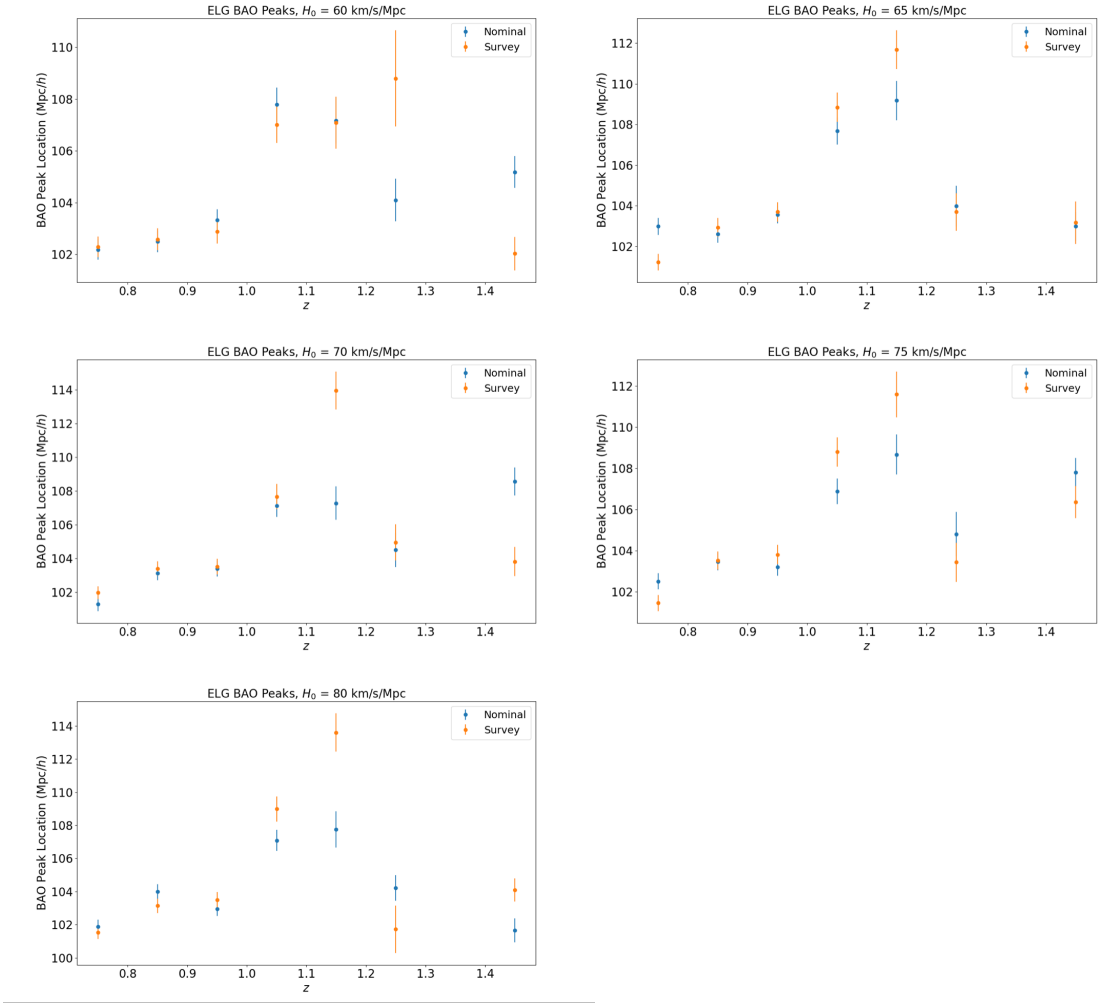

Figure 2.2: The measured BAO peak locations for ELGs under Nominal and Survey conditions. Each plot shows a cosmology with a different H_0 value, ranging from $50 < H_0 < 90$ km/s/Mpc at intervals of 5 km/s/Mpc.

Table 2.5: QSO BAO Peak Locations under Nominal Conditions (Mpc/h)

Redshift Range	$h = 0.6$	$h = 0.65$	$h = 0.7$	$h = 0.75$	$h = 0.8$
$1.5 < z < 2.0$	103.5 ± 3.1	102.9 ± 3.9	104.0 ± 3.8	101.6 ± 3.3	104.7 ± 3.6
$2.0 < z < 2.5$	109.4 ± 5.3	105.7 ± 6.6	106.3 ± 4.0	104.3 ± 1.3	104.2 ± 1.7

Table 2.6: QSO BAO Peak Locations under Survey Conditions (Mpc/h)

Redshift Range	$h = 0.6$	$h = 0.65$	$h = 0.7$	$h = 0.75$	$h = 0.8$
$1.5 < z < 2.0$	102.4 ± 3.9	102.6 ± 4.0	105.2 ± 4.5	103.5 ± 4.9	104.0 ± 3.3
$2.0 < z < 2.5$	104.2 ± 1.2	104.1 ± 1.4	103.7 ± 2.3	105.6 ± 9.9	104.1 ± 1.5

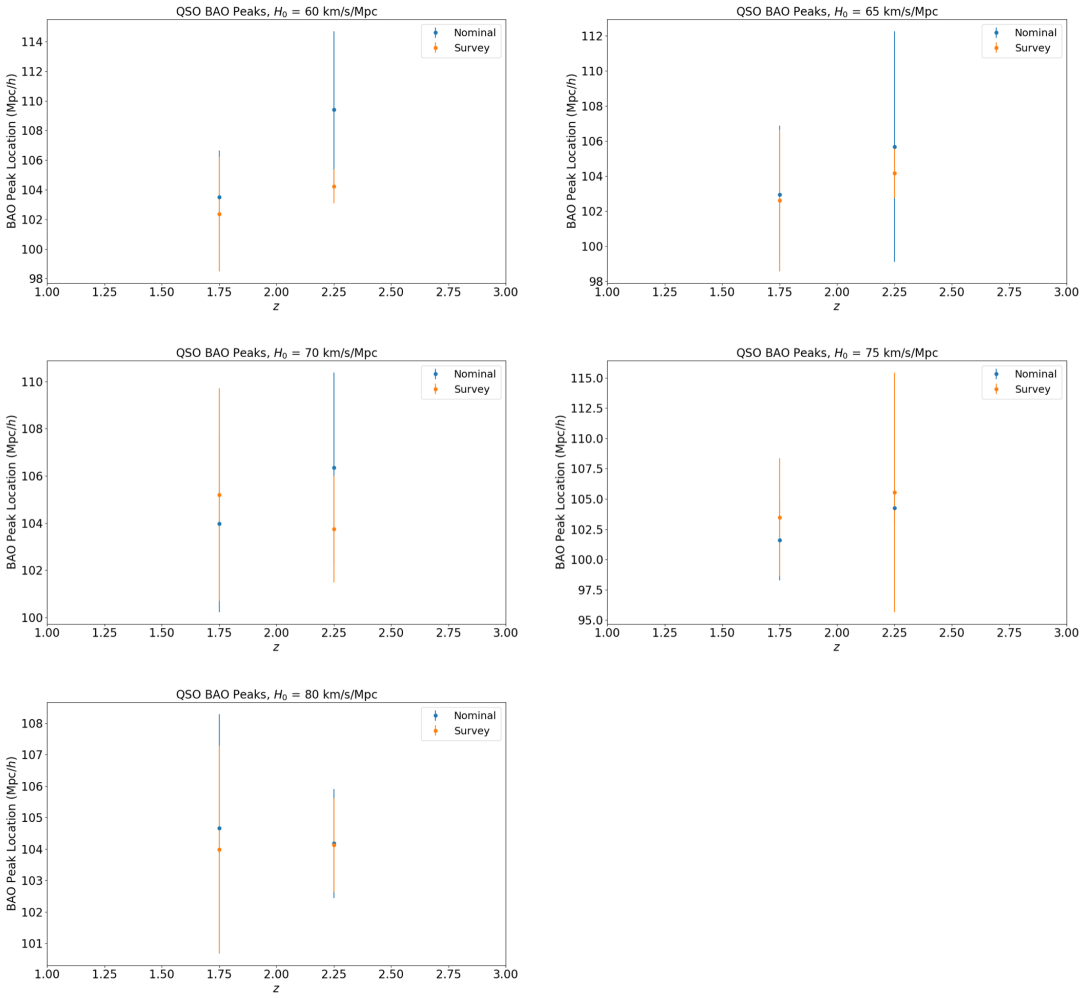

Figure 2.3: The measured BAO peak locations for QSOs under Nominal and Survey conditions. Each plot shows a cosmology with a different H_0 value, ranging from $50 < H_0 < 90$ km/s/Mpc at intervals of 5 km/s/Mpc.

Table 2.7: Systematic Error on BAO Measurements per Target Type

Target Type	Systematic Error (Mpc/h)
LRG	0.4
ELG	0.3
QSO	0.5

BIBLIOGRAPHY

[1] A. Einstein, *Explanation of the perihelion motion of mercury from the general theory of relativity*, *Sitzungsber. Preuss. Akad. Wiss. Berlin (Math. Phys.)* **1915** (1915) 831–839. 1

[2] A. M. Nobili and C. M. Will, *The real value of mercury's perihelion advance*, *Nature* **320** (1986) 39. 1

[3] A. Friedmann, *On the curvature of space*, *General Relativity and Gravitation* **31** (1999) 1991–2000. 2

[4] G. Lemaitre, *A homogeneous universe of constant mass and increasing radius accounting for the radial velocity of extra-galactic nebulae*, in *Annales de la Société Scientifique de Bruxelles*, vol. 47, pp. 49–59, 1927. 2

[5] E. Hubble, *A relation between distance and radial velocity among extra-galactic nebulae*, *Proceedings of the National Academy of Sciences* **15** (1929) 168–173. 2

[6] A. G. Riess, A. V. Filippenko, P. Challis, A. Clocchiatti, A. Diercks, P. M. Garnavich et al., *Observational evidence from supernovae for an accelerating universe and a cosmoblogical constant*, *The Astronomical Journal* **116** (1998) 1009. 2, 7, 15, 16

[7] S. Perlmutter, G. Aldering, G. Goldhaber, R. Knop, P. Nugent, P. Castro et al., *Measurements of ω and λ from 42 high-redshift supernovae*, *The Astrophysical Journal* **517** (1999) 565. 2, 7, 15, 16

[8] N. Aghanim, Y. Akrami, M. Ashdown, J. Aumont, C. Baccigalupi, M. Ballardini et al., *Planck 2018 results. vi. cosmological parameters*, *arXiv preprint arXiv:1807.06209* (2018) . 7, 166

[9] L. Anderson, E. Aubourg, S. Bailey, F. Beutler, V. Bhardwaj, M. Blanton et al., *The clustering of galaxies in the sdss-iii baryon oscillation spectroscopic survey: baryon acoustic oscillations in the data releases 10 and 11 galaxy samples*, *Monthly Notices of the Royal Astronomical Society* **441** (2014) 24–62. 7

[10] A. Sandage, *The distance scale*, in *Problems of Extra-Galactic Research*, vol. 15, p. 359, 1962. 10

[11] S. Chandrasekhar, *The maximum mass of ideal white dwarfs*, *The Astrophysical Journal* **74** (1931) 81. 12

[12] K. Maeda and Y. Terada, *Progenitors of type ia supernovae*, *International Journal of Modern Physics D* **25** (2016) 1630024. 12, 17

[13] D. Arnett, *Supernovae and nucleosynthesis*, *European Journal of Physics* **17** (1996) 366. 12

[14] C. D. Matzner and C. F. McKee, *The expulsion of stellar envelopes in core-collapse supernovae*, *The Astrophysical Journal* **510** (1999) 379. 13

[15] D. Kasen, "Supernova spectra." xiv, 15

[16] R. Barbon, F. Ciatti and L. Rosino, *On the light curve and properties of type i supernovae.*, *Astronomy and Astrophysics* **25** (1973) 241–248. 15

[17] I. P. Pskovskii, *Light curves, color curves, and expansion velocity of type i supernovae as functions of the rate of brightness decline*, *Soviet Astronomy* **21** (1977) 675–682. 15

[18] M. M. Phillips, *The absolute magnitudes of type ia supernovae*, *The Astrophysical Journal* **413** (1993) L105–L108. 15

[19] M. Hamuy, M. Phillips, N. B. Suntzeff, R. A. Schommer, J. Maza, R. Smith et al., *The morphology of type ia supernovae light curves*, *arXiv preprint astro-ph/9609063* (1996) . 15

[20] M. Phillips, P. Lira, N. B. Suntzeff, R. Schommer, M. Hamuy and J. Maza, *The reddening-free decline rate versus luminosity relationship for type ia supernovae*, *The Astronomical Journal* **118** (1999) 1766. 15

[21] D. o. P. Durham University, "Things that go bang in the night." xiv, 16

[22] S. Benetti, E. Cappellaro, P. A. Mazzali, M. Turatto, G. Altavilla, F. Bufano et al., *The diversity of type ia supernovae: evidence for systematics?*, *The Astrophysical Journal* **623** (2005) 1011. 17

[23] R. P. Kirshner and J. Kwan, *Distances to extragalactic supernovae*, *The Astrophysical Journal* **193** (1974) 27–36. 17, 129

[24] J. Vinkó and K. Takáts, *The expanding photosphere method: Progress and problems*, . 17, 129

[25] G. Dhungana, R. Kehoe, J. Vinkó, J. M. Silverman, J. Wheeler, W. Zheng et al., *Extensive spectroscopy and photometry of the type iip supernova 2013ej*, *The Astrophysical Journal* **822** (2016) 6. 17, 55, 70, 110, 111, 127, 129, 130

[26] L. Dessart and D. J. Hillier, *Distance determinations using type ii supernovae and the expanding photosphere method*, *Astronomy & Astrophysics* **439** (2005) 671–685. 17, 18, 119, 132

[27] R. G. Eastman, B. P. Schmidt and R. Kirshner, *The atmospheres of type ii supernovae and the expanding photosphere method*, *The Astrophysical Journal* **466** (1996) 911. 17

[28] J. Vinkó, K. Takáts, T. Szalai, G. H. Marion, J. C. Wheeler, K. Sárneczky et al., *Improved distance determination to m 51 from supernovae 2011dh and 2005cs*, *Astronomy & Astrophysics* **540** (2012) A93. 18, 129

[29] M. Hauser, R. Arendt, T. Kelsall, E. Dwek, N. Odegard, J. Weiland et al., *The cobe diffuse infrared background experiment search for the cosmic infrared background. i. limits and detections*, *The Astrophysical Journal* **508** (1998) 25. 19

[30] L. Verde, H. Peiris, D. N. Spergel, M. Nolta, C. Bennett, M. Halpern et al., *First-year wilkinson microwave anisotropy probe (wmap)* observations: Parameter estimation methodology*, *The Astrophysical Journal Supplement Series* **148** (2003) 195. 19

[31] J.-M. Lamarre, J. Puget, F. Bouchet, P. A. Ade, A. Benoit, J. Bernard et al., *The planck high frequency instrument, a third generation cmb experiment, and a full sky submillimeter survey*, *New Astronomy Reviews* **47** (2003) 1017–1024. 19

[32] D. J. Eisenstein, I. Zehavi, D. W. Hogg, R. Scoccimarro, M. R. Blanton, R. C. Nichol et al., *Detection of the baryon acoustic peak in the large-scale correlation function of sdss luminous red galaxies*, *The Astrophysical Journal* **633** (2005) 560. 19

[33] S. D. Landy and A. S. Szalay, *Bias and variance of angular correlation functions*, *The Astrophysical Journal* **412** (1993) 64–71. 20

[34] W. Percival, "large-scale structure results & predictions." xiv, 20

[35] J.-P. Luminet, *The status of cosmic topology after planck data*, *Universe* **2** (2016) 1. 21

[36] C. W. Akerlof, R. Kehoe, T. McKay, E. Rykoff, D. Smith, D. Casperson et al., *The rotse-iii robotic telescope system*, *Publications of the Astronomical Society of the Pacific* **115** (2003) 132. xv, 23, 24, 25, 50, 51

[37] R. M. Quimby, *Superluminous supernovae*, *Proceedings of the International Astronomical Union* **7** (2011) 22–28. 27

[38] R. M. Quimby, F. Yuan, C. Akerlof and J. C. Wheeler, *Rates of superluminous supernovae at z 0.2*, *Monthly Notices of the Royal Astronomical Society* **431** (2013) 912–922. 27, 120

[39] E. Chatzopoulos, J. C. Wheeler, J. Vinko, Z. Horvath and A. Nagy, *Analytical light curve models of superluminous supernovae: χ2-minimization of parameter fits*, *The Astrophysical Journal* **773** (2013) 76. 27

[40] R. M. Quimby, G. Aldering, J. C. Wheeler, P. Höflich, C. W. Akerlof and E. S. Rykoff, *Sn 2005ap: A most brilliant explosion*, *The Astrophysical Journal Letters* **668** (2007) L99. 27, 120

[41] G. J. Hill, H. E. Nicklas, P. J. MacQueen, C. Tejada, F. J. C. Duenas and W. Mitsch, *Hobby-eberly telescope low-resolution spectrograph*, in *Optical Astronomical Instrumentation*, vol. 3355, pp. 375–386, International Society for Optics and Photonics, 1998. 34, 128, 130

[42] A. Aghamousa, J. Aguilar, S. Ahlen, S. Alam, L. E. Allen, C. A. Prieto et al., *The desi experiment part i: science, targeting, and survey design*, *arXiv preprint arXiv:1611.00036* (2016) . xv, xvi, 35, 41, 42, 43, 44, 58, 61, 79, 147

[43] A. Aghamousa, J. Aguilar, S. Ahlen, S. Alam, L. E. Allen, C. A. Prieto et al., *The desi experiment part ii: Instrument design*, *arXiv preprint arXiv:1611.00037* (2016) . xv, xvii, 35, 37, 38, 39, 40, 41, 60, 76, 83, 85

[44] G. Gutierrez, R. W. Besuner, D. Brooks, P. Doel, B. Flaugher, D. Friend et al., *As-built new mayall telescope top end for the desi project*, in *Ground-based and Airborne Instrumentation for Astronomy VII*, vol. 10702, p. 107027Y, International Society for Optics and Photonics, 2018. xv, 36

[45] K. Honscheid, A. E. Elliott, E. Buckley-Geer, B. Abreshi, F. Castander, L. da Costa et al., *The desi instrument control systems: status and early testing*, in *Software and Cyberinfrastructure for Astronomy V*, vol. 10707, p. 107071D, International Society for Optics and Photonics, 2018. 35

[46] R. J. Glenn, "Desi opens its 5,000 eyes to capture the colors of the cosmos." xv, 38

[47] N. Padmanabhan, T. Budavári, D. J. Schlegel, T. Bridges, J. Brinkmann, R. Cannon et al., *Calibrating photometric redshifts of luminous red galaxies*, *Monthly Notices of the Royal Astronomical Society* **359** (2005) 237–250. 41

[48] D. J. Eisenstein, J. Annis, J. E. Gunn, A. S. Szalay, A. J. Connolly, R. Nichol et al., *Spectroscopic target selection for the sloan digital sky survey: The luminous red galaxy sample*, *The Astronomical Journal* **122** (2001) 2267. 42

[49] A. Loeb and R. Barkana, *The reionization of the universe by the first stars and quasars*, *Annual review of astronomy and astrophysics* **39** (2001) 19–66. 43

[50] S. Veilleux and D. E. Osterbrock, *Spectral classification of emission-line galaxies*, *The Astrophysical Journal Supplement Series* **63** (1987) 295–310. 43

[51] D. G. Monet, S. E. Levine, B. Canzian, H. D. Ables, A. R. Bird, C. C. Dahn et al., *The usno-b catalog*, *The Astronomical Journal* **125** (2003) 984. 48, 70

[52] D. J. Schlegel, D. P. Finkbeiner and M. Davis, *Maps of dust infrared emission for use in estimation of reddening and cosmic microwave background radiation foregrounds*, *The Astrophysical Journal* **500** (1998) 525. 48, 105

[53] M. Bessell, *Ubvri passbands.*, *Publications of the Astronomical Society of the Pacific* **102** (1990) 1181. 48, 49, 124

[54] M. Skrutskie, R. Cutri, R. Stiening, M. Weinberg, S. Schneider, J. Carpenter et al., *The two micron all sky survey (2mass)*, *The Astronomical Journal* **131** (2006) 1163. 48

[55] D. D. McCarthy, *The julian and modified julian dates*, *Journal for the History of Astronomy* **29** (1998) 327–330. 49

[56] D. J. Cavalieri, *Nasa sea ice validation program for the defense meteorological satellite program special sensor microwave imager*, *Journal of Geophysical Research: Oceans* **96** (1991) 21969–21970. 50

[57] N. Gehrels, G. Chincarini, P. Giommi, K. Mason, J. A. Nousek, A. Wells et al., *The swift gamma-ray burst mission*, *The Astrophysical Journal* **611** (2004) 1005. 50

[58] S. Barthelmy, *Gcn and voevent: A status report*, *Astronomische Nachrichten: Astronomical Notes* **329** (2008) 340–342. 50

[59] P. W. Roming, T. E. Kennedy, K. O. Mason, J. A. Nousek, L. Ahr, R. E. Bingham et al., *The swift ultra-violet/optical telescope*, *Space Science Reviews* **120** (2005) 95–142. 55, 121

[60] K. Tsvetkova, A. Holl and L. Balazs, *Digital plate archive for supernova search at konkoly observatory*, *Baltic Astronomy* **17** (2008) 405–413. 55

[61] A. V. Filippenko, W. Li, R. Treffers and M. Modjaz, *The lick observatory supernova search with the katzman automatic imaging telescope*, in *International Astronomical Union Colloquium*, vol. 183, pp. 121–130, Cambridge University Press, 2001. 55, 68

[62] E. L. Wright, P. R. Eisenhardt, A. K. Mainzer, M. E. Ressler, R. M. Cutri, T. Jarrett et al., *The wide-field infrared survey explorer (wise): mission description and initial on-orbit performance*, *The Astronomical Journal* **140** (2010) 1868. 56

[63] A. Dey, D. J. Schlegel, D. Lang, R. Blum, K. Burleigh, X. Fan et al., *Overview of the desi legacy imaging surveys*, *The Astronomical Journal* **157** (2019) 168. xxv, 57

[64] K. Horne, *An optimal extraction algorithm for ccd spectroscopy.*, *Publications of the Astronomical Society of the Pacific* **98** (1986) 609. 59

[65] A. S. Bolton and D. J. Schlegel, *Spectro-perfectionism: an algorithmic framework for photon noise-limited extraction of optical fiber spectroscopy*, *Publications of the Astronomical Society of the Pacific* **122** (2010) 248. xvii, 59, 77, 78

[66] P. Cerulo, G. A. Orellana and G. Covone, *The evolution of brightest cluster galaxies in the nearby universe–i. colours and stellar masses from the sloan digital sky survey and wide infrared survey explorer*, *Monthly Notices of the Royal Astronomical Society* **487** (2019) 3759–3775. 62

[67] J. A. Newman, M. C. Cooper, M. Davis, S. Faber, A. L. Coil, P. Guhathakurta et al., *The deep2 galaxy redshift survey: design, observations, data reduction, and redshifts*, *The Astrophysical Journal Supplement Series* **208** (2013) 5. 66

[68] G. Dhungana, *Cosmological Distance measurements with ROTSE Supernovae IIP and Observational Systematics on DESI Emission Line Galaxy Clustering*. PhD thesis, Southern Methodist University, SMU Scholar, 5, 2018. 66, 70, 72, 110, 120, 130, 132, 134

[69] J. Oke, J. Cohen, M. Carr, J. Cromer, A. Dingizian, F. Harris et al., *The keck low-resolution imaging spectrometer*, *Publications of the Astronomical Society of the Pacific* **107** (1995) 375. 68, 128

[70] O. Yaron and A. Gal-Yam, *Wiserep—an interactive supernova data repository*, *Publications of the Astronomical Society of the Pacific* **124** (2012) 668. 68, 130

[71] J. Guillochon, J. Parrent, L. Z. Kelley and R. Margutti, *An open catalog for supernova data*, *The Astrophysical Journal* **835** (2017) 64. 69, 130

[72] E. Bertin and S. Arnouts, *Sextractor: Software for source extraction*, *Astronomy and Astrophysics Supplement Series* **117** (1996) 393–404. 70

[73] A. A. Henden, M. Templeton, D. Terrell, T. Smith, S. Levine and D. Welch, *Vizier online data catalog: Aavso photometric all sky survey (apass) dr9 (henden+, 2016)*, *yCat* (2016) II–336. 75, 130

[74] D. Crawford, *Empirical calibration of the ubvy, beta systems. i. the f-type stars.*, *The Astronomical Journal* **80** (1975) 955–971. 79

[75] G. Gilmore, S. Randich, M. Asplund, J. Binney, P. Bonifacio, J. Drew et al., *The gaia-eso public spectroscopic survey*, *The Messenger* **147** (2012) 25–31. 79

[76] R. Yan, C. Tremonti, M. A. Bershady, D. R. Law, D. J. Schlegel, K. Bundy et al., *Sdss-iv/manga: spectrophotometric calibration technique*, *The Astronomical Journal* **151** (2015) 8. 79

[77] J. Comparat, T. Delubac, S. Jouvel, A. Raichoor, J. Kneib, C. Yèche et al., *Sdss-iv eboss emission-line galaxy pilot survey*, *Astronomy & Astrophysics* **592** (2016) A121. 79

[78] M. V. Newberry, *Signal-to-noise considerations for sky-subtracted ccd data*, *Publications of the Astronomical Society of the Pacific* **103** (1991) 122. 94

[79] C. Stoughton, R. H. Lupton, M. Bernardi, M. R. Blanton, S. Burles, F. J. Castander et al., *Sloan digital sky survey: early data release*, *The Astronomical Journal* **123** (2002) 485. 94

[80] D. Madison and W. Li, *Supernova 2007gr in ngc 1058*, *CBET* (2007) . 103

[81] S. Valenti, N. Elias-Rosa, S. Taubenberger, V. Stanishev, I. Agnoletto, D. Sauer et al., *The carbon-rich type ic sn 2007gr: the photospheric phase*, *The Astrophysical Journal Letters* **673** (2008) L155. 103, 104, 105, 111, 112, 113, 115, 116, 118

[82] R. M. Crockett, J. R. Maund, S. J. Smartt, S. Mattila, A. Pastorello, J. Smoker et al., *The birth place of the type ic supernova 2007gr*, *The Astrophysical Journal Letters* **672** (2007) L99. 103, 108, 115, 118

[83] Z. Paragi, A. van der Horst, M. Tanaka, G. B. Taylor, C. Kouveliotou, J. Granot et al., *Sn2007gr: a normal type ic supernova with a mildly relativistic radio jet*, in *10th European VLBI Network Symposium and EVN Users Meeting: VLBI and the new generation of radio arrays*, vol. 125, p. 095, SISSA Medialab, 2011. 104, 118

[84] A. M. Soderberg, A. Brunthaler, E. Nakar, R. A. Chevalier and M. F. Bietenholz, *Radio and x-ray observations of the type ic sn 2007gr reveal an ordinary, non-relativistic explosion*, *The Astrophysical Journal* **725** (2010) 922. 104, 118

[85] N. Silbermann, P. Harding, B. F. Madore, R. C. Kennicutt Jr, A. Saha, P. B. Stetson et al., *The hubble space telescope key project on the extragalactic distance scale. vi. the cepheids in ngc 925*, *The Astrophysical Journal* **470** (1996) 1. 104, 118

[86] M. Hamuy, *Observed and physical properties of core-collapse supernovae*, *The Astrophysical Journal* **582** (2003) 905. 104, 119

[87] J. Terry, G. Paturel and T. Ekholm, *Local velocity field from sosie galaxies-i. the peebles' model*, *Astronomy & Astrophysics* **393** (2002) 57–68. 104, 118, 158

[88] F. Bianco, M. Modjaz, M. Hicken, A. Friedman, R. Kirshner, J. Bloom et al., *Multi-color optical and near-infrared light curves of 64 stripped-envelope core-collapse supernovae*, *The Astrophysical Journal Supplement Series* **213** (2014) 19. 105

[89] D. J. Hunter, S. Valenti, R. Kotak, W. Meikle, S. Taubenberger, A. Pastorello et al., *Extensive optical and near-infrared observations of the nearby, narrow-lined type ic sn 2007gr: days 5 to 415*, *Astronomy & Astrophysics* **508** (2009) 371–389. 105, 113, 114, 116, 117, 118

[90] D. Dimitrov, D. Kjurkchieva and M. Danailova, *Bv r ccd photometric observations of sn 2007gr*, *Bulgarian Astronomical Journal* **15** (2011) 57–64. 105, 115, 116, 117

[91] A. Kumar, S. B. Pandey, R. Konyves-Toth, R. Staten, J. Vinko, J. C. Wheeler et al., *Sn 2010kd: Photometric and spectroscopic analysis of a slow-decaying superluminous supernova*, *The Astrophysical Journal* **892** (2020) 28. xx, 110, 120, 121, 123, 125, 129

[92] R. Chornok, A. V. Filippenko, W. Li and R. J. Foley, *Supernova 2007gr in ngc 1058*, *CBET* (2007) . 111, 113

[93] A. Gal-Yam, *Luminous supernovae*, *Science* **337** (2012) 927–932. 120

[94] J. Vinko, W. Zheng, A. Romadan, R. Quimby, N. Whallon, S. B. Pandey et al., *Supernova 2010kd*, *CBET* (2010) . 120, 123

[95] A. Pastorello, S. Smartt, M. Botticella, K. Maguire, M. Fraser, K. Smith et al., *Ultra-bright optical transients are linked with type ic supernovae*, *The Astrophysical Journal Letters* **724** (2010) L16. 120, 128

[96] R. Roy, *Investigation of Energetic Cosmic Explosions and their after effects*. PhD thesis, Kumaun University, 12, 2012. xx, 121, 123

[97] T. Poole, A. Breeveld, M. Page, W. Landsman, S. Holland, P. Roming et al., *Photometric calibration of the swift ultraviolet/optical telescope*, *Monthly Notices of the Royal Astronomical Society* **383** (2008) 627–645. 122

[98] R. Thomas, P. Nugent and J. Meza, *Synapps: data-driven analysis for supernova spectroscopy*, *Publications of the Astronomical Society of the Pacific* **123** (2011) 237. 129

[99] M. Nicholl, S. J. Smartt, A. Jerkstrand, C. Inserra, S. Sim, T.-W. Chen et al., *On the diversity of superluminous supernovae: ejected mass as the dominant factor*, *Monthly Notices of the Royal Astronomical Society* **452** (2015) 3869–3893. 129

[100] J. M. Silverman, R. J. Foley, A. V. Filippenko, M. Ganeshalingam, A. J. Barth, R. Chornock et al., *Berkeley supernova ia program–i. observations, data reduction and spectroscopic sample of 582 low-redshift type ia supernovae*, *Monthly Notices of the Royal Astronomical Society* **425** (2012) 1789–1818. 130

[101] T. Faran, D. Poznanski, A. Filippenko, R. Chornock, R. J. Foley, M. Ganeshalingam et al., *A sample of type ii-l supernovae*, *Monthly Notices of the Royal Astronomical Society* **445** (2014) 554–569. 134

[102] T. M. Davis and M. I. Scrimgeour, *Deriving accurate peculiar velocities (even at high redshift)*, *Monthly Notices of the Royal Astronomical Society* **442** (2014) 1117–1122. 135

[103] R. Graziani, H. Courtois, G. Lavaux, Y. Hoffman, R. Tully, Y. Copin et al., *The peculiar velocity field up to z 0.05 by forward-modelling cosmicflows-3 data*, *Monthly Notices of the Royal Astronomical Society* **488** (2019) 5438–5451. 136

[104] R. Kessler, A. C. Becker, D. Cinabro, J. Vanderplas, J. A. Frieman, J. Marriner et al., *First-year sloan digital sky survey-ii supernova results: Hubble diagram and cosmological parameters*, *The Astrophysical Journal Supplement Series* **185** (2009) 32. 137

[105] T. M. Davis, L. Hui, J. A. Frieman, T. Haugbølle, R. Kessler, B. Sinclair et al., *The effect of peculiar velocities on supernova cosmology*, *The Astrophysical Journal* **741** (2011) 67. 137

[106] A. Johnson, C. Blake, J. Koda, Y.-Z. Ma, M. Colless, M. Crocce et al., *The 6df galaxy survey: cosmological constraints from the velocity power spectrum*, *Monthly Notices of the Royal Astronomical Society* **444** (2014) 3926–3947. 137

[107] S. W. Skillman, M. S. Warren, M. J. Turk, R. H. Wechsler, D. E. Holz and P. Sutter, *Dark sky simulations: Early data release*, *arXiv preprint arXiv:1407.2600* (2014) . xxii, 143, 144, 145

[108] P. A. Ade, R. Aikin, M. Amiri, D. Barkats, S. Benton, C. A. Bischoff et al., *Bicep2. ii. experiment and three-year data set*, *The Astrophysical Journal* **792** (2014) 62. 144

[109] P. S. Behroozi, R. H. Wechsler and H.-Y. Wu, *The rockstar phase-space temporal halo finder and the velocity offsets of cluster cores*, *The Astrophysical Journal* **762** (2012) 109. 144

[110] A. A. Berlind, D. H. Weinberg, A. J. Benson, C. M. Baugh, S. Cole, R. Davé et al., *The halo occupation distribution and the physics of galaxy formation*, *The Astrophysical Journal* **593** (2003) 1. 144

[111] K. M. Gorski, E. Hivon, A. J. Banday, B. D. Wandelt, F. K. Hansen, M. Reinecke et al., *Healpix: A framework for high-resolution discretization and fast analysis of data distributed on the sphere*, *The Astrophysical Journal* **622** (2005) 759. 145

[112] A. J. Ross, F. Beutler, C.-H. Chuang, M. Pellejero-Ibanez, H.-J. Seo, M. Vargas-Magana et al., *The clustering of galaxies in the completed sdss-iii baryon oscillation spectroscopic survey: Observational systematics and baryon acoustic oscillations in the correlation function*, *Monthly Notices of the Royal Astronomical Society* **464** (2017) 1168–1191. 146, 155, 161

[113] B. Leistedt, H. V. Peiris, F. Elsner, A. Benoit-Lévy, A. Amara, A. H. Bauer et al., *Mapping and simulating systematics due to spatially varying observing conditions in des science verification data*, *The Astrophysical Journal Supplement Series* **226** (2016) 24. 155

[114] M. Sinha and L. Garrison, *Corrfunc: Blazing fast correlation functions on the cpu*, *Astrophysics Source Code Library* (2017) . 157

[115] P. A. Ade, N. Aghanim, M. Arnaud, M. Ashdown, J. Aumont, C. Baccigalupi et al., *Planck 2015 results-xiii. cosmological parameters*, *Astronomy & Astrophysics* **594** (2016) A13. 158

[116] P. Peebles, *Statistical analysis of catalogs of extragalactic objects. i. theory*, *The Astrophysical Journal* **185** (1973) 413–440. 158

[117] L. Anderson, E. Aubourg, S. Bailey, D. Bizyaev, M. Blanton, A. S. Bolton et al., *The clustering of galaxies in the sdss-iii baryon oscillation spectroscopic survey: baryon acoustic oscillations in the data release 9 spectroscopic galaxy sample*, *Monthly Notices of the Royal Astronomical Society* **427** (2012) 3435–3467. 158, 160, 162

[118] H. Gil-Marín, W. J. Percival, A. J. Cuesta, J. R. Brownstein, C.-H. Chuang, S. Ho et al., *The clustering of galaxies in the sdss-iii baryon oscillation spectroscopic survey: Bao measurement from the los-dependent power spectrum of dr12 boss galaxies*, *Monthly Notices of the Royal Astronomical Society* **460** (2016) 4210–4219. 161

[119] A. G. Riess, L. M. Macri, S. L. Hoffmann, D. Scolnic, S. Casertano, A. V. Filippenko et al., *A 2.4% determination of the local value of the hubble constant*, *The Astrophysical Journal* **826** (2016) 56. 166

[120] M. Still, P. Roming, K. Mason, A. Blustin, P. Boyd, A. Breeveld et al., *Swift uvot detection of grb 050318*, *The Astrophysical Journal* **635** (2005) 1187.

[121] R. Nolthenius, *Rphot release 2.0: a ubvri and occultation photometry acquisition and reduction software package for pc-based observatories*, in *Research Amateur Astronomy*, vol. 33, p. 135, 1992.

[122] R. Thomas, *Syn++: Standalone sn spectrum synthesis*, *Astrophysics Source Code Library* (2013) .

[123] G. Marion, P. J. Brown, J. Vinkó, J. M. Silverman, D. J. Sand, P. Challis et al., *Sn 2012cg: Evidence for interaction between a normal sn ia and a non-degenerate binary companion*, *The Astrophysical Journal* **820** (2016) 92.

[124] D. Foreman-Mackey, D. W. Hogg, D. Lang and J. Goodman, *emcee: the mcmc hammer*, *Publications of the Astronomical Society of the Pacific* **125** (2013) 306.

[125] C. B. D'andrea, M. Sako, B. Dilday, J. A. Frieman, J. Holtzman, R. Kessler et al., *Type ii-p supernovae from the sdss-ii supernova survey and the standardized candle method*, *The Astrophysical Journal* **708** (2009) 661.

[126] H. Mo, Y. Jing and G. Börner, *On the error estimates of correlation functions*, *The Astrophysical Journal* **392** (1992) 452–457.

[127] M. Crocce, A. Ross, I. Sevilla-Noarbe, E. Gaztanaga, J. Elvin-Poole, S. Avila et al., *Dark energy survey year 1 results: galaxy sample for bao measurement*, *Monthly Notices of the Royal Astronomical Society* **482** (2019) 2807–2822.

[128] R. Roy, *Investigation of energetic cosmic explosions and their after effects*, .

[129] I. Arcavi, A. Gal-Yam, S. B. Cenko, D. B. Fox, D. C. Leonard, D.-S. Moon et al., *Caltech core-collapse project (cccp) observations of type ii supernovae: evidence for three distinct photometric subtypes*, *The Astrophysical Journal Letters* **756** (2012) L30.

[130] N. Kaiser, *A sparse-sampling strategy for the estimation of large-scale clustering from redshift surveys*, *Monthly Notices of the Royal Astronomical Society* **219** (1986) 785–790.

[131] M. Vargas-Magana, D. D. Brooks, M. M. Levi and G. G. Tarle, *Unraveling the universe with desi*, *arXiv preprint arXiv:1901.01581* (2019) . 166